Numerical Investigations of Incompressible Buoyancy-driven Flows over Wide Parametric Ranges using Lattice Boltzmann Method

A thesis submitted in partial fulfillment of the requirements for the award of the degree of

Doctor of Philosophy

by

Shikha Bhuyan

Roll No: 146103040

under the guidance of

Prof. Dipankar Narayan Basu

Department of Mechanical Engineering

Indian Institute of Technology Guwahati

Guwahati- 781039, Assam, India

April 2024

भारतीय प्रौद्योगिकी संस्थान गुवाहाटी
Indian Institute of Technology Guwahati

SELF DECLARATION

I, Shikha Bhuyan, hereby declare that the thesis entitled "***Numerical Investigations of Incompressible Buoyancy-driven Flows over Wide Parametric Ranges using Lattice Boltzmann Method***" is my original work and has not been submitted elsewhere for any degree or examination. This thesis represents my own research conducted under the supervision of Prof. Dipankar Narayan Basu from Department of Mechanical Engineering at Indian Institute of Technology, Guwahati (IITG).

April, 2024

Name: Shikha Bhuyan
Roll No: 146103040
Department of Mechanical Engineering
Indian Institute of Technology Guwahati

भारतीय प्रौद्योगिकी संस्थान गुवाहाटी
Indian Institute of Technology Guwahati

CERTIFICATE

This is to certify that the work contained in this thesis entitled "***Numerical Investigations of Incompressible Buoyancy-driven Flows over Wide Parametric Ranges using Lattice Boltzmann Method***" by **Shikha Bhuyan**, bearing roll no.**146103040** has been carried out under my supervision and that this work has not been submitted elsewhere for a degree.

April, 2024

Supervisor: **Prof. Dipankar Narayan Basu**

Associate Professor,
Department of Mechanical Engineering,
Indian Institute of Technology Guwahati

भारतीय प्रौद्योगिकी संस्थान गुवाहाटी
Indian Institute of Technology Guwahati

Acknowledgements

I stand humbled and deeply grateful as I pen down these words of gratitude, for the completion of this journey would not have been possible without the unwavering support and encouragement from countless individuals who have been instrumental in shaping my path.

First and foremost, I express my sincere gratitude to my esteemed supervisor, Prof. Dipankar Narayan Basu, whose unwavering guidance and mentorship have been a beacon of light throughout this research endeavor. His profound expertise, insightful feedback, and constant motivation have not only enriched this thesis but have also shaped me into a better researcher and individual.

I express my heartfelt gratitude to my doctoral committee; the chairman, Prof. Amaresh Dalal, the committee member, Prof. Gavara Madhusudhana and external member, Prof. Raghavendra Gupta for their prompt review of my work and valuable feedback. Their insightful suggestions played a pivotal role in refining and shaping the current form of this thesis. Their support and guidance have been instrumental in enhancing the quality of my research.

I am indebted to the faculty members of the Department of Mechanical Engineering at Indian Institute of Technology Guwahati, whose passion for imparting knowledge and dedication to academic excellence have laid the foundation for my intellectual growth. Their stimulating lectures and thought-provoking discussions have expanded my horizons, inspiring me to explore new frontiers in the realm of science and engineering.

Heartfelt appreciation goes out to my dear friends and colleagues who have stood by my side, offering encouragement, camaraderie, and occasional comic relief. Your presence has made this journey not only fulfilling but also enjoyable.I would like to extend special appreciation to my friend, Dr. Sambit Mazumdar, for providing unwavering support and encouragement throughout my entire thesis journey. His presence and assistance have been invaluable, making my research experience even more rewarding.

I extend my gratitude to the support staff and administrators at Indian Institute of Technology Guwahati

for their tireless efforts in maintaining a conducive research environment. Their invaluable assistance has streamlined various processes and allowed me to focus wholeheartedly on my academic pursuits. Additionally, I would like to express my appreciation to Tezpur University, my workplace, for their continued support throughout my research journey at IIT Guwahati.

To my beloved family, who have been my unwavering pillars of strength, I owe the deepest gratitude. Your unconditional love, constant encouragement, and unwavering belief in my abilities have been the driving force behind my accomplishments. You have been my rock, providing solace during moments of doubt and rejoicing in every triumph.

The acknowledgment would be incomplete without mentioning my beloved husband, Mr. Goutom Ain. His love, understanding, and unwavering support have been the driving force behind my accomplishments throughout this thesis journey. I am deeply grateful for his constant encouragement and belief in my abilities, which have been pivotal in making this research endeavor successful.

Lastly, I offer my profound gratitude to the universe, for its mysterious ways of orchestrating serendipitous encounters and providing opportunities that have shaped my academic journey.

This thesis stands as a testament to the cumulative efforts of all those who have touched my life in profound ways. Each interaction, whether big or small, has left an indelible mark on my journey, and for that, I am eternally thankful.

As I step into the future with a heart full of gratitude, I am mindful of the responsibility that comes with the knowledge I have gained. I pledge to utilize this knowledge to contribute positively to society and continue my pursuit of knowledge and excellence.

Shikha Bhuyan

Abstract

This thesis presents a practical and significant advancement in the Lattice Boltzmann Method (LBM) for buoyancy-driven flow in a single fluid phase. Utilizing the D2Q9 lattice and the LBGK method in two dimensions, the developed LBM codes demonstrate excellent performance across a wide range of problems. Special attention is given to ensuring accurate and realistic parameterizations, thoroughly validated both qualitatively and quantitatively through rigorous exercises.

The thesis begins by validating the newly developed LBM code through simulations of various benchmark isothermal and thermal flow problems. Next, the thermal lattice Boltzmann method (TLBM) is applied to study natural convection problems. The study introduces non-Boussinesq simulations, considering temperature-dependent fluid properties, and compares them to the traditional Boussinesq approach. The results reveal that non-Boussinesq simulations exhibit higher values of entropy generation and Nusselt numbers, reflecting a more accurate representation of fluid behavior. Furthermore, the role of fluid friction in entropy generation is examined, and it is found that as Rayleigh number (Ra) increases, the contribution of entropy generation due to fluid friction becomes more prominent, exceeding that of heat transfer at a critical Ra value of 10^6. This highlights the increasing significance of fluid friction in overall entropy production, particularly beyond the critical Ra.

The fundamental focus of this thesis is to delve into the intricate dynamics of buoyancy-driven flow within confined spaces. This encompasses a comprehensive exploration of the behaviors and phenomena associated with fluid motion induced by density differences, particularly when subject to constraints imposed by enclosed environments. Throughout the current research work, various instances of buoyancy-driven flow, seeking a nuanced understanding of the underlying mechanisms that govern fluid behavior in such scenarios have meticulously been examined. By shedding light on these intricacies, the thesis aims to contribute valuable insights to the broader understanding of fluid dynamics, especially within the context of buoyancy-driven flows in confined spaces. Furthermore, the research explores mixed convection problems on three different configurations, investigating influential parameters (Ri, Re, Pr, ϕ), and optimizing their effects on heat transfer and entropy generation, providing new insights into this field. The three distinct cases are: (i) Top lid moving in forward direction and bottom lid is kept stationary (Case 1); (ii) Both top and bottom lids moving in forward direction (Case 2); (iii) Both top and bottom lids moving in opposite direction (Case 3). Comparing the three cavity configurations, it is observed that heat transfer rate and irreversibility are minimum for Case 1, followed by Case 2 and Case 3, for

all varying parameters. The inclination angle (ϕ) has a notable impact on both Nusselt number and entropy generation values, reaching their maximum limit at $\phi = 40^0$ for Case 1 and 2, and $\phi = 50^0$ for Case 3. However, the friction coefficient remains relatively constant for all three cases, regardless of the inclination angle. The maximum heat transfer rate and entropy generation are achieved at $\phi = 90^0$ for all cases. In addition to this, the study of aspect and velocity ratio suggests that increasing the aspect ratio to AR=4 and decreasing the velocity ratio leads to decreased irreversibility, which may improve the overall performance of the system.

This study extends the applicability of the developed models by exploring a unified approach to investigate the influence of nanofluids on the thermal-hydraulic behavior of natural circulation loops (NCLs). The goal is to optimize these systems by reducing entropy generation and improving performance using isothermal boundary conditions at the heater and cooler sections of the NCL. The investigation involves a transient study of NCLs, observing their time-dependent response under various thermal boundary conditions. These considered conditions include isothermal (CT), constant heat flux (CHT), linearly increasing (LI), linearly decreasing (LD), and sinusoidal heat flux conditions. The impact of different heat flux boundary conditions on heat transfer and entropy generation is thoroughly explored. The sinusoidal heat flux condition demonstrates higher heat transfer rates due to induced temperature and velocity fluctuations, resulting in enhanced convective heat transfer through fluid mixing. On the other hand, the linearly decreasing flux condition exhibits the highest fluctuation in entropy generation among the different heat flux boundary conditions.

Contents

List of Figures

List of Tables

भारतीय प्रौद्योगिकी संस्थान गुवाहाटी
Indian Institute of Technology Guwahati

Nomenclature

Nomenclature

Be	Bejan number
c_p	Specific heat of the fluid at constant pressure (J/kgK)
c_s	Lattice speed of sound (m/s)
Cu	Copper
D	Diameter of the channel (m)
dt, dx	Time and space step (s)
e_i	Discrete lattice velocity
F	Body force per unit volume (N/m^3)
f	Momentum distribution function
F_i	Lattice buoyancy force
g	Gravitational acceleration (m/s^2)
g	Thermal distribution function
Gr	Grashof number $(-)$
H	Height (m)
k	Thermal conductivity (W/mK)
L	Length (m)
Ma	Mach number $(-)$
Nu	Nusselt number $(-)$

p	Static pressure (N/m^2)
Pr	Prandtl number $(-)$
r	Radial distance (m)
Ra	Rayleigh number $(-)$
Re	Reynolds number $(-)$
Ri	Richardson number $(-)$
S_Ψ	Local non-dimensional entropy generation due to fluid friction
S_θ	Local non-dimensional entropy generation due to heat transfer
S_l	Dimensional total entropy generation (J/K)
S_T	Local non-dimensional entropy generation
T	Temperature (K)
U, V	Non-dimensional velocity components in X and Y directions, respectively
u, v	Velocity components in x and y directions, respectively (m/s)
W	Width (m)
w_i	Weight function
X, Y	Non-dimensional Cartesian coordinate
x, y	Cartesian coordinates (m)

Greek Symbols

α	Thermal diffusivity (m^2/s)
β	Thermal expansion coefficient (K^{-1})
Δt	Lattice time step
Δx	Lattice space step
γ	Non-Boussinesq parameter
μ	Dynamic viscosity (kg/ms)

Ω	Collision matrix
ϕ	Inclination angle
ρ, ρ_0	Density of fluid and ambience, respectively (kg/m^3)
τ	Lattice single relaxation time
θ	Non-dimensional temperature
φ	Volume fraction
ϑ	Kinematic viscosity (m^2/s)

Subscripts

$2D$	Two-dimensional
∞	Ambient
eff	Effective
nf	Nanofluid
b	Bottom
c	Cold
f	Base fluid
h	Hot
i	Number of the distribution function
m	Modified
o	Reference
s	Solid
t	Top

Superscripts

$-$	Average

/	Inner length
*	Non-dimensional variable
eq	Equilibrium
◦	Degree

Abbreviations

AR	Aspect ratio
BC	Boundary condition
BE	Boltzmann equation
BGK	Bhatnagar-Gross-Krook
CFD	Computational fluid dynamics
LB	Lattice Boltzmann
LBE	Lattice Boltzmann equation
LBM	Lattice Boltzmann method
LGA	Lattice gas automata
NCL	Natural circulation loop
SRT	Single relaxation time
TLBM	Thermal lattice Boltzmann method

Chapter 1

Introduction

Buoyancy-driven flow, also known as natural convection, is a fascinating phenomenon that occurs when the movement of fluid is driven primarily by density differences resulting from temperature variations within the fluid. This natural mechanism plays a crucial role in various natural and engineering systems, ranging from geophysical processes to industrial applications. The behavior of buoyancy-driven flow depends on several factors, including temperature difference, fluid properties, geometry of the system, and boundary conditions. The resulting flow patterns can vary from simple, steady-state convection cells to complex, time-dependent phenomena, such as plumes, jets, and vortices. Studying buoyancy-driven flow involves a combination of theoretical analysis, numerical simulations, and experimental investigations. Mathematical models, such as the Navier-Stokes equations coupled with energy equations, provide a theoretical framework for understanding and predicting the behavior of buoyancy-driven flows. Computational fluid dynamics (CFD) simulations enable researchers to visualize and analyze these flows in complex geometries, while experimental techniques such as flow visualization and thermography provide valuable insights into the physical phenomena. In conclusion, buoyancy-driven flow is a fascinating area of fluid dynamics that arises from density variations caused by temperature gradients. Its understanding and control are crucial for a wide range of practical applications, from energy-efficient building design to industrial processes and environmental studies. By studying and harnessing the principles of buoyancy-driven flow, scientists and engineers can optimize designs, enhance performance, and improve the overall efficiency of various systems.

This thesis will present a 2D buoyancy-driven fluid simulation based on the lattice Boltzmann method.

1.1 Classification of buoyancy-driven flow

Buoyancy-driven flow can be classified into different types based on various factors such as the geometry of the system, the driving mechanism, and the flow regime.

(i) Vertical and horizontal flows: Buoyancy-driven flows can be classified based on the orientation of the flow with respect to the gravity vector. Vertical flows occur when the fluid motion is predominantly in the vertical direction, such as the upward movement of warm air or the downward sinking of cold air. Horizontal flows, on the other hand, take place when the fluid motion is primarily in the horizontal plane, like the flow of hot air along a ceiling or the spreading of a heated fluid layer on a horizontal surface.

(ii) Enclosed and unconfined flows: Buoyancy-driven flows can also be categorized based on the confinement of the flow. Enclosed flows occur within enclosed spaces or channels, such as air circulation within a room or the flow of fluid in a closed pipe. Unconfined flows, on the other hand, involve the motion of fluid in open environments, such as natural convection in the atmosphere or the movement of water in a lake due to temperature differences.

(iii) Forced and natural convection: Buoyancy-driven flows can be further classified based on the dominant driving mechanism. Free convection refers to situations where the buoyancy force resulting from temperature differences is the sole driving force for fluid motion. This commonly occurs in systems where forced convection is negligible. Forced convection, on the other hand, arises when external forces (such as forced flow due to fans or pumps) contribute to the fluid motion. Mixed convection occurs in situations where both natural and forced convection coexists, and the relative strengths of these driving forces determine the flow behavior.

(iv) Flow regimes: Buoyancy-driven flows can exhibit various flow regimes depending on the strength of the driving forces and the system characteristics. These regimes can range from laminar to turbulent. In laminar flows, the fluid motion is smooth and ordered, whereas, in turbulent flows, the fluid motion is highly chaotic and unpredictable. The transition between laminar and turbulent flow regimes can occur as the driving forces or system parameters change.

It is important to note that these classifications are not mutually exclusive, and a buoyancy-driven flow can fall into multiple categories simultaneously, depending on the specific characteristics of the system

under consideration. The classification helps in understanding and characterizing the flow behavior and aids in the analysis and design of the systems involving buoyancy-driven flow.

1.2 Literature review

Significant contributions to our understanding of fluid dynamics and heat transfer have been made through pioneering research on buoyancy-driven flow. The German physicist Franz Grashof conducted a series of experiments in the late 19th century to study natural convection. He investigated the relationship between buoyancy forces and the heat transfer characteristics of fluids. Grashof's work laid the foundation for understanding the fundamental principles governing natural convection. The German engineer Wilhelm Nusselt developed a heat transfer correlation known as the Nusselt number in 1920s, which relates the convective heat transfer coefficient to fluid properties and flow conditions. His research provided a quantitative understanding of convective heat transfer in natural convection and remains widely used in engineering calculations and design. The advent of computational fluid dynamics in the latter half of the 20th century revolutionized the study of buoyancy-driven flow. Numerical simulations using computational methods, such as finite volume and finite element techniques, have enabled researchers to investigate complex flow phenomena, optimize designs, and predict heat transfer rates in natural convection systems. With advancements in experimental techniques, researchers have been able to visualize and measure flow patterns, temperature fields, and heat transfer rates in buoyancy-driven flows. Techniques such as particle image velocimetry, laser-induced fluorescence, and infrared thermography have provided detailed insights into the complex nature of natural convection. These pioneering research efforts, along with subsequent studies, have significantly expanded our understanding of buoyancy-driven flow, leading to improved designs, energy-efficient systems, and enhanced heat transfer technologies in various fields, including building design, electronics cooling, energy systems, and environmental sciences.

1.2.1 Natural and mixed convection in enclosures

Flow inside enclosures has been extensively researched in this context throughout the years [2–7] . Several studies have been conducted to better understand the fluid dynamics and thermal behavior of forced convection [2, 6] and mixed convection [8, 9] in lid-driven cavity flows regarding convection heat transfer. Fundamental fluid mechanics and heat transfer studies such as cooling of microelectronics

components and heat transfer in compact heat exchangers both benefit from a thorough understanding of buoyancy-induced flow [10–13]. This heat transfer mode has been the subject of numerous recent scientific papers worldwide.

Thermal flow in a square cavity with two adiabatic horizontal walls (i.e., Neumann boundary conditions) and two thermally fixed vertical walls (i.e., Dirichlet boundary conditions), where the left wall is hotter than the right, is the standard benchmark test for numerical techniques. Two non-dimensional quantities, the Prandtl number (Pr) and the Rayleigh number (Ra), govern this flow. The Prandtl number, which is often considered to be 0.71 for air and 7 for water near temperature, is the ratio of momentum to thermal diffusivity. The crucial Rayleigh number, which specifies whether the convection boundary layer is laminar or turbulent ($Ra = 10^6$ for turbulent flows), determines when convection begins.

The authors Gau et al. [14] and Rahli et al. [15], analyzed the flow patterns and heat transfer characteristics in the channels using experimental and numerical methods. They explored the effects of various parameters such as channel geometry, temperature difference, and fluid properties on the secondary flow and heat transfer enhancement. They provide insights into the mechanisms behind secondary flow and its impact on convective heat transfer. Understanding these phenomena can help improve heat transfer efficiency and optimize the design of heat exchange systems. As highlighted by them the parameters like Reynold's number (Re), Rayleigh number (Ra), Prandtl number (Pr), and the transverse aspect ratio (A, width to height ratio) have a great impact on heat transfer mode. Gau et al. [14] conducted experimental investigations focusing on the secondary airflow structure and heat transfer enhancement in both horizontal parallel-plate and convergent channels. In the horizontal channel configuration, the bottom wall, heated uniformly, is horizontal, while the opposing wall is insulated and inclined to the horizontal plate, creating a convergence angle of 2° for the convergent channel. The channel is characterized by an aspect ratio (width to height) of 5.56 and a ratio of channel length to height at the entrance of 0.04. Operating conditions include a Reynolds number ranging from 99 to 1999, a buoyancy parameter (Gr/Re^2) spanning from 1.4 to 896, and a Prandtl number of 9.6 for the airflow. In their investigation, Rahli et al. [15] examined a horizontal rectangular duct's geometry. They considered the fluid to be incompressible and Newtonian, and the laminar flow was modeled using the 3D incompressible Navier-Stokes equations under the Boussinesq assumption. The duct experiences heating from the bottom and cooling from the top, with constant concentrations applied to the bottom and top walls. At the duct entry, known values for fluid temperature and concentration are specified. Furthermore, zero thermal and

specie fluxes are applied to the other longitudinal boundaries.

The objective of the study made by Rodrigues et al. [16] is to geometrically optimize a lid-driven cavity in a two-dimensional area with mixed convective, incompressible, laminar flows. The Nusselt number (Nu) and the dimensionless heat transfer rate (q') serve as performance metrics. With $Re = 400$, $Pr = 6.0$, and two different Richardson numbers ($Ri = Gr/Re^2 = 0.1$ and 1.0). These Richardson numbers represented scenarios of forced convective dominance (Ri = 0.1) and equilibrium between forced and natural convection (Ri = 1.0). All simulations have been run for a stable stratified mixed convection flow. Results showed that a significant factor in the theoretical design advice is the performance indicator choice. It was demonstrated that the designs that maximize the Nusselt number did not lead necessarily to the highest heat transfer rate, showing that this parameter depends on the balance between the Nusselt number and heat exchange area.

The early numerical research on mixed convection was in 2D since it was difficult to simulate the intricate process because it is so complex. Preliminary findings of a numerical examination of mixed convection heat transfer in a horizontal and inclined channel (aspect ratio A=10), evenly heated from below, are presented by Ozsunar et al. [17]. Gr values varied from 7×10^5 to 4×10^6, while Reynolds numbers ranged from 50 to 2000. The findings indicate that the buoyancy-driven secondary vortex flow, the initiation of instability, and the resulting heat transfer enhancement are influenced by the Gr^*, Re numbers, and inclination angle. Larger Gr^* values lead to the upstream movement of thermal instability onset. Thermal instabilities are postponed with higher Re numbers and inclination angles. Increasing the inclination angle not only achieves heat transfer enhancement prior to instability onset but also delays the formation of the secondary flow. The fluctuations in local Nusselt number values increase with an increase in the Gr^* number, while they decrease with increasing Reynolds number. Higher Grashof numbers result in a slower attainment of fully developed flow conditions. In summary, the buoyancy-driven secondary flow can enhance heat transfer by up to 250 percent, as indicated by the maximum Nusselt number obtained. The evolutionary CFD techniques assisted Bammou et al. [18] to resolve complicated flow and see the role generation process in mixed convection in detail. Depending on whether the flow is developing or completely evolved in a mixed convection flow, different heat transmission characteristics were applied. Meyer and colleagues investigated thermal entrance length and Nusselt number in mixed convection regime identified three distinct regions for developing laminar flow and proposed new correlations for mixed convection in the three regions [19–22]. It was found that the

flow transitioned faster with increasing free convection effects and Reynolds number.

1.2.2 Natural circulation loop

A natural circulation loop (NCL), also known as a natural circulation system or a thermosiphon, is a type of heat transfer loop that operates without the need for any mechanical pumps. It relies on the principle of buoyancy-driven flow to circulate a fluid (usually a liquid) in a closed loop. In a natural circulation loop, the fluid circulates due to the density difference caused by temperature variations within the loop. When a fluid is heated, it becomes less dense and tends to rise, creating an upward flow. As the heated fluid rises, it transfers heat to its surroundings, which causes it to cool down and become denser. The denser fluid then descends, completing the loop. One common example of a natural circulation loop is a solar water heater. In this system, sunlight heats the water in a collector, causing it to rise and flow into a storage tank. As the hot water is drawn from the tank for use, colder water from the bottom of the tank replaces it, completing the circulation loop. Natural circulation loops have some advantages over systems that rely on mechanical pumps. They are simpler in design, have lower maintenance requirements, and can operate without electricity. However, they have certain limitations, such as slower circulation rates and a limited ability to overcome high resistance or pressure drops in the system.

In engineering and industrial applications, natural circulation loops are often used in steam generators, nuclear reactors, and certain types of heat exchangers. They can be designed and optimized based on the specific requirements of the application, considering factors such as fluid properties, system geometry, and thermal loads.

To ensure that the system works as planned, the designers must carefully analyze the variables affecting natural circulation in each application. To get an optimal design that offers acceptable thermal performance and to prevent undesirable dynamic behavior such as flow instabilities or flow reversals, it is crucial to understand the fundamental factors affecting the performance of NCL. Extensive research on superabounds with numerical and experimental studies is being made which are based on the dependence of various geometric parameters, apt numerical modeling, the orientation of heater, and cooler on NCLs. A thorough review can be cited in [23–27]. The findings indicate that the most stable orientation is when both the heater and cooler are vertical, while the least stable orientation is when both are horizontal, despite the latter allowing for the highest flow rate according to steady state analysis. When considering a specific heater orientation, the loop with a vertical cooler is more stable than the one with a horizontal

cooler. Similarly, when considering a specified cooler orientation, the loop with a vertical heater is more stable than the one with a horizontal heater.

The theoretical model and experimental findings also indicate that thermal stratification is the cause of instability, leading to the hot plug remaining trapped just below the elbow in the vertical down leg. Therefore, placing the cooler just below the elbow in the vertical down leg improves stability as shown in Figure 1.1. Other methods to mitigate instability include increasing the L/D (length-to-diameter ratio) and St (Stanton number).Increasing the St beyond a certain value can completely eliminate the instability, while increasing the L/D can only shift the unstable zone without eliminating it entirely. The influence of heater and cooler lengths on stability was examined using the linear method for the orientation where both the heater and cooler are horizontal. The results show that the heater length has only a marginal effect on stability, whereas the cooler length has a significant impact. Increasing the lengths of both the heater and cooler enhances stability.

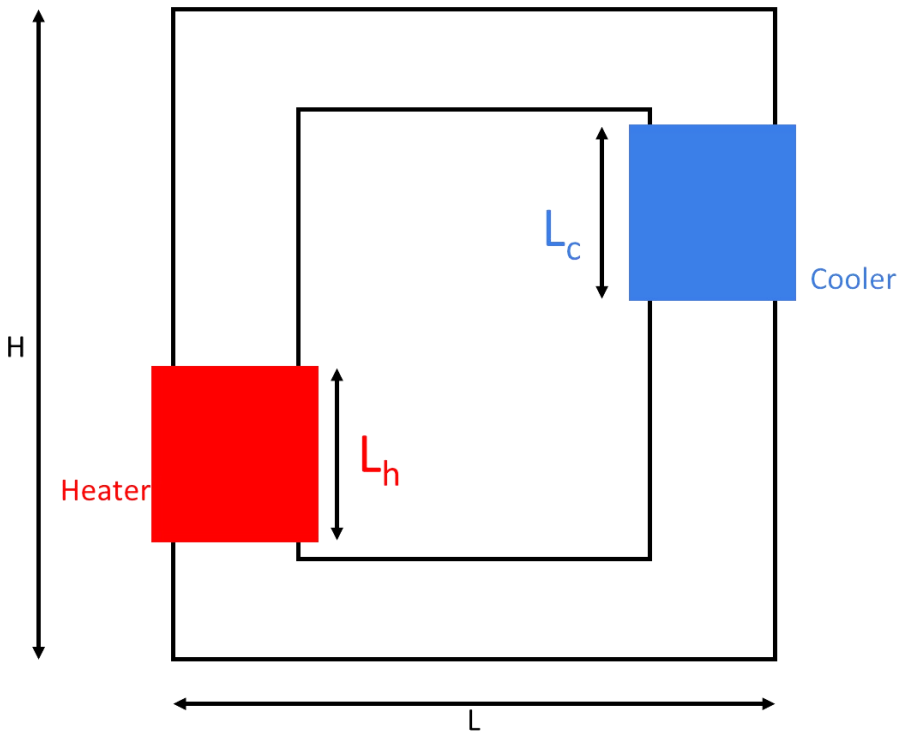

Figure 1.1: A theortical model for a natural circulation loop

NCL is a self-sustaining system, making it challenging to manage any flow-related factors from the outside once the system is in operation. For this reason, it is crucial to examine the function of various geometric parameters during the design stage itself. The natural circulation effect was studied

on conventional solar still by Rahmani et. al [28]. An experimental approach was attempted in a rectangular natural circulation loop. They concluded that separating the condenser from the still enhances the temperature difference between the water and condenser wall and hence a large difference in density can be obtained due to differences in fluid thermodynamic conditions.

Krishnani and Basu [29] numerically analyzed the effect of loop inclination on the stability of NCL. The research was carried out under specific operating circumstances and inclination degrees. Because of the reduction in effective gravitational acceleration and a concomitant decline in local buoyancy effects, it was discovered to have a considerable stabilizing influence on tilt. By raising the tilt angle, the loop can be stabilized in a shorter time period, but at the cost of a lower steady-state flow rate. For the chosen geometry, the best tilt angle is found to be 15 degrees, which results in the loop's stability fluctuating the least. Vijayan et. al [30] studied the effect of loop diameter on the steady state and stability behavior of single-phase and two-phase NCLs. They found that the loop diameter plays an important role in the stability behavior.

A collection of general governing equations, dimensionless groups, and associated reference parameters were created by Basu et al. [31]. In this study, a recommended reference temperature drop was proposed to enable the simulation of various heat input modes while maintaining the integrity of the mathematical model. Additionally, suitable friction factor and heat transfer correlations were determined, along with the definition of a unified parameter to characterize the system. Here the authors have developed and discussed the analytical solutions for several representative loops operating under steady-state conditions and compared the results with a range of existing experimental studies. They also concluded that the use of Richardson number (Ri) as characterizing parameter seems a better choice from a unification point of view, compared to the convenional Grashof number Gr_m. These mathematical models are used to forecast the effectiveness of loops and propose a reference temperature decline and various heat input patterns. In a rectangle natural circulation loop, Nayak et al.'s [32] investigation focused on the natural circulation process. They created mathematical models and ran simulations of the loop's stable properties. The conservation equations for mass, momentum, and energy in the transient phase are solved using the finite difference technique. The study employs both linear and nonlinear analyses to investigate this behavior. Interestingly, the stability maps obtained through both approaches exhibit close agreement with each other. Notably, the nonlinear analysis reveals that perturbation increments from 5% to 35% do not significantly affect the loop's stability behavior. Moreover, the frequency of oscillations is observed

to be linked to the loop circulation time.

1.2.3 Effect of Nanofluids on entropy generation and heat transfer

The development of advanced heat transfer fluids received considerable coverage from researchers and scientists over the last few years. Regular fluids (ethylene glycol, oil, water) are commonly used in industrial and engineering applications. However, the heat transfer rate of these fluids is limited due to weak thermal conductivity. Therefore, to resolve its deficiency, a single form of nanosized particles is applied to the above-mentioned fluids and called a 'nanofluid'. This term was introduced by Choi and Eastman [33] for the first time in 1995. To name a few, the advantages of utilizing nanofluids filled in a rectangular enclosure were examined by Khanfer et al. [34] and Oztop and Abu-Nada [35].

Optimum conditions were found by Mamourian et. al. [36] by optimizing the mixed convection heat transfer with entropy generation in a wavy surface square lid-driven cavity filled with Cu–water nanofluid. When the values of the Ri number (Richardson number) and the volume fraction of Cu nanoparticles are increased, the mean Nusselt number decreases. This phenomenon can be attributed to the fact that an increase in nanoparticle volume fraction results in an increase in fluid viscosity, which subsequently decreases the velocity field. Also, the elevated nanoparticle volume fraction leads to a reduction in temperature gradients, thereby decreasing the entropy generation rate. Therefore, an increased nanoparticle volume fraction contributes to a decrease in both the mean Nusselt number and the entropy generation rate.

Roy et al. [37] examined the role of moving horizontal walls on entropy generation during mixed convection within entrapped triangular cavities. The study was performed for moving horizontal walls involving isothermally hot inclined walls and cold horizontal walls (case 1) or isothermally cold inclined walls and hot horizontal walls (case 2). It is found that at $Pr = 0.026$ and $Gr = 10^5$, the minimum entropy generation with a higher heat transfer rate occurs for $Re = 100$ within both the upper and lower cavities, irrespective of the cases. Overall, it is found that, at $Pr = 7.2$ and $Gr \geq 10^4$, $Re = 100$ may be suitable based on the reasonable entropy generation (S_{total}) with a higher heat transfer rate (Nu_t or Nu_b) within the upper and lower cavities, irrespective of the cases. At $Pr = 7.2$ and $Gr \approx 10^5$, $Re = 10$ may be suitable based on the minimum entropy generation (S_{total}) with reasonable heat transfer rate (Nu_t or Nu_b) within the upper cavity for case 1 and lower cavity for case 2. Nayak et al. [38] examined the heat transfer and entropy generation in mixed convection within an inclined skewed cavity using finite volume

method. The effects of relevant parameters such as, Richardson number ($0.1 \leq Ri \leq 5$), Reynolds number ($100 \leq Re \leq 1000$), nanoparticle volume fraction ($0 \leq \phi \leq 0.2$) on the mixed convection of nanofluid are studied by considering acute to obtuse skew angle and inclination angle between -300° to 300°. It was reported that increasing the fraction of nanoparticles enhances the heat transfer as well as the net entropy generation. It was also found that the heat transfer rate and irreversibility in the system are sensitive to the inclination angle. The average Nusselt number and the net entropy generation show independence to the inclination angle at negligible buoyancy effect. The average Nusselt number and total entropy generation increase with the increase of the Richardson number at a fixed Reynolds number. Entropy generation decreases and the heat transfer increases as the skew angle is increased up to 90°.

The entropy generation in Poiseuilli-Benard channel flow was analyzed by Abbassi et al. [39]. It was found that the maximum entropy generation is localized at areas where heat exchanged between walls and flow is maximum. There is no significant entropy generation seen in the main flow. A numerical-based work was done by Khorasanizadeh et al. [40] to study the impact of nanoparticles on entropy generation for a lid-driven square cavity mixed convection case. The authors reported that the addition of nanoparticles to the base fluid affects the entropy generation, flow pattern, and thermal behavior, especially at high Rayleigh numbers and low Reynolds numbers. However, the minimum entropy generation occurs in pure fluid at low Rayleigh numbers and low Reynolds numbers. Hence, a proper choice of parameters is essential if enhanced heat transfer and minimum increased entropy generation are expected. The simultaneous effects of Richardson number and inclination angle on entropy generation and heat transfer were examined by Bahiraei et al. [41]. The authors concluded by this study of mixed convection of CuO-water nanofluid that, an increase in inclination angle from 0° to 75° leads to an increase of convection heat transfer and a decrease of total entropy generation and consequently, a proper heat exchange together with low irreversibility is achieved. An increase in the concentration of the nanofluid has several effects: it enhances the thermal entropy generation rate, reduces the frictional entropy generation rate, and leads to an increase in the convective heat transfer coefficient. When the Richardson number is increased, both the heat transfer rate and the thermal and total entropy generation rates are enhanced. However, the frictional entropy generation rate does not exhibit significant variation. Additionally, the temperature of the nanofluid increases as the Richardson number increases.

1.2.4 Non-Boussinesq approximation

Joseph Valentin Boussinesq is the name most associated with modeling natural convection. In 1897, he proposed the jarring simplification of the natural convection issue that now bears his name: the Boussinesq model [42] ignores density differences aside from in the gravity term of the momentum equation. Importantly, this enabled the treatment of natural convection (NC) flows in an incompressible framework, substantially enhancing their mathematical tractability. The Navier—Stokes (NS) equations that control fluid motion were created by Claude Navier and George Stokes in 1850 and 1845, respectively. Nearly fifty years later, Boussinesq [42] developed his renowned approximation for NC issues. After some time, Josef [43] realized that Anton Oberbeck [44] had used the same idea in his explanation of heat conduction in liquids to account for currents produced by thermal gradients. In honor of their respective contributions, the model is now generally referred to as the Oberbeck—Boussinesq (OB) approximation. The following presumptions are used to establish the OB approximation:

- Minimal temperature variations
- Minimal viscous heat transfer
- Stable thermophysical characteristics
- Small hydrostatic pressure changes and the linear density state equation

Previous research has made clear that the Boussinesq approach is used for all numerical models. Assuming the linear change of density with temperature in the body force term and treating the density as constant in all other terms greatly streamlines the analysis. Further simplifying the modeling method is the treatment of the residual thermophysical properties as constants, which removes the equation of state from the analysis. However, for various kinds of fluids, the thermophysical characteristics of the field diverge considerably with operating temperature. It follows that the presumption that thermophysical characteristics are constant results in a major mistake. At greater power or temperature disparities, the error might become even more pronounced.

Gray and Giorgini conducted one of the first investigations to ascertain the precise range of the OB approximation performance [45]. They determined the valid temperature difference range of the OB approximation application in air and water as, respectively, less than 28.6 ℃ and 1.25 ℃ at a restricted

length scale of $L_{\text{ref}} \ll 8.3 \times 10^4$ cm and $L_{\text{ref}} \ll 2.4 \times 10^5$ cm by considering all fluid properties as linear functions of two state variables (temperature and pressure) at a reference temperature of $T_0 = 15$ and a reference pressure of $p_0 = 1$ atm. They got the ranges of $\Delta T/L_{\text{ref}} \ll 1020$ cm/℃ and $T/L_{\text{ref}} \ll 9.9 \times 10^4$ cm/℃ for air and water, respectively, to ignore the pressure work element in the energy calculation. From a physical point of view, non-Boussinesq effects arise in a wide range of circumstances. Each of the coefficients that are considered constant in the Boussinesq approximation may independently be assumed variables in order to set up a departure from this limit. In many physical and industrial applications such as thermal insulation systems, chemical vapor deposition reactors, atmospheric flows, and combustion processes, the temperature differences reach tens and hundreds of degrees. In such situations, all assumptions used to justify the Boussinesq approximation fail, and a different modeling approach is required that can account for realistic non-linear fluid property variations.

Frohlich et al. [46] dealt with large departures from the Boussinesq limit by considering the two-dimensional, periodic Rayleigh Benard problem as an example. The main effect investigated here is a strong variation in the density considered primarily as a function of temperature as it is accounted for by the low Mach number equations. Additionally, the effect of temperature-dependent viscosity and heat conductivity is considered. It turns out that non-Boussinesq effects are more and more confined to small parts of the domain as the Rayleigh number increases so that their influence on the mean properties of the flow diminishes. The findings suggest that in cases with large density variations, the Boussinesq approximation becomes inaccurate, and its limitations need to be considered. The departures from the Boussinesq approximation can have significant effects on the flow patterns, temperature distribution, and convective heat transfer rates in the Rayleigh–Bénard problem. It highlights the importance of recognizing and accounting for departures from the Boussinesq approximation in the study of convection problems, particularly in situations where density variations are significant.

Zhang et al. [47] numerically studied the non-Boussinesq effect in the thermal convection in an air-filled horizontal concentric annulus by using a variable property-based lattice-Boltzmann flux solver (VPLBFS), With the radial temperature difference ratio of 1, the radius ratio of 2, and the Rayleigh number in the range of 10^4 - 10^6, the study revealed the complicated flow instability behavior under non-Boussinesq conditions and its tight association with heat transfer characteristics. Also, it demonstrated the necessity of considering the integral effect of the total variation in fluid properties and highlighted the essential role of the fluid density variation. The study explores various solutions, including the VPS (variable property

system), CPS (constant property system), and four other solutions considering partial variations in fluid properties, in order to analyze the influence of non-Boussinesq effects on flow instability and heat transfer characteristics in the context of thermal convection. As the Rayleigh number (Ra) increases, the VPS predicts complex flow instability behaviors. The heat transfer characteristics are closely linked to these flow instability behaviors, often accompanied by transitions in flow patterns. The VDS (variable density system), which considers fluid density variation, closely resembles the VPS, emphasizing the significance of fluid density variation. The VCS (variable conductivity system), accounting for thermal conductivity variation, is the second closest approximation. Both the VDS and VCS partially reproduce flow instability behaviors but underestimate the heat transfer rate and inaccurately predict pattern transition onset. Other solutions, including CPS, PBAS (partial Boussinesq approximation system), and VVS (variable viscosity system), fail to predict flow instability behavior. These findings suggest that the flow instability behavior in thermal convection with large temperature differences in a wide-gap annulus is more diverse than predicted by CPS under the Boussinesq approximation. Future experimental results are needed to confirm the critical Ra number for the transition to chaos when the Boussinesq approximation is invalid, which appears to be higher than predicted by CPS.

The validity of Boussinesq approximation in transient simulation on single-phase natural circulation loops was studied by Krishnani and Basu [48]. The results were obtained by solving transient governing equations and running simulations using the simple Boussinesq model and comprehensive modulation of all important thermophysical variables. They discovered that the Boussinesq approach is ineffective for determining the nonlinear stability of single-phase NCLs, especially at higher power levels. Furthermore, simulation using the Boussinesq approximation takes substantially longer to capture flow initiation in the loop, and the discrepancy between the two models grows as heater output increases.

1.2.5 Lattice Boltzmann method

The LBM gained popularity due to its ability to handle complex flows with ease, including those involving non-linear physics and complex geometries. Buoyancy-driven flows, characterized by the presence of density gradients induced by temperature or compositional variations, posed a significant challenge for traditional numerical methods due to the coupling between velocity, temperature, and pressure.

The LBM, with its inherent mesoscopic nature and the capability to simulate fluid flow and heat transfer simultaneously, offered a promising solution for buoyancy-driven flow simulations. Researchers

recognized the potential of LBM in capturing the complex flow patterns, heat transfer, and fluid dynamics associated with buoyancy-driven flows.

In the early 2000s, researchers began exploring the application of LBM to buoyancy-driven flows. They extended the LBM formulation to incorporate buoyancy effects and developed appropriate boundary conditions to simulate various scenarios of natural convection, such as Rayleigh-Bénard convection and vertical/horizontal wall-driven convection [49–51]. Rayleigh–Benard convection involves the examination of fluid flow and heat transfer between two parallel plates with a temperature difference. To simulate such complex fluid dynamics, the authors employ the LBE method. The authors discuss the implementation and optimization of the LBE method on the parallel processor, allowing for efficient simulations of convection phenomena.

Numerical studies employing LBM in buoyancy-driven flows showcased its advantages, such as the ability to handle complex geometries, parallelizability, and inherent ability to capture flow instabilities and transitional phenomena. LBM also demonstrated good agreement with experimental and other numerical results, establishing its credibility as a viable tool for buoyancy-driven flow simulations.

Since then, the use of LBM in buoyancy-driven flow simulations has continued to grow. Researchers have expanded its applications to study heat transfer in various configurations, including enclosures, porous media, and complex geometries. They have also investigated multiphase flows and coupled phenomena, such as heat and mass transfer.

The employment of LBM in buoyancy-driven flow simulations has provided valuable insights into the understanding of fluid behavior in natural convection, plumes, and other buoyancy-driven phenomena. Ongoing research and advancements in LBM continue to refine its capabilities and enhance its applicability to a wide range of fluid flow problems, including buoyancy-driven flows.

Burgos et al. [52] investigated a mixed convection flow problem in a channel stream and square hollow. The key findings of the study include identifying the essential Ri values for the transition from laminar to turbulent flow regimes and the impact of corner vortices on heat transfer. They evaluated the outcomes between LBM and Fluent (a commercial piece of software), and they found that there is strong agreement between the two.

1.3 Motivations and research objectives

In the realm of buoyancy-driven flow simulations, conventional numerical methods such as the finite volume and finite difference methods have been extensively employed. These studies have predominantly focused on analyzing heat transfer rates, particularly in natural and mixed convection flows, often using a constant fluid property formulation. However, limitations arise when significant temperature differences are present, potentially impacting the accuracy of these analyses. Moreover, there is a notable scarcity of investigations exploring entropy generation analysis within these flows.

Despite the vast body of research in convective heat transfer, particularly in mixed convection flows, there remains a gap in the literature concerning comprehensive studies that consider both heat transfer and entropy generation. While some numerical investigations utilizing conventional computational fluid dynamics (CFD) methods have delved into these aspects, the utilization of the lattice Boltzmann method (LBM) in such contexts remains relatively scarce. This scarcity serves as a compelling motivation to explore the application of the LBM in buoyancy-driven flow simulations. Unlike conventional methods, the LBM offers unique advantages, including its ability to handle complex geometries, ease of parallelization, and capability to simulate multiple physics simultaneously. Furthermore, the LBM presents an opportunity to overcome limitations associated with traditional numerical approaches, particularly in accurately capturing fluid behavior in the presence of significant temperature gradients.

While a limited number of studies have begun to explore the application of LBM in this domain, there is still much ground to cover. These preliminary investigations provide valuable insights into the feasibility and potential of using LBM for buoyancy-driven flow simulations. However, a comprehensive understanding of the key results, limitations, and challenges identified in these studies is essential to underscore the importance and necessity of further research in this area.

Therefore, this study aims to address these research gaps by conducting comprehensive simulations that not only analyze heat transfer rates but also investigate entropy generation within buoyancy-driven flows. By leveraging the capabilities of the LBM, this research endeavors to provide novel insights into the complex phenomena associated with natural and mixed convection, ultimately contributing to the advancement of computational fluid dynamics in this domain.Furthermore, the available literature suggests that there is a minimal amount of research on understanding the influence of thermal boundary conditions and working fluids on enhancing the reliability of natural circulation loops, with only a few

researchers addressing this area. To the best of the author's knowledge, no LBM study has been reported yet for analyzing convection flow inside a natural circulation loop.

1.3.1 Objective of the thesis

Based on the extensive literature survey, the following objectives for the thesis are finalized:

- Mesoscopic numerical investigations of natural convection in closed cavities using Boussinesq and non-Boussinesq approximations;
- Identification of optimized configuration using heat transfer characteristics and entropy generation for mixed convection in a square cavity;
- Numerical simulation and parametric analysis of rectangular natural circulation loop using nanofluids as working fluids;
- Analyses of various kinds of thermal boundary conditions on a natural circulation loop following an unified approach.

1.4 Thesis outline

The thesis has been organized into seven chapters. The brief contents of the chapters are described below.

Chapter 1 provides an overview of buoyancy-driven flow and conducts a literature survey to assess the existing research landscape. The survey highlights limitations in previous studies, particularly regarding heat transfer analysis and entropy generation in such flows. By identifying these gaps, the motivation for the present thesis work is clarified, emphasizing the need for further investigation. The final objectives of the thesis are outlined, delineating the specific aims and goals that will guide the research. These objectives serve as a roadmap for the subsequent chapters, shaping the direction of the investigation into buoyancy-driven flow phenomena.

In Chapter 2, a concise overview of the lattice Boltzmann method (LBM) is presented, including the implementation technique of the single-relaxation time (SRT) model and various boundary condition treatments. To validate the capabilities of the developed in-house LBM code, isothermal and thermal benchmark cavity flow problems are simulated using both SRT lattice Boltzmann models. The results

obtained demonstrate good agreement with previously published findings, highlighting the competence of the code. This success provides confidence in extending the code to investigate various configurations in future studies.

Chapter 3 is dedicated to exploring the suitability of the single-relaxation time (SRT) thermal lattice Boltzmann model in complex flow systems. The primary focus is to investigate the effects of substantial temperature differences on entropy generation and heat transfer within a cavity. Additionally, this study delves into the formulation of the non-Boussinesq approximation to account for non-isothermal conditions more accurately.

Chapter 4 of the thesis centers around numerical simulations conducted on mixed convection in a square enclosure. Three different configurations are considered, and the simulations employ the thermal lattice Boltzmann model. The main motivation behind this research is to examine the fluid dynamics within the cavity, considering the combined influence of lid driving and buoyancy effects. The aim is to identify optimized parameter sets or conditions that enable efficient heat transfer and minimize entropy generation.

Chapter 5 of the thesis focuses on the numerical modeling of a natural circulation loop using the lattice Boltzmann method. The primary objective is to investigate the impact of nanofluids under specific thermal conditions. The study aims to enhance the understanding of how nanofluids influence the performance and behavior of the natural circulation loop.

Chapter 6 deals with the natural circulation loop and its influence under different thermal boundary conditions.This chapter gives an comparative analysis of performance of a natural circulation loop subjected to diffrent heat flux conditions.

In Chapter 7, a summary of the notable findings from the thesis is provided, highlighting the key discoveries and outcomes. Additionally, potential directions for future research are discussed, focusing on further exploration and investigation to unveil new insights and unexplored aspects related to the subject matter.

भारतीय प्रौद्योगिकी संस्थान गुवाहाटी
Indian Institute of Technology Guwahati

Chapter 2

The essence of the lattice Boltzmann method

2.1 Development of Lattice Boltzmann method

The lattice Boltzmann method (LBM) is a numerical technique used to simulate fluid flows. It is derived from the lattice gas automata (LGA) model, which is a cellular automaton approach to simulate fluid dynamics at the mesoscopic level. LGA represents fluids as collections of particles moving on a lattice, where each particle can move in a discrete direction. In this approach, the system's macroscopic quantities can be determined by taking averages of the microscopic quantities across space or time. However, because the microscopic state is constantly changing, there will always be statistical noise in the macroscopic quantities [53].

In 1988, a solution to the issue of statistical noise in LGAs was put forward by McNamara and Zanetti [54] in the form of LBM. It provides an efficient and flexible way to simulate fluid flows, especially for complex geometries and boundary conditions. It has gained popularity due to its ability to handle a wide range of fluid phenomena, including multiphase flows, heat transfer, and turbulence. The connection between LGA and LBM lies in the discretization of the Boltzmann equation and the adoption of discrete lattice velocities to simulate fluid dynamics.

2.2 Lattice structure in LBM

In LBM, it is assumed that all particles exist at fixed positions known as nodes on a lattice. These lattices consist of a regular arrangement of particles within the domain. Consequently, all particles are

required to adhere to and move along these predetermined paths, effectively limiting the system's degrees of freedom. The particles must follow the lattice links and undergo collisions at specific lattice sites. The lattice structure is symbolized by lattice model DmQn, where m represents the number of dimensions and n denotes the number of discrete particle velocities or linkages at each lattice node.

Lattice model

A lattice model refers to the specific arrangement of lattice points or nodes in the simulation domain. The lattice can have different geometries, such as a square lattice, hexagonal lattice, or cubic lattice, depending on the type of flow being simulated and the desired accuracy. It plays a crucial role in determining the dynamics of the fluid flow. It defines the connectivity and neighborhood relationships between lattice nodes, which are used to propagate and exchange information during the simulation. The most used lattice models in LBM are the D2Q9 [55] and D3Q19 [56] lattices.

The lattice Boltzmann method, with its lattice model, offers several advantages, such as simplicity in handling complex geometries, straightforward implementation on parallel architectures, and the ability to simulate a wide range of flow phenomena, including multiphase flows and turbulent flows. Each lattice node in the lattice model stores the distribution functions associated with the discrete velocities. During each time step, the distribution functions are updated based on collision and streaming processes, which simulate the interactions and movements of fluid particles.

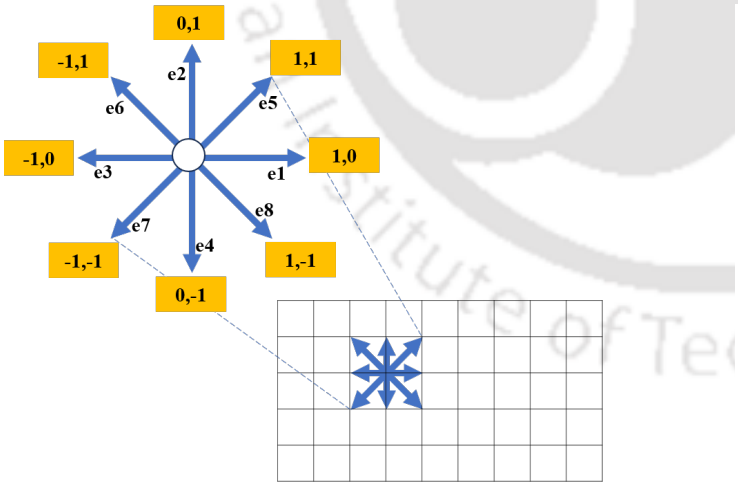

Figure 2.1: D2Q9 lattice model

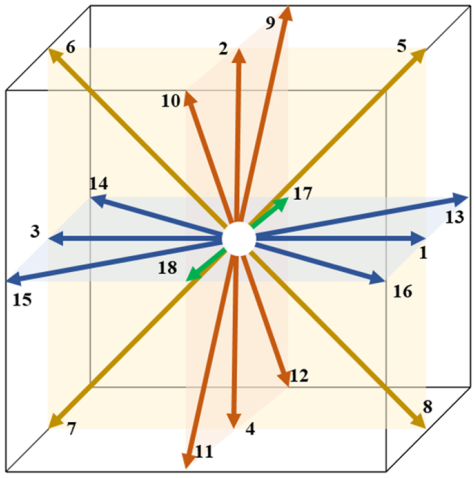

Figure 2.2: D3Q19 lattice model

The D2Q9 lattice as shown in Figure 2.1 is a two-dimensional lattice with nine discrete velocities. Each node in the lattice has eight neighboring nodes, connected by eight links. During the streaming process, the particle distribution functions (PDF) with their corresponding velocities $\mathbf{e}_i$ are transported from one

node to its neighboring node along these links within a unit of time. While the D3Q19 lattice as shown in Figure 2.2 is a three-dimensional lattice with 19 discrete velocities. Each node has eighteen neighbors connected by eighteen links. These velocities are typically chosen to satisfy specific properties, such as Galilean invariance and isotropy.

2.3 Boltzmann equation

The Boltzmann equation is a fundamental equation in statistical mechanics that describes the behavior of a dilute gas at the molecular level. It provides a statistical description of the distribution of particles in gas and how they interact with each other. The Boltzmann equation is derived from the principles of kinetic theory, which focuses on the motion of individual particles in a gas and their collisions.

Representing the particle density in the position $\mathbf{x}+d\mathbf{x}$ and momentum $\mathbf{p}+d\mathbf{p}$ at time t as a continuous function, $f(\mathbf{x}, \mathbf{p}, t)\, d\mathbf{x}\, d\mathbf{p}$.

If collisions between particles are neglected in a system, the particles will continue to move in the direction they were originally headed without any changes in their velocities. In this case, the particle distribution at time t can be used to determine the particle distribution at a slightly later time, $t + dt$, where dt represents a small-time step.

$$f\left(\mathbf{x} + \frac{\mathbf{p}}{m}dt, \mathbf{p} + d\mathbf{p}, t + dt\right) d\mathbf{x}\, d\mathbf{p} = f(\mathbf{x}, \mathbf{p}, t) d\mathbf{x}\, d\mathbf{p} \tag{2.1}$$

where, $\mathbf{p}/m = \mathbf{e}$ being a velocity and $d\mathbf{p} = \mathbf{F}\, dt$, $\mathbf{F}$ being an external force at $\mathbf{x}$. However, if collisions between the particles are considered, some particles at $(\mathbf{x}, \mathbf{p}, t)$ will not reach $(\mathbf{x} + \frac{\mathbf{p}}{m}\, dt, \mathbf{p} + d\mathbf{p}, t + dt)$ as they have been collided out of this path. Also, other particles will arrive at $(\mathbf{x} + \frac{\mathbf{p}}{m}\, dt, \mathbf{p} + d\mathbf{p}, t + dt)$ because they are collided into this path. This difference in particles is represented as $\Omega\, d\mathbf{x}\, d\mathbf{p}\, dt$ and thus equation (2.2) becomes:

$$f\left(\mathbf{x} + \frac{\mathbf{p}}{m}\, dt, \mathbf{p} + d\mathbf{p}, t + dt\right)\, d\mathbf{x}\, d\mathbf{p} - f(\mathbf{x}, \mathbf{p}, t)\, d\mathbf{x}\, d\mathbf{p} = \Omega\, d\mathbf{x}\, d\mathbf{p}\, dt \tag{2.2}$$

2.3.1 Discretization of Boltzmann equation

The discretization of the Boltzmann equation is a crucial step in numerical methods like the Lattice Boltzmann Method (LBM). Discretization involves approximating the continuous Boltzmann equation by discretizing the physical domain, velocity space, and time. The physical domain, representing the fluid flow region, is divided into a discrete lattice structure (Figure 2.1). Typically, a regular grid, such as a cubic lattice or a hexagonal lattice, is used. Each lattice site represents a specific position in the domain.

The simulation involved here employs quantities that are connected to real values through the lattice spacing (Δx) and the time step (Δt). An example of this relationship is seen in the physical particle speeds ($\mathbf{e}_{i,\text{ph}}$) within the lattice, which can be expressed as follows:

$$\mathbf{e}_{i,\text{ph}} = \frac{\Delta x}{\Delta t}\mathbf{e}_{i,\ell} \tag{2.3}$$

where $\mathbf{e}_{i,\ell}$, normalized by Δx and Δt, is in lattice units. In lattice units, we have $|\mathbf{e}_{i,\ell}| = 1$ for all i, and $\Delta t = 1$. Also, $\mathbf{e}_{i,\text{ph}} = \frac{\Delta x}{\Delta t}$ is in physical units.

The lattice Boltzmann evolved equation (2.5) is the discretization form of equation (2.3). Neglecting the external forces and normalizing mass m to 1, so that $\mathbf{p} = \mathbf{e}$, the velocity $\mathbf{e}$ can be limited to $\mathbf{e}_i$, which can be used to tile the entire space. Thus, with discrete velocities, $f(\mathbf{x}, \mathbf{e}, t)$ can be replaced by $f_i(\mathbf{x}, t)$ with no information loss.

The Boltzmann equation, named after the Austrian physicist Ludwig Boltzmann [57], governs the evolution of the distribution function $f_i(\mathbf{x}, t)$, where i represents the velocity ($\mathbf{e}_i$) at a particular node as discussed in section 2.2. It describes how the distribution function changes over time due to particle collisions and interactions.

With no collision, the equation can be written as:

$$f_i(\mathbf{x} + \Delta\mathbf{x}, t + \Delta t) = f_i(\mathbf{x}, t) \tag{2.4}$$

The above equation (2.4) says that for every time step Δt, a particle with speed $\mathbf{e}_i$ will move to the next node, retaining the same speed. Adding the collision to the equation using the collision operator, $\Omega_i(\mathbf{x}, t)$, for each i, the equation becomes:

$$f_i(\mathbf{x} + \Delta\mathbf{x}, t + \Delta t) - f_i(\mathbf{x}, t) = \Omega_i(\mathbf{x}, t) \tag{2.5}$$

where $\Omega_i(\mathbf{x}, t)$ gives us the number of particles that were collided into or away from direction $\mathbf{e}_i$ at position $\mathbf{x}$ and time t. The Boltzmann equation (equation (2.6)) embodies the conservation laws of mass, momentum, and energy. However, solving the Boltzmann equation analytically for complex dynamics is challenging due to the complexity of the collision term. This gives rise to the closure problem where approximations and simplifications are needed to close the equations and make them solvable. By understanding the Boltzmann equation and its connection to statistical mechanics and kinetic theory, researchers have developed numerical methods like LBM to simulate fluid flows and capture macroscopic phenomena from microscopic interactions.

Distribution function

The distribution function, denoted by $f(\mathbf{x}, \mathbf{e}, t)$, which represents the probability density of finding a particle at a lattice site with a specific velocity, is discretized. At each lattice site and for each discrete velocity, a distribution function value is assigned. This discrete distribution function is usually denoted as $f(\mathbf{x}, \mathbf{e}, t)$, where $\mathbf{x}$ represents the lattice site position.

2.3.2 Linearization of the collision operator

The Boltzmann equation is a fundamental equation in kinetic theory that describes the evolution of the distribution function of particles in a gas due to collisions. The collision operator in the Boltzmann equation is non-linear and represents the interactions between particles. The standard model to simplify the collision expression is called the BGK approximation and was proposed by Bhatnagar et al. [58]. It is expressed as:

$$\Omega_{i,\mathrm{BGK}}(\mathbf{x}, t) = \frac{(f_i^{\mathrm{eq}} - f_i)}{\tau} \tag{2.6}$$

Here, f_i^{eq} is a Maxwellian distribution representing the local equilibrium. During each collision, the distribution function f_i undergoes a change proportional to the deviation from the local equilibrium f_i^{eq}. This correction is influenced by the relaxation time τ, which determines the extent of the modification. The relaxation time τ typically depends on the properties of the gas and its current state. However, in the simplified BGK approximation, it is treated as a single constant value.

Equilibrium distribution function

As discussed in subsection 2.2.2, the equilibrium distribution function f^{eq} is a Maxwell distribution.

The macroscopic flow speed e, density ρ, and fluid temperature T parametrize the Maxwell distribution (sometimes also called Maxwell-Boltzmann distribution). It is written for 3-dimensions as:

$$f^M = \rho(\frac{m^2}{2\pi RT})^{\frac{3}{2}} e^{-\frac{(\mathbf{e}-\mathbf{u})^2 m^2}{2RT}} \tag{2.7}$$

where, R is the Boltzmann constant, and m is the mass of a particle. For a particle of unit mass and dimension D:

$$f(\mathbf{u}) = \frac{\rho}{(2\pi RT)^{\frac{D}{2}}} e^{-\frac{(\mathbf{e}-\mathbf{u})^2}{2RT}} \tag{2.8}$$

Expanding the above equation using Taylor expansion upto 3^{rd} order.

$$\begin{aligned}
f(0+\mathbf{u}) &= \beta e^{\left(\frac{\mathbf{e}\cdot\mathbf{u}}{RT} - \frac{\mathbf{u}^2}{2RT}\right)} \\
&= f(0) + \mathbf{u}f'(0) + \frac{\mathbf{u}^2}{2} f''(0) + O(\mathbf{u}^3) \\
&= \beta \cdot \left\{ 1 + \mathbf{u} \cdot \left[\beta \frac{1}{RT} e^{\left(\frac{\mathbf{e}\cdot\mathbf{u}}{RT} - \frac{\mathbf{u}^2}{2RT}\right)} \cdot (\mathbf{e}-\mathbf{u}) \right] \right. \\
&\quad \left. + \frac{\mathbf{u}^2}{2} \beta \left[\frac{1}{(RT)^2} e^{\left(\frac{\mathbf{e}\cdot\mathbf{u}}{RT} - \frac{\mathbf{u}^2}{2RT}\right)} \cdot (\mathbf{e}-\mathbf{u})^2 + \frac{1}{RT} \cdot (-1) \right] \right\} + O(\mathbf{u}^3) \\
&= \beta \left(1 + \frac{\mathbf{e}\cdot\mathbf{u}}{RT} + \frac{(\mathbf{e}\cdot\mathbf{u})^2}{2(RT)^2} - \frac{\mathbf{u}^2}{2RT} \right)
\end{aligned}$$

where, $\beta = \frac{\rho}{(2\pi RT)^{\frac{D}{2}}} e^{-\frac{\mathbf{e}^2}{2RT}}$

Therefore,

$$f^{\text{eq}} = \frac{\rho}{(2\pi RT)^{\frac{D}{2}}} e^{-\frac{\mathbf{e}^2}{2RT}} \left(1 + \frac{\mathbf{e}\cdot\mathbf{u}}{RT} + \frac{(\mathbf{e}\cdot\mathbf{u})^2}{2(RT)^2} - \frac{\mathbf{u}^2}{2RT} \right) \tag{2.9}$$

The above equation is not properly discretized. Thus, the discrete equilibrium distribution function is written as:

$$f_i^{\text{eq}} = \rho w_i \left\{ 1.0 + \frac{\mathbf{e}_i \cdot \mathbf{u}}{C_s^2} + \frac{(\mathbf{e}_i \cdot \mathbf{u})^2}{2C_s^4} - \frac{\mathbf{u}^2}{2C_s^2} \right\} \tag{2.10}$$

The weighing factor w_i for D2Q9 lattice model is given by [57]:

$$w_i = \left\{ \begin{array}{ll} \frac{4}{9} & \text{if } i = 0 \\ \frac{1}{9} & \text{if } i = 1, \ldots, 4 \\ \frac{1}{36} & \text{if } i = 5, \ldots, 8 \end{array} \right\} \tag{2.11}$$

The weighing factor w_i for D3Q19 lattice model is given by [54]:

$$w_i = \left\{ \begin{array}{ll} \frac{1}{3} & \text{if } i = 0 \\ \frac{1}{18} & \text{if } i = 1, \ldots, 6 \\ \frac{1}{36} & \text{if } i = 7, \ldots, 18 \end{array} \right\} \tag{2.12}$$

Also, the discrete velocity $\mathbf{e}_i$ for D2Q9 model is specifically written as [57]:

$$\mathbf{e}_i = \left\{ \begin{array}{ll} (0,0) & \text{if } i = 0 \\ c\left(\cos\left(\frac{(i-1)\pi}{2}\right), \sin\left(\frac{(i-1)\pi}{2}\right)\right) & \text{if } i = 1, \ldots, 4 \\ \sqrt{2}c\left(\cos\left(\frac{(2i-9)\pi}{4}\right), \sin\left(\frac{(2i-9)\pi}{4}\right)\right) & \text{if } i = 5, \ldots, 8 \end{array} \right\} \tag{2.13}$$

And for D3Q19 model is written as[54]:

$$\mathbf{e}_i = \left\{ \begin{array}{ll} (0,0) & \text{if } i = 0 \\ c\left(\cos\left(\frac{(i-1)\pi}{2}\right), \sin\left(\frac{(i-1)\pi}{2}\right)\right) & \text{if } i = 1, \ldots, 4 \\ \sqrt{2}c\left(\cos\left(\frac{(2i-9)\pi}{4}\right), \sin\left(\frac{(2i-9)\pi}{4}\right)\right) & \text{if } i = 5, \ldots, 8 \end{array} \right\} \tag{2.14}$$

2.4 Lattice Boltzmann model

Modeling a domain for lattice Boltzmann simulation involves two fundamental steps: streaming and collision.

Collision and Streaming term

The simplicity of the BGK collision model makes it popular and widely used in lattice Boltzmann

simulations. The model was introduced by Bhatnagar, Gross, and Krook in 1954 (so is called BGK model), which simplifies the collision process by assuming a relaxation towards a local equilibrium distribution function. In the context of the Lattice Boltzmann Method, the BGK collision model assumes that the fluid approaches a local equilibrium state after each collision step.

The fully discretized Boltzmann equation with BGK collision operator as discussed in section 2.2 is written as:

$$f_i(\mathbf{x} + \mathbf{e}_i\Delta t, t + \Delta t) = f_i(\mathbf{x}, t) - \frac{\Delta t}{\tau}\left(f_i(\mathbf{x}, t) - f_i^{\text{eq}}(\mathbf{x}, t)\right) \tag{2.15}$$

This equation (2.15) can be decomposed into two distinct part as discussed below:

i. The first part is collision (or relaxation):

$$f_i^*(\mathbf{x}, t) = f_i(\mathbf{x}, t) - \frac{\Delta t}{\tau}\left(f_i(\mathbf{x}, t) - f_i^{\text{eq}}(\mathbf{x}, t)\right) \tag{2.16}$$

where, f_i^* represents the distribution function after collision.

ii. The second part is streaming (or propagation):

$$f_i(\mathbf{x} + \mathbf{e}_i\Delta t, t + \Delta t) = f_i^*(\mathbf{x}, t) \tag{2.17}$$

The collision term in the Boltzmann equation, which accounts for particle interactions as shown in Figure 2.3, is approximated using relaxation processes. In LBM, the relaxation process is often modeled by a linearized relaxation operator. This operator relaxes the distribution functions towards their equilibrium values based on local macroscopic quantities, such as density and velocity.

A streaming step as shown in Figure 2.4 is performed after the collision step. During the streaming step, the distribution functions are propagated from one lattice site to its neighboring sites according to the discrete velocities. This step ensures the advection of particles in the simulated fluid flow. particles in the simulated fluid flow.

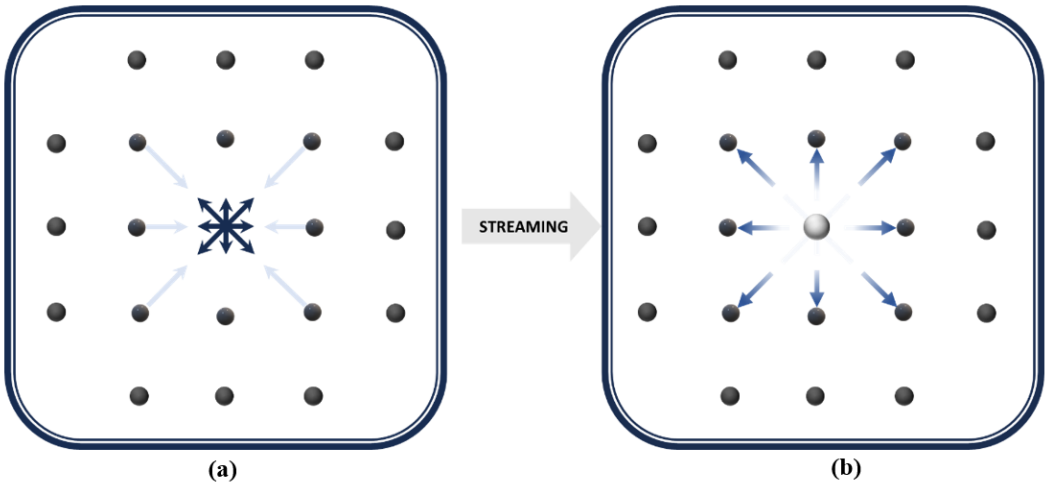

Figure 2.3: Collision process

Figure 2.4: Streaming process

Time step

The time variable in the Boltzmann equation is also discretized. The continuous time derivative $\frac{\partial f}{\partial t}$ is approximated by a difference operator, typically a finite difference scheme. This allows for the time evolution of the distribution function to be computed iteratively.

2.4.1 SRT model

The SRT-LBM model stands for "Single-Relaxation-Time Lattice Boltzmann Method." The SRT-LBM [55] is a specific variant of the lattice Boltzmann method that uses a single relaxation time for the collision process. The relaxation time controls the rate at which the distribution functions reach an equilibrium state after the collision. This efficient model is used for both isothermal and thermal flows.

i. **SRT-LBM model for isothermal flow**

The governing equation for the lattice BGK model with a single relaxation time (SRT) is:

$$f_i(\mathbf{x} + \mathbf{e}_i\Delta t, t + \Delta t) = f_i(\mathbf{x}, t) - \frac{1}{\tau_v}(f_i(\mathbf{x}, t) - f_i^{eq}(\mathbf{x}, t)) \tag{2.18}$$

The single relaxation time (τ_v) determines the lattice-level kinematic viscosity, $\nu = c_s^2\Delta t(\tau_v - 0.5)$. It relaxes the discrete momentum distribution function (f_i) towards its equilibrium distribution

function (f_i^{eq}) in the collision process. Here, c_s represents the isothermal model's speed of sound and is given by:

$$c_s = \frac{1}{\sqrt{3}}\Delta x\sqrt{\frac{2}{\tau_0}} \tag{2.19}$$

ii. **SRT-LBM model for thermal flow**

The simulation of thermal problems is introduced in a simplified approach by Peng et al. [59]. The discretized lattice Boltzmann equation for momentum distribution function is given as:

$$f_i(\mathbf{x}+\mathbf{e}_i\Delta t, t+\Delta t) = f_i(\mathbf{x},t) - \frac{1}{\tau_v}(f_i(\mathbf{x},t) - f_i^{eq}(\mathbf{x},t)) + S_i \tag{2.20}$$

Here, S_i is the force term added to the collision process. The most popular forcing schemes are as follows:

(a) Luo's force model [60]:

$$F_i = -3w_i\rho\mathbf{e}_i \cdot \frac{\mathbf{F}}{c_s^2} \tag{2.21}$$

(b) Shan and Chen's model [61]:

$$F_i = -3w_i\left(\frac{\mathbf{e}_i - \mathbf{u}}{c_s^2} + 3\frac{\mathbf{e}_i\cdot\mathbf{u}}{c_s^4}\mathbf{c}_i\right)\cdot\mathbf{F} \tag{2.22}$$

(c) Guo's force model [62]:

$$F_i = w_i\left(1-\frac{1}{2\tau_v}\right)\left[\frac{\mathbf{e}_i-\mathbf{u}}{c_s^2} + \frac{\mathbf{e}_i(\mathbf{e}_i\cdot\mathbf{u})}{c_s^4}\right]\mathbf{F} \tag{2.23}$$

This SRT model of thermal flow considered two distinct particle distribution function. Equation 2.18 represents momentum distribution function-based lattice Boltzmann equation. However, the thermal part is simulated using temperature distribution function-based lattice Boltzmann equation. The discretized lattice Boltzmann equation for temperature distribution function is given as:

$$g_i(\mathbf{x}+\mathbf{e}_i\Delta t, t+\Delta t) = g_i(\mathbf{x},t) - \frac{1}{\tau_\theta}(g_i(\mathbf{x},t) - g_i^{\mathrm{eq}}(\mathbf{x},t)) \tag{2.24}$$

The single relaxation time parameter τ_θ determines the thermal diffusivity $\alpha = c_s^2 \Delta t(\tau_\theta - 0.5)$. The LB viscosity depends on the values of the relaxation time (τ), LB velocity (u_{lb}), and the grid spacing (Δx). However, in LBM, there is an additional constraint to simulate incompressible flow, which states that the LBM velocity should be less than the lattice speed of sound (c_s). This constraint ensures that the fluid remains in the regime of incompressible flow. The limitation of $0.5 < \tau < 1.5$ has been kept into consideration during the simulations to ensure that the viscosity and thermal diffusivity are positive.

To satisfy this constraint and accurately simulate incompressible flow, the discretization parameters such as the grid spacing (Δx) or the number of lattice nodes (N) need to be appropriately tuned for the specific problem. The choice of these parameters should be such that the LBM velocity remains below the lattice speed of sound.

By tuning the discretization parameters, the LBM simulation can accurately capture the flow behavior and achieve stable results while satisfying the incompressibility constraint. Proper parameter selection is essential in LBM to ensure accurate and reliable simulations of fluid flow problems.

2.4.2 Lattice Boltzmann algorithm

This section is written considering the D2Q9 lattice model. The basic algorithm for the lattice Boltzmann simulation is nicely depicted in Figure 2.5.

The macroscopic parameters are obtained by taking moments of the distribution function. Fluid density ρ and velocity $\mathbf{u}$ are calculated by taking the 0^{th} and 1^{st} moments of f_i respectively and are calculated as follows:

$$\rho = \sum_{i=0}^{8} f_i \tag{2.25}$$

$$\rho \mathbf{u} = \sum_{i=0}^{8} f_i \mathbf{e}_i \tag{2.26}$$

Also, the macroscopic temperature for thermal model is calculated taking 0^{th} moments of g_i and is given by:

$$\theta = \sum_{i=0}^{8} g_i \tag{2.27}$$

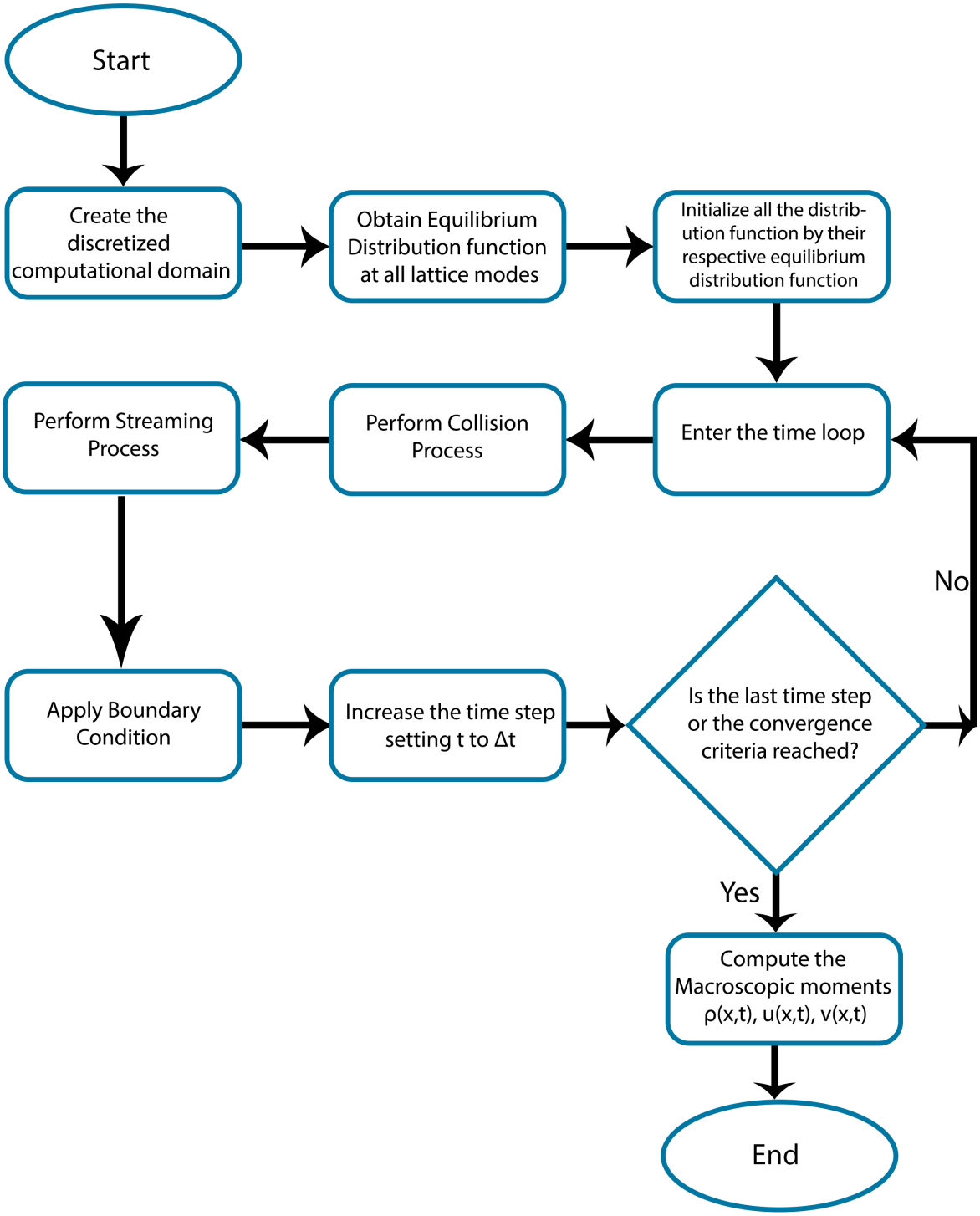

Figure 2.5: LBM algorithm

2.5 Lattice Boltzmann method in incompressible flow and some benchmark problems

The lid-driven cavity, buoyancy-induced natural convection in a cavity are commonly used benchmark problems in computational fluid dynamics (CFD) to assess the accuracy and performance of numerical methods, including lattice Boltzmann method (LBM) codes, for both isothermal and thermal flows, respectively. These problems are discussed in sub-section 2.5.1 and 2.5.2.

2.5.1 Lid-driven cavity flow problem

In this problem, a square cavity as shown in Figure 2.6 is considered with a lid that moves at a constant velocity while the other walls remain stationary. Also, the boundary conditions applied are depicted in the above Figure. The objective is to simulate the flow patterns and velocity distributions within the cavity. This benchmark is often used to test the accuracy of numerical methods in capturing the corner vortices and the effects of boundary conditions.

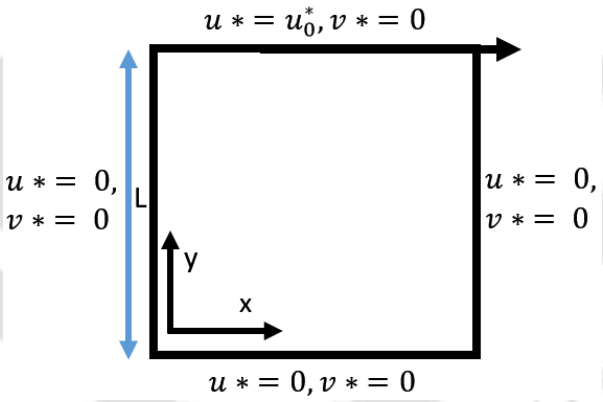

Figure 2.6: Computational domain for lid-driven cavity flow

As shown in Figure 2.6, the upper lid moves with a velocity u_0^* and the other 3 walls are stationary. The LBM code is written for 3 different Re: 100, 400, and 1000 in a uniform grid size of 201×201. To check the validity of the code, the results are compared with the existing literature [1] in terms of streamline contours, horizontal velocity u along the vertical centerline, and the vertical velocity v along the horizontal centerline of the cavity (Figure 2.7). The results are found to be in good agreement with the existing one.

The following steps are considered:

i. Non-dimensionalities and setting the inputs: The non-dimensional forms of the variables are expressed as follows:

$$x^* = \frac{x}{L}, \quad y^* = \frac{y}{L}, \quad u^* = \frac{u}{u_0}, \quad v^* = \frac{v}{u_0}$$

where, L is the length of the cavity and the reference length as shown in the Figure 2.6.

Based on the above variables, the Reynolds number (Re) is set as:

$$Re = \frac{u_0^* L}{\nu} \tag{2.28}$$

Keeping the consistency of equation 2.28, the other significant parameter like momentum relaxation time τ_v as discussed in sub-section 2.3.1 is calculated.

ii. Executing the time loop: After initialization of the required parameters, it enters the time loop and ends until the velocity error meets the convergence criteria of 10^{-8} as given by equation 2.9.

$$\frac{\|\mathbf{u}^{(n+1)} - \mathbf{u}^{(n)}\|}{\|\mathbf{u}^{(n+1)}\|} < 10^{-8}, \tag{2.29}$$

where $\mathbf{u}^{(n)}$ represents the velocity at iteration n, $\mathbf{u}^{(n+1)}$ represents the velocity at iteration $n+1$.

iii. Post processing: As the convergence criteria is reached, the macroscopic velocities u and v are calculated using equation 2.26.

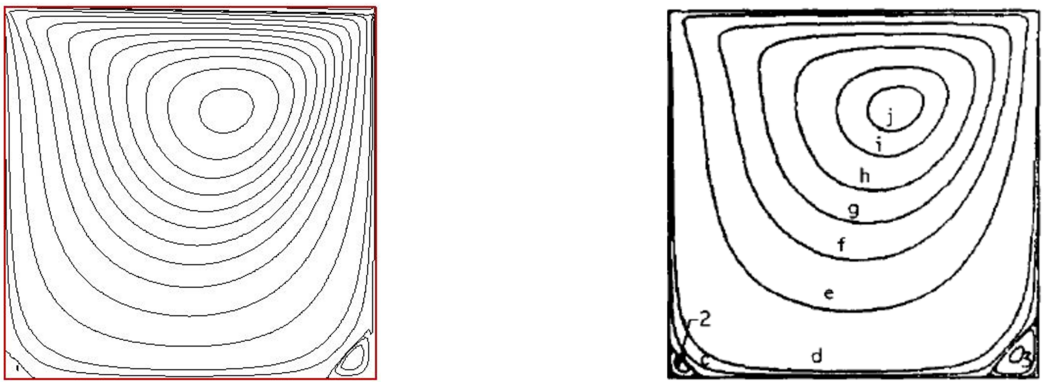

(a) (b)

Re=100

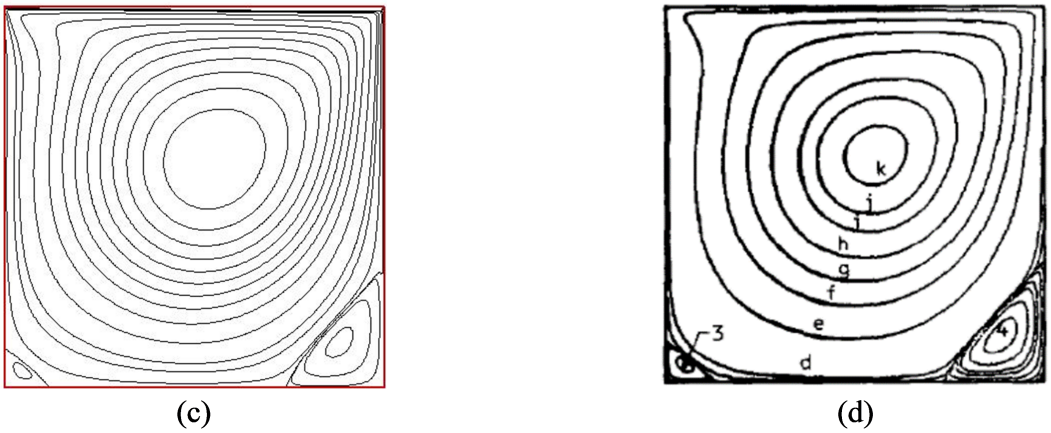

(c) (d)

Re=400

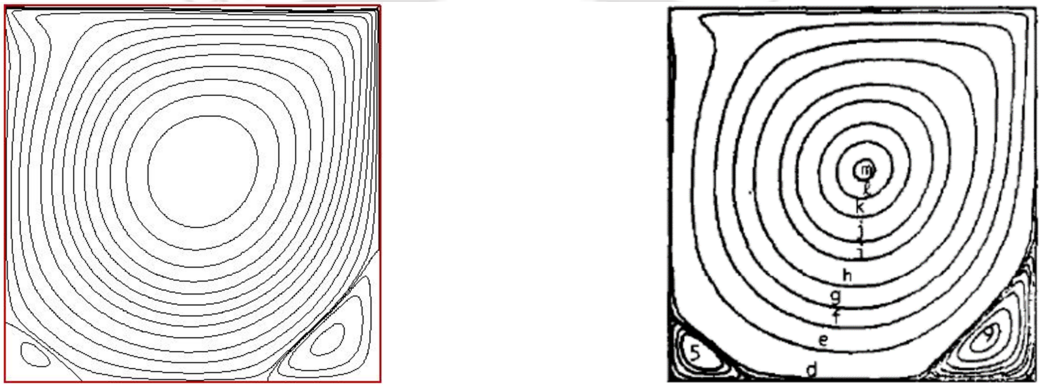

(e) (f)

Re=1000

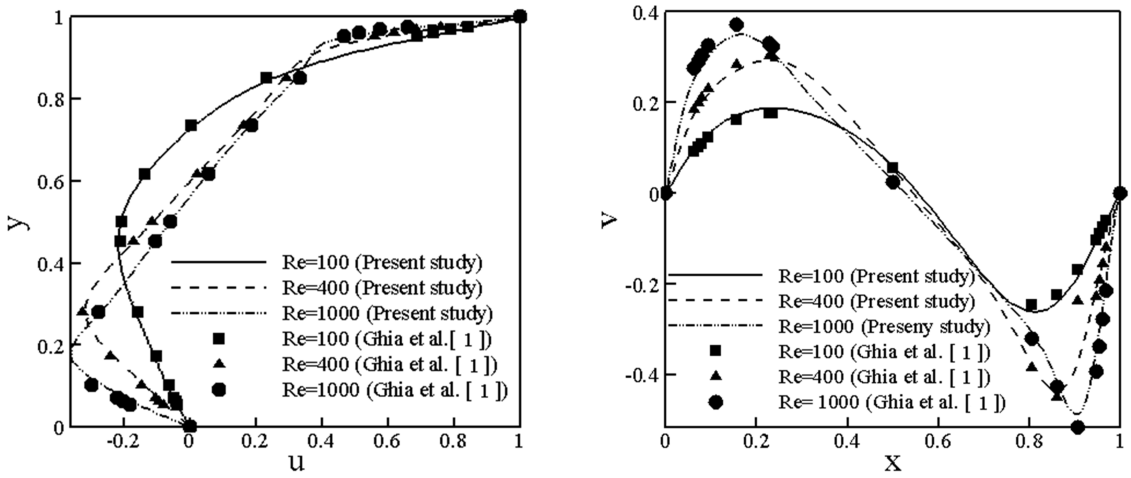

(g) (h)

Horizontal and Vertical velocity

Figure 2.7: Comparison of results in terms of streamline contours, dimensionless horizontal velocity u at $y = 0.5$ (left panel) and vertical velocity v at $x = 0.5$ (right panel) with Ghia et al. [1] for Re = 100, Re = 400, and Re = 1000.

2.5.2 Natural convection in a square cavity

Natural convection in a square cavity is often used as a benchmark problem to validate the LBM-SRT thermal flow problems. The benchmark problem typically involves the following setup as shown in Figure 2.8.

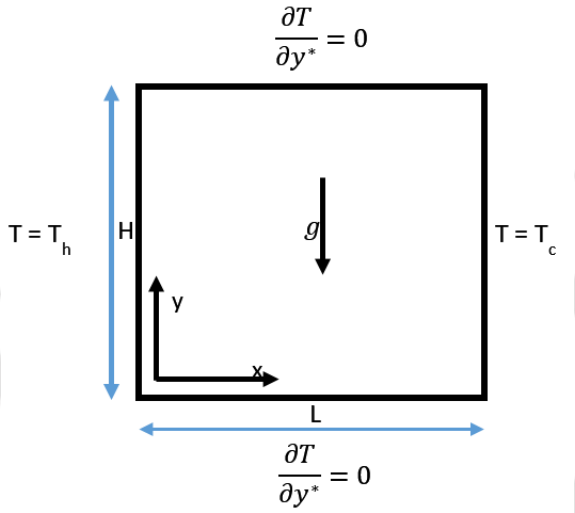

Figure 2.8: Domain geometry for natural convection in a square cavity

Grid independency test:

An extensive mesh testing procedure is conducted to guarantee a grid independent solution. Four different mesh combinations are used for the case of $Ra = 10^3$, $Pr = 0.71$. The present code is tested for grid independence by calculating the average Nusselt number (Nu) on the left hot wall and is shown in Table 2.1.

Table 2.1: Grid independence test for natural convection

S.No.	Grid Size	Av Nu
1	70×70	1.1200
2	100×100	1.1190
3	150×150	1.1180
4	200×200	1.1179

The converged value (Nu = 1.1179) is compared to other known values reported by other researcher

and the value compares very well with other values obtained in literature [63]. Therefore, the grid size 200×200 is used for the present simulation work.

Now, for the result validation, a code is written with the input parameters of $Ra = 10^6$ and $Pr = 0.71$. And to check the validity of the code, the results are compared with the existing literature [63] in terms of streamline contours, temperature θ (right) in the horizontal mid-plane of square cavity at $Ra = 10^6$ (Figure 2.9). The results are found to be in good agreement with the existing one.

The following steps are considered:

i. Non-dimensionalities and setting the inputs:

The non-dimensional forms of the variables are expressed as follows:

$$x^* = \frac{x}{H}, \quad y^* = \frac{y}{H}, \quad u^* = \frac{u}{u_0}, \quad v^* = \frac{v}{u_0}, \quad \theta = \frac{T - T_c}{T_h - T_c}. \tag{2.30}$$

where, L and H are the length and height of the cavity, respectively. Here, H is the reference length as shown in the Figure 2.8.

Based on the above variables, the Rayleigh number (Ra) is set as:

$$\text{Ra} = \frac{g\beta(T_w - T_\infty)L^3}{\nu\alpha}. \tag{2.31}$$

The Rayleigh number (Ra) is defined as the product of the Grashof number (Gr) and the Prandtl number (Pr).

$$Ra = GrPr.$$

where, Gr = $\frac{g\beta(T_w - T_\infty)L^3}{\nu^2}$ and Pr = $\frac{\nu}{\alpha}$.

As discussed in section 2.3, Guo's model [61] amongst the 3 force model is considered to calculate the external force F which is defined as the external force per unit volume due to the presence of buoyancy force and is given by:

$$F = \rho g\beta(\theta - \theta_m) \tag{2.32}$$

Keeping the consistency of Equation 2.31, the other parameters like momentum relaxation time τ_v and thermal relaxation time τ_θ as discussed in subsection 2.3.1 are calculated.

ii. Boundary conditions:

The cavity walls can have different thermal boundary conditions. As shown in the Figure 2.8, top and bottom walls are applied with the adiabatic conditions and left and right walls are assigned with isothermal conditions.

- Isothermal Walls: The walls are maintained at constant temperatures, such as hot and cold walls. This is also called the Dirichlet boundary condition in CFD environment.
- Adiabatic Walls: The walls are assumed to be thermally insulated, meaning no heat transfer occurs through the walls. The temperature is uniform throughout the cavity at a specified initial condition.

iii. Executing the time loop:

After initialization of the required parameters, it enters the time loop and ends until the error meets the convergence criteria of 10^{-8}.

iv. Post processing:

As the convergence criteria is reached, the macroscopic velocities u, v, and θ are calculated using Equation 2.26 and 2.27.

The reference velocity can be chosen as:

$$u_0 = \sqrt{g\beta(T_w - T_\infty)L} \tag{2.33}$$

Nusselt number

The Nusselt number (Nu) is a dimensionless quantity used in heat transfer analysis to characterize the convective heat transfer of a fluid. It is named after Wilhelm Nusselt, a German engineer who made significant contributions to the field of heat transfer. The Nusselt number is defined as the ratio of convective heat transfer to conductive heat transfer across a fluid boundary layer. Mathematically, it is expressed as:

$$Nu = \frac{hL}{k} \tag{2.34}$$

The Nusselt number provides information about how effectively heat is being transferred by convection relative to conduction. A higher Nusselt number indicates a greater contribution of convective heat transfer, suggesting that the fluid is more efficient in transferring heat. The convective heat transfer coefficient (h) represents the ability of the fluid to transfer heat through convection. It is influenced by several factors, including fluid properties, flow conditions, and surface geometry. The characteristic length (L) is typically a characteristic dimension of the system, such as the length of a heat transfer surface (presently considered) or the diameter of a pipe. The thermal conductivity (k) represents the ability of the material to conduct heat.

The average Nu for the whole domain ($\overline{Nu}$), along the vertical left ($\overline{Nu_l}$) and right ($\overline{Nu_r}$) walls are respectively calculated using the below-mentioned equations 2.35-2.37 [58].

$$\overline{\text{Nu}} = \frac{1}{L^2}\int_0^L \int_0^L \text{Nu}\, dx\, dy \tag{2.35}$$

$$\overline{\text{Nu}_l} = \frac{1}{L}\int_0^L \text{Nu}_y\, dx \tag{2.36}$$

$$\overline{\text{Nu}_r} = \frac{1}{L}\int_0^L \text{Nu}_y\, dx \tag{2.37}$$

where, Nu = $u\theta - \frac{\partial\theta}{\partial x}$ and $\text{Nu}_y = -\frac{\partial\theta}{\partial x}$ are local Nusselt numbers at all fluid nodes and at the vertical surfaces, respectively.

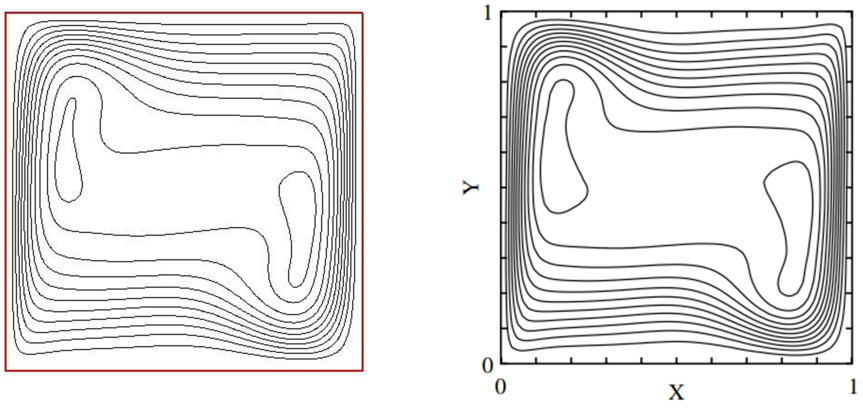

(a) (b)

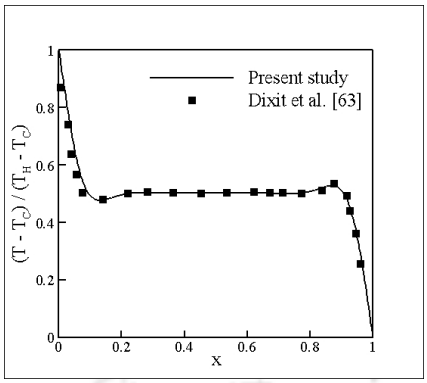

(c)

Figure 2.9: Comparison of results in terms of streamline contours ((a) streamline contour for the present study and (b) streamline contour published by Dixit et al. [63]) and (c) temperature θ in the horizontal mid-plane of square cavity at $Ra = 10^6$.

2.6 Summary

In this chapter, a brief background on the lattice Boltzmann method (LBM), an implementation technique is provided, and different boundary condition treatments. The objective of the work is to validate their in-house LBM codes using benchmark isothermal and thermal flow problems.

The lattice Boltzmann method is a numerical technique used to simulate fluid flow and transport phenomena. It is based on a kinetic theory approach, where the fluid is represented by a distribution function that evolves according to discrete Boltzmann equations on a lattice. LBM has gained popularity due to its ability to handle complex geometries, parallelizability, and ease of implementation. The SRT model is a simpler form of LBM, where a single relaxation time is used to relax the distribution functions towards a local equilibrium and is employed in this work to get an insight.

Boundary conditions play a crucial role in LBM simulations. The present work elaborates on different treatments for boundary conditions, which ensure the correct representation of fluid behavior at the boundaries of the computational domain.

The comparisons with published results and the agreement suggest that the codes, with some additional features, can be used with confidence to compute flows associated with newer physics, provided additional problem-specific validation tests are conducted.

Chapter 3

Investigation of natural convection in square cavity implementing non-Boussinesq approximation

3.1 Introduction

Natural convection, also referred to as free convection, is a process of mass and heat transfer driven solely by density differences within a fluid. It occurs when there are temperature variations within the fluid, creating density gradients that induce fluid motion. Unlike forced convection, which relies on external sources such as pumps or fans to generate fluid movement, natural convection occurs spontaneously without any external intervention. The underlying principle of natural convection is that as a fluid is heated, it becomes less dense and rises, while cooler, denser fluid descends. This natural movement sets up a continuous circulation pattern, enabling the transfer of heat from hotter regions to cooler regions.

Natural convection is commonly observed in various natural and industrial scenarios, including air currents in a room, atmospheric circulation, geothermal systems, and cooling of electronic components. Understanding and controlling natural convection are crucial in many engineering applications to optimize heat transfer and ensure efficient system performance.

The Boussinesq approximation, widely used for numerical simulations of natural convection, simplifies the equations by assuming negligible density variation except for buoyancy. It is effective for small temperature differences but becomes less accurate as temperature differences increase. In such cases, non-

Boussinesq formulations or advanced numerical techniques are required for more accurate simulations. While the Boussinesq approximation remains the most common approach, its accuracy is limited to small temperature differences, necessitating alternative methods for accurate performance in cases with larger temperature variations.

Multiple studies have been conducted in the literature to investigate heat transfer rates in these scenarios. Although there have been numerous studies on heat transfer rates in natural and mixed convection, there is a lack of research specifically focusing on entropy generation analysis. Additionally, the utilization of the thermal lattice Boltzmann method (TLBM) for such analysis is relatively limited. Thus, the present study aims to investigate entropy generation and heat transfer in a square cavity using TLBM. The objective of this chapter is to examine the impact of a significant temperature difference on entropy generation and heat transfer within the cavity. Furthermore, this study explores the formulation of non-Boussinesq approximation, which has not been addressed in previous research, to the best knowledge of the author.

3.2 Mathematical modeling of the problem

The physical system considered for the current problem consists of a closed fluid square cavity with side L as shown in Figure 3.1.

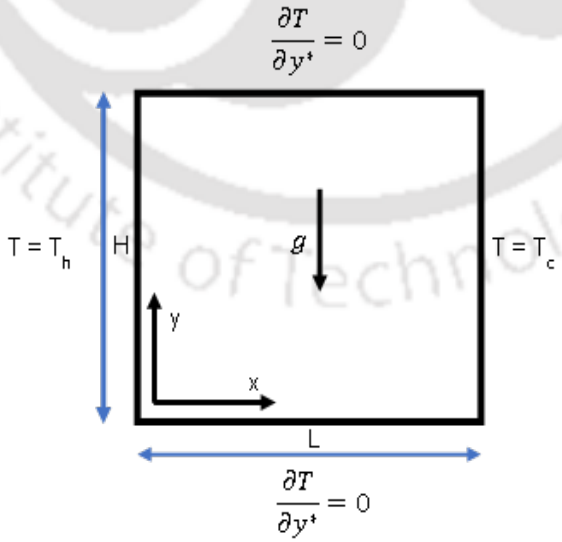

Figure 3.1: Domain geometry for natural convection in a square cavity

In the current study, the four walls of the flow configuration exhibit a no-slip impermeable velocity boundary condition. Specifically, the left wall is assigned a uniformly high temperature, while the right vertical wall is uniformly cooled. The top and bottom walls, on the other hand, are thermally insulated. A schematic diagram of the flow configuration is provided in Figure 3.1, presenting the boundary conditions in a dimensional representation. In the present work, the numerical modeling for the natural convection is performed using the lattice Boltzmann method. Initially, the Boussinesq approximation is employed. Thus, as discussed in section 2.3, Guo's model [61] among the 3 force models is considered to calculate the external force F which is defined as the external force per unit volume due to the presence of buoyancy force and is given by:

$$F_i = \rho g \beta (\theta - \theta_m) e_g \tag{3.1}$$

With the above considerations, the density and temperature distribution functions, i.e., f and g, are calculated by solving the lattice Boltzmann equation (LBE). After introducing the external force, the general form of the lattice Boltzmann equation for the flow field can be written as:

$$f_i(\mathbf{x} + \mathbf{e}_i \Delta t, t + \Delta t) = f_i(\mathbf{x}, t) + \frac{\Delta t}{\tau_v} \left[f_i^{\text{eq}}(\mathbf{x}, t) - f_i(\mathbf{x}, t) \right] + (\Delta t \times \mathbf{e}_i \times \mathbf{F}_i) \tag{3.2}$$

And for the temperature field,

$$g_i(\mathbf{x} + \mathbf{e}_i \Delta t, t + \Delta t) = g_i(\mathbf{x}, t) + \frac{\Delta t}{\tau_g} \left[g_i^{\text{eq}}(\mathbf{x}, t) - g_i(\mathbf{x}, t) \right] \tag{3.3}$$

Corresponding to the above LBE, the respective equilibrium functions for momentum and energy equations are:

$$f^{\text{eq}}(\mathbf{x}, t) = w_i \cdot \rho(\mathbf{x}, t) \left[1 + \frac{1}{2} \left(\frac{\mathbf{e} \cdot \mathbf{u}}{c_s^2} \right) + \frac{3}{2} \left(\frac{\mathbf{e} \cdot \mathbf{u}}{c_s^2} \right)^2 - \frac{1}{2} \left(\frac{\mathbf{u} \cdot \mathbf{u}}{c_s^2} \right) \right] \tag{3.4}$$

$$g^{\text{eq}}(\mathbf{x}, t) = w_i \cdot \theta(\mathbf{x}, t) \left[1 + \frac{\mathbf{e} \cdot \mathbf{u}}{c_s^2} \right] \tag{3.5}$$

where f_i and g_i are distribution functions, $\mathbf{x}$ is the position vector, $\mathbf{e}_i$ is the velocity vector, t is time, Δt is the time step, τ_v and τ_g are relaxation times, $\mathbf{F}_i$ is the external force vector, ρ is density, $\mathbf{u}$ is the velocity

field, θ is temperature, w_i are weight coefficients, and c_s is the speed of sound.

Boundary conditions: The cavity walls can have different thermal boundary conditions. As shown in the Figure 3.1, top and bottom walls are applied with the adiabatic conditions and left and right walls are assigned with isothermal conditions.

- **Isothermal Walls:** The walls are maintained at constant temperatures, such as hot and cold walls. This is also called the Dirichlet boundary condition in CFD environment.
- **Adiabatic Walls:** The walls are assumed to be thermally insulated, meaning no heat transfer occurs through the walls. The temperature is uniform throughout the cavity at a specified initial condition. This is also called the Neumann boundary condition in CFD environment.

Finally, macroscopic variable for the considered D2Q9 lattice model can be calculated in terms of above variables with the following formulations:

$$\rho = \sum_{i=0}^{8} f_i \tag{3.6}$$

$$\rho \mathbf{u} = \sum_{i=0}^{8} f_i \mathbf{e}_i \tag{3.7}$$

$$\theta = \sum_{i=0}^{8} g_i \tag{3.8}$$

3.2.1 Non-dimensional parameters

To identify the appropriate dimensionless parameters for description of natural circulation, following dimensionless variables can be defined:

$$x^* = \frac{x}{L}, \quad y^* = \frac{y}{H}, \quad u^* = \frac{u}{u_0}, \quad v^* = \frac{v}{u_0}, \quad \theta = \frac{T - T_c}{T_h - T_c} \tag{3.9}$$

Where, u_0 is a reference velocity that is unknown. The reference velocity can be chosen as:

$$u_0 = \sqrt{g\beta(T - T_\infty)L} \tag{3.10}$$

Thereby, Reynolds number $Re = \frac{u_0 L}{\nu} = \frac{\sqrt{g\beta(T_w - T_\infty)L^3}}{\nu}$. Pr is the Prandtl number which reflects the ratio between the momentum and thermal diffusion.

Also, another dimensionless number called the Grashoff number, Gr, holds importance in natural convection, representing the ratio of buoyancy force and the viscosity force acting on the fluid and is given by:

$$Gr = \frac{g\beta(T_w - T_\infty)L^3}{\nu^2} \tag{3.11}$$

3.2.2 Non-Boussinesq approximation

Most of the available investigations on variable property effects only emphasize the temperature-dependent viscosity effects. Viscosity is an important parameter controlling the momentum transport. The variable viscosity influences the velocity field and may affect the energy transport process indirectly. Also, the parameter controlling the energy or heat transfer process is thermal diffusion. Thereby, the temperature or pressure dependence of thermal diffusion may influence heat transfer characteristics greatly.

In the present work, a new-proposed model [47, 64] is employed named as variable property thermal lattice BGK (VPTLBGK) model. Unlike available studies employing conventional numerical schemes such as the finite difference, finite volume, finite element, and the boundary element methods, the VPTLBGK model is based on lattice Boltzmann method for fluid flow and heat transfer. As reported by Chenoweth et al. [65] that, the Boussinesq approximation can lead to significant errors in the velocity and temperature fields when the temperature difference is above a value on the order of 20% of the mean temperature. The thermophysical quantities, the specific heat C_p, the density ρ, the kinematic viscosity ν, the thermal diffusivity α, and the volumetric expansion coefficient β, are functions of local temperature (T). However, both ν and α increase rapidly with T, while the other parameters are weaker functions of temperature and hence can be kept constant during simulation, considering that the pressure variation is negligible in the temporal evolution.

In the VPTLBGK model, the variations in both ν and α are considered. Just like traditional models, the variation in ρ is neglected except for that in the buoyancy force term. The kinematic viscosity ν and thermal diffusivity α are functions of local temperature and are calculated using Sutherland's law. The dimensionless thermal conductivity k and dynamic viscosity μ are calculated using the following relation:

$$k = \theta^{\frac{3}{2}} \frac{1 + S_k}{\theta + S_k} \quad \text{and} \quad \mu = \theta^{\frac{3}{2}} \frac{1 + S_\mu}{\theta + S_\mu} \tag{3.12}$$

where $S_k = 0.368$ and $S_\mu = 0.648$ are considered in the Sutherland law.

Traditionally, the two relaxation times are specified at the beginning and then keep constant as time advances. However, in the present model, as kinematic viscosity ν and thermal diffusivity α are functions of local temperature and the respective relaxation times are the function of these two parameters. Thereby, the changes are incorporated in the numerical simulation accordingly.

3.2.3 Post-processing parameters

Nusselt number, entropy generation plays a crucial role to analyze the obtained results. The formulations are mentioned below:

i. Nusselt Number: The average Nusselt number along the left hot wall ($\overline{\text{Nu}}_h$) and right cold wall ($\overline{\text{Nu}}_c$) are respectively calculated using the below-mentioned equations 3.13 and 3.14 [58].

$$\overline{\text{Nu}}_h = \frac{1}{L_h} \int_0^L \overline{\text{Nu}}_x \, dy \tag{3.13}$$

$$\overline{\text{Nu}}_c = \frac{1}{L_c} \int_0^L \overline{\text{Nu}}_x \, dy \tag{3.14}$$

where $\overline{\text{Nu}}_x = -\frac{\partial \theta}{\partial x}$ are the local Nusselt numbers at all fluid nodes and at the vertical surfaces, respectively.

ii. Entropy Generation: The existence of a thermal gradient between the vertical walls of the enclosure sets the fluid in a non-equilibrium state, which causes entropy generation in the system. According to local thermodynamic equilibrium with linear transport theory, the local entropy generation for a two-dimensional Cartesian system is given by [66]:

$$\dot{S}_l = \frac{k}{T_0^2} \left(\left(\frac{\partial T}{\partial x} \right)^2 + \left(\frac{\partial T}{\partial y} \right)^2 \right) + \frac{\mu}{T_0} \left[2 \left(\frac{\partial u}{\partial x} \right)^2 + 2 \left(\frac{\partial v}{\partial y} \right)^2 + \left(\frac{\partial u}{\partial y} + \frac{\partial v}{\partial x} \right)^2 \right] \tag{3.15}$$

The local entropy generation can be made dimensionless by using the dimensionless variables listed in subsection 3.2.2. The total entropy generation consists of two components: entropy generation

due to heat transfer (S_θ) and due to fluid friction (S_Ψ). Thus, the local total entropy generation can be given by the below equation 3.16:

$$\dot{S}_{l,T} = \dot{S}_{l,\theta} + \dot{S}_{l,\Psi} \tag{3.16}$$

where,

$$\dot{S}_{l,\theta} = \left(\frac{\partial\theta}{\partial X}\right)^2 + \left(\frac{\partial\theta}{\partial Y}\right)^2 \quad \text{and} \quad \dot{S}_{l,\Psi} = \varphi\left[2\left(\frac{\partial U}{\partial X}\right)^2 + 2\left(\frac{\partial V}{\partial Y}\right)^2 + \left(\frac{\partial U}{\partial Y} + \frac{\partial V}{\partial X}\right)^2\right]$$

and $\varphi = \frac{\mu T_0}{k}\left(\frac{\alpha}{L\Delta T}\right)^2$.

3.3 Results and discussion

Natural convection for two different cases of force term approximation is considered in the present work. A comprehensive analysis is made to study the effect of large temperature difference in terms of Ra (10^3–10^7) on fluid flow and heat transfer for each case at Pr=0.71.

3.3.1 Streamline contours

The streamline contours are shown in Figure 3.2 for the above discussed configuration at Ra=10^3 for both Boussinesq and non-Boussinesq approximation.

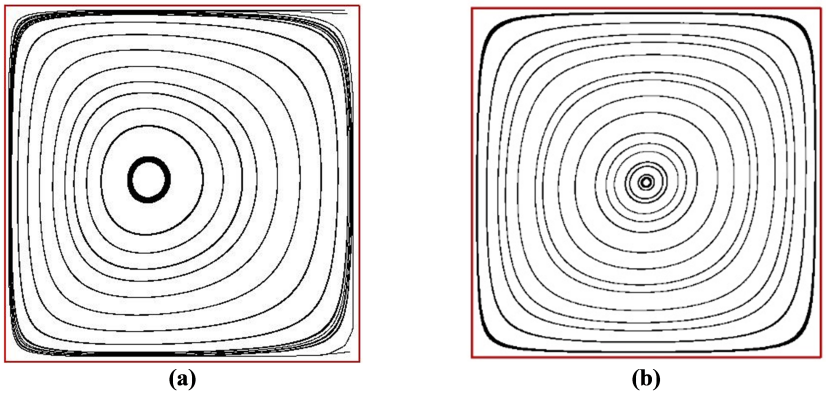

Figure 3.2: Streamline contours at $Ra = 10^3$ (a) Using Boussinesq approximation (b) Using non-Boussinesq approximation

The streamline contours are shown in Figure 3.3 for the above discussed configuration at Ra=10^4 for both Boussinesq and non-Boussinesq approximation.

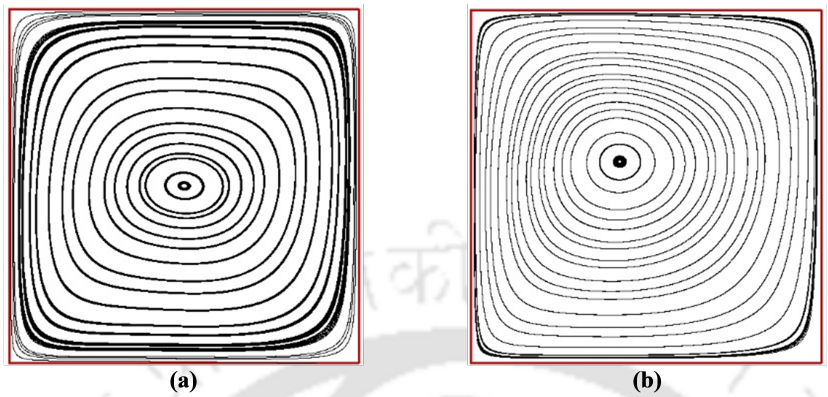

Figure 3.3: Streamline contours at Ra =10^4 (a) Using Boussinesq approximation (b) Using non-Boussinesq approximation

The streamline contours are shown in Figure 3.4 for the above discussed configuration at Ra=10^5 for both Boussinesq and non-Boussinesq approximation.

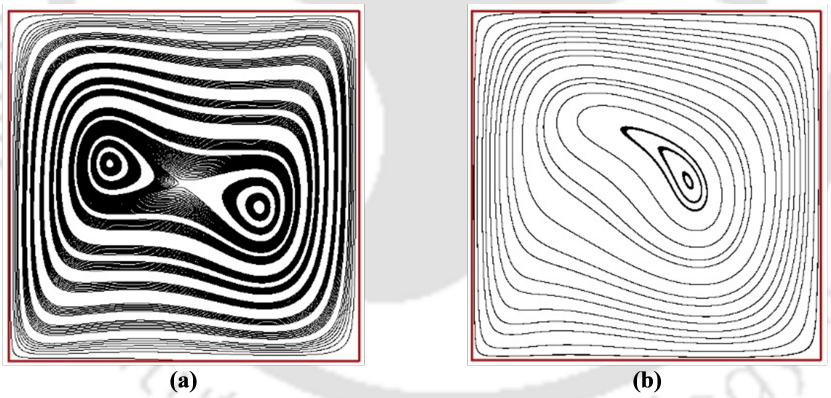

Figure 3.4: Streamline contours at Ra=10^5 (a) Using Boussinesq approximation (b) Using non-Boussinesq approximation

The streamline contours are shown in Figure 3.5 for the above discussed configuration at Ra 10^6 for both Boussinesq and non-Boussinesq approximation.

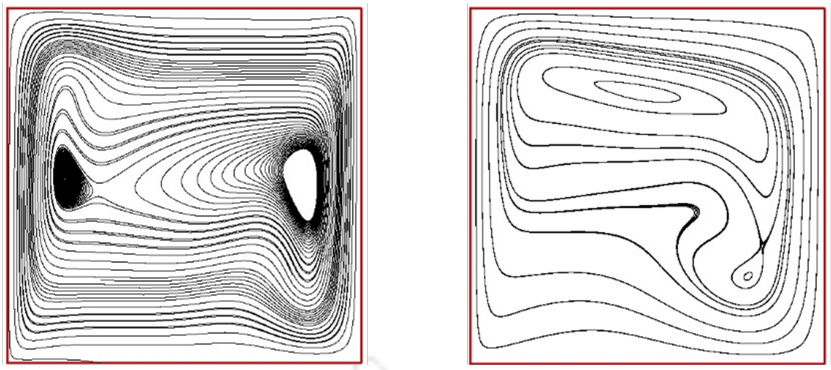

Figure 3.5: Streamline contours at Ra=10^6 (a) Using Boussinesq approximation (b) Using non-Boussinesq approximation

The streamline contours are shown in Figure 3.6 for the above discussed configuration at Ra=10^7 for both Boussinesq and non-Boussinesq approximation.

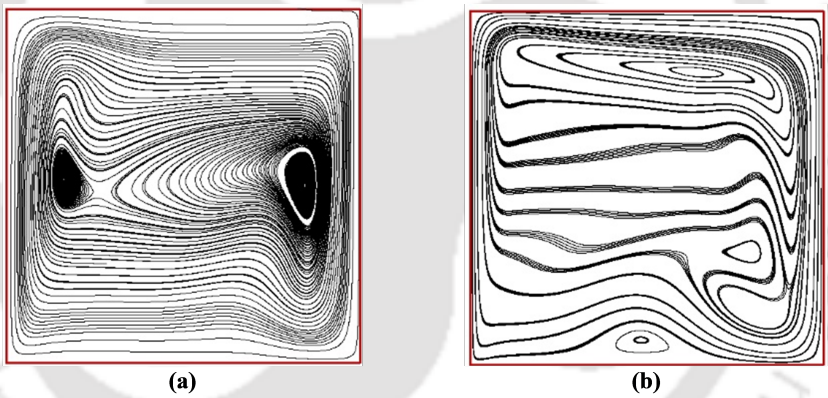

Figure 3.6: Streamline contours at Ra=10^7 (a) Using Boussinesq approximation (b) Using non-Boussinesq approximation

The Boussinesq approximation is a common simplification used in fluid dynamics, especially for buoyancy-driven flows. It assumes that density variations in the fluid are small except in buoyancy terms. The observed behavior as depicted in Figure 3.2 (a) through 3.6 (a) show the streamline contours for 5 different Ra ranging for 10^3 to 10^7 and is aligned with the predictions made using the Boussinesq approximation. This means that the simplified model is effective in capturing the fundamental physics of the fluid behavior under the influence of buoyancy and the compressibility effect. At low Rayleigh numbers, a single vortex is observed at the center of the fluid domain. As the Rayleigh number increases,

the central streamlines become elliptical in shape due to higher velocities along the top and bottom walls. This change in shape occurs as the buoyancy-driven flow becomes more pronounced. Further increases in the Rayleigh number result in the appearance of secondary vortices, contributing to the complexity of the flow patterns.

These contours provide a visual representation of the flow behavior, showcasing the intricate paths that the fluid takes due to buoyancy-driven convection. One notable observation is the lack of centro-symmetric (symmetrical with respect to the center) properties in these contours. This lack of symmetry is attributed to the presence of the compressibility effect. In natural convection, the compressibility effect refers to the impact of changes in gas density on the convective heat transfer process. As the fluid moves due to buoyancy-driven convection, it experiences pressure changes, and its density varies along the flow path. These density changes, in turn, affect the compressibility of the fluid. The compressibility effect is particularly relevant in cases where the temperature differences are large enough to cause significant variations in the fluid density, leading to substantial changes in the flow behaviour and heat transfer characteristics. It is observed that, the single vortex at the centre is observed at low Ra. With increase in Ra, the central stream lines get distorted and become elliptical in shape which occurs due to higher velocity along the top and bottom walls. With further increase in Ra, secondary vortices appear.

The counterpart of the Boussinesq approximation representation is depicted in Figure 3.2 (b) through 3.6 (b). The streamlines adjacent to the vertical walls show increased density, while the main flow exhibits peripheral currents. Furthermore, as similar pattern reported by Boufia et al. [67] asymmetrical small rolls can be observed, shifted towards the vertical walls. This confirms the better prediction of buoyancy force and compressibility effect with increasing Ra.

3.3.2 Isotherm contours

The isotherm contours are shown in Figure 3.7 for the above discussed configuration at Ra=10^3 for both Boussinesq and non-Boussinesq approximation.

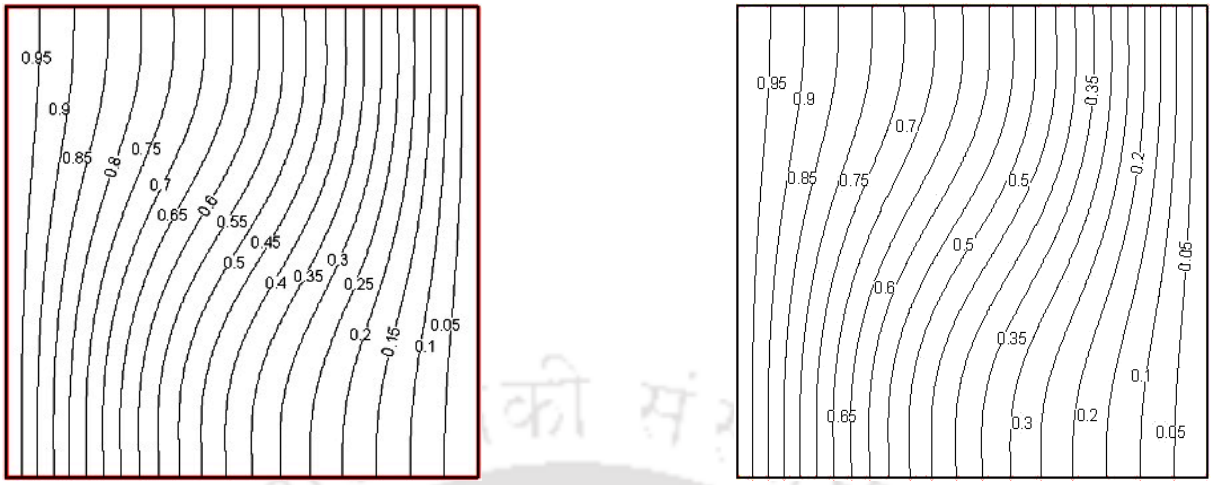

(a) **(b)**

Figure 3.7: Isotherm contours at Ra=10^3 (a) Using Boussinesq approximation (b) Using non-Boussinesq approximation

The isotherm contours are shown in Figure 3.8 for the above discussed configuration at Ra=10^4 for both Boussinesq and non-Boussinesq approximation.

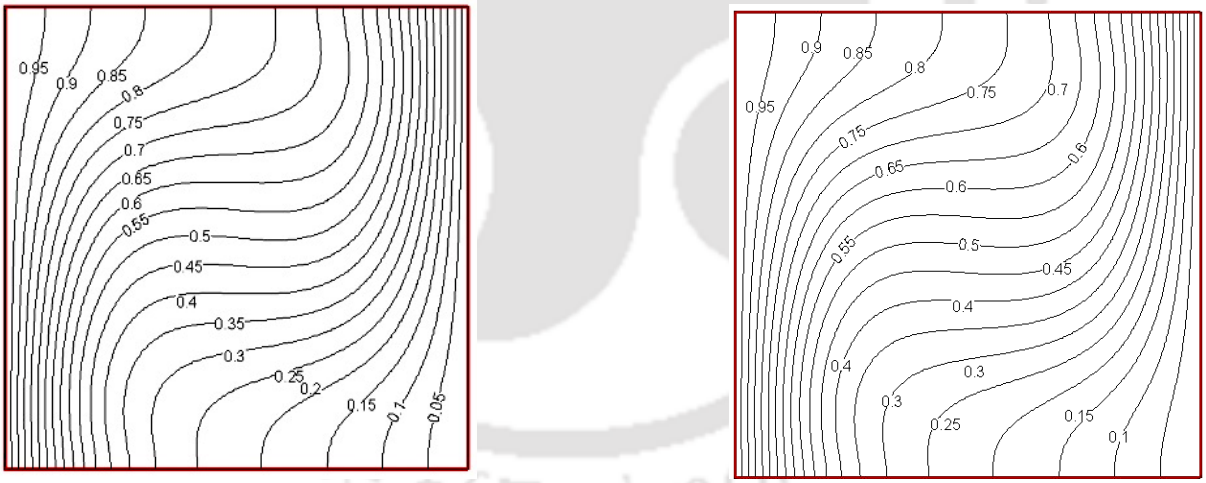

(a) **(b)**

Figure 3.8: Isotherm contours at Ra=10^4 (a) Using Boussinesq approximation (b) Using non-Boussinesq approximation

The isotherm contours are shown in Figure 3.9 for the above discussed configuration at Ra=10^5 for both Boussinesq and non-Boussinesq approximation.

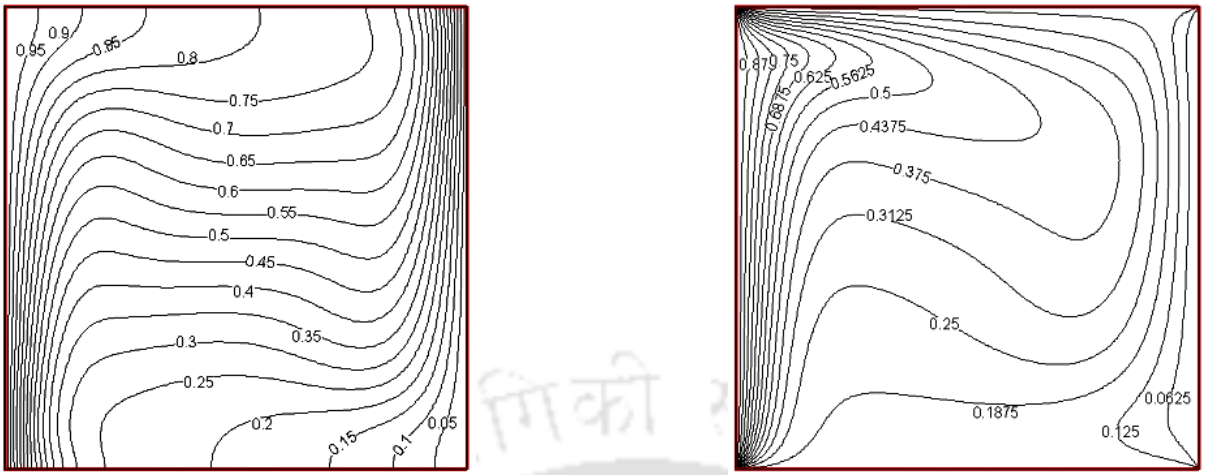

(a) **(b)**

Figure 3.9: Isotherm contours at Ra=10^5 (a) Using Boussinesq approximation (b) Using non-Boussinesq approximation

The isotherm contours are shown in Figure 3.10 for the above discussed configuration at Ra=10^6 for both Boussinesq and non-Boussinesq approximation.

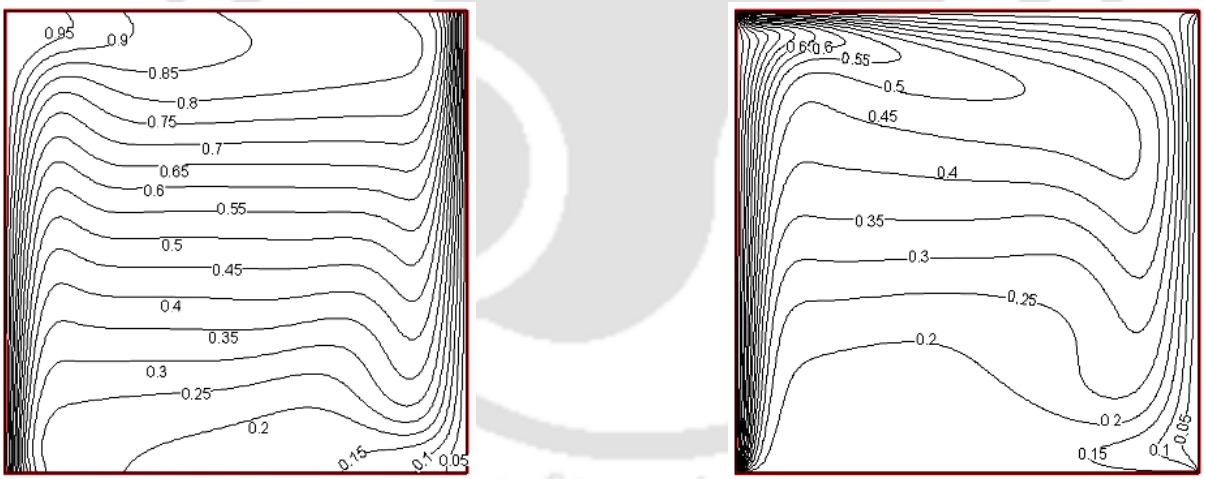

(a) **(b)**

Figure 3.10: Isotherm contours at Ra=10^6 (a) Using Boussinesq approximation (b) Using non-Boussinesq approximation

The isotherm contours are shown in Figure 3.11 for the above discussed configuration at Ra=10^7 for both Boussinesq and non-Boussinesq approximation.

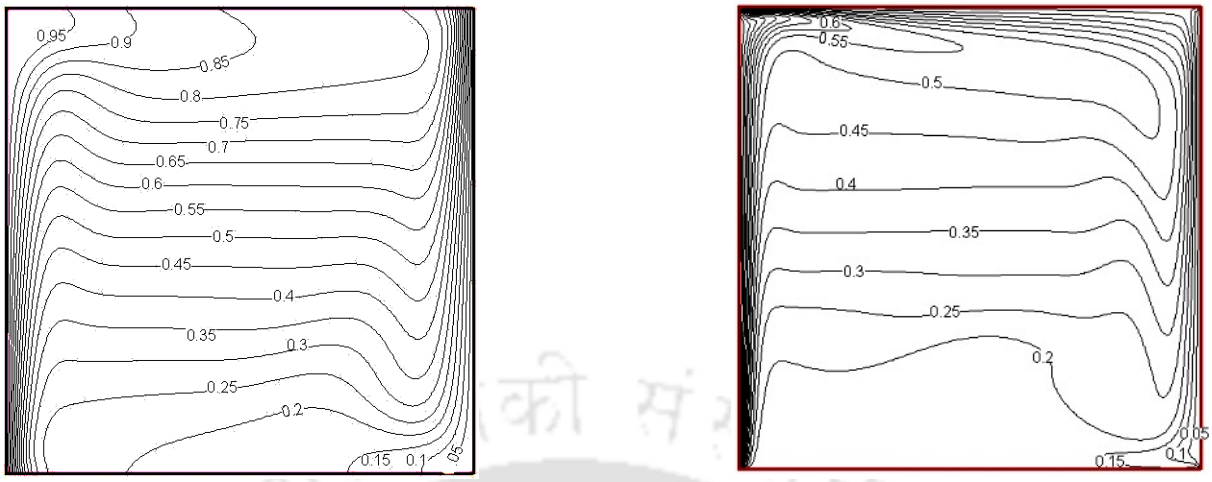

(a) **(b)**

Figure 3.11: Isotherm contours at Ra=10^7 (a) Using Boussinesq approximation (b) Using non-Boussinesq approximation

Figures 3.7 through 3.11 present a series of visual representations depicting the heat transfer characteristics in the cavity. At low Rayleigh numbers (Ra), the heat transfer is primarily governed by conduction. In this regime, the heat is predominantly transferred through direct contact between adjacent particles. The temperature gradients are relatively gradual, leading to smooth isotherm patterns across the cavity.

As the Rayleigh number increases, the significance of convection becomes evident. In the plots, this transition is marked by the emergence of a horizontal line at the center of the cavity. This indicates the presence of a strong horizontal current or convective flow within the cavity. In a convective mode, the heat is not solely transmitted through particle-to-particle interaction but also through bulk fluid motion, which can significantly enhance heat transfer rates.

The subsequent observation points out that the system is predominantly occupied by horizontal isotherms. This prevalence of horizontal temperature contours underscores the dominance of the convection mode in the overall heat transfer process. This is a significant shift from the earlier conduction-dominated regime. Convection's ability to move large volumes of fluid enables faster heat transport, resulting in more pronounced and concentrated temperature gradients.The Boussinesq approximation simplifies density changes, except in buoyancy terms, whereas the non-Boussinesq model considers the full impact of density variations on the fluid behavior.Especially at higher Ra values, these differences manifest in the isotherm patterns. The non-Boussinesq model predicts temperature distributions that deviate from the Boussinesq approximation. These discrepancies suggest that accounting for the complete

effects of density variations is crucial at higher Rayleigh numbers, as they lead to distinct flow patterns and temperature distributions.As Ra increases, density variations within the fluid become more pronounced. These density changes are intricately linked to the flow behavior and temperature distribution. Higher Ra values result in more complex flow patterns and temperature gradients. This underscores the importance of accurately modeling the density changes, particularly when investigating scenarios involving significant buoyancy-driven effects.

3.3.3 Comparative study for temperature variation at mid-y plane for $10^4 < Ra < 10^6$

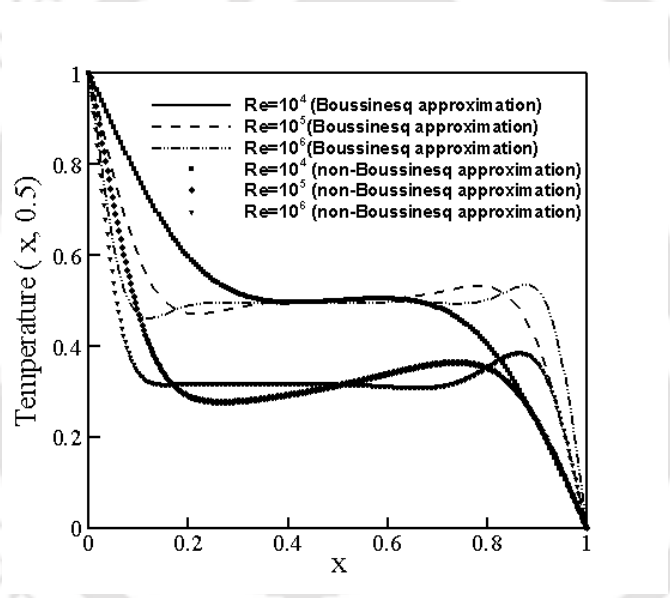

Figure 3.12: Comparative temperature variation at mid-y plane for $Ra = 10^4$–10^6

Figure 3.12 presents a comparative analysis of temperature variations using both the Boussinesq and non-Boussinesq approximations for three different Rayleigh numbers (Ra). In both scenarios, there is a noticeable transition in the heat transfer mechanism from conduction to convection, as evidenced by the isotherms.

When the Ra value is low, the dominant mode of heat transfer is conduction. As the Ra value increases, the temperature profiles in the cavity become more horizontal, indicating a shift towards convective heat transfer. Near the center of the cavity, the temperature profile exhibits a change in slope, indicating a significant variation in temperature. Additionally, steep temperature gradients can be observed near the

cavity walls.

For low Ra values, the temperature profiles of the non-Boussinesq case closely resemble those obtained using the Boussinesq approximation, making it difficult to distinguish between the two cases. However, the symmetry observed under the Boussinesq approximation breaks down in the non-Boussinesq case. This breakdown is attributed to variations in the transport coefficients, which become more pronounced as the flow becomes more compressible. The influence of these variations is particularly noticeable in the core region of the cavity, where the temperature undergoes significant changes.

3.3.4 Comparative study for Nusselt number at $10^3 < Ra < 10^7$

The effect of Rayleigh number (Ra) has been studied, and the comparative plot for average Nusselt number of hot and cold walls ($\bar{N}u_h$ and $\bar{N}u_c$) is shown in Figure 3.13.

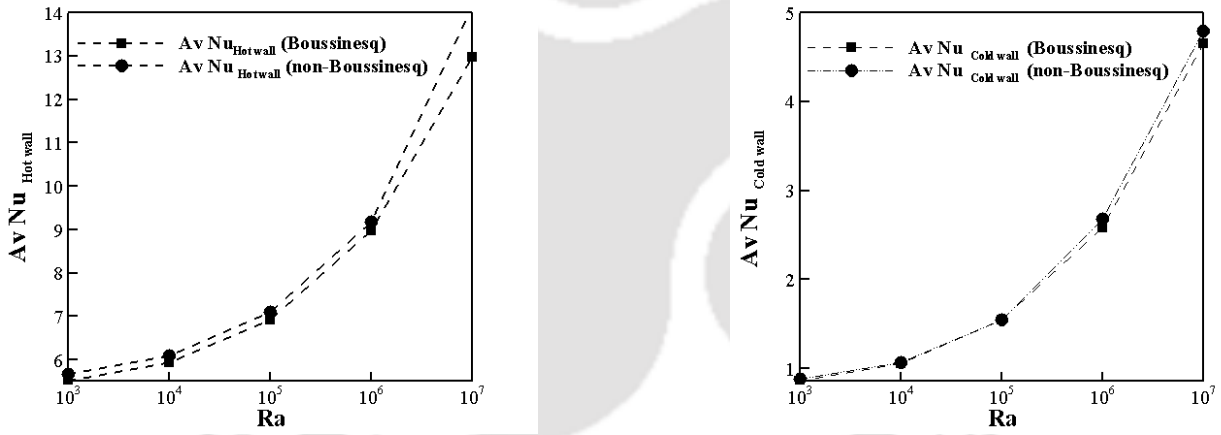

(a) Average Nusselt number variation over left hot wall ($\bar{N}u_h$)

(b) Average Nusselt number variation over left hot wall ($\bar{N}u_c$)

Figure 3.13: Variation of average Nusselt number varying Ra = 10^4–10^7 over (a) left hot wall, $\bar{N}u_h$ (left panel) and (b) right cold wall, $\bar{N}u_c$ (right panel)

3.3.5 Comparative study for entropy generation at $10^3 < Ra < 10^7$

The effect of Rayleigh number has been studied, and the comparative plot for average entropy generation due to heat transfer ($\bar{S}_\theta$) and fluid friction ($\bar{S}_\Psi$) is shown in Figure 3.14.

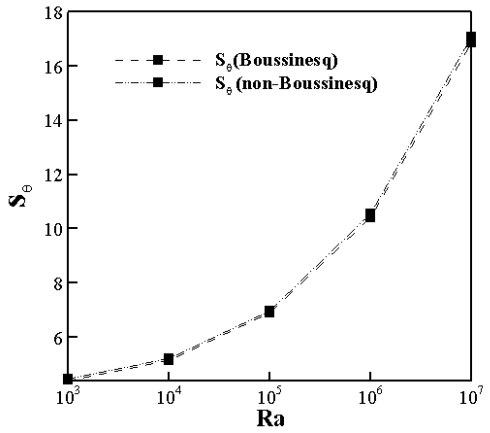

(a) Average entropy generation due to heat transfer ($\bar{S}_\theta$)

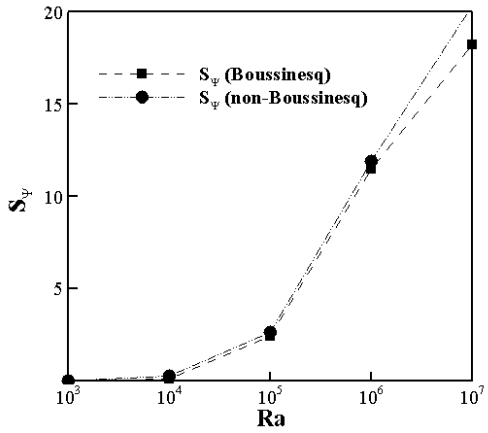

(b) Average entropy generation due to fluid friction ($\bar{S}_\Psi$)

Figure 3.14: Variation of entropy generation varying Ra = 10^4-10^7 for (a) Heat transfer ($\bar{S}_\theta$, left panel), and (b) Fluid friction ($\bar{S}_\Psi$, right panel)

From the above Figure 3.13 and 3.14 it can infer that; Ra has a strong influence on the Nu and entropy generation variation and the heat transfer rate and irreversibility (entropy generation) varies almost linearly with increase in Ra. This implies that, the intensification of Ra accelerates the flow which increases the temperature and velocity gradients inside the fluid domain.

As the Rayleigh number increases, indicating a stronger buoyancy effect, the convective heat transfer becomes more dominant, leading to higher Nusselt numbers. This implies that the rate of heat transfer through convection increases compared to conduction.

Similarly, the Rayleigh number influences the variation of entropy generation in a system. Entropy generation is associated with the irreversible processes occurring within the system. With higher Rayleigh numbers, the convective heat transfer intensifies, resulting in increased fluid mixing and higher entropy generation due to fluid friction. This is because the buoyancy forces drive stronger fluid motion, leading to increased velocity gradients and shear stresses, which contribute to higher entropy production. This is true for both the simulations under Boussinesq and Non-Boussinesq conditions.

It is observed from Figure 3.14 (b) that, with increase in Ra, entropy generation due to fluid friction ($\bar{S}_\Psi$)) increases and surpasses the entropy generation due to heat transfer ($\bar{S}_\theta$) at a critical value of Ra= 10^6. This indicates that the dissipation of energy due to fluid friction plays a more significant role in the overall entropy production compared to heat transfer. This is because for small thermal Grashof number, there is practically no convection and the entropy generation due to fluid friction is minimum,

consequently the total entropy generation is reduced to almost the entropy generation due to heat transfer. The higher entropy generation due to fluid friction at high Ra can be attributed to the inherent dissipative nature of fluid flow. The presence of viscosity and the conversion of kinetic energy into heat during fluid motion result in increased entropy production ($\bar{S}_\Psi$).

Also, in non-Boussinesq simulations, it is observed that the values of entropy and the Nusselt number (Nu) tend to be greater compared to those obtained from the Boussinesq approximation. These deviations are maximum (9.13% for Nusselt number and 11.9% for entropy generation) at the highest value of Ra = 10^7. This is because the Boussinesq approximation assumes that the fluid properties, such as density, remain constant except for a buoyancy term in the governing equations. It neglects the dependency of fluid properties on temperature variations, which is a valid assumption for small temperature differences. The inclusion of these additional factors in non-Boussinesq simulations leads to higher values of entropy and Nu compared to the Boussinesq approximation.

The variations in fluid properties with temperature contribute to increased entropy generation, as the non-uniformity in the fluid properties introduces additional irreversibilities.

Again, the temperature-dependent fluid properties influence the heat transfer coefficient, resulting in enhanced heat transfer through convection. Hence, greater variations of these parameters are observed at higher Ra values.

3.4 Summary

In the present work, the numerical modeling for the natural convection is performed using the lattice Boltzmann method to study the influence of variable thermal property on buoyancy driven flow. The impact of significant temperature difference on entropy generation and heat transfer within the cavity is analyzed considering both Boussinesq and non-Boussinesq approximation in the simulations ranging from Ra=10^3- 10^7.

The salient features of the numerical study are as follows:

(i) The transition from conduction to convection in the heat transfer mechanism is observed as the Rayleigh number (Ra) increases. At low Ra values, conduction heat transfer mode dominates, while at higher Ra values, convection becomes more significant, resulting in a strong influence on Nu and entropy generation. Thus, understanding and controlling the Rayleigh number is important

for optimizing heat transfer efficiency and minimizing entropy generation.

(ii) The non-Boussinesq simulations show higher values of entropy and Nu compared to the Boussinesq approximation for all values of Ra. The inclusion of temperature-dependent fluid properties in non-Boussinesq simulations leads to increased entropy generation and higher Nusselt numbers.

(iii) As the Rayleigh number (Ra) increases, the entropy generation due to fluid friction ($\bar{S}_\Psi$) becomes more prominent and exceeds the entropy generation caused by heat transfer ($\bar{S}_\theta$) at a critical Ra value of 10^6. This signifies that the dissipation of energy resulting from fluid friction plays a greater role in overall entropy production compared to heat transfer, particularly beyond Ra = 10^6.

Chapter 4

Parametric analysis of mixed convection in a square cavity using SRT-LBM

4.1 Introduction

The thermal analysis of lid-driven systems with horizontally and vertically sliding walls has attracted significant attention over the years, primarily due to their expanding utilization in various fields such as lubrication technologies, electronic cooling, solar systems, food processing, and nuclear reactors. Modeling of these engineering problems where mixed convection flow and heat transfer occurs have been reported by many studies. And, the study considers mixed convection to be more intricate compared to other forms of convection due to the combination of two distinct forces: the buoyancy force resulting from temperature differences and the shear force induced by the movement of walls.

The performance of mixed convection in a system is dependent on several key parameters. The Richardson number (Ri) plays a crucial role in determining the dominance of either buoyancy-driven or forced convection. A higher Ri indicates a stronger buoyancy effect, leading to enhanced natural convection, while a lower Ri signifies a stronger forced convection regime. The Reynolds number (Re) influences the flow behavior, with higher Re values promoting more dominant forced convection. The Prandtl number (Pr) affects the thermal boundary layer thickness and heat transfer characteristics, with higher Pr leading to thicker thermal boundary layers. The Grashof number (Gr) quantifies the relative significance of buoyancy forces to viscous forces and determines the strength of buoyancy-driven flows. As Gr increases, the impact of buoyancy forces becomes more pronounced. Other factors such as

aspect ratio, boundary conditions, and geometry of the system also affect mixed convection performance. Understanding the interplay and dependence of these parameters is essential for predicting and optimizing mixed convection phenomena, enabling efficient system design and enhanced heat transfer performance.

Existing research literature indicates the availability of numerous numerical and experimental investigations on natural and mixed convection within cavities, focusing on the influential factors. These studies primarily employ conventional numerical techniques like the finite volume method and finite difference method while taking 1st law of thermodynamics of heat transfer analysis into consideration. However, there is a paucity of research utilizing the lattice Boltzmann method (LBM) for studying these phenomena. Besides, to the best of the author's knowledge, a numerical investigation on the optimization of effective parameters on mixed convection heat transfer and entropy generation has not yet been reported.

Thereby, the study is further explored and in the present work numerical simulations on mixed convection in a square enclosure using 3 different configurations are performed using the thermal LBM model. The motivation behind the current work is to investigate the fluid dynamics inside the cavity under the combined effect of both driving the lid and the buoyancy effect.

4.2 Mathematical modelling of the problem

The analysis is done for a square cavity of length L, where 3 different configurations are considered as illustrated in Figure 4.1.

The first one is with the top lid moving in the forward direction (case 1), the second one with both top and bottom lids moving in the forward direction (case 2), and the third one then moves both the lids in opposite directions (case 3). The no-slip boundary conditions are applied to all four stationary walls. Dirichlet boundary conditions are applied to the left and right walls (the left wall is a hot wall). Neumann boundary conditions are applied to top and bottom boundaries to represent the adiabatic conditions as shown in Figure 4.1

As discussed in Chapter 2 and Chapter 3, Guo's model is considered to calculate the external force F of buoyancy. The D2Q9 lattice model-based thermal lattice Boltzmann method is employed for the current simulations.

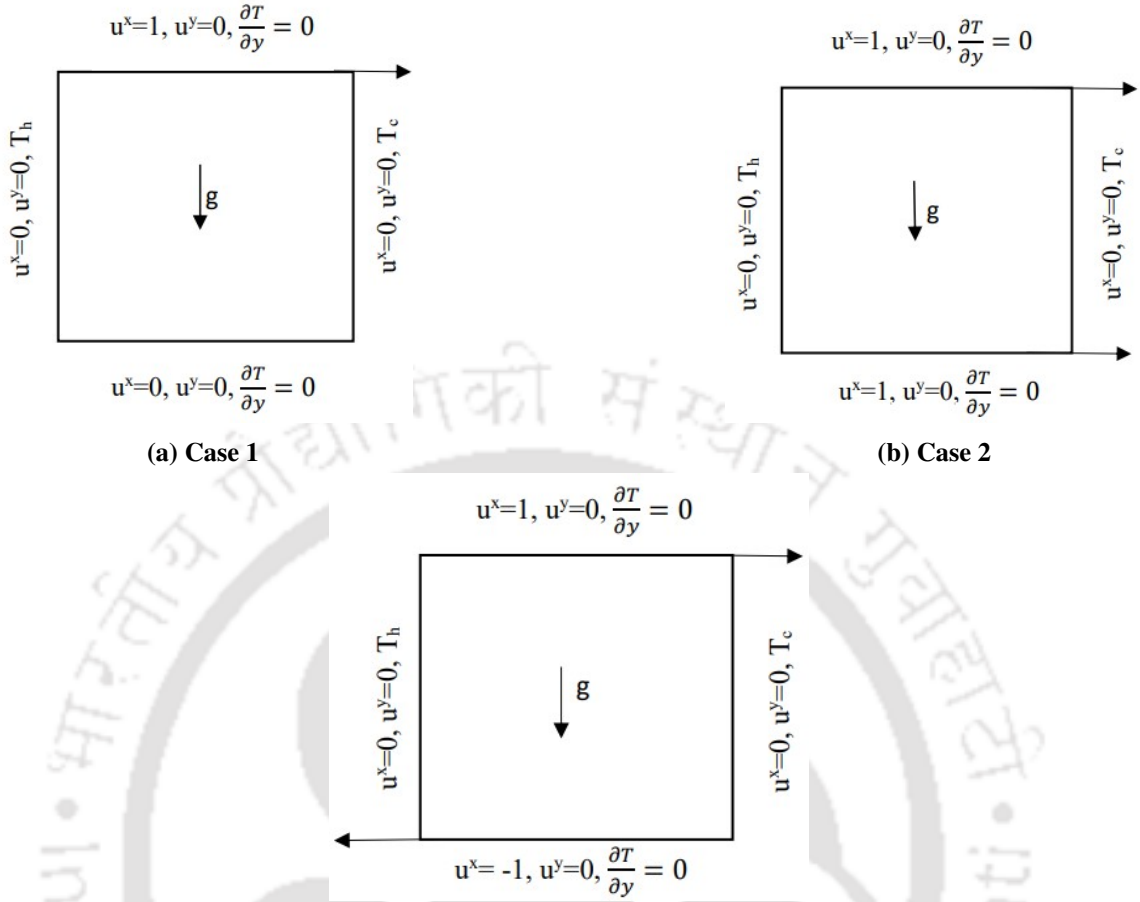

Figure 4.1: Computation geometry flow configuration with boundary conditions

Post-processing parameters:

As mentioned above, the results are discussed in terms of streamline contours, isotherms, Nusselt number, entropy generation, and skin friction. The formulations for calculating Nusselt number and entropy generation are mentioned in subsection 3.2.3 (Equation 3.13 through 3.14). The formulation for skin friction is mentioned below:

(i) **Skin coefficient of friction (C_f):**

The skin friction coefficient in the dimensional computational domain is calculated by using equation 4.1.

$$C_f = \frac{\tau_w}{0.5\rho u^2} \tag{4.1}$$

At the lattice level, it is calculated using equation 4.2:

$$C_f = \frac{2}{Re}\frac{\partial U}{\partial Y} \tag{4.2}$$

where, τ_w is the dimensional shear stress.

Following is the description of the steps for the LBM simulations as shown in Figure 4.2.

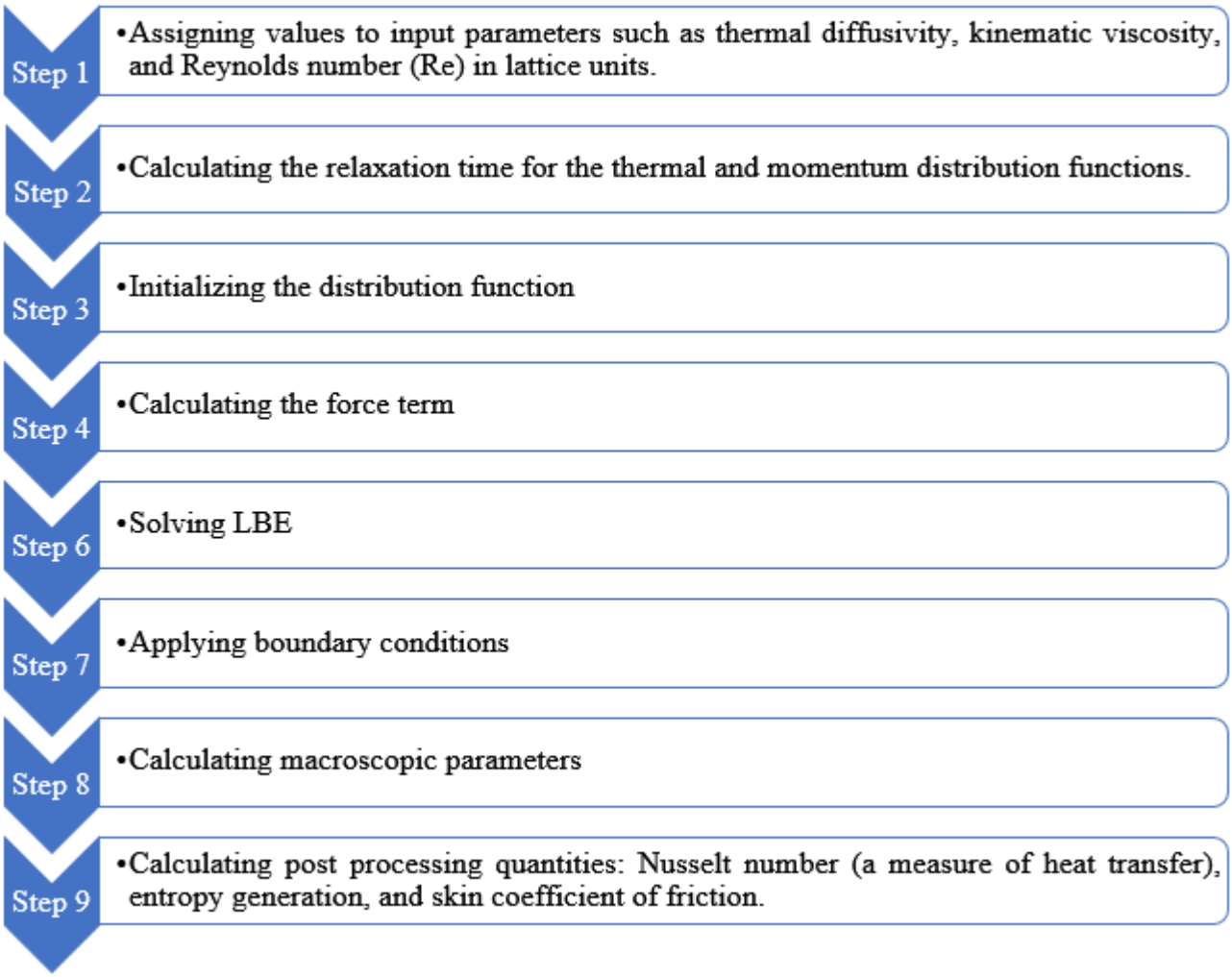

Figure 4.2: Steps followed in the simulations

These steps outline the process of conducting a simulation using the given equations and procedures that are discussed in chapters 2 and 3.

4.3 Code validation and grid independence test

An extensive mesh testing procedure is conducted to guarantee a grid independent solution. Eight different mesh combinations were used for the case of Ri=0.01, Re=100, Pr = 0.71. The simulations are performed taking Neumann boundary conditions for left and right adiabatic walls and Dirichlet boundary conditions for top (hot) and bottom (cold) walls.

Table 4.1: Grid independence test for mixed convection

S.no.	Grid Size	Av Nu
1	150×150	1.69
2	180×180	1.79
3	200×200	1.88
4	220×220	1.90
5	250×250	1.95
6	280×280	1.97
7	300×300	1.99
8	320×320	2.00

The present code was tested for grid independence by calculating the average Nusselt number on the top wall. The configuration depicting case 1 in the present study is used for validating the code with the existing literature,

With reference to Table 4.1, the obtained value for the Nusselt number of grid size 300×300 and 320×320 are almost close. Thereby, 300×300 of grid size is emloyed for the current study. The results are validated with other standard references[1,2] and is shown in Figure 4.3.

Again, the streamlines contour and isotherm contours obtained with the input parameters of Re=500, Ri=0.4 and Pr=1 are shown in Figure 4.4(a) and is compared with existing results shown in Figure 4.4(b) published by Moallemi et al. [68]. The primary circulation occupies the entire cavity, accompanied by minor cells observed near the bottom corners. Isotherms concentrate in close proximity to the bottom lid, indicative of pronounced temperature gradients in that vicinity. However, within the bulk of the cavity, aside from this localized area, weak temperature gradients predominate, implying efficient mixing facilitated by vigorous circulations.

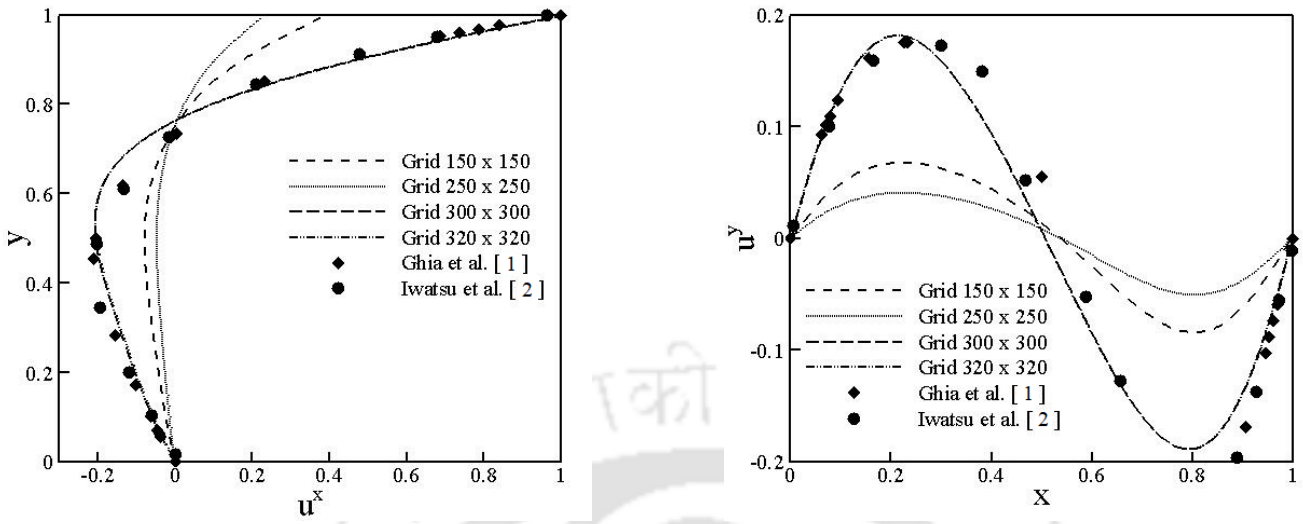

(a) (b)

Figure 4.3: Comparison of results in terms of dimensionless horizontal velocity u^x at $y = 0.5$ (left panel) and vertical velocity u^y at $x = 0.5$ (right panel) with Ghia et al. [1] and Iwatsu et al. [2]

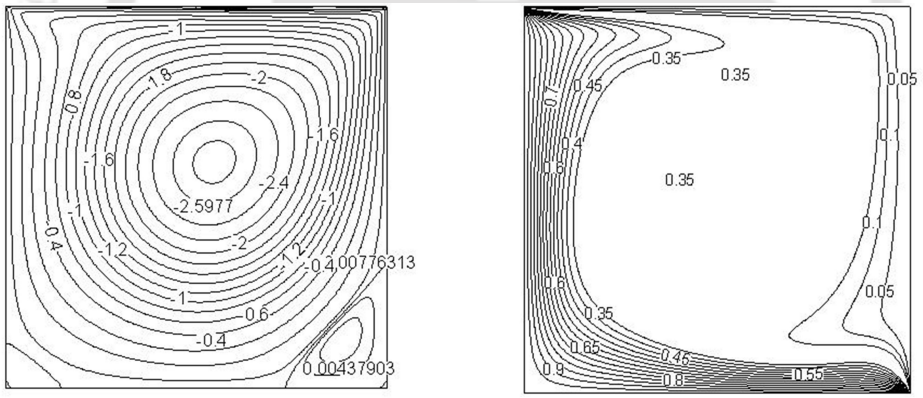

(a)

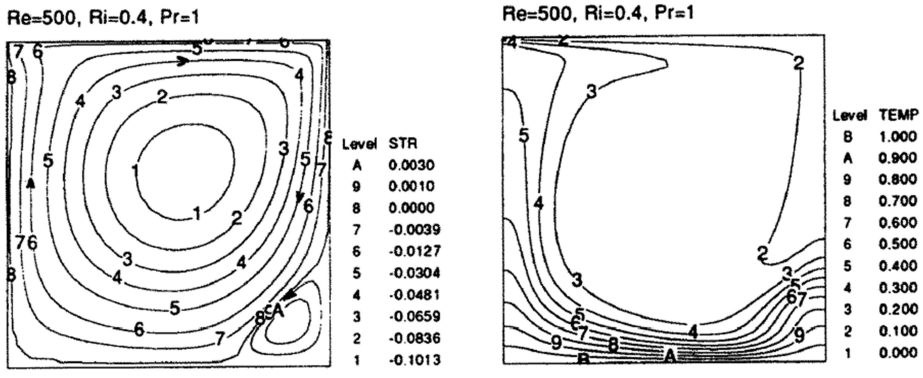

(b)

Figure 4.4: Comparison of present results in terms of streamlines contours (Figures (a) and (b)) and isotherm contours (Figure (b)) with Moallemi et al.[68].

4.4 Results and discussion

A thorough evaluation of the above-mentioned mixed convection based configurations has been conducted using the SRT-LBM approach. The simulations utilize the validated code and incorporate multiple parameters to analyze their impact on the system. The parameters under consideration are as follows:

(i) Effect of Richardson number

(ii) Effect of Prandtl number

(iii) Effect of Reynolds number

(iv) Effect of inclination angle

(v) Effect of aspect ratio

(vi) Effect of velocity ratio

The results obtained through the present simulations are discussed below.

4.4.1 Effect of Richardson number (Ri)

The simulations are done at Re=100 and Pr=0.71 varying Ri at 0.1, 0.5, 1 and 10. The effect of Ri is shown below and comparison between all the three cases are depicted in terms of streamlines (Figure 4.5, 4.6 and 4.7), isotherms (Figure 4.8, 4.9 and 4.10), velocity at the mid-plane (Figure 4.11, 4.12 and 4.13).

a) **Streamline contours**

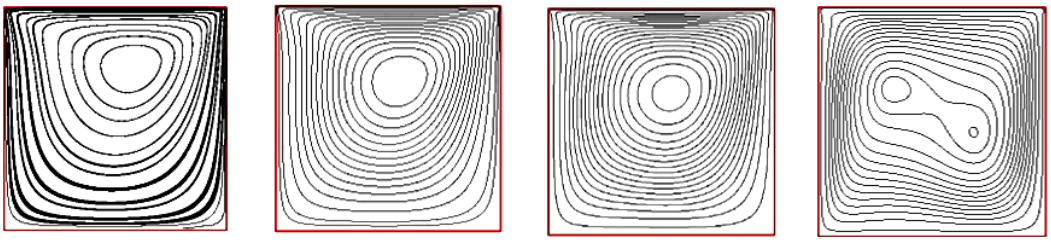

Figure 4.5: Streamline contours for case 1 for the effect of Ri

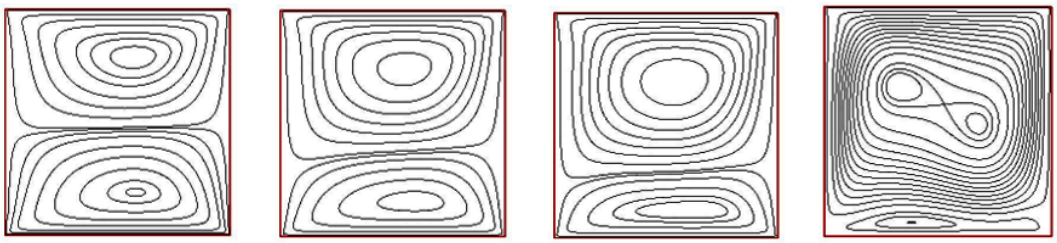

Figure 4.6: Streamline contours for case 2 for the effect of Ri

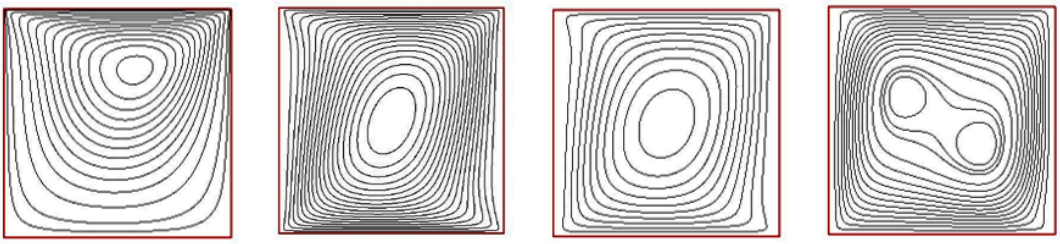

Figure 4.7: Streamline contours for case 3 for the effect of Ri

Figure 4.5 through 4.7 depicts a detailed flow analysis for all three cases in terms of effect of Ri. Ri=0.1 shows that the forced convection plays a dominant role and recirculation flow is mostly generated only by moving lids and Ri=10 implies the dominating impact of natural convection.

The streamlines in case 1 show a single vortex at the center near the top lid at low Ri. With the increase in Ri, the central streamline gets distorted and shifts to downward direction due to buoyancy effect. The dominance of natural convection can be seen in a more pronounced manner in the isotherm contours where increasing the Ri leads the horizontal line at the centre of the cavity.

b) **Isotherm contours**

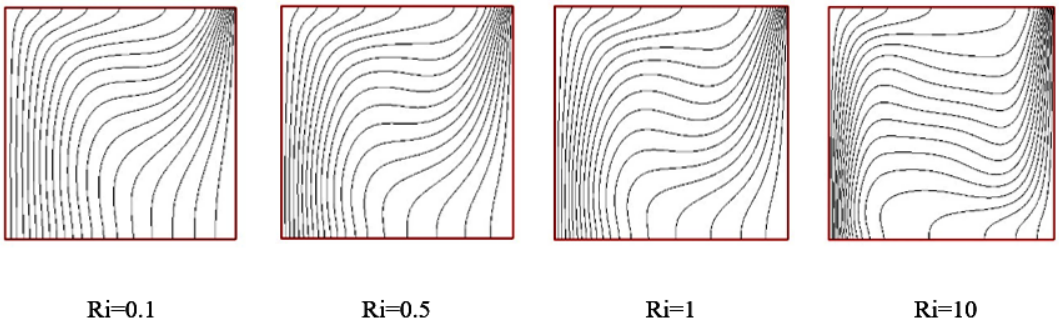

Figure 4.8: Isotherm contours for case 1 for the effect of Ri

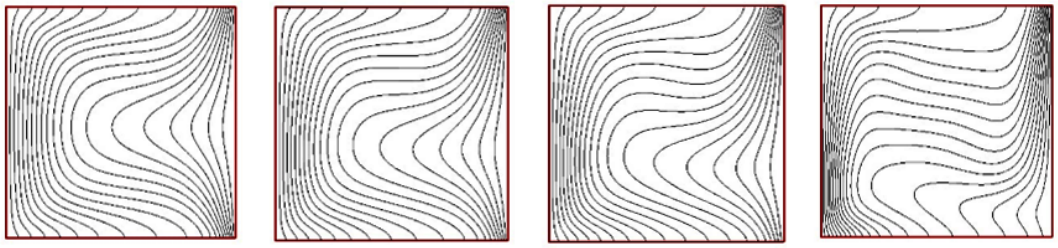

Figure 4.9: Isotherm contours for case 2 for the effect of Ri

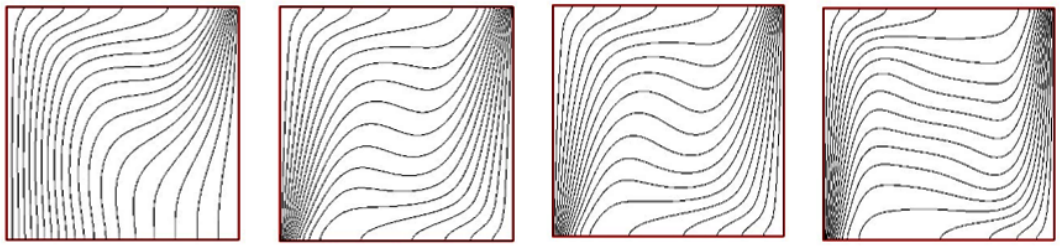

Figure 4.10: Isotherm contours for case 3 for the effect of Ri

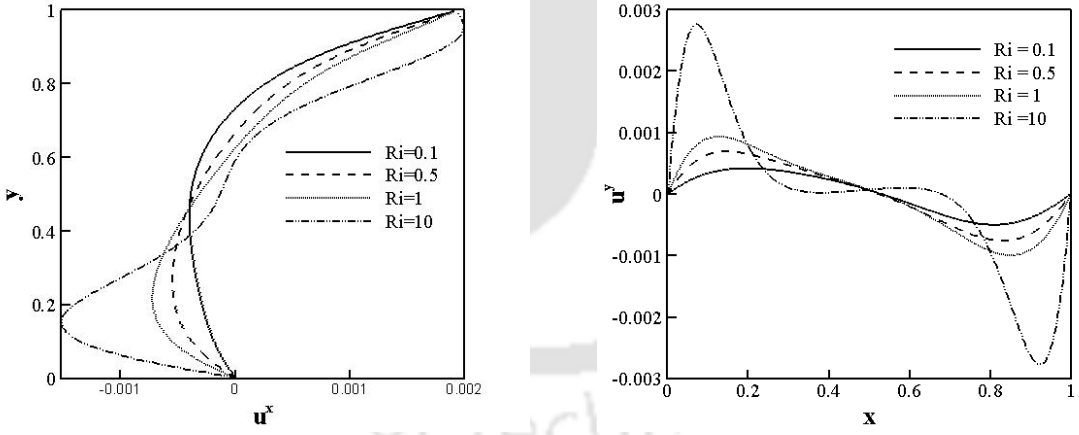

Figure 4.11: Velocity profiles for case 1 for the effect of Ri at (a) mid-X plane (left panel), (b) mid-Y plane (right panel)

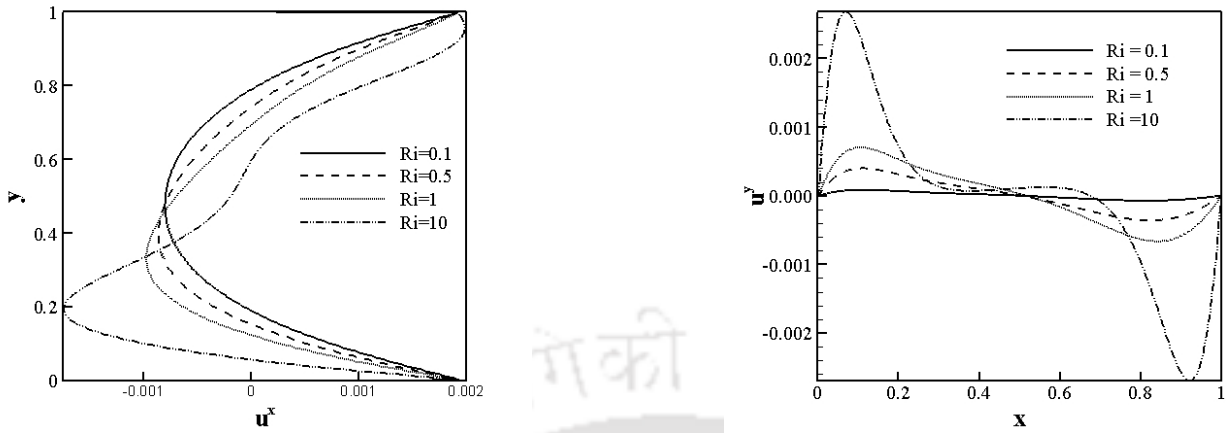

(a) **(b)**

Figure 4.12: Velocity profiles for case 2 for the effect of Ri at (a) mid-X plane (left panel), (b) mid-Y plane (right panel)

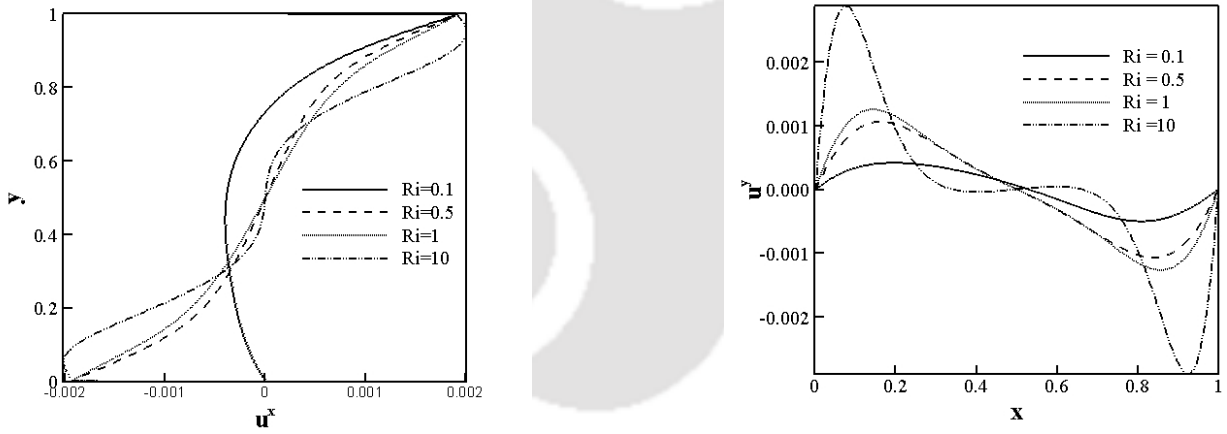

(a) **(b)**

Figure 4.13: Velocity profiles for case 3 for the effect of Ri at (a) mid-X plane (left panel), (b) mid-Y plane (right panel)

In case 2, at low Ri, the cavity get occupied with equal recirculation at the top and bottom of the cavity. This configuration of the convection corresponds to forced convection due to the fact that two equal shear generating effects on top and bottom walls are expected. With further increase in Ri, the configuration of recirculation gets deteriorated as the buoyancy force takes the upper hand over shear force. A symmetric velocity at mid-horizontal plane can be seen in Figure 4.12 that shows the negligible effect of buoyancy force at low Ri which gets significant with the enhancement of Ri where the velocity profile gets more

inclined near the bottom wall. The isotherms in this case also shows that, the temperature contours form a densely cluster portion near the hot wall. Due to strong recirculation at the centre of the cavity, the isotherms deviate as shown in the figure. With increasing effect of buoyancy (Ri>1), the core of the primary circulating cell moves upward and the flow becomes weak which results in flat isotherms.

In case 3, it is observed from the streamline contours that, the clockwise single recirculation flow is created due to moving lids in the opposite direction. This is because the fluid rises along the right hot wall and sinks on the left cold wall due to forces generated by buoyancy and by shear. The combined effect of both free and forced convection is visible through the symmetric U^x and ^{y} profiles for the whole range of Ri.

Moreover, the detailed velocity profile at the mid vertical plane in Figure 4.13 shows the velocity profile turns to more negative profile at higher Ri. This is an indication of a stratified flow in the cavity, which is obtained in case of natural convection in differentially heated cavities.

4.4.2 Effect of Prandtl number (Pr)

The simulations are done at Re=50 and Ri=0.1 varying Pr at (0.065 (Molten metal), 1.38 (Gaseous ammonia), 7 (water)). The effect of Pr is shown below and comparison between all the three cases are depicted in terms of streamlines, isotherms, velocity at the mid-plane in Figure 4.14 through 4.22.

a) **Streamline contours**

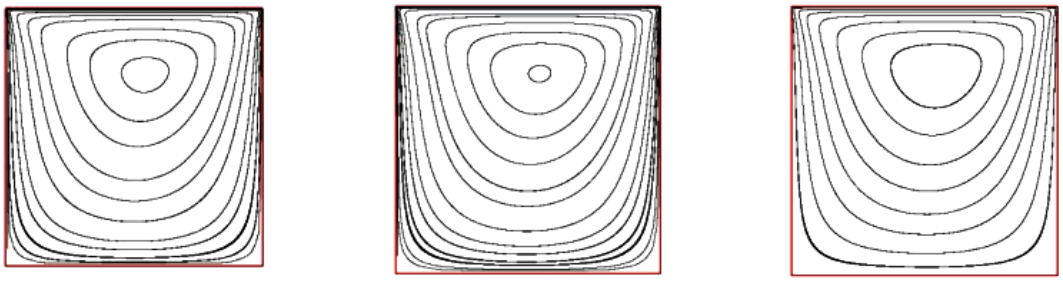

Figure 4.14: Streamline contours for case 1 for the effect of Pr

As it can be seen from the streamline contours that, the Prandtl number has a minimal effect on the flow characteristics at lower values. In this regime, the dominant factor influencing the flow in the cavity is the shear action of the moving lid, rather than temperature and buoyancy variations.

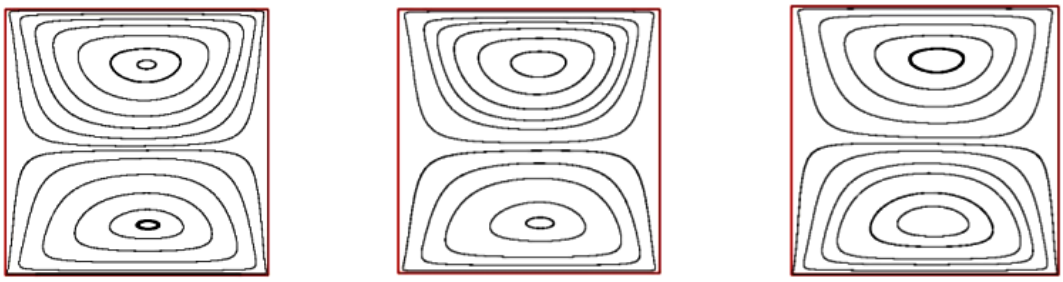

Figure 4.15: Streamline contours for case 2 for the effect of Pr

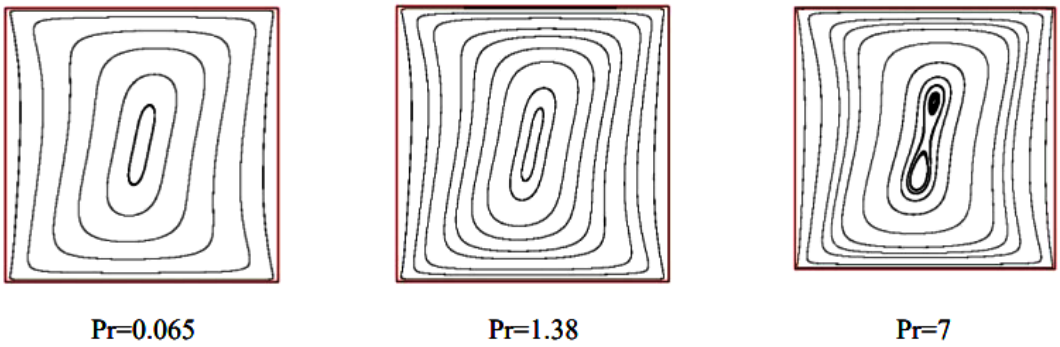

Figure 4.16: Streamline contours for case 3 for the effect of Pr

Therefore, as confirmed by the established notion by Bahiraei et al. [69] the flow behavior remains independent of the Prandtl number when the Richardson number (Ri) is much less than 1.

However, as the Prandtl number increases and reaches higher values, its influence becomes more significant. This effect holds true for all three cases under consideration. The isotherm contours validate this claim, which depict the temperature distribution within the cavity. The changes in these contours with varying Prandtl numbers would provide evidence of the Prandtl number's impact on the flow at higher values.

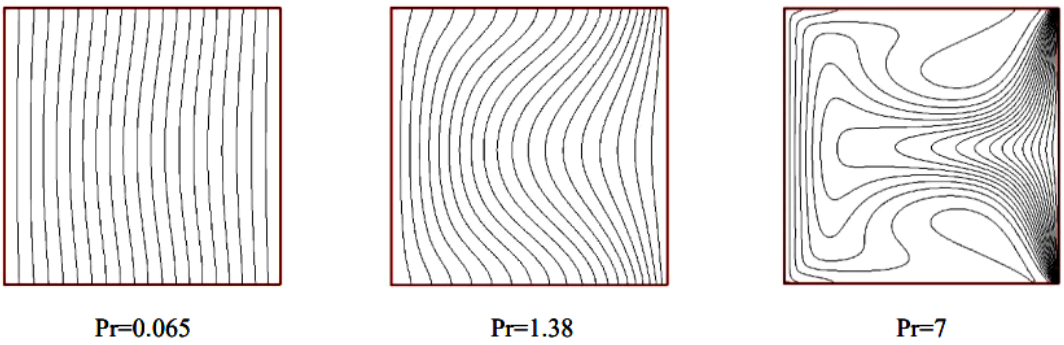

Figure 4.18: Isotherm contours for case 2 for the effect of Pr

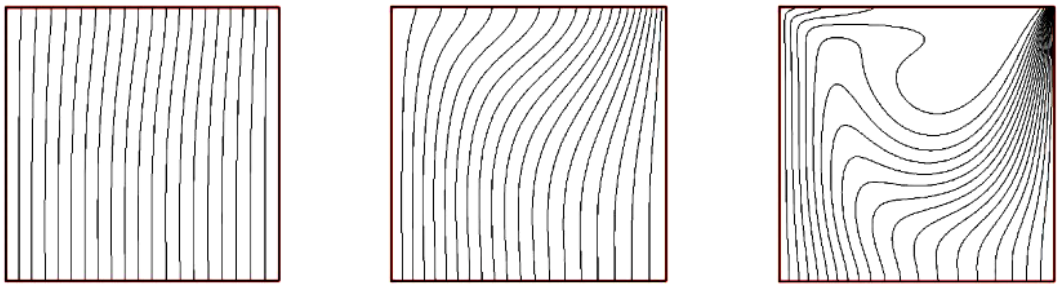

Figure 4.17: Isotherm contours for case 1 for the effect of Pr

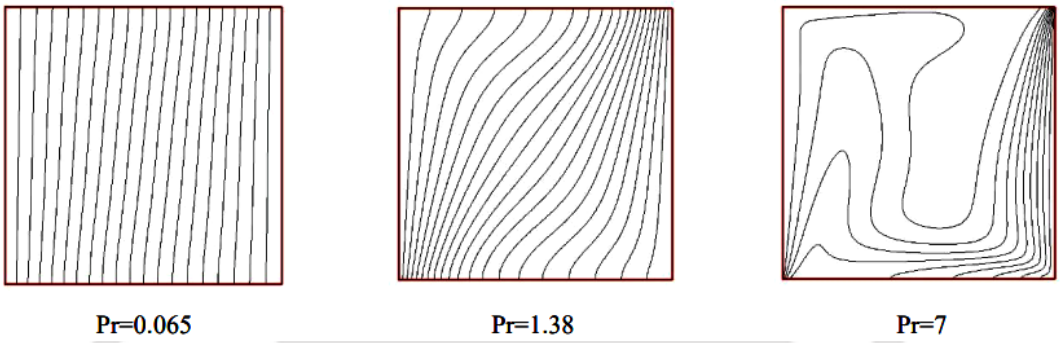

Figure 4.19: Isotherm contours for case 3 for the effect of Pr

The observation regarding the isotherm contours suggests that at lower values of the Prandtl number (Pr), heat transfer within the cavity is primarily driven by conduction, as indicated by the orientation of the horizontal isotherms in Figures 4.17, 4.18, and 4.19. In conduction-dominated heat transfer, heat is mainly transferred through the solid-like behavior of the fluid, where thermal energy diffuses from regions of higher temperature to lower temperature without significant fluid motion. As Pr increases while maintaining constant values of Reynolds number (Re) and Richardson number (Ri), the heat transfer mechanism shifts towards convection. This transition occurs because higher Pr fluids exhibit a greater propensity for convective heat transfer due to their reduced thermal diffusivity, allowing for more efficient heat transfer through the movement of the fluid itself. Consequently, with an increase in Pr, the isotherm contours depict the formation of circulating temperature loops, indicating the enhancement of convective heat transfer within the cavity. Therefore, the variation in Pr influences the dominant mode of heat transfer, transitioning from conduction-dominated to convection-dominated as Pr increases, thereby affecting the overall heat transfer behavior within the system.

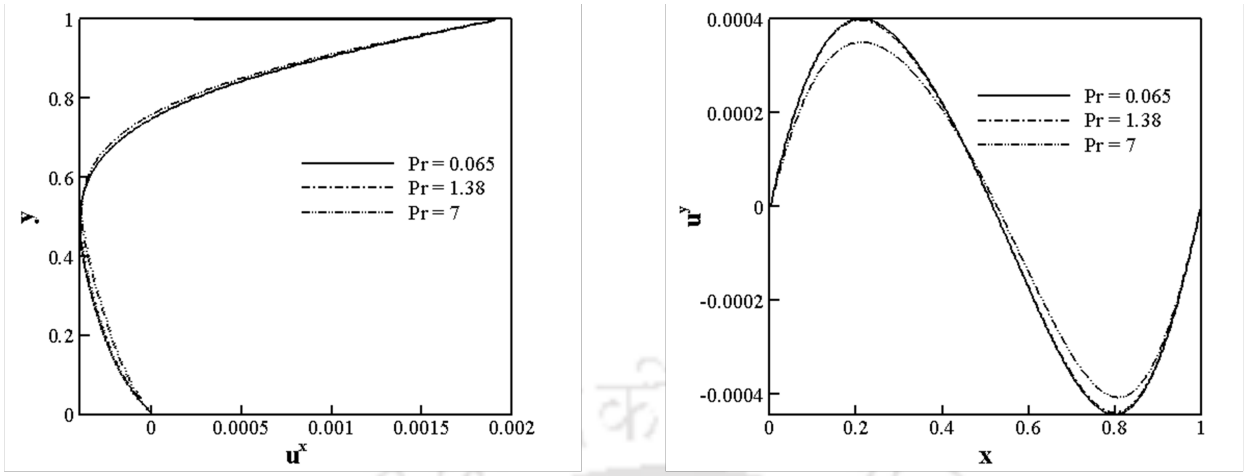

(a) (b)

Figure 4.20: Velocity profiles for case 1 for the effect of Pr at (a) mid-X plane (left panel), (b) mid-Y plane (right panel)

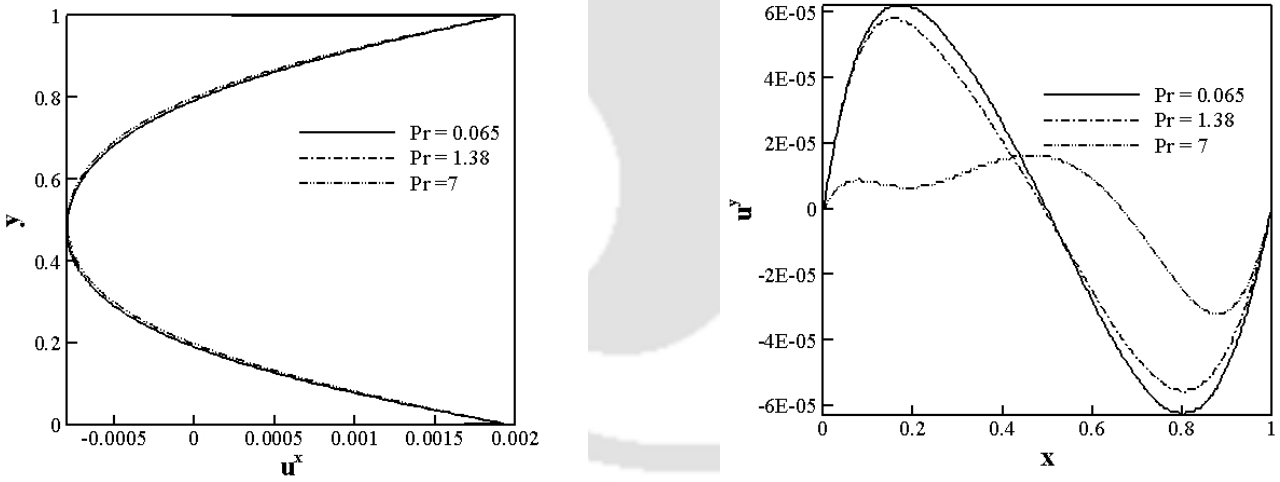

(a) (b)

Figure 4.21: Velocity profiles for case 2 for the effect of Pr at (a) mid-X plane (left panel), (b) mid-Y plane (right panel)

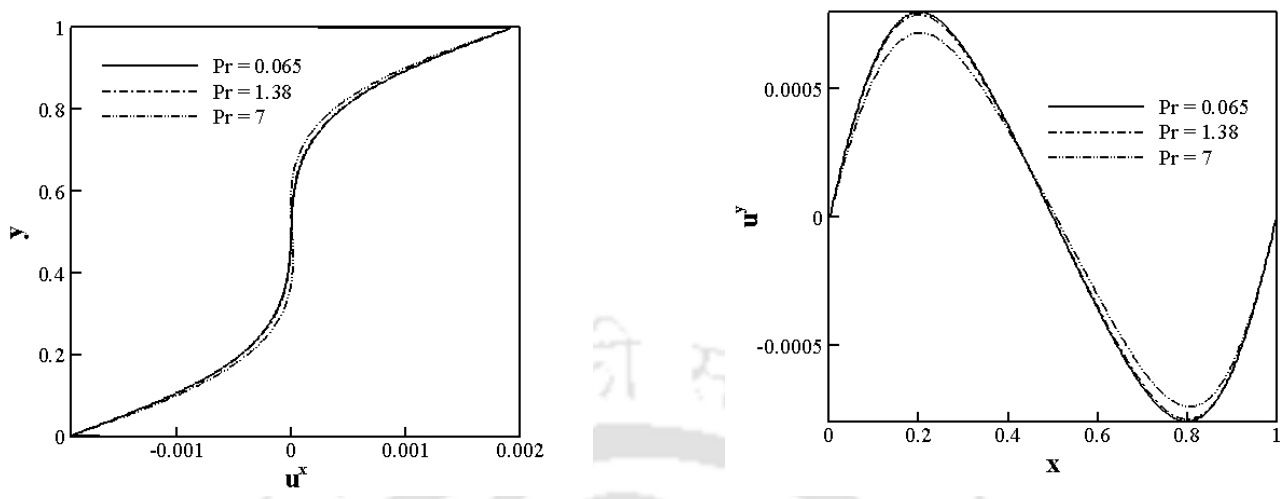

Figure 4.22: Velocity profiles for case 3 for the effect of Pr at (a) mid-X plane (left panel), (b) mid-Y plane (right panel)

The mid-horizontal velocity profile shows an insignificant effect of Pr for all the three cases. However, flow field retards and changes its sign to negative direction in middle of the cavity with growth in heat dissipation in cavity which can be confirmed from velocity profiles at mid vertical plane which is true for all the three cases.

4.4.3 Effect of Reynolds number (Re)

The simulations are done at Ri=0.1 and Pr=0.71 varying Re at 50, 100 and 200. The effect of Re is shown below and comparison between all the three cases are depicted in terms of streamlines, isotherms, velocity at the mid-plane in Figures 4.23 through 4.31.

From the streamline contours as shown in Figure 4.23, 4.24 and 4.25 that, the effect of Re has a significant role in flow behavior.As it can be observed for all cases (1,2 and 3) that, the recirculation zone shifts toward right with increase in Re . This occurs due to increase of driving force in the forward direction in case 1 and case 2. This is because higher Reynolds numbers typically correspond to increased flow velocities or momentum within the fluid. As a result, the flow tends to exert stronger forces on the fluid in the forward direction, causing the recirculation zone to shift towards the right.

a) **Streamline contours**

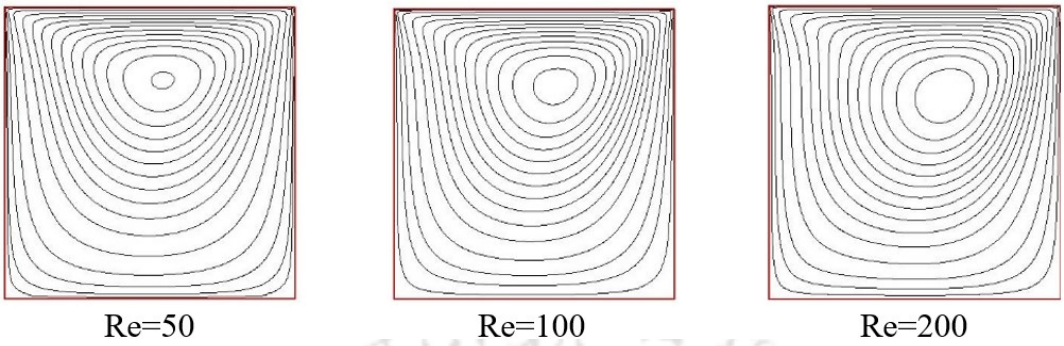

Figure 4.23: Streamline contours for case 1 for the effect of Re

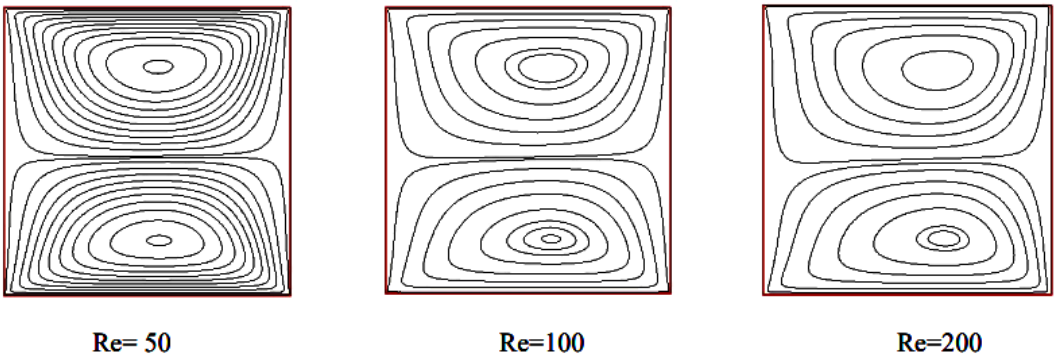

Figure 4.24: Streamline contours for case 2 for the effect of Re

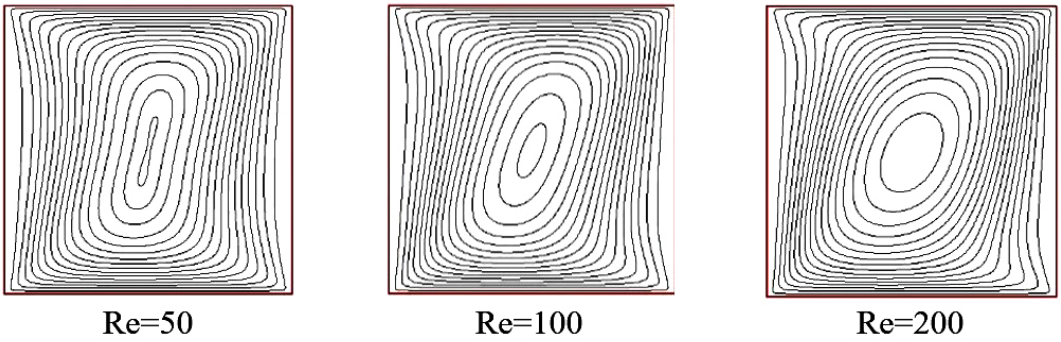

Figure 4.25: Streamline contours for case 3 for the effect of Re

This shift can be attributed to the enhanced momentum and inertia of the fluid, which promotes the displacement of the recirculation zone towards the direction of the primary flow. However, the case 3 shows an unlikely behavior as compared to the previous cases as both the lids move in opposite

direction and contributes equally in the driving force effect on the top and bottom lids leading to a clockwise single recirculation zone inside the cavity.

b) **Isotherm contours**

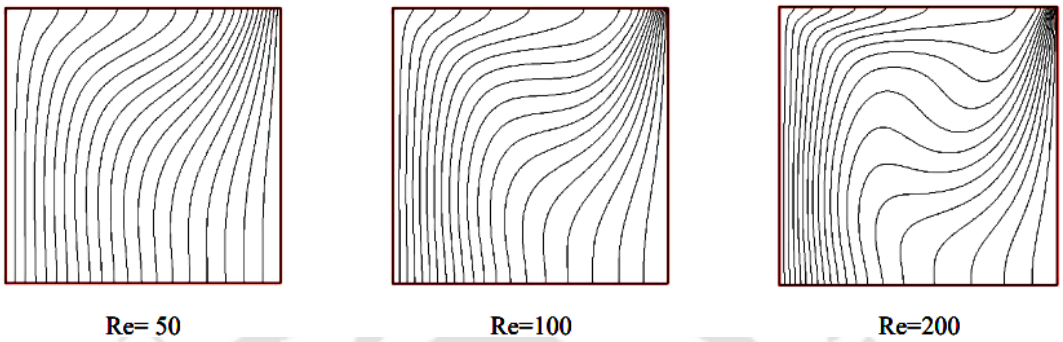

Figure 4.26: Isotherm contours for case 1 for the effect of Re

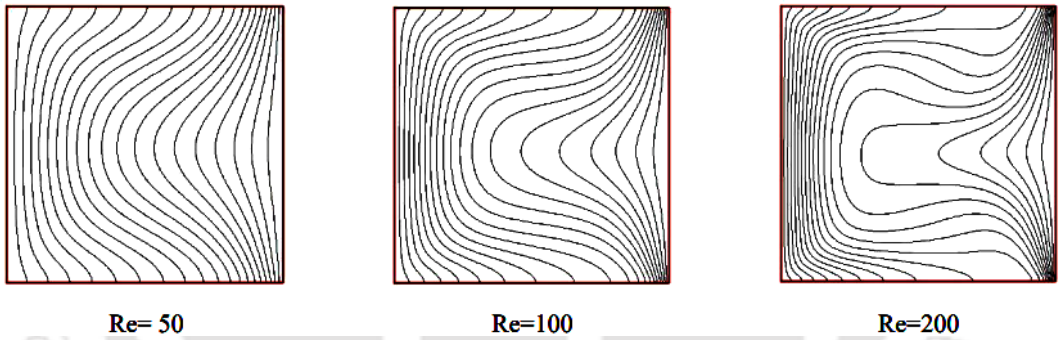

Figure 4.27: Isotherm contours for case 2 for the effect of Re

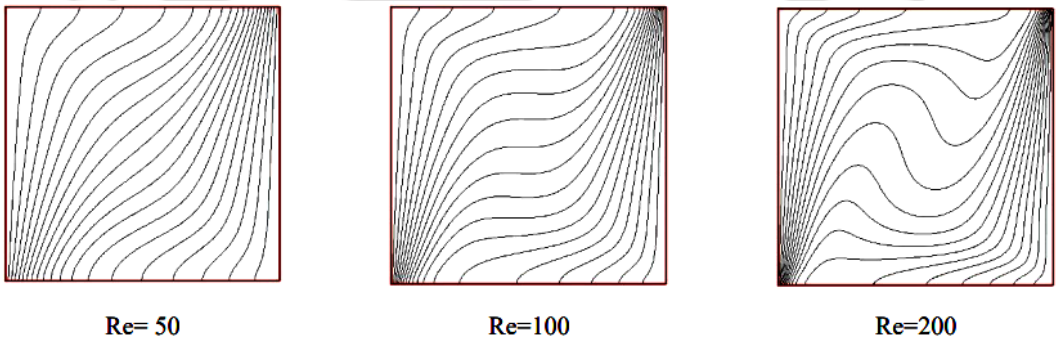

Figure 4.28: Isotherm contours for case 3 for the effect of Re

The effect of Re can also be understood from the isotherms as shown in Figure 4.26 to 4.28. For all the cases at low Re, the isotherms are almost vertical. With enhancement of Re, the temperature circulation loop can be clearly seen enhancing the heat transfer rate.

It can also be observed that, fluid molecules near the heated surface gain heat through direct contact (i.e conduction) with the surface and then transfer that heat to adjacent fluid layers through molecular interactions precisely with convection mode of heat transfer. This dual mechanism of heat transfer ensures efficient distribution of thermal energy throughout the fluid domain, contributing to overall heat transfer within the system.

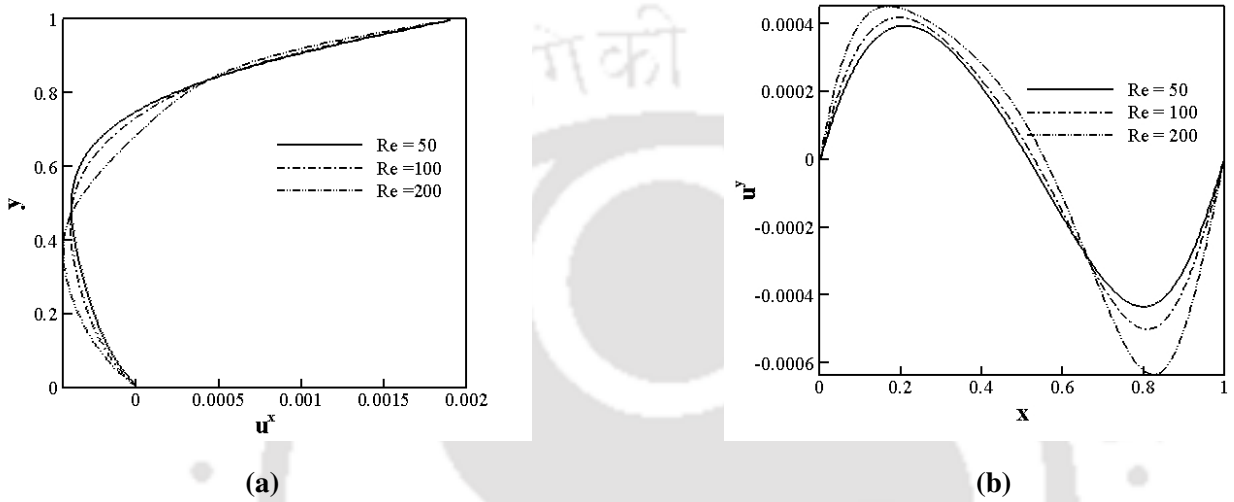

(a) **(b)**

Figure 4.29: Velocity profiles for case 1 for the effect of Re at (a) mid-X plane (left panel), (b) mid-Y plane (right panel)

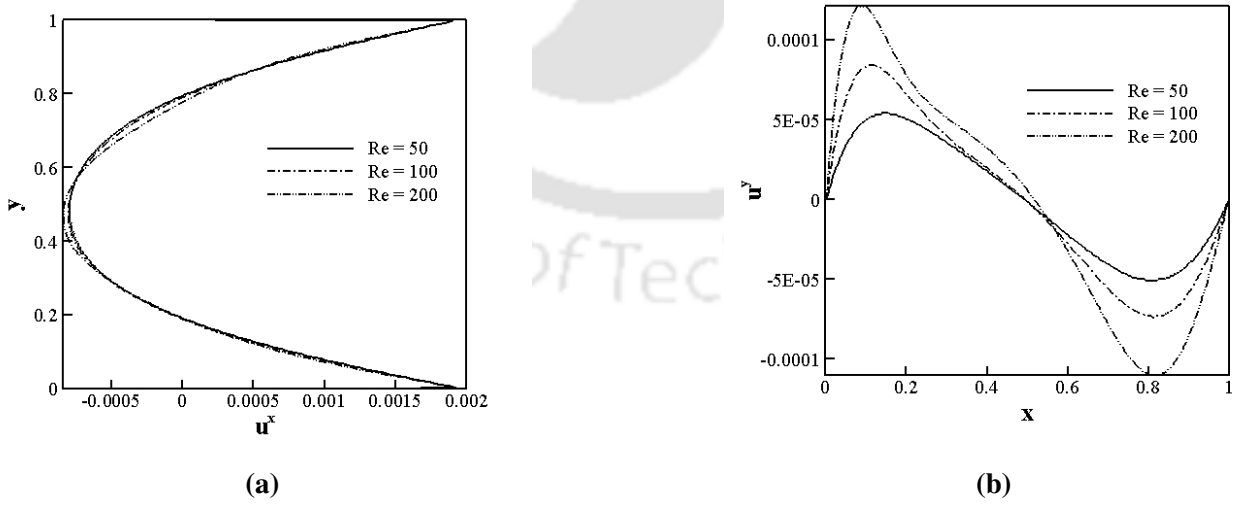

(a) **(b)**

Figure 4.30: Velocity profiles for case 2 for the effect of Re at (a) mid-X plane (left panel), (b) mid-Y plane (right panel)

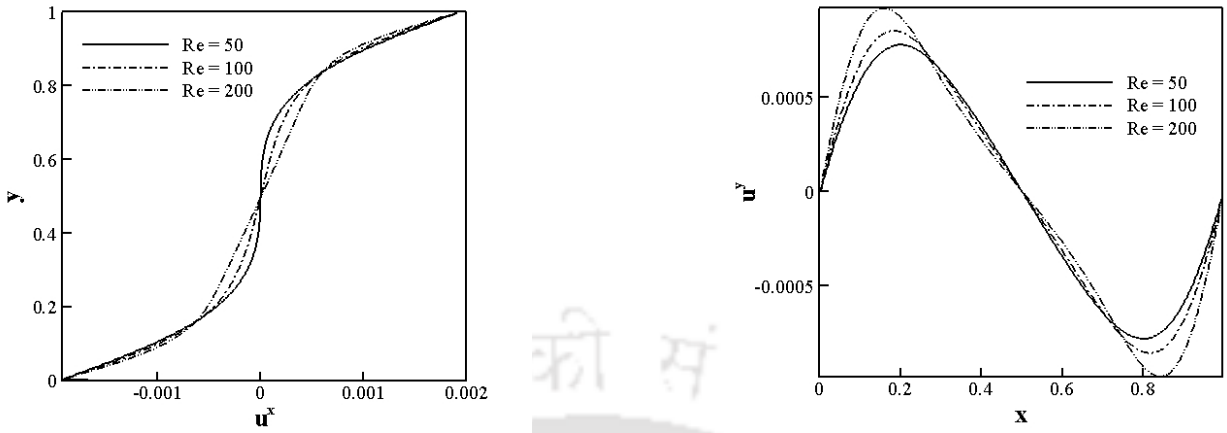

Figure 4.31: Velocity profiles for case 3 for the effect of Re at (a) mid-X plane (left panel), (b) mid-Y plane (right panel)

The symmetric velocity distribution inside the cavity can be seen from the mid-horizontal plane where the velocity profile shifts towards the downward direction. For low Re numbers, the velocity profile is curved. At higher Re, curvature starts to disappear. The profile becomes linear in the most part of the cavity. Linear profiles in the central core indicate the uniform vortices region generated in the cavity at higher Re numbers. The vertical velocity increases from zero and starts decreases in the middle of the cavity and once again it increases finally reaches zero at the wall. For higher Re, the increase of velocity is sharper and gradually decreases. Moreover, at constant Ri, increasing the Re implies the decreasing value in Grashof number (Gr) implying the enhanced impact of viscous force.

4.4.4 Effect of inclination angle, (ϕ)

The simulations are done taking Ri=10, Re=100 and Pr=0.71 and varying the inclination angles,ϕ at 0^0, 30^0, 40^0,50^0, $60^0$and 90^0. The effect of inclination angle is shown below and comparison between all the three cases are depicted in terms of streamlines, isotherms, velocity at the mid-plane in Figures 4.32 through 4.40. The angle of inclination (ϕ) is defined by the angle between a hot left wall and the vertical in such a way that ϕ = 90° represents the situation of an enclosure heated from top wall.

a) **Streamline contours**

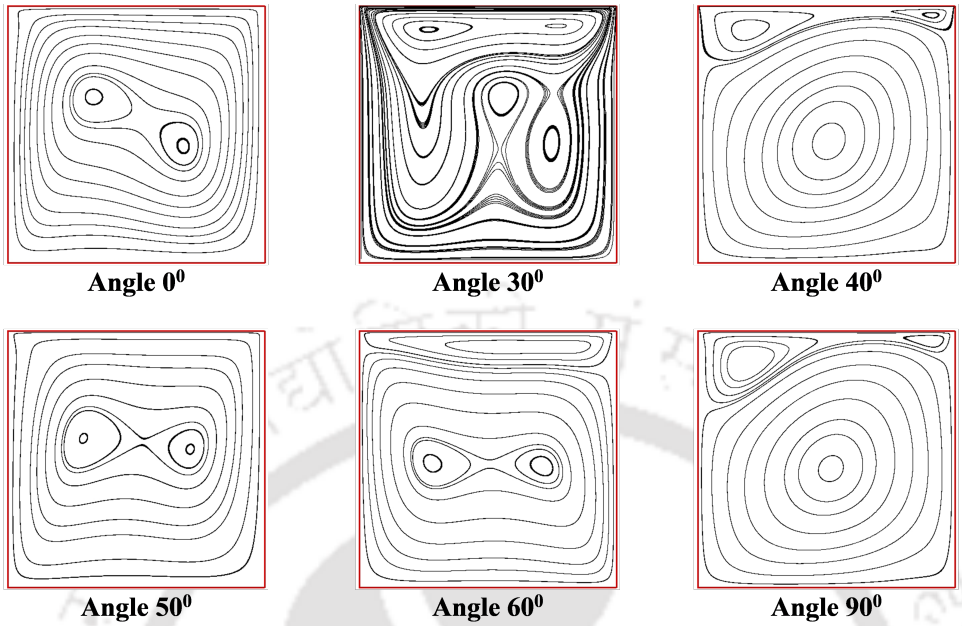

Figure 4.32: Streamline contours for case 1 for effect of inclination angle at angles (a) ϕ = 0° (b) ϕ = 30°, (c) ϕ = 40°, (d) ϕ = 50°, (e) ϕ = 60°, (f) ϕ = 90°

When buoyancy forces dominate as for Ri=10, inclination angle has a significant effect on the thermal and hydrodynamic fluid parameters and heat transfer.

For the lower angle of inclination, three circulation loops are observed in case 1. Strong cells in the upper half and two weaker cells in the mid-cavity which are generated due to forcing of the top moving wall are observed. As the inclination angle (ϕ) is increased, the two cells merge, a large rotational cell covers the whole space of the cavity with a smaller (compared to the previous one) elongated vortex near the top wall. The phenomenon shows its persistence with further increase in the inclination angle. This is because when inclination increases to further clockwise direction, buoyancy and forced convection are in the same direction, wherein the small recirculation bubble is diminished and the primary bubble covers the whole of the cavity. In these cases, the fluid near the cold surface moves easily toward the hot surface. With increase in ϕ= 60^0 and then 90^0, the secondary vortex reappears near the top wall. This can also be seen from the Figure 4.38 depicting the velocity in mid-horizontal and vertical planes which shows a sudden increase in velocity.

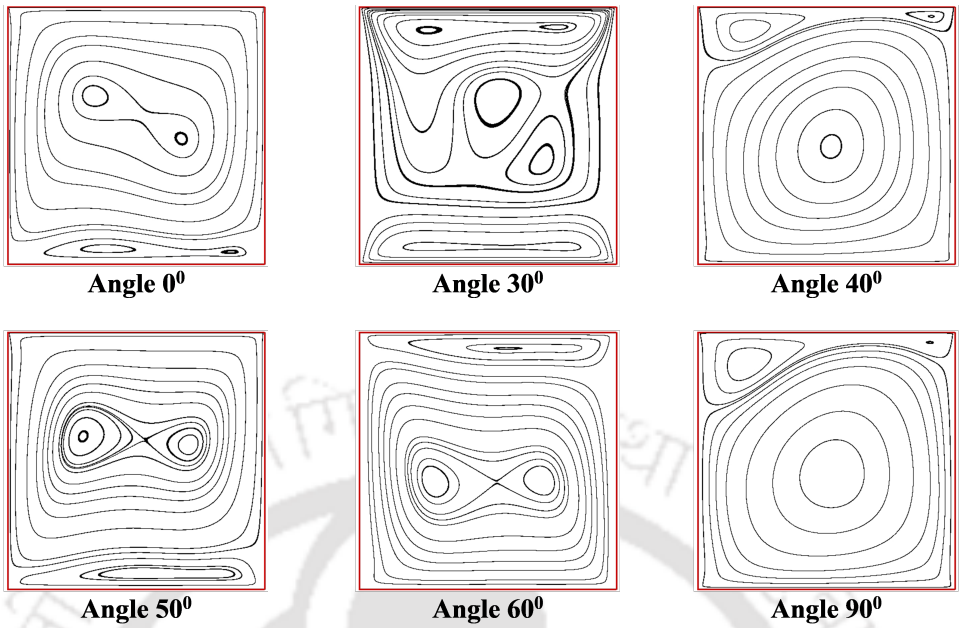

Figure 4.33: Streamline contours for case 2 for effect of inclination angle at (a) $\phi = 0°$ (b) $\phi = 30°$, (c) $\phi = 40°$, (d) $\phi = 50°$, (e) $\phi = 60°$, (f) $\phi = 90°$

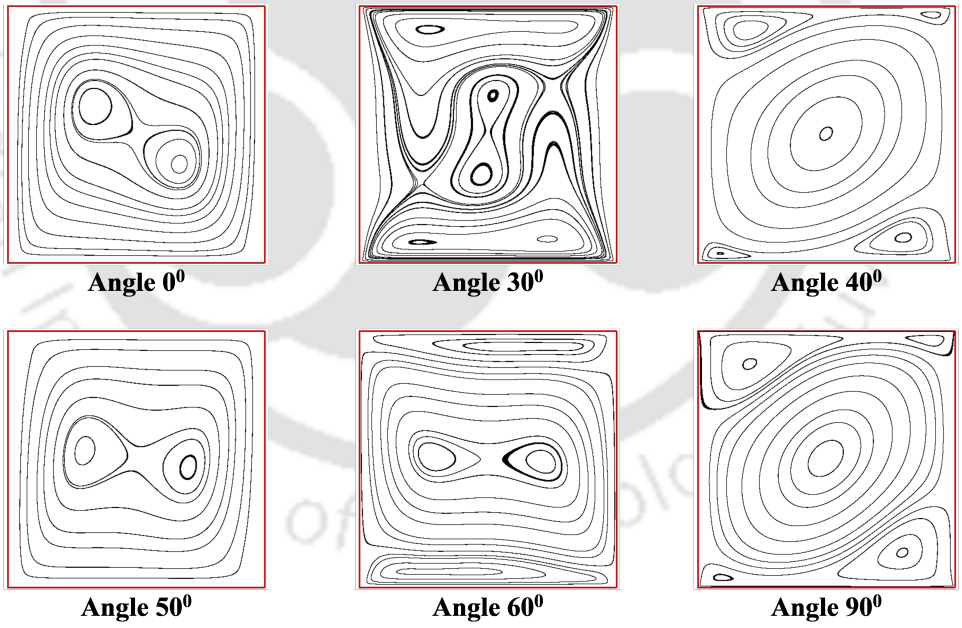

Figure 4.34: Streamline contours for case 3 for effect of inclination angle at (a) $\phi = 0°$ (b) $\phi = 30°$, (c) $\phi = 40°$, (d) $\phi = 50°$, (e) $\phi = 60°$, (f) $\phi = 90°$

The similar physics can be employed in order to understand the flow behavior for case 2 and case 3. For case 2, similar kind of flow behavior is observed with an additional secondary vortex at the

bottom wall. However, in case 3 symmetric circulation loops can be seen due to movement of lids in the opposite directions at lower value of ϕ.

b) **Isotherm contours**

At high Ri, the flow become more uniform, thus enhancing the cooling effect in the enclosure and this can be further enhanced with the influence of ϕ. The straight isotherms, which are almost perpendicular to the top and bottom walls for lower value of ϕ can be seen in Figures 4.35 through 4.37, which is also shown in Figure 4.38 through 4.40 with a linear straight temperature profile for ϕ= 30^0 that represents the conduction heat transfer in this region.

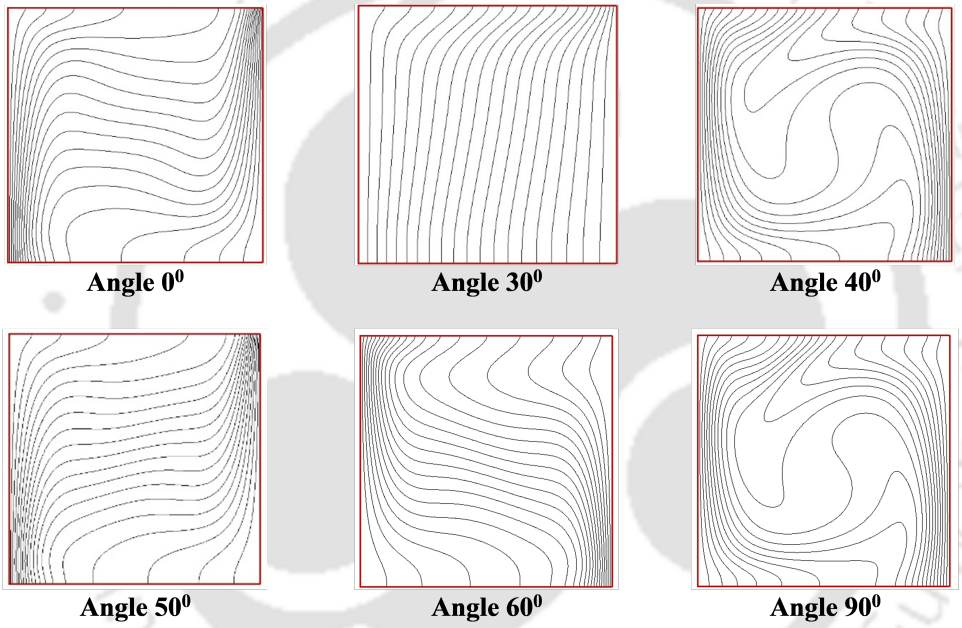

Figure 4.35: Isotherm contours for case 1 for effect of inclination angles (a) ϕ = 0° (b) ϕ = 30°, (c) ϕ = 40°, (d) ϕ = 50°, (e) ϕ = 60°, (f) ϕ = 90°

With increase in ϕ, temperature profiles become horizontal line in the cavity. The curve changes slope near the centre of the cavity. A steep variation of temperature can be clearly seen near the walls as depicted by the temperature in mid-vertical plane. The value ϕ=40^0 leads to less temperature difference in the central region of the cavity as shown by the isotherm contours resulting in uniform distribution of heat and hence accelerating the heat transfer rate. With further increase in ϕ beyond 40^0 thin thermal boundary layers can be seen in the isotherm contours. This is due to the high temperature variations close to these walls. With further increase in angle ϕ=90^0, heat transfer rate

increases as can be seen in the isotherms in all the three cases with the recirculation loops.

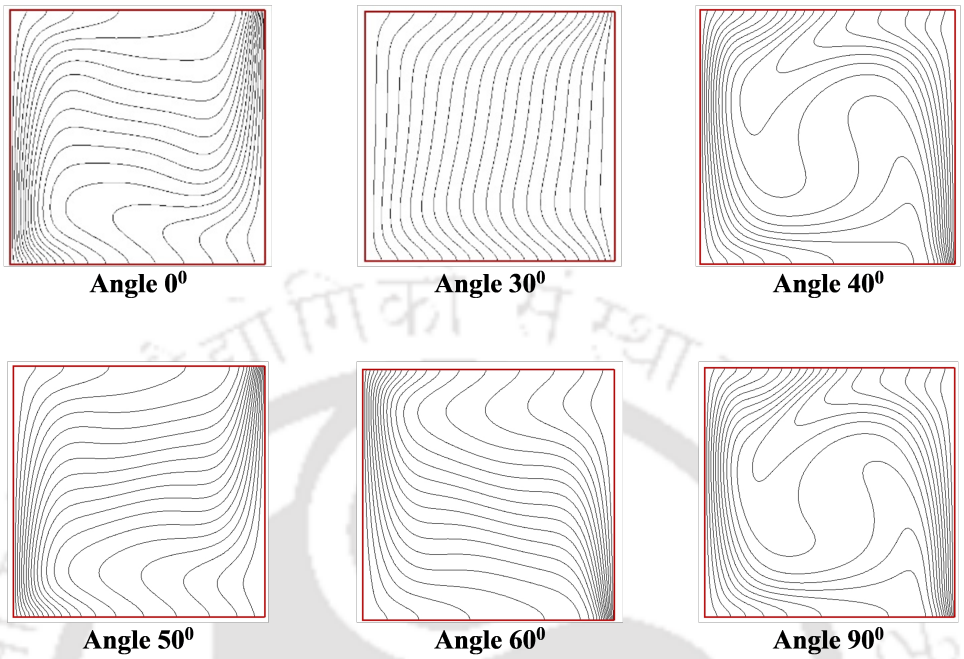

Figure 4.36: Isotherm contours for case 2 for effect of inclination angles (a) $\phi = 0°$ (b) $\phi = 30°$, (c) $\phi = 40°$, (d) $\phi = 50°$, (e) $\phi = 60°$, (f) $\phi = 90°$

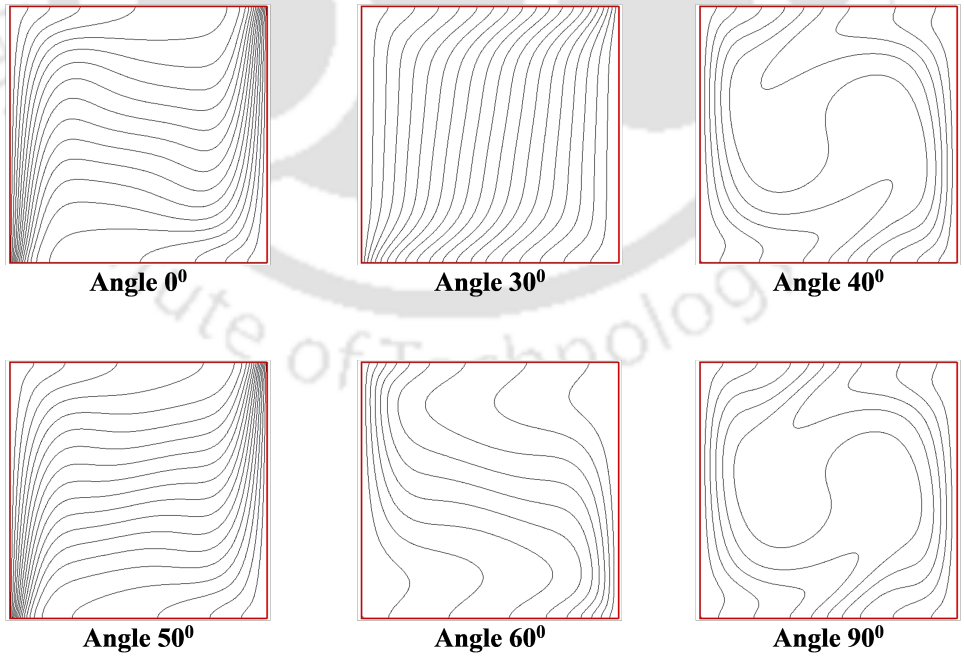

Figure 4.37: Isotherm contours for case 3 for effect of inclination angles (a) $\phi = 0°$ (b) $\phi = 30°$, (c) $\phi = 40°$, (d) $\phi = 50°$, (e) $\phi = 60°$, (f) $\phi = 90°$

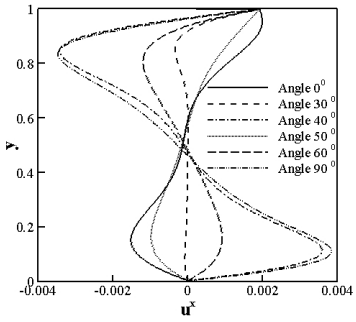

(a) Velocity at mid-X plane

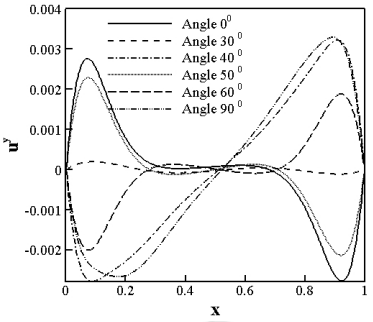

(b) Velocity at mid-Y plane

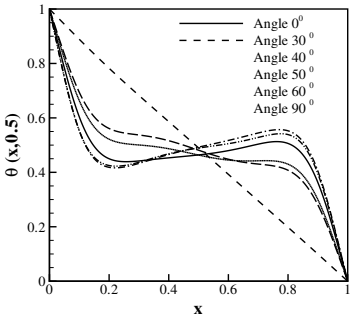

(c) Temperature at mid-Y plane

Figure 4.38: Velocity and temperature profiles for case 1 for effect of inclination angle

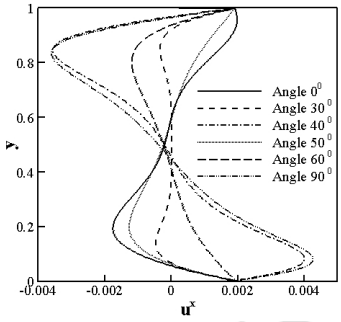

(a) Velocity at mid-X plane

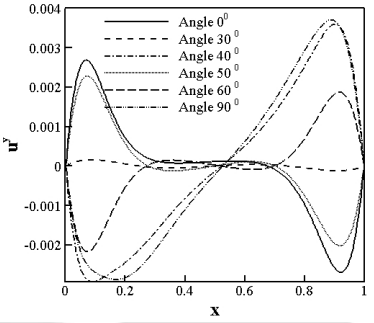

(b) Velocity at mid-Y plane

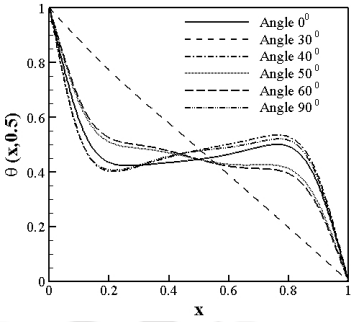

(c) Temperature at mid-Y plane

Figure 4.39: Velocity and temperature profiles for case 2 for effect of inclination angle

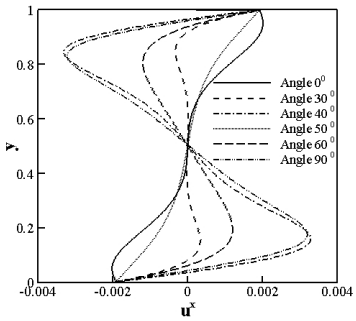

(a) Velocity at mid-X plane

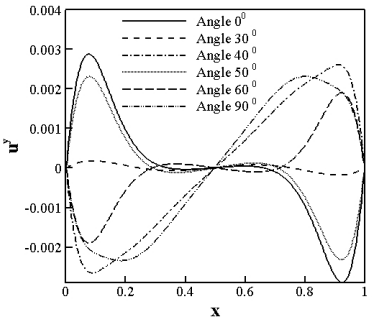

(b) Velocity at mid-Y plane

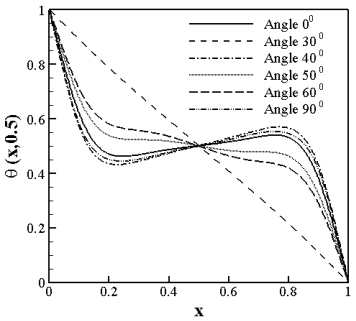

(c) Temperature at mid-Y plane

Figure 4.40: Velocity and temperature profiles for case 3 for effect of inclination angle

4.4.5 Effect of Richardson number, Reynolds number, Prandtl number and inclination angle

a) **Richardson number**

The performance analysis to depict the effect of Richardson number (Ri) is shown in a comparison mode between all the three cases 1,2 and 3 in terms of average Nusselt number ($\overline{Nu}_h$ and $\overline{Nu}_c$), local Nusselt number (Nu_h), average entropy generation ($\overline{S}_\theta$ and $\overline{S}_\Psi$), local entropy generation (S_θ and S_Ψ) and friction coefficient (C_f) in the Figures 4.41 through 4.47 below.

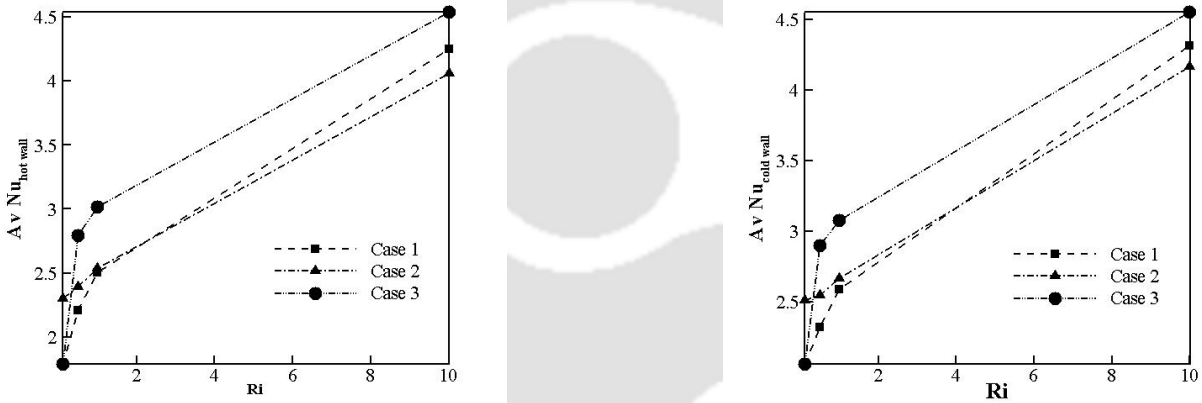

Figure 4.41: Comparison results of average Nusselt number (a) $\overline{Nu}_h$ over hot wall, (b) $\overline{Nu}_c$ over cold wall for the effect of Ri

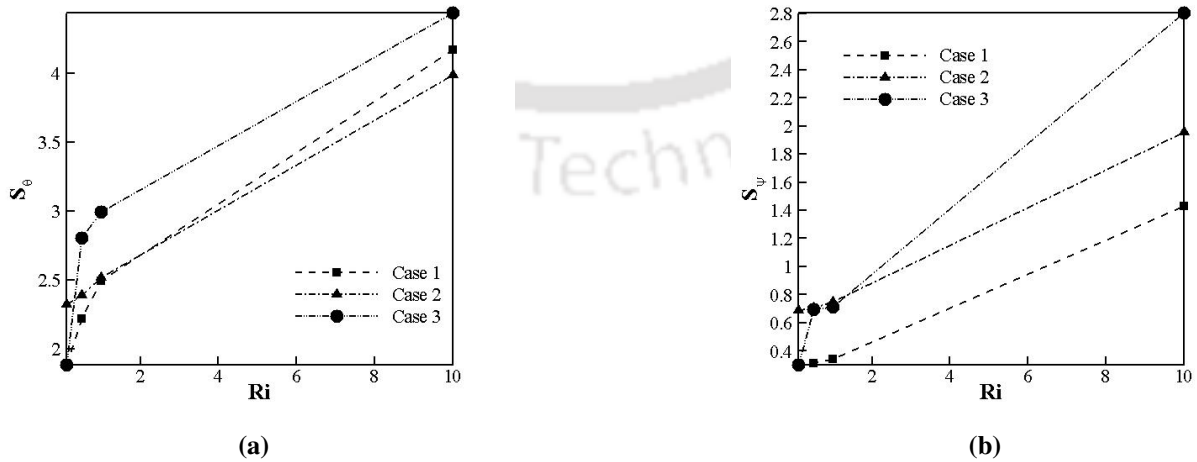

Figure 4.42: Comparison results of average entropy generation (a) due to heat transfer ($\overline{\boldsymbol{S}}_{\boldsymbol{\theta}}$) and (b) due to fluid friction ($\overline{\boldsymbol{S}}_{\boldsymbol{\Psi}}$) over hot wall for the effect of Ri

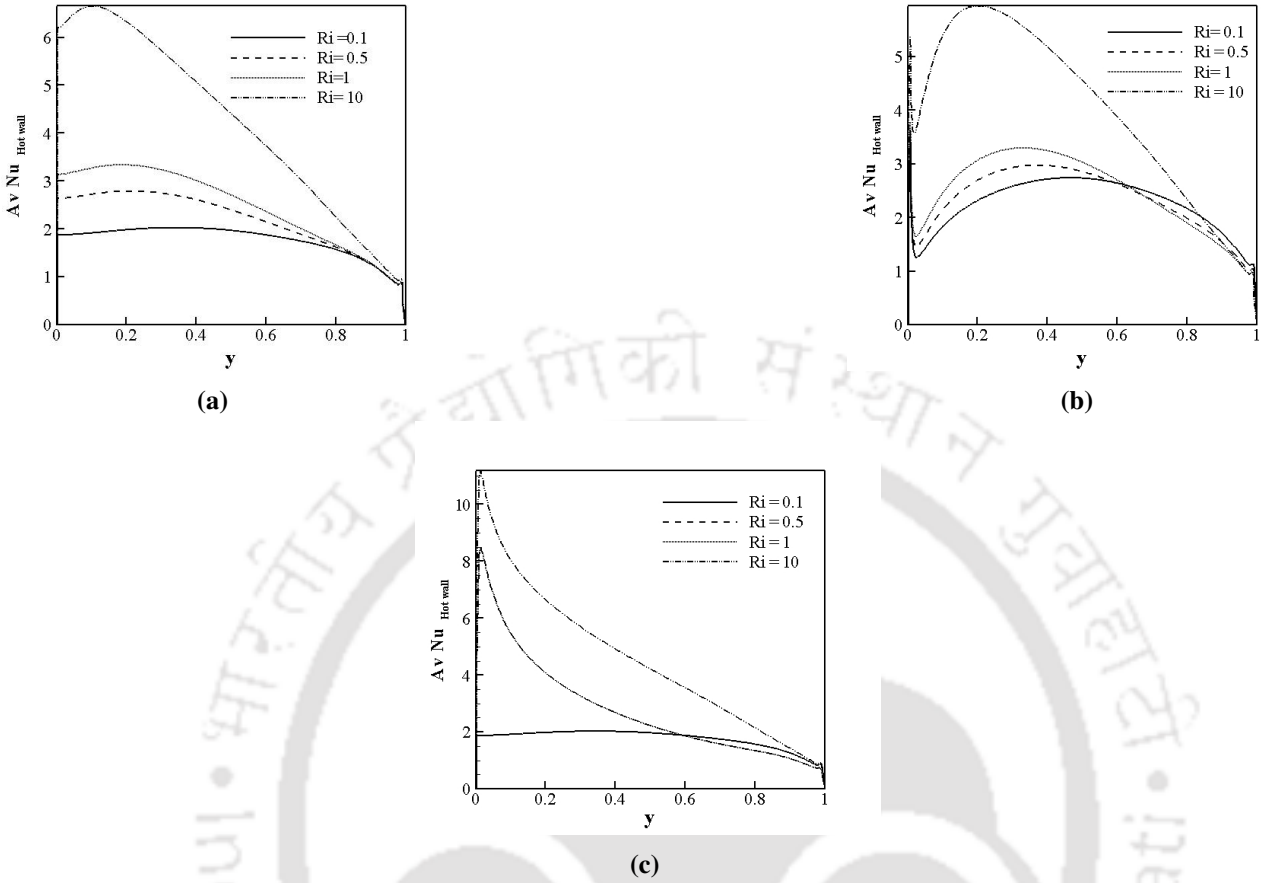

Figure 4.43: Comparison results of average Nusselt number ($\overline{Nu_h}$) over hot wall for (a) case 1, (b) case 2 and, (c) case 3 for the effect of Ri

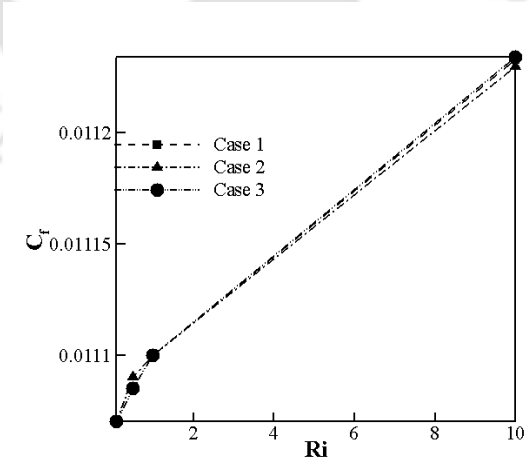

Figure 4.44: Comparison results of local friction coefficient (C_f) over top wall for the effect of Ri

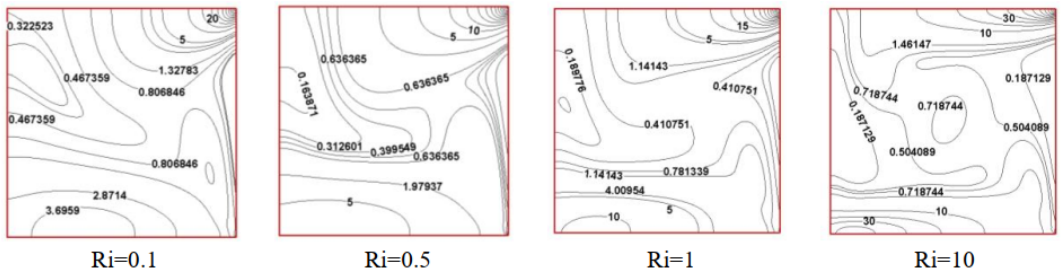

(a)

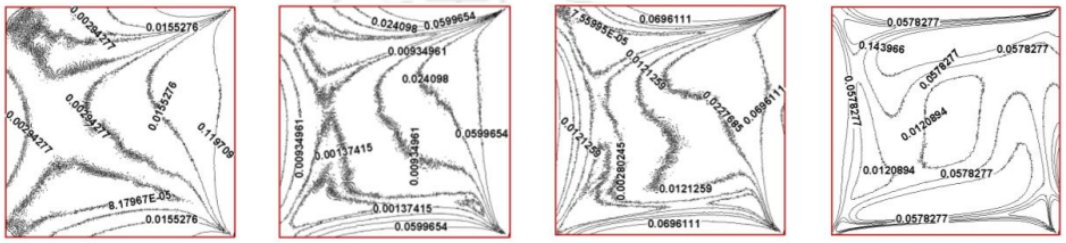

(b)

Figure 4.45: Local entropy generation (a) heat transfer (S_θ) and (b) fluid friction (S_Ψ) for case 1 for the effect of Ri

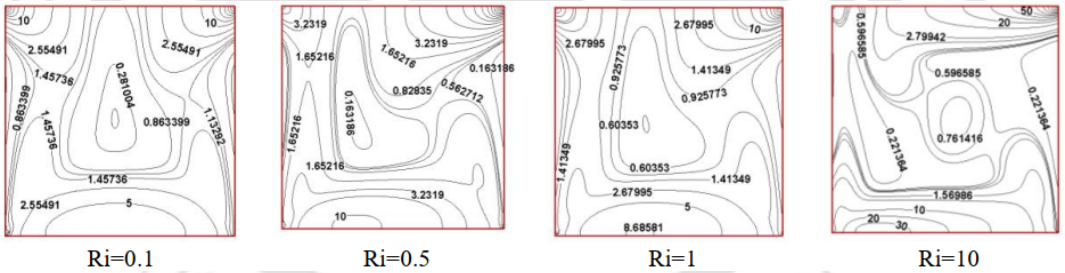

(a)

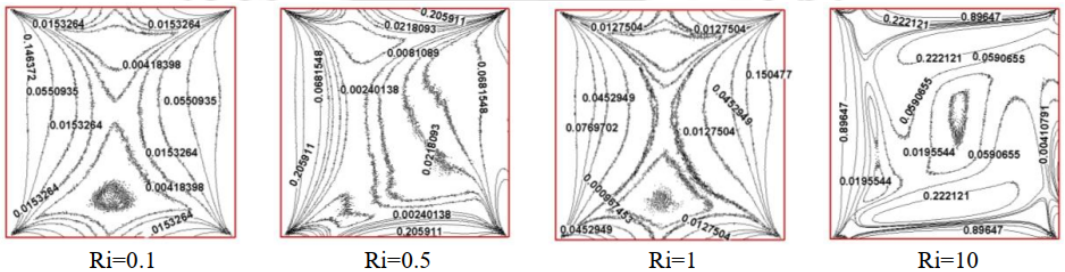

(b)

Figure 4.46: Local entropy generation (a) heat transfer (S_θ) and (b) fluid friction (S_Ψ) for case 2 for the effect of Ri

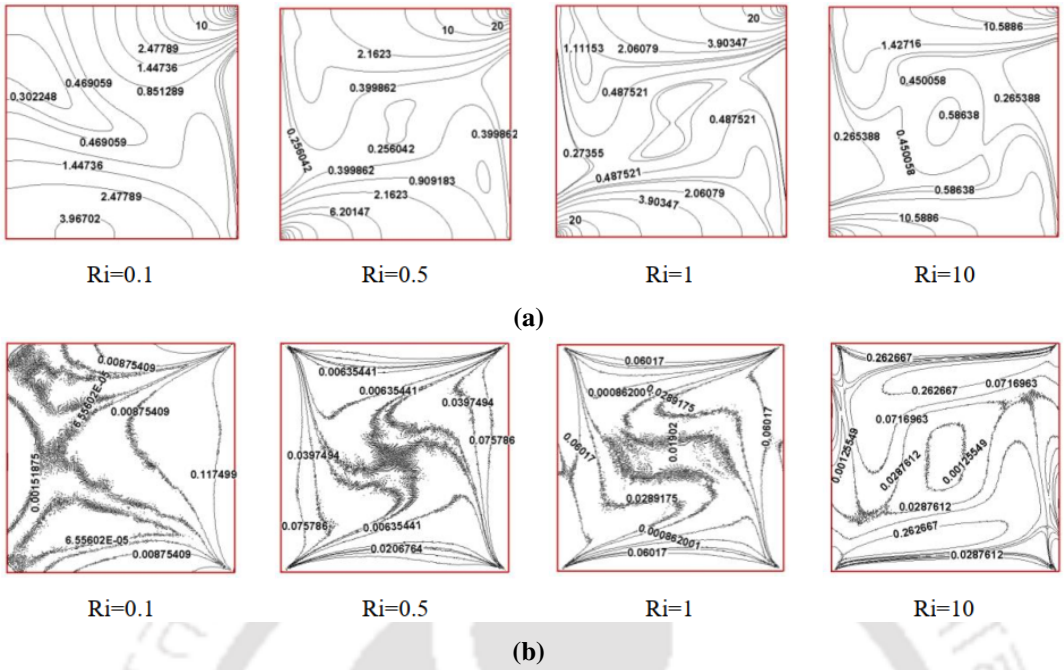

Figure 4.47: Local entropy generation (a) heat transfer (S_θ) and (b) fluid friction (S_Ψ) for case 3 for the effect of Ri

From the Figures of this section 4.4.5. it can be inferred that, all the parameters namely Ri, Pr, Re and ϕ has a strong influence on the Nu and entropy generation and friction coefficient. Firstly, it has been observed for all cases that, with increase in Ri from 0.1 to 10, the average Nu at both the left and the right wall increases reaching its maximum value at Ri=10. However, maximum values of average Nusselt number ($\overline{Nu}_h$ and $\overline{Nu}_c$), local Nusselt number (Nu_h), average entropy generation ($\overline{S}_\theta$ and $\overline{S}_\Psi$), local entropy generation (S_θ and S_Ψ) are observed in case 3, followed by case 1 and then case 2. This is because, due to the vigorous circulation of vortices, the flow divides into two streams as depicted by the streamline contours (Figure 4.5-4.7). Correspondingly, when the heat transfer is more from the heated walls, entropy generation also gets increased.

However, $\overline{S}_\Psi$ for case 2 is found to be greater than that of case 1 due to the both lids in a moving condition contributing more chaos and irreversibility. This can also be confirmed by the S_Ψ contours as shown in Figure 4.45 and 4.46.

Also, it has been observed that the average Nu at the right cold wall is always greater than the left wall confirming the positive or good heat transfer.

The magnitude of friction coefficient also found to be increased with increasing effect of Buoyancy

effect. The above findings are also found to be true for the other two cases. The maximum C_f is found to be in case 3 and minimum in case 2.

b) **Prandtl number**

The performance analysis to depict the effect of Prandtl number (Pr) is shown in a comparison mode between all the three cases 1,2 and 3 in terms of average Nusselt number ($\overline{Nu}_h$ and $\overline{Nu}_c$), local Nusselt number (Nu_h), average entropy generation ($\overline{S}_\theta$ and $\overline{S}_\Psi$), local entropy generation (S_θ and S_Ψ) and friction coefficient (C_f) in the Figures 4.48 through 4.54 below.

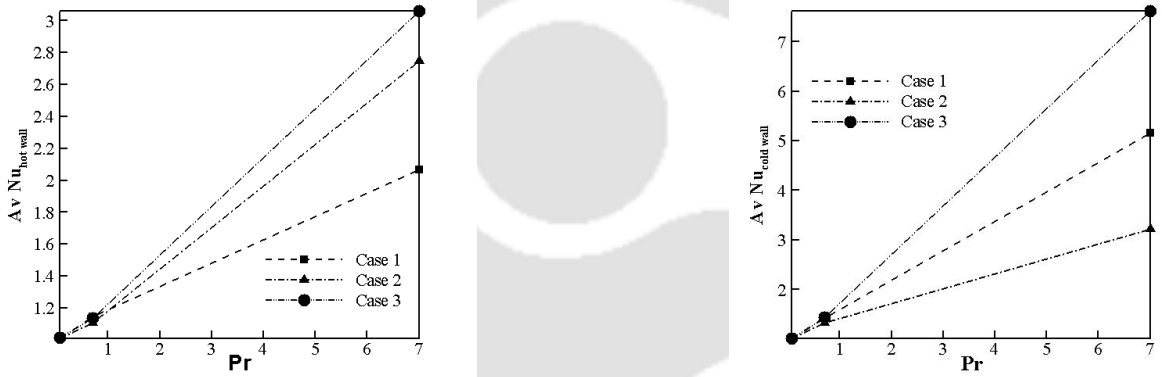

Figure 4.48: Comparison results of average Nusselt number (a) $\overline{Nu}_h$ over hot wall, (b) $\overline{Nu}_c$ over cold wall for the effect of Pr

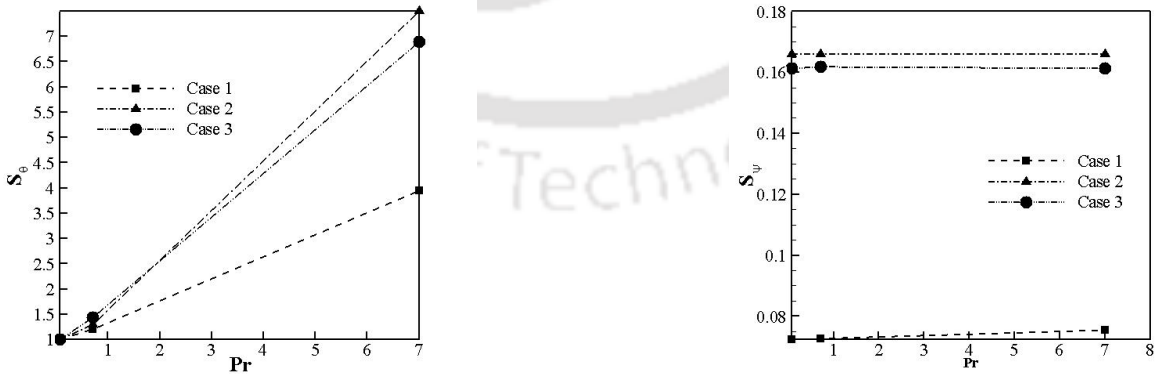

Figure 4.49: Comparison results of average entropy generation (a) heat transfer ($\overline{S}_\theta$) and (b) fluid friction ($\overline{S}_\Psi$) over hot wall for the effect of Pr

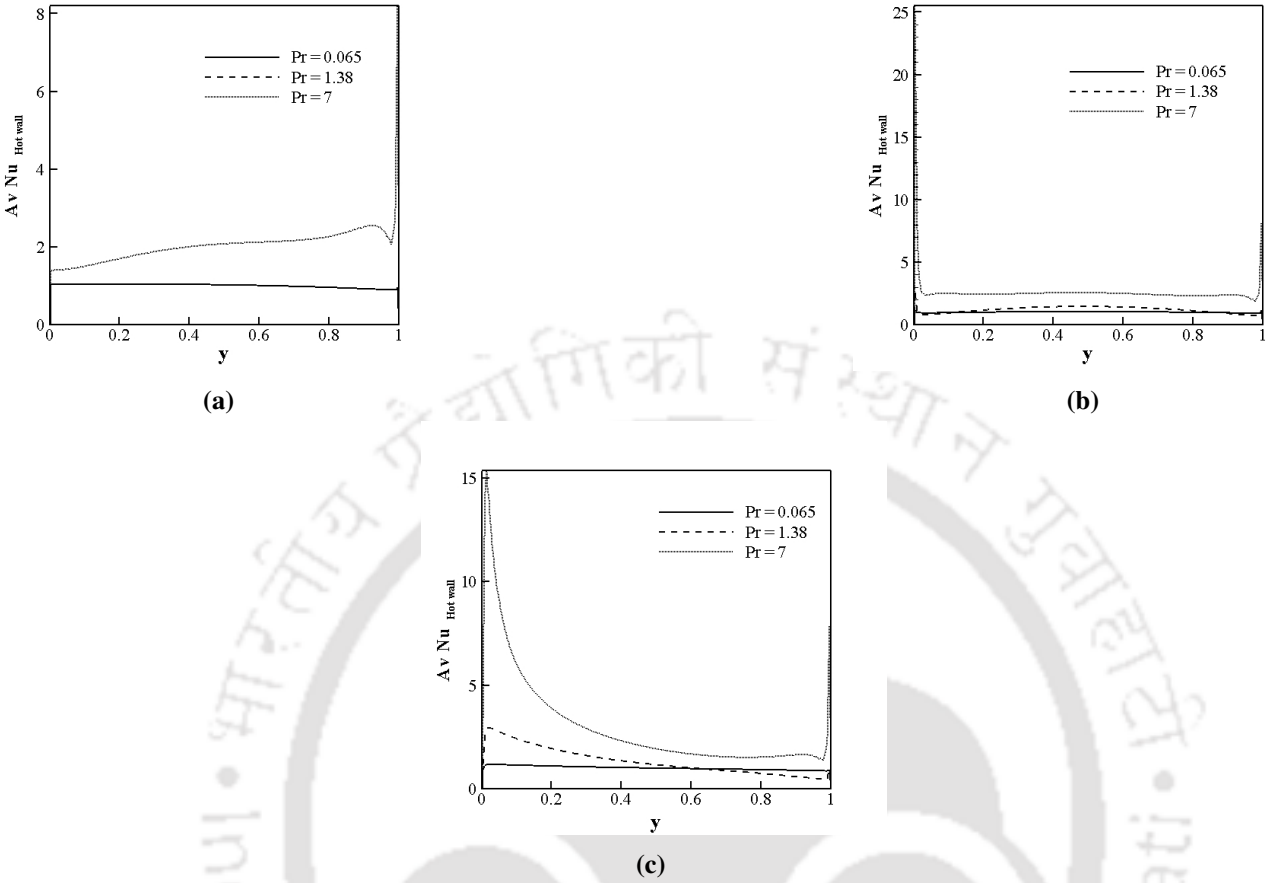

Figure 4.50: Comparison results of local Nusselt number ($\overline{Nu}_h$) over hot wall for (a) case 1, (b) case 2 and, (c) case 3 for the effect of Pr

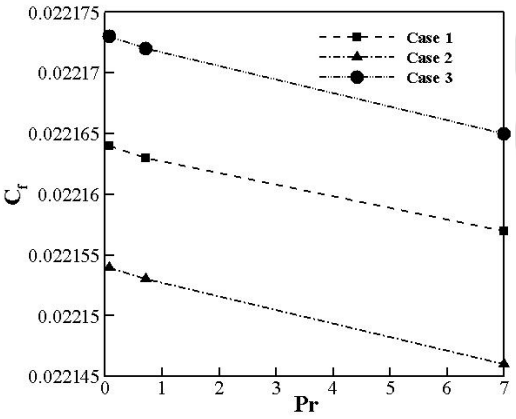

Figure 4.51: Comparison results of local friction coefficient (C_f) over top wall for the effect of Pr

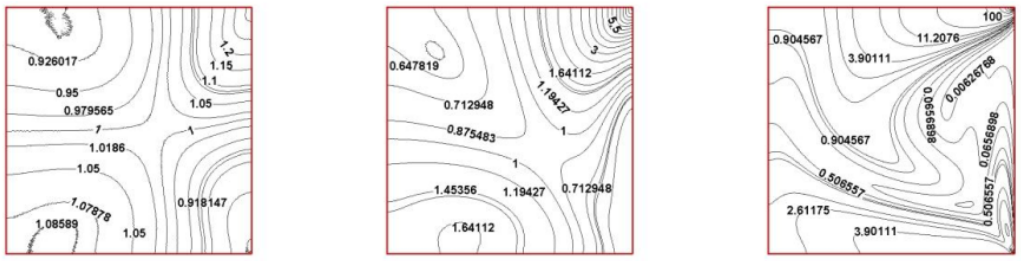

(a)

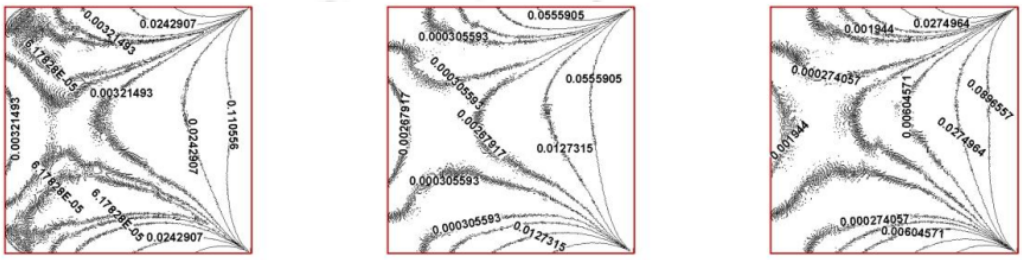

(b)

Figure 4.52: Local entropy generation (a) heat transfer (S_θ) and (b) fluid friction (S_Ψ) for case 1 for the effect of Pr

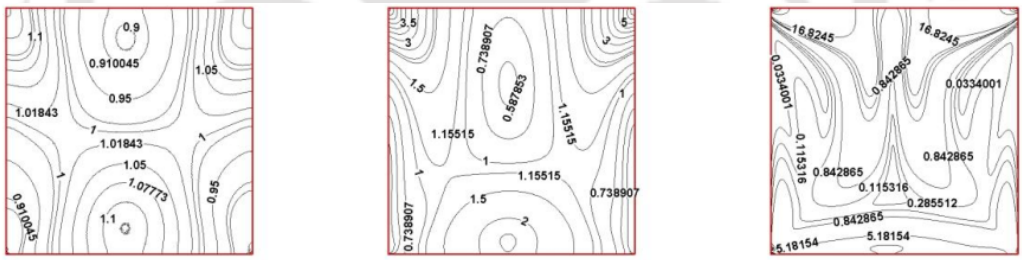

(a)

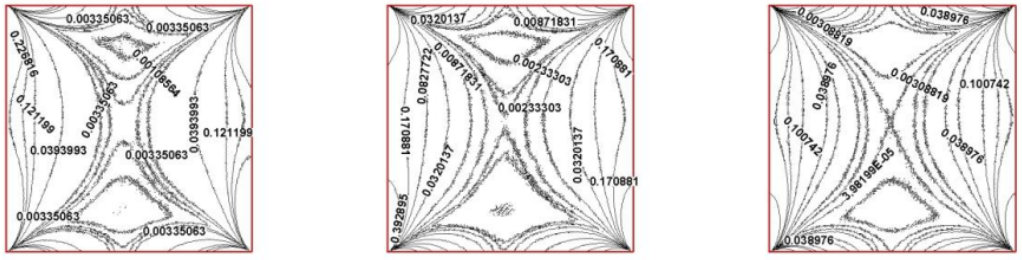

(b)

Figure 4.53: Local entropy generation (a) heat transfer (S_θ) and (b) fluid friction (S_Ψ) for case 2 for the effect of Pr

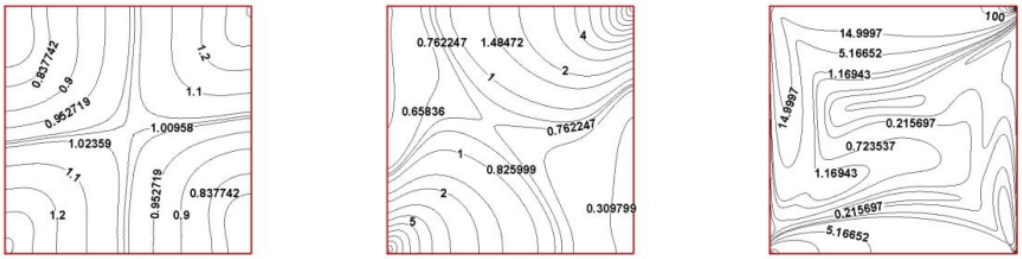

Pr=0.065 Pr=1.38 Pr=7

(a)

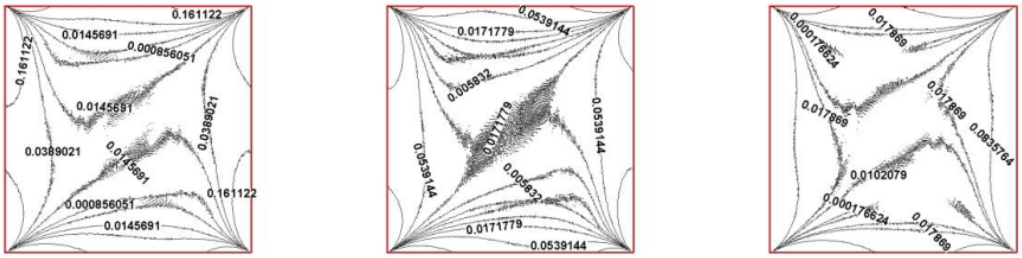

Pr=0.065 Pr=1.38 Pr=7

(b)

Figure 4.54: Local entropy generation (a) heat transfer (S_θ) and (b) fluid friction (S_Ψ) for case 3 for the effect of Pr

With increase in Pr, both average Nusselt number ($\overline{Nu_h}$ and $\overline{Nu_c}$), local Nusselt number (Nu_h), average entropy generation ($\overline{S}_\theta$ and $\overline{S}_\Psi$), local entropy generation (S_θ and S_Ψ) increases. This is because as Pr increases, the hydrodynamic boundary layer thickness increases. For Pr>1, an increase in Pr decreases the thermal boundary layer thickness as compared to the hydrodynamic layer thickness. This change essentially acts to increase the heat flux which is reflected in the increasing of Nu and entropy generation. A significant increase in heat transfer and entropy generation is observes at Pr=7. This is found to be valid for the other two cases. However, the magnitude of friction coefficient does not change much all the cases.

The $\overline{S}_\Psi$ for case 1 is found to have very minimal value as compared to case 2 followed by case 3. As, in case 2 and 3, both lids moving in forward and opposite directions unlike case 1 where only top lid is contributing the frictional effects.

Also, the analysis highlights that the vertical walls of the cavity contribute significantly to the generation of entropy due to both thermal and fluid irreversibilities. This is because, the vertical walls are experiencing higher temperature gradients, leading to increased thermal irreversibilities.

Additionally, S_θ and S_Ψ patterns near the vertical walls are more complex, causing higher fluid irreversibilities as shown in Figure 4.52, 4.53 and 4.54.

c) **Reynolds number**

The performance analysis to depict the effect of Reynolds number (Re) is shown in a comparison mode between all the three cases 1,2 and 3 in terms of average Nusselt number ($\overline{Nu}_h$ and $\overline{Nu}_c$), local Nusselt number (Nu_h), average entropy generation ($\overline{S}_\theta$ and $\overline{S}_\Psi$), local entropy generation (S_θ and S_Ψ) and friction coefficient (C_f) in the Figures 4.55 through 4.61 below.

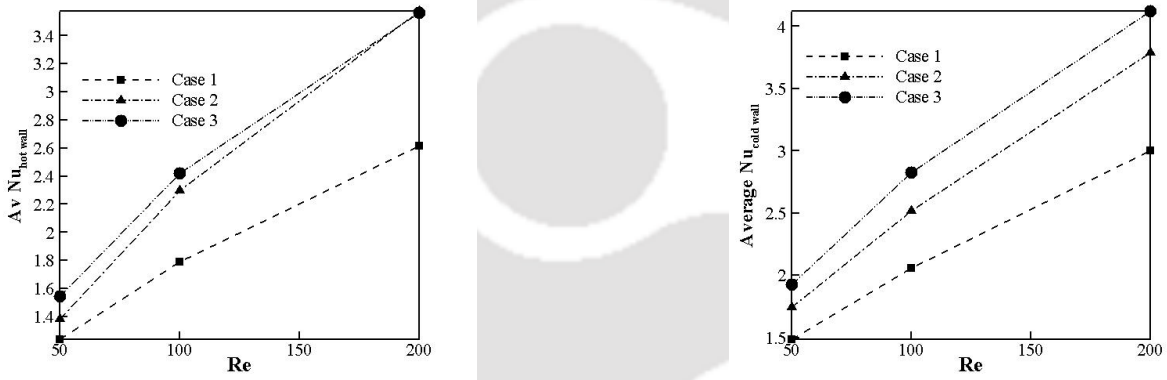

Figure 4.55: Comparison results of average Nusselt number (a) $\overline{Nu}_h$ over hot wall, (b) $\overline{Nu}_c$ over cold wall for the effect of Re

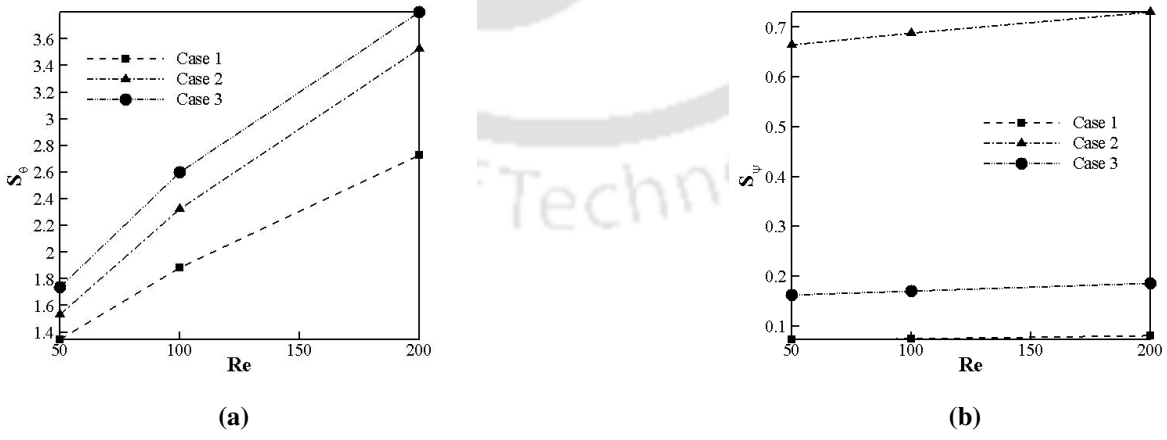

Figure 4.56: Comparison results of average entropy generation (a) heat transfer ($\overline{\boldsymbol{S}}_{\boldsymbol{\theta}}$) and (b) fluid friction ($\overline{\boldsymbol{S}}_{\boldsymbol{\Psi}}$) over hot wall for the effect of Re

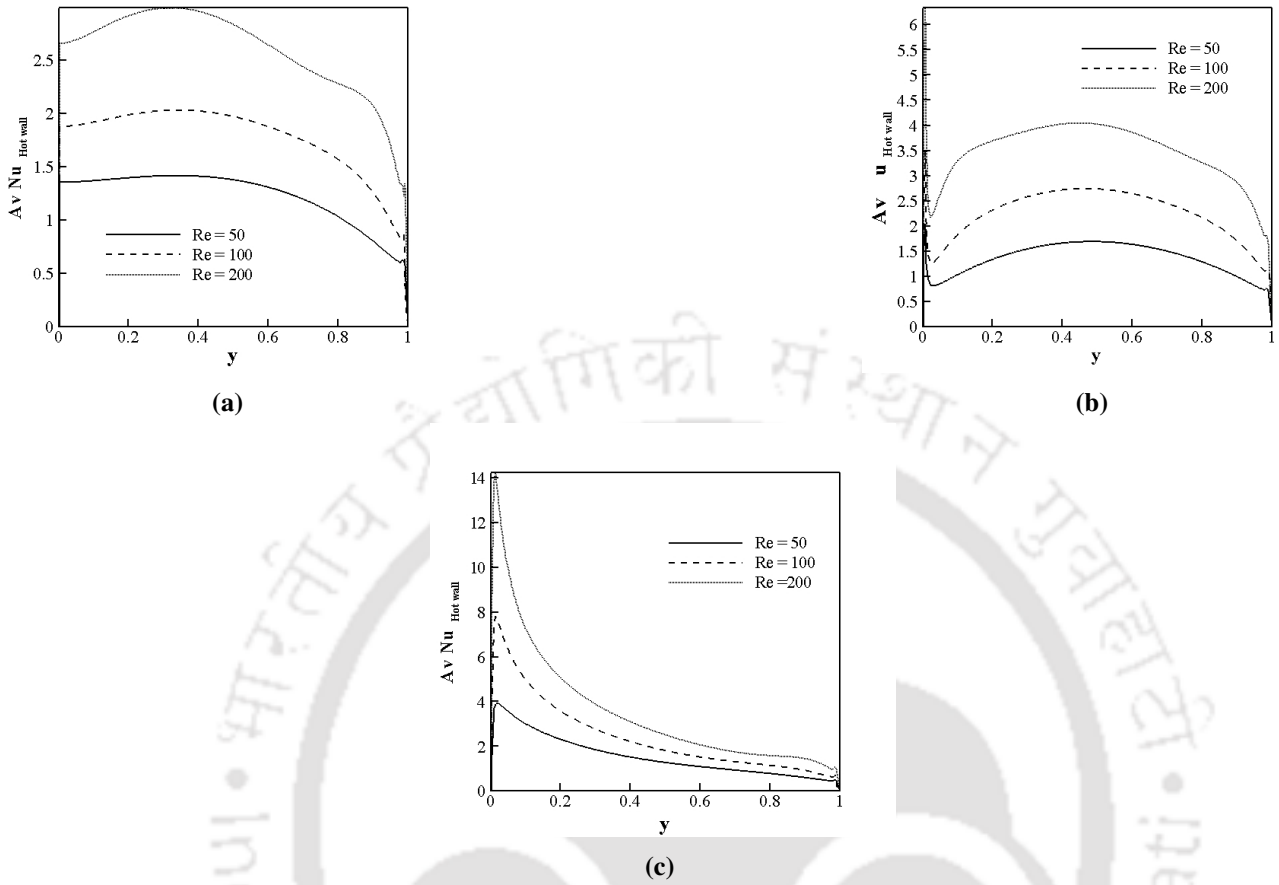

Figure 4.57: Comparison results of local Nusselt number ($\overline{Nu}_h$) over hot wall for (a) case 1, (b) case 2 and, (c) case 3 for the effect of Re

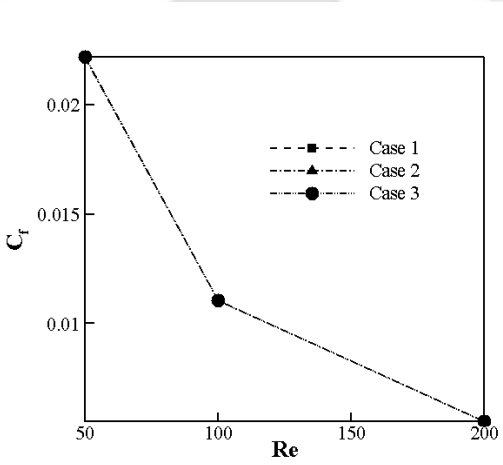

Figure 4.58: Comparison results of local friction coefficient (C_f) over top wall for the effect of Re

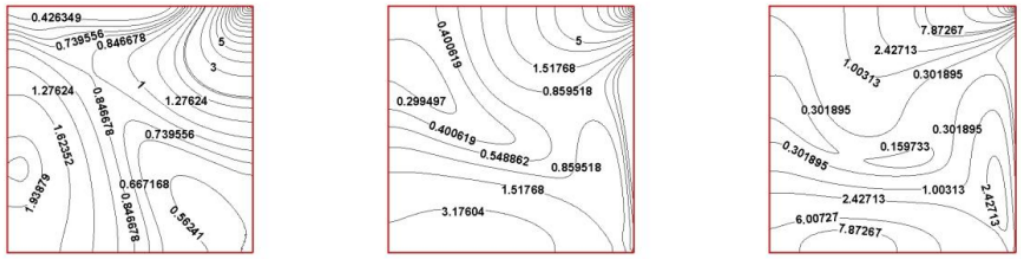

Re=50 Re=100 Re=200

(a)

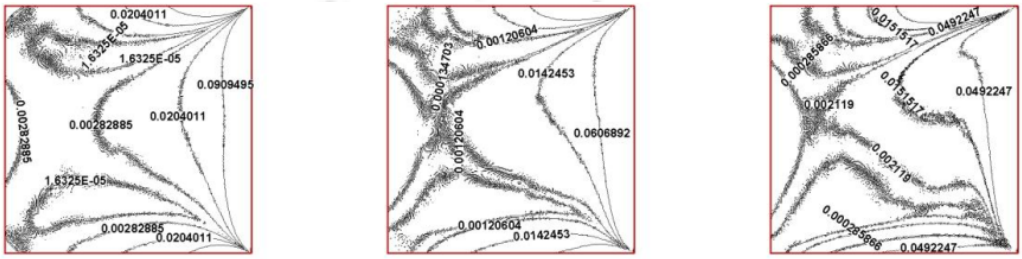

Re=50 Re=100 Re=200

(b)

Figure 4.59: Local entropy generation (a) heat transfer (S_θ) and (b) fluid friction (S_Ψ) for case 1 for the effect of Re

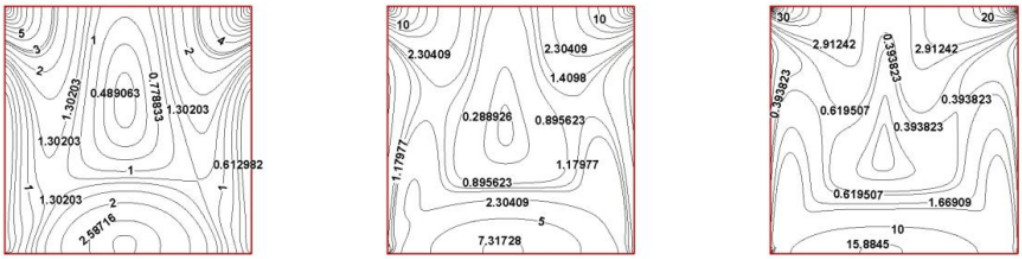

Re=50 Re=100 Re=200

(a)

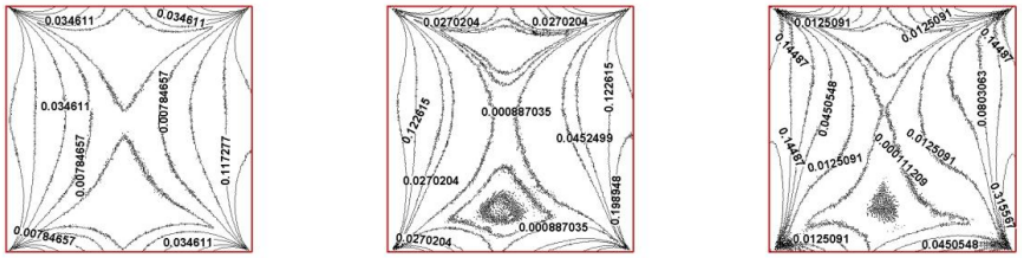

Re=50 Re=100 Re=200

(b)

Figure 4.60: Local entropy generation (a) heat transfer (S_θ) and (b) fluid friction (S_Ψ) for case 2 for the effect of Re

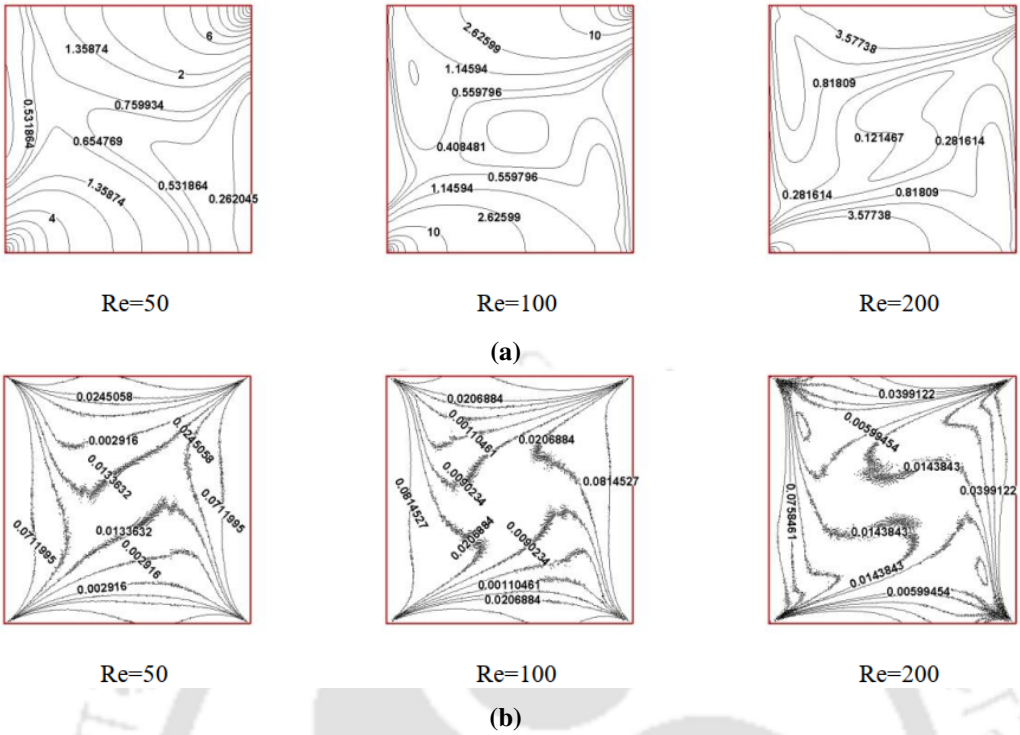

Figure 4.61: Local entropy generation (a) heat transfer (S_θ) and (b) fluid friction (S_Ψ) for case 3 for the effect of Re

With increase in Re, both average Nusselt number ($\overline{Nu}_h$ and $\overline{Nu}_c$), local Nusselt number (Nu_h), average entropy generation ($\overline{S}_\theta$ and $\overline{S}_\Psi$), local entropy generation (S_θ and S_Ψ) increases. This is because increasing the Re number implies the increase in lid velocities resulting in enhanced forced convection. It has been found that, the magnitude of Nu at both left and right wall and the entropy generation increases from case 1 to case 3 for all values of Re. This is due to the increased circulation of flow from case 1 to case 3. However, with increase in Re decreases the magnitude of friction coefficient and has negligible impact due to fluid flow configurations.

Also, like the effect of Pr, $\overline{S}_\Psi$ for case 1 is negligible as compared to case 2 followed by case 3.

d) **Inclination angle**

The performance analysis to depict the effect of inclination angle (ϕ) is shown in a comparison mode between all the three cases 1,2 and 3 in terms of average Nusselt number ($\overline{Nu}_h$ and $\overline{Nu}_c$), average entropy generation ($\overline{S}_\theta$ and $\overline{S}_\Psi$), local entropy generation (S_θ and S_Ψ) and friction coefficient (C_f) in the Figures 4.62 through 4.67 below.

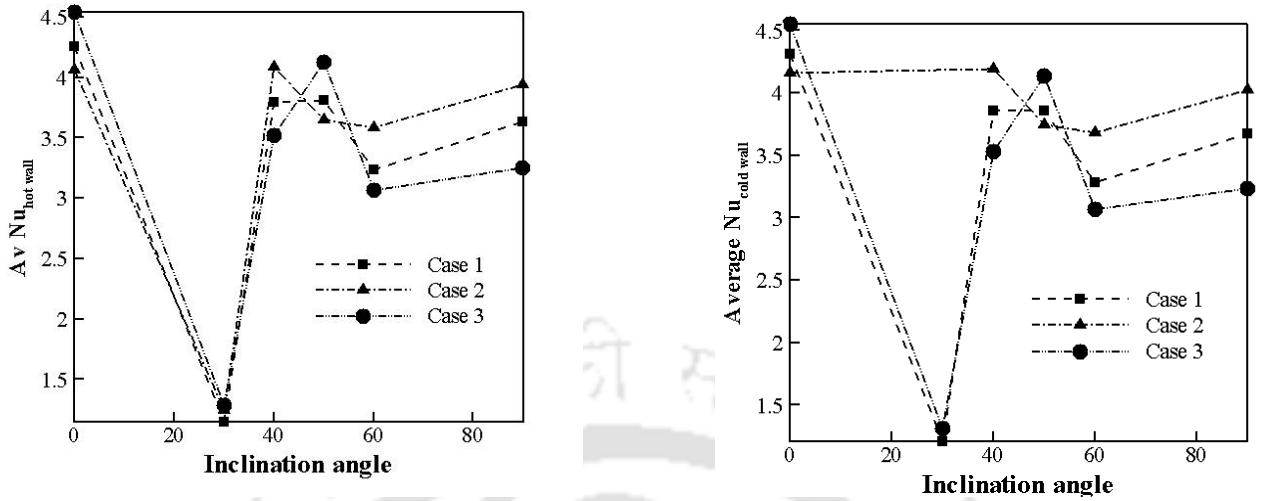

Figure 4.62: Comparison results of average Nusselt number (a) $\overline{Nu_h}$ over hot wall, (b) $\overline{Nu_c}$ over cold wall for the effect of ϕ

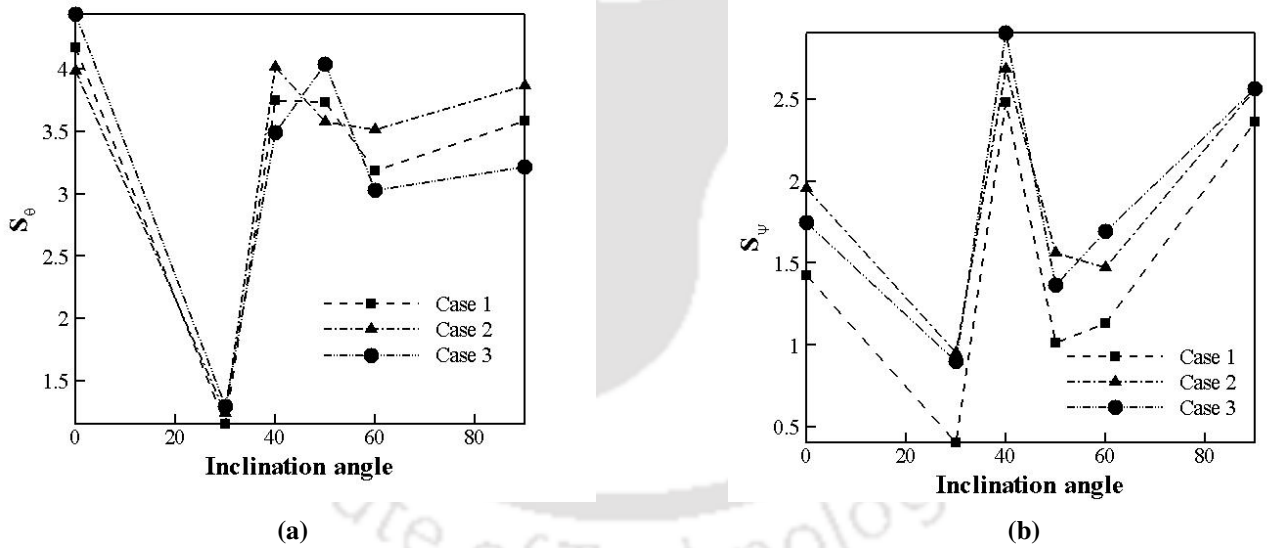

Figure 4.63: Comparison results of average entropy generation (a) heat transfer ($\overline{S}_{\theta}$) and (b) fluid friction ($\overline{S}_{\Psi}$) over the hot wall for the effect of ϕ.

It is observed that from Figure 4.62 and 4.63, inclination angle has a pronounced effect on both the Nu and entropy generation values. Initially at ϕ=0^0, heat transfer and entropy generation are found to be high for all the cases and then decreases with increase in inclination angle.

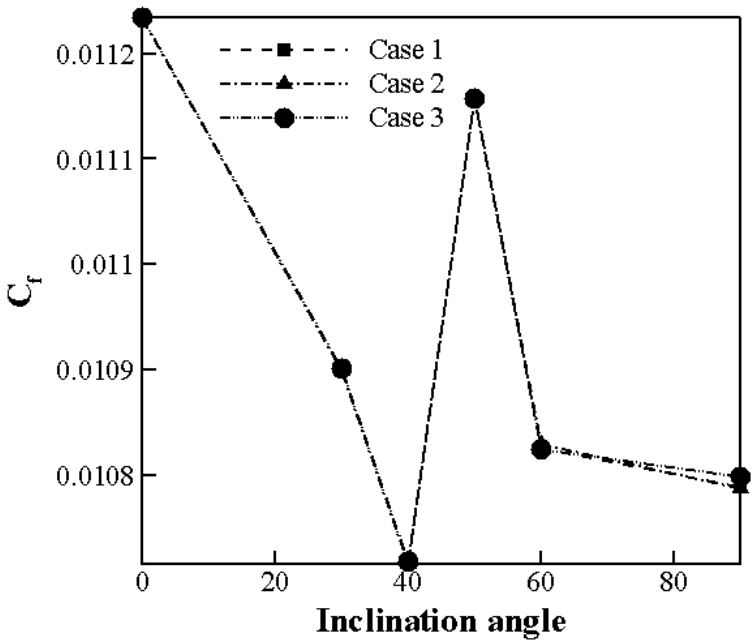

Figure 4.64: Comparison results of local friction coefficient (C_f) over top wall for the effect of ϕ

The values reach its maximum limit at the inclination angle, ϕ =40^0 for case 1 and 2 and ϕ=50^0 for case 3. Indeed, for these inclination angles for the respective cases, buoyancy acts along both the active and adiabatic walls, there is more work done on the fluid by buoyancy thus increasing the total entropy generation via the augmentation of the convective heat transfer (Nu). As the inclination angle is further increased, the velocity of the fluid diminishes because buoyancy and pressure oppose each other in the intrusion layer. This decreases the heat transfer rate and entropy generation due to viscous effects. At ϕ =90^0, Nu and irreversibility is found to be increasing. However, as depicted in Figure 4.64, an inclination angle of 40 ^{0}, the skin friction coefficient reaches its minimum value compared to all other inclination angles ranging from 0 to 90 ^{0}. This observation suggests that the flow conditions at this particular inclination angle result in reduced frictional forces acting on the surface of the object or boundary. This could be due to factors such as favorable flow patterns, reduced boundary layer thickness, or a decrease in viscous effects at this specific angle. The minimum value of the skin friction coefficient at 40 ^{0} indicates an optimal configuration for minimizing frictional losses in the flow system.

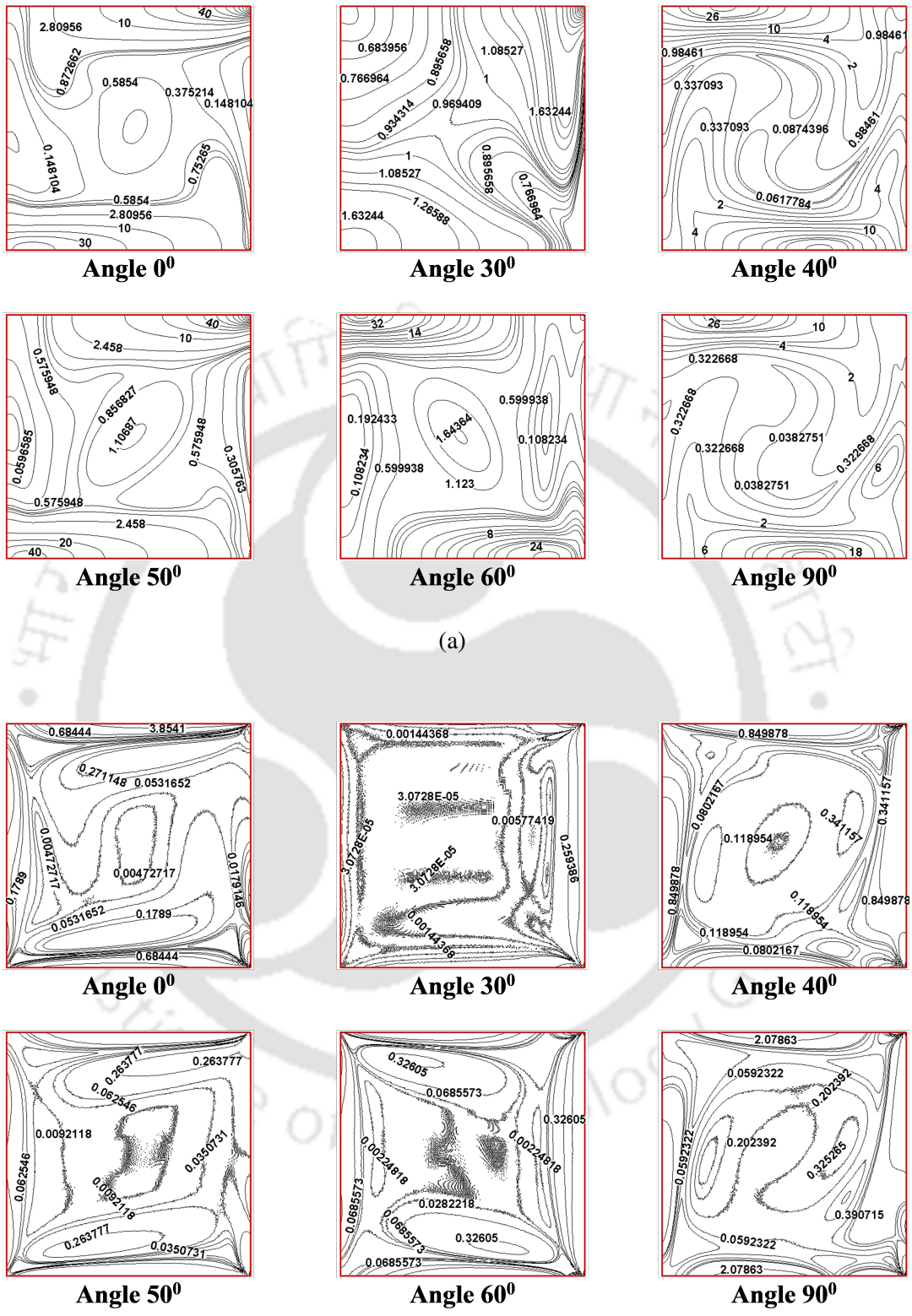

Figure 4.65: (a)Local entropy generation due to heat transfer (S_θ) and (b) Local entropy generation due to fluid friction (S_Ψ) for case 1 for the effect of ϕ at (A) ϕ=0^0, (B) ϕ=30^0, (C) ϕ=40^0, (D) ϕ=50^0, (E) ϕ=60^0 and (F) ϕ=90^0

As observed in Figure 4.65(a), the variations in values in local entropy generation due to heat transfer (S_θ) is in concordance with its corresponding isotherm contours as S_θ is a function of temperature. The maximum local entropy generation due to heat transfer S_θ are mostly concentrated near the hot wall at all inclination angles. However, the magnitudes get decreased due to decrease in buoyancy force with inclination angle. The highest value is found to be S_θ=40 near the moving lid at ϕ=0^0 and ϕ=50^0.

As observed in Figure 4.65(b), the variations in values in local entropy generation due to fluid friction (S_Ψ) is in concordance with its corresponding isotherm contours as S_Ψ is a function of U^x and U^y velocities. At all inclination angles, the highest concentration of local entropy generation resulting from fluid friction, S_Ψ is primarily observed near walls of the cavity. However, as the inclination angle increases, the magnitudes of entropy generation decrease due to a reduction in buoyancy force and thus the velocity and then again increases. Specifically, the maximum value of S_Ψ is found to be 0.8499 near the moving lid for inclination angles of ϕ=40^0.

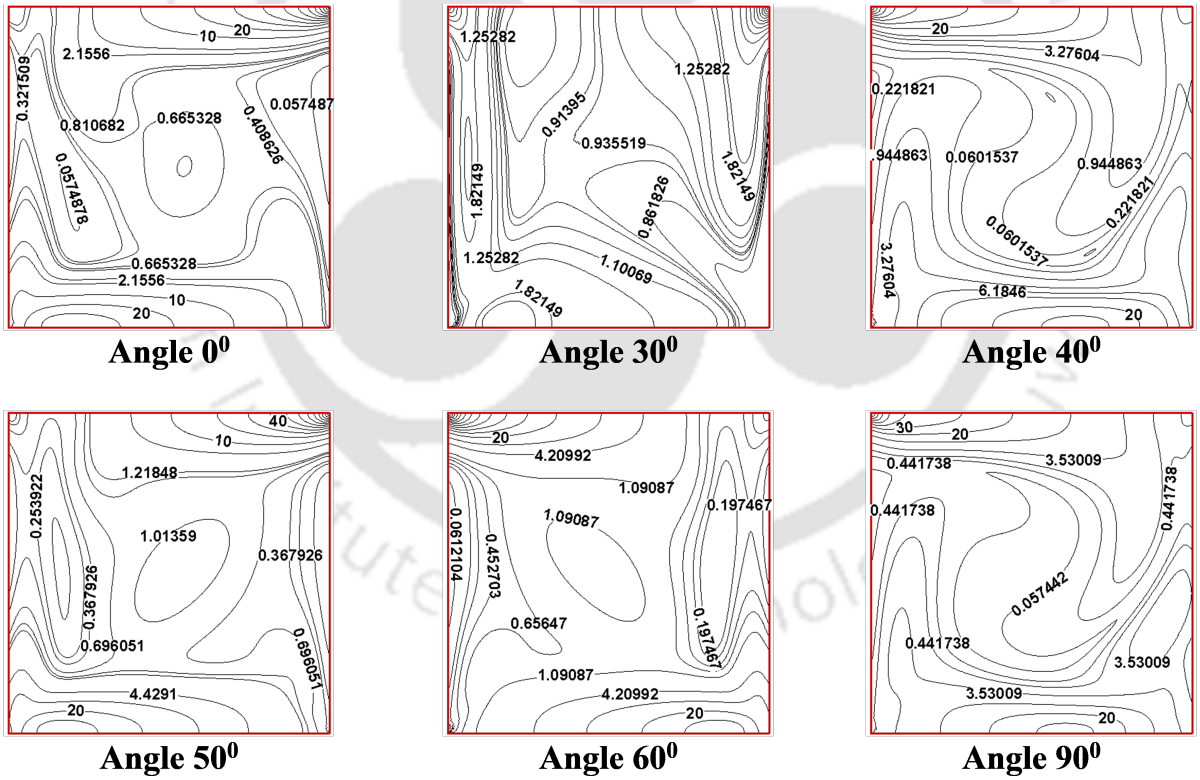

(a)

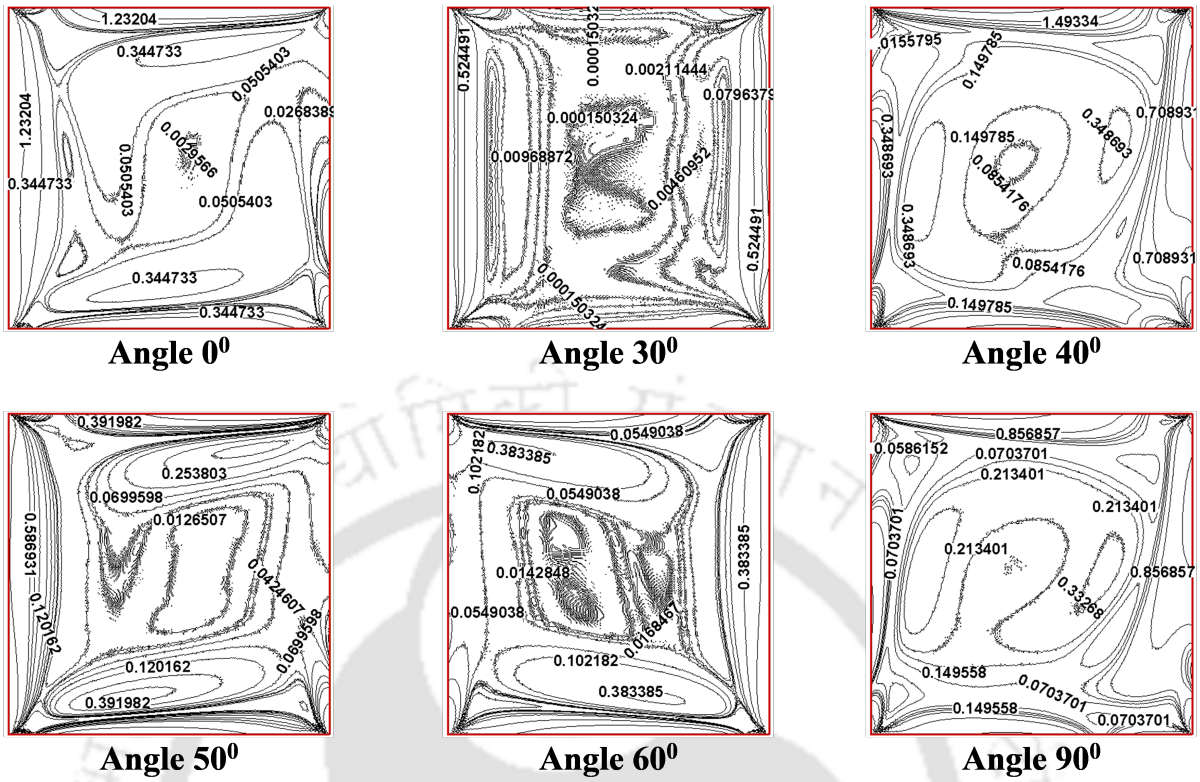

(b)

Figure 4.66: (a)Local entropy generation due to heat transfer (S_θ) and (b) Local entropy generation due to fluid friction (S_Ψ) for case 1 for the effect of Ia at angles (A) ϕ=0^0, (B) ϕ=30^0, (C) ϕ=40^0, (D) ϕ=50^0, (E) ϕ=60^0 and (F) ϕ=90^0

As case 2 represents both lid moving in forward direction with same magnitude of velocities, forced convection get induced near the walls. Due to this, the maximum local entropy generation due to heat transfer S_θ are mostly observed near the moving top and bottom walls at all inclination angles. The maximum magnitude of 40 is found to be at ϕ=50^0 followed by the next highest magnitude of 4.291 near the top and bottom walls.

As depicted in Figure 4.66(b), across all inclination angles, the greatest accumulation of local entropy generation caused by fluid friction, known as S_Ψ, is predominantly observed near the cavity walls. However, as the inclination angle increases, the magnitudes of entropy generation decrease initially due to a decline in the buoyancy force, resulting in reduced velocity. Subsequently, as the inclination angle continues to increase, the magnitudes of entropy generation begin to rise once more obtaining highest magnitude at ϕ=40^0.

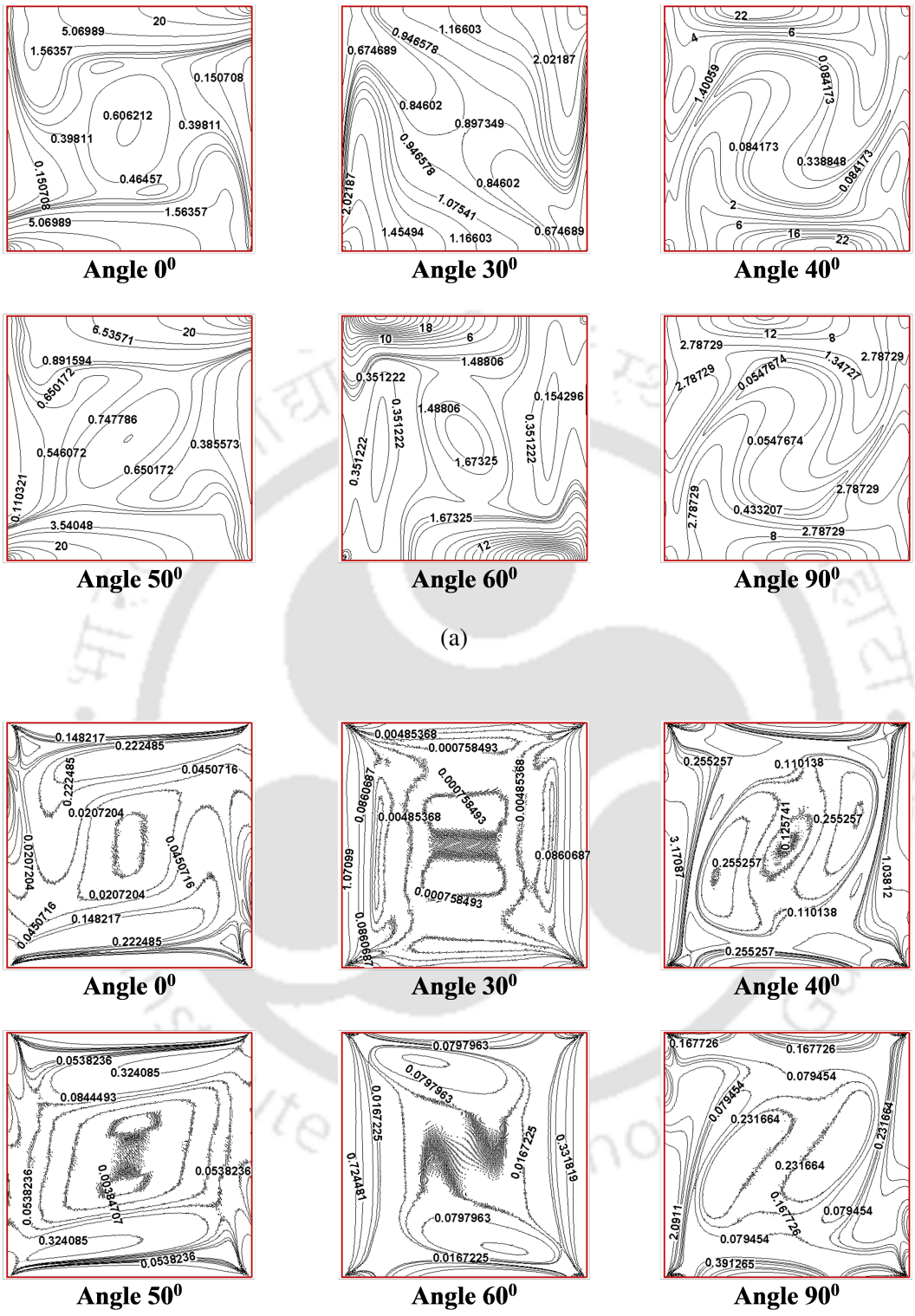

Figure 4.67: (a)Local entropy generation due to heat transfer (S_θ) and (b) Local entropy generation due to fluid friction (S_Ψ) for case 1 for the effect of Ia at angles (A) ϕ=0^0, (B) ϕ=30^0, (C) ϕ=40^0, (D) ϕ=50^0, (E) ϕ=60^0 and (F) ϕ=90^0

Amongst all the three cases, the entropy generation due to heat transfer (S_θ) and due to fluid friction (S_Ψ) with respect to case 3 (Figure 4.67(a) and 4.67(b)) is found to be highest as both lid moving in opposite directions inducing forced convection in both the opposing ways. Like the previous discussed cases, the highest magnitude of S_θ=6.5357 is resulted at the angular position of ϕ=50^0.

Also, as shown in Figure 4.67(b) highest magnitude of S_Ψ=3.1708 is reported at the angular position of ϕ=40^0 in cas 3 which is also highest amongst all the three configurations.

4.4.6 Effect of aspect ratio of top and bottom lids on average Nu

The performance analysis is shown in a comparison mode between all the three cases in terms of average Nusselt number ($\overline{Nu}_h$ and $\overline{Nu}_c$), entropy generation ($\overline{S}_\theta$ and $\overline{S}_\Psi$) and friction coefficient ($\boldsymbol{C_f}$) in the Table 4.2, 4.3 and 4.4 respectively. The simulations are done at AR=1, 2 and 4 (at inclination angles of ϕ=0^0, 30^0, 60^0 and 90^0) keeping constant values of Ri, Re and Pr at 10, 100 and 0.71 respectively. The aspect ratio in this study is taken as the ratio of height and length (L/H) of the cavity.

The comparative values for average Nu ($\overline{Nu}_h$ and $\overline{Nu}_c$) over hot and cold walls are shown in Table 4.2.

Table 4.2: Comparison of results obtained for average Nu ($\overline{Nu}_h$ and $\overline{Nu}_c$) for the effect of aspect ratio

Case	ϕ	AR=1		AR=2		AR=4	
		$\overline{Nu}_h$	$\overline{Nu}_c$	$\overline{Nu}_h$	$\overline{Nu}_c$	$\overline{Nu}_h$	$\overline{Nu}_c$
Case 1	0^0	4.25237	4.310728	3.28361	2.128074	2.518056	2.5362
	30^0	1.14407	1.20672	1.168796	1.9748	0.991631	1.554812
	60^0	3.23174	3.27881	2.915064	2.941596	2.059341	2.59638
	90^0	3.63211	3.66991	3.412612	4.213216	2.66072	2.84567
case 2	0^0	4.061	4.163	3.291781	3.354651	2.52055	2.560578
	30^0	1.244	1.353	1.24701	1.30609	0.95819	1.578304
	60^0	3.582	3.678	2.293215	3.164631	2.147416	2.743874
	90^0	3.93885	4.02499	3.103095	4.563657	2.544561	2.753596
Case 3	0^0	3.582	3.678	2.994013	2.24114	2.611622	2.605293
	30^0	3.93885	4.02499	0.94896	1.627925	0.905062	1.48949
	60^0	3.062653	3.064155	2.408351	3.28015	2.057221	2.564104
	90^0	3.252939	3.233030	2.528638	4.00391	2.445264	2.620417

As reported in the Table 4.2, average Nu ($\overline{Nu}_h$ and $\overline{Nu}_c$) over hot and cold walls decreases with increase in aspect ratio which is true for all the cases at increasing inclination angle. This trend can be attributed to the higher mass flow rate near the cavity walls, which facilitates enhanced heat transfer activity.

When the aspect ratio is larger, the channel becomes narrower, and the fluid flow is forced to concentrate closer to the walls. This results in a higher velocity near the walls, which leads to increased mass flow rate resulting in enhancing the convective heat transfer process. Furthermore, this trend remains consistent even as the inclination angle increases.

The comparative values for average entropy generation due to heat transfer and fluid friction ($\overline{S}_\theta$ and $\overline{S}_\Psi$) are shown in Table 4.3 .

Table 4.3: Comparison of results obtained for average entropy generation due to heat transfer and fluid friction ($\overline{S}_\theta$ and $\overline{S}_\Psi$) for the effect of aspect ratio

Case	ϕ	AR=1		AR=2		AR=4	
		$\overline{S}_\theta$	$\overline{S}_\Psi$	$\overline{S}_\theta$	$\overline{S}_\Psi$	$\overline{S}_\theta$	$\overline{S}_\Psi$
Case 1	0^0	4.25237	4.310728	4.137879	3.737515	3.112831	0.075443
	30^0	1.14407	1.20672	1.402315	0.113405	2.626942	0.283304
	60^0	3.23174	3.27881	3.409164	0.735809	4.340492	1.2365
	90^0	3.63211	3.66991	4.683241	0.92732	5.603483	1.11263
Case 2	0^0	4.061	4.163	3.815387	0.049447	3.995007	0.076622
	30^0	1.244	1.353	1.680772	0.26359	2.711084	0.30472
	60^0	3.582	3.678	3.61625	0.864602	3.785917	2.8262
	90^0	3.93885	4.02499	4.462242	1.33621	4.39855	2.3682
Case 3	0^0	4.536593	4.548713	3.894281	2.687671	3.331223	0.075431
	30^0	1.283300	1.308622	1.798845	0.241206	1.878454	0.283304
	60^0	3.062653	3.064155	3.635304	0.864602	3.520417	2.46388
	90^0	3.252939	3.233030	4.95079	1.14995	4.171451	1.6797

Similar trends are also observed for average entropy generation due to heat transfer and fluid friction ($\overline{S}_\theta$ and $\overline{S}_\Psi$) as reported in Table 4.3.

As mentioned before, the higher mass flow rate near the cavity walls promotes enhanced heat transfer activity. This means that there is more efficient transfer of heat between the hot and cold walls of the

cavity. Consequently, a lower average Nusselt number (Nu) is observed, indicating higher convective heat transfer. However, when considering entropy generation, a different perspective is necessary. Entropy generation is related to the irreversibilities and losses in the system. While enhanced heat transfer activity is desirable for efficient energy exchange, it can also contribute to higher entropy generation. The increased fluid motion, turbulence, and higher mass flow rate near the cavity walls, which enhance heat transfer, also lead to increased fluid friction and thermal irreversibilities. These irreversibilities result in an increase in entropy generation within the system. Thus, higher entropy generations are observed at AR=4 as compared to AR=2. Also, the the minimum average entropy generation due to heat transfer and fluid friction ($\overline{S}_\theta$ and $\overline{S}_\psi$) are reported in the simulation results of AR=1 at the inclination angle of ϕ=90^0.

Table 4.4: Comparison of results obtained for friction coefficient (C_f) for the effect of aspect ratio

Case	ϕ	AR=1		AR=2		AR=4	
		Top wall	Bottom wall	Top wall	Bottom wall	Top wall	Bottom wall
Case 1	0^0	-0.011	0.000	0.0248	0.00691	-0.4312	0.000002
	30^0	-0.0109	0.000000	-0.0214	0.000001	-0.0424	0.000001
	60^0	-0.0108	0.000001	-0.0216	0.000001	-0.4193	0.000003
	90^0	-0.0108	0.000000	-0.0326	0.000001	-0.0434	0.000002
Case 2	0^0	-0.0112	0.0115	-0.0221	0.02293	-0.0431	0.0458
	30^0	-0.0109	0.0115	-0.0214	0.0229	-0.0424	0.0458
	60^0	-0.0108	0.0115	-0.0213	0.0230	-0.4194	0.0458
	90^0	-0.0108	0.0115	-0.2110	0.0229	-0.4341	0.0458
Case 3	0^0	-0.01123	-0.0115	0.0284	0.0321	-0.0431	-0.0458
	30^0	-0.0109	-0.0115	-0.0216	-0.0229	-0.0424	-0.0458
	60^0	-0.0108	-0.0115	0.0212	-0.0229	-0.0419	-0.0458
	90^0	-0.0108	-0.0115	-0.0211	0.0229	-0.0419	-0.0458

As observed in Table 4.4, the friction coefficient C_f, increases with increase in aspect ratio which is valid for all inclination angles. This can be attributed to the fact that, an increase in aspect ratio may lead to higher velocities and stronger fluid motion, potentially resulting in higher friction coefficients. Also, it

is observed that, for all the three cases viz both lids move forward, and the top lid moves forward while the bottom lid moves backward, negative shear stress is observed on the top lid for all cases and on the bottom lid for Case 3. This phenomenon suggests that the fluid exerts forces in the opposite direction to the movement of the solid boundaries (the lids), resulting in resistance or drag experienced by the lids due to the fluid flow. This oppositional force leads to the manifestation of negative shear stress, indicating the complex interaction between the lid motion and the fluid flow patterns within the cavity.

4.4.7 Effect of velocity ratio of top and bottom lids on average Nu

The performance analysis is shown in a comparison mode between all the three cases in terms of average Nusselt number ($\overline{Nu}_h$ and $\overline{Nu}_c$), entropy generation ($\overline{S}_\theta$ and $\overline{S}_\Psi$) and friction coefficient in the Table 4.5 below. The simulations are done at three velocity ratios between top and bottom lids: 1:1, 1:0.5, 1:0.25 keeping constant values of Ri, Re and Pr at 10, 100 and 7 respectively.

Table 4.5: Performance analysis at varying velocity ratio

Case	Velocity Ratio	Average Nu		Entropy Generation		Friction Coefficient (C_f)	
		Left wall	Right wall	Heat transfer	Fluid friction	Top wall	Bottom wall
Case 2	1:1	9.1608	9.7343	9.0244	0.7660	-0.0220	0.0121
	1:0.5	8.8908	9.4831	8.5577	0.6851	-0.0220	0.0115
	1:0.25	8.6216	9.1300	8.3345	0.6013	-0.0220	0.0057
Case 3	1:1	9.9480	9.9517	9.4087	0.9528	-0.0221	-0.0230
	1:0.5	9.4786	9.6535	9.9593	0.6463	-0.0221	-0.0221
	1:0.25	9.1734	9.4577	8.8199	0.5744	-0.0221	-0.0057

The notable impact observed in Table 4.5 regarding the difference in velocity ratio between the top and bottom boundary can be attributed to the complex interplay between fluid dynamics and heat transfer. When the velocity ratio is set to 1:1, there is a higher rate of fluid motion near both boundaries, promoting more effective heat transfer. However, this increased fluid motion also results in higher friction between the fluid and the boundaries, leading to elevated irreversibility within the system. This heightened irreversibility indicates that a significant portion of the energy input is lost to dissipative processes, which is generally undesirable. Conversely, reducing the velocity ratio decreases the disparity in fluid

motion between the boundaries, thereby lowering friction and reducing irreversibility. This adjustment maintains satisfactory heat transfer performance while minimizing energy losses, resulting in a more efficient process.

4.5 Summary

A mixed convection flow simulation is performed taking Richardson number (0.1, 05, 1, 10), Prandtl number (0.065 (Molten metal), 1.38 (Gaseous ammonia), 7 (water)), Reynolds number (50, 100,200) and inclination angle (30^0, 40^0, 50^0 and 60^0), aspect ratio (1,2 and 4) and velocity ratio (1:1, 1:0.5 and 1:0.25) as the parameters. The motivation behind the current work is to investigate the fluid dynamics inside the cavity under the combined effect of both driving the lid and the buoyancy effect and suggest an optimized combination of these parameters in order to get optimal heat transfer and entropy generation.
This mixed convection study is made for three distinct cases:

(i) Top lid moving in forward direction and bottom lid is kept stationary (Case 1);

(ii) Both top and bottom lids moving in forward direction (Case 2);

(iii) Both top and bottom lids moving in opposite direction (Case 3);

The salient features of the mixed convection study are as follows:

(i) (a) For all the three cases, the average Nusselt number and net entropy generation increases with increase in Richardson number and Reynolds number attaining its maximum values at Ri=10 and Re=200 respectively. Hence, it can be concluded that, the buoyancy force enhances the heat transfer and hence also the net entropy generation.

(b) For all the three cases, the effect of Prandtl number is insignificant at lower values. However, it shows its impact at higher value. Thus, for constant value of Re and Ri, improvement in Pr results in overall advancement in heat transfer with the formation of circulating temperature loops leading to enhanced heat transfer rate and net entropy generation.

(c) Out of three cavity configurations, heat transfer rate and the irreversibility are minimum for the case 1 followed by case 2 and then case 3. This is true for all the varying parameters.

(d) The inclination angle has a pronounced effect on both the Nu and entropy generation (both $\overline{S}_\theta$ and $\overline{S}_\Psi$) values. The values reach its maximum limit at the inclination angle, ϕ=40^0 for case 1 and 2 and ϕ=50^0 for case 3. However, the inclination angle has not shown any pronounced effect in the friction coefficient value which remains almost constant for all the three cases. However, inclination angle, ϕ=90^0 gives the maximum heat transfer rate and entropy generation for all the cases.

(e) The contribution of fluid friction is found to be significant in the entropy generation during high values of Ri and Re as it aids to trigger the fluid motion. It has lesser variations under the changes in Pr. Hence, the irreversibility is reported purely due to heat transfer.

(f) The magnitude of friction coefficient also found to be increased with increasing effect of buoyancy effect (Ri) in case 1. The above findings are also found to be true for the other two cases. However, it is not respondent towards the Prandtl number. Contradictory to reaction to Ri, the magnitude of friction coefficient decreases with increase in Re.

(g) The variation of aspect ratio has a pronounced effect on optimizing heat transfer and entropy generation.

(h) With varying the velocity ratios of the top and bottom lids, the irreversibility, heat transfer rate and friction coefficient gets affected. The 1:1 velocity ratio is found to have maximum heat transfer rate and high friction coefficient. However, along with the enhancement of the Nu, irreversibility also gets increased which is not suitable for any process. It gets decreased with the decreasing velocity ratio for both the cases which may lead to satisfactory performance.

Chapter 5

Investigation of natural circulation loop with nanofluids using SRT-LBM

5.1 Introduction

After the Fukushima accident in 2011, there was a renewed focus on enhancing the safety features of nuclear reactors. One of the key concepts that gained prominence was passive safety, which refers to the ability of a system to safely shut down and cool itself without relying on active mechanisms or external power sources. In a passive safety system, the natural circulation loop (NCL) plays a crucial role in ensuring adequate cooling even during a loss of power or shutdown scenario.

NCLs, driven by the principle of natural convection, have practical applications beyond nuclear reactors. They are used in solar water heating systems to transfer heat from solar collectors to storage tanks. Geothermal heating and cooling systems utilize natural circulation loops to exchange heat with the ground for building climate control. Passive cooling systems in buildings rely on natural airflow and convection to create self-driven circulation loops, reducing the need for mechanical ventilation. Heat exchangers and steam generators also benefit from natural circulation loops, facilitating heat transfer without external pumps. In passive solar space heating, natural circulation loops distribute thermal energy stored from sunlight. These examples highlight the versatility of natural circulation loops in various engineering applications, utilizing natural convection for efficient heat transfer and system operation. By integrating the concept of passive safety with the natural circulation loop and using an appropriate working fluid, system designs can enhance safety and reduce the reliance on active components.

Research on nanofluids has gained significant attention in recent years due to their unique thermal and transport properties. Nanofluids are suspensions of nanoparticles in a base fluid, typically water or oil. The addition of nanoparticles to the base fluid alters its thermophysical properties, such as thermal conductivity, viscosity, and heat transfer characteristics.

Based on the literature survey, it is evident that previous research on NCLs mainly utilized conventional numerical techniques like the finite volume method. Furthermore, most of these studies focused on fluids with Prandtl numbers close to unity and emphasized heat transfer analysis based on the first law of thermodynamics. To the best of the authors' knowledge, no previous research has explored the effects of different nanofluids on heat transfer and entropy generation in this type of flow condition and using LBM. Hence, this study seeks to contribute to the understanding of these factors and their influence on flow behavior and thermal performance.

In contrast, the current study aims to fill these gaps by considering nanofluids and investigating the impact on heat transfer and entropy generation in this specific flow scenario. It has also been observed that very less modeling of the natural circulation loop is made having maximum heat transfer and minimum irreversibility. Thus, in the present work, numerical modeling for the natural circulation loop is done using the lattice Boltzmann method due to its simplicity with various parametric evaluations. Also, the modeling is extended to have the essence of non-Boussinesq approximation which adds to the novelty of the current work.

5.2 Mathematical modeling of the problem

The flow configuration of the natural circulation loop for the current study along with their boundary conditions is illustrated in Figure 5.1. The loop comprises two horizontal arms positioned opposite each other, with a heater and a cooler placed on these arms. The remaining sections of the loop are effectively insulated. The dimensions of the loop are as follows: a uniform diameter of D = 50 mm, a height of H = 1 m, and a width of W = 1 m. The inner length of the heater of $L_h^{/}$ = 0.8 m is taken, while the cooler measures $L_c^{/}$ = 0.8 m. To analyze the system, dimensionless groups based on the conservation equations are determined.

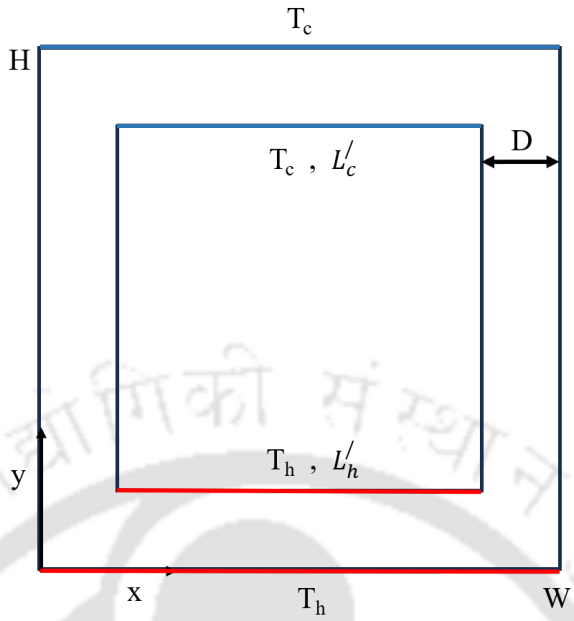

Figure 5.1: Schematic diagram for the computational domain of the natural circulation loop

5.2.1 Boussinesq and non-Boussinesq approximation

The governing equations for natural convection flow are indeed complex and often require simplifications to obtain a solution. The Boussinesq approximation is one of the most used approximations in natural convection problems. The Boussinesq approximation assumes that the density variation in the continuity equation can be neglected, and the density difference is approximated as a pure temperature effect, neglecting the influence of pressure on density. Thus,

$$(\rho_\infty - \rho) = \rho g \beta (T - T_\infty) \tag{5.1}$$

This approximation is valid when the term $\beta\ (T\ -\ T_\infty)$ is much smaller than 1, where β is the coefficient of thermal expansion, T is the temperature, and T_∞ is the reference temperature.

However, there are certain cases where the Boussinesq approximation is not applicable such as systems with large temperature differences. In such cases, the density variation with temperature becomes significant, and the Boussinesq approximation may lead to inaccurate results.

In the present work, the numerical modeling for the natural circulation loop is performed using the lattice Boltzmann method. Initially, the Boussinesq approximation is employed. Thus, as discussed in section 2.3, Guo's model [61] among the 3 force models is considered to calculate the external force F

which is defined as the external force per unit volume due to the presence of buoyancy force and is given by:

$$F_i = \rho g \beta (T_\infty - T_e) e_g \tag{5.2}$$

However, the approach proposed by Mayeli et al. [70] is then utilized to modify the governing equations and present a new form of these equations. Thereby, the modified force term becomes:

$$F_i = \rho g \beta (T_\infty - T_e)(e_g - \gamma (U \cdot \nabla) U) \tag{5.3}$$

Equation 5.3 is like the momentum equation with the Boussinesq approximation, except for an additional inertial buoyancy term on the right side. This extra term modifies the local direction and strength of gravity within the flow. It means that regions with higher spatial accelerations deviate from the Boussinesq buoyancy approximation. The γ parameter quantifies the strength of these deviations, indicating how significant the inertial buoyancy effects are compared to the gravitational forces acting on the flow.

With the above considerations, the density and temperature distribution functions i.e. the f and g are calculated by solving the lattice Boltzmann equation (LBE). After introducing the external force, the general form of lattice Boltzmann equation for the flow field can be written as:

$$f_i(\mathbf{x} + \mathbf{e_i}\Delta t, t + \Delta t) = f_i(\mathbf{x}, t) + \frac{\Delta t}{\tau_v}[f_i^{eq}(\mathbf{x}, t) - f_i(\mathbf{x}, t)] + (\Delta t \times \overrightarrow{e_i} \times F_i) \tag{5.4}$$

And for the temperature field,

$$g_i(\mathbf{x} + \mathbf{e_i}\Delta t, t + \Delta t) = g_i(\mathbf{x}, t) + \frac{\Delta t}{\tau_g}[g_i^{eq}(\mathbf{x}, t) - g_i(\mathbf{x}, t)] \tag{5.5}$$

Corresponding to the above LBE, respective equilibrium functions for momentum and energy equation are:

$$f^{eq}(\mathbf{x}, t) = w_i \cdot \rho(x, t) \left[1 + \frac{1}{2}\frac{(\mathbf{e} \cdot \mathbf{u})}{c_s^2} + \frac{3}{2}\frac{(\mathbf{e} \cdot \mathbf{u})^2}{c_s^2} - \frac{1}{2}\frac{(\mathbf{u} \cdot \mathbf{u})}{c_s^2}\right] \tag{5.6}$$

$$g^{eq}(\mathbf{x},t) = w_i \cdot \theta(x,t)\left[1 + \frac{(\mathbf{e}\cdot\mathbf{u})}{c_s^2}\right] \tag{5.7}$$

The boundary conditions as illustrated in Figure 5.1 are applied in the following forms:

U=V=0, at x=0, L, $0 \leq y \leq H$, U=V=0, at y=0, H, $0 \leq x \leq L$

$\frac{\partial\theta}{\partial Y} = 0 \;\; at\; X = 1, 0 \leq Y \leq 1$, left adiabatic arm

$\frac{\partial\theta}{\partial Y} = 0 \;\; at\; X = 0, 0 \leq Y \leq 1$, right adiabatic arm

$\theta = 1 \quad at\; Y = 0, 0 \leq X \leq 1$, heated bottom arm

$\theta = 0 \quad atY = 1, 0 \leq X \leq 1$, cold top arm

Finally, macroscopic variable for the considered D2Q9 lattice model can be calculated in terms of above variables with the following formulations:

$$\rho = \sum_{i=0}^{8} f_i \tag{5.8}$$

$$\rho u = \sum_{i=0}^{8} f_i \mathbf{e}_i \tag{5.9}$$

$$\theta = \sum_{i=0}^{8} g_i \tag{5.10}$$

5.2.2 Non-dimensional parameters

To identify the appropriate dimensionless parameters for description of natural circulation, following dimensionless variables can be defined:

$$x^* = \frac{x}{L}, \quad y^* = \frac{y}{H}, \quad u^* = \frac{u}{u_0}, \quad v^* = \frac{v}{u_0}, \quad \theta = \frac{T - T_c}{T_h - T_c} \tag{5.11}$$

where, u_0 is a reference velocity that is unknown. The reference velocity can be chosen as:

$$u_0 = \sqrt{g\beta\,(T - T_\infty)\,L}$$

Thereby, $Re = \frac{u_0 L}{\vartheta} = \frac{\sqrt{g\beta(T_w - T_\infty)L^3}}{\vartheta}$. Pr is Prandtl number which reflects the ratio between the momentum and thermal diffusion. Also, another dimensionless number called Grashoff number, Gr

holds importance in natural convection which represents the ratio of buoyancy force and the viscosity force acting on the fluid and is given by:

$$Gr = \frac{g\beta(T_w - T_\infty)L^3}{\vartheta^2} \tag{5.12}$$

5.2.3 Mathematical modelling for nanofluids

The present study includes the calculations for 2D flow. It is assumed that the base fluid and the nanoparticles flow at the same velocity and are in thermodynamic equilibrium. The properties of the nanofluids are assumed to be constant except the density. The kinematic viscosity, thermal diffusivity and other thermodynamic properties are estimated using existing literature [71]. The inputs in the present code is feed in terms of Pr.

The viscosity of the nanofluid containing a dilute suspension of small rigid spherical particles is used for effective viscosity in the present work as mentioned below:

$$\mu_{\text{eff}} = \frac{\mu_f}{(1-\varphi)^{1/4}} \tag{5.13}$$

The effective density of the nanofluid at reference temperature is defined as:

$$\rho_{nf,0} = (1-\varphi)\rho_{f,0} + \varphi\rho_{s,0} \tag{5.14}$$

Here,φ is the volume fraction of solid particles, and the subscripts, $f,\ nf$ and s stands for base fluid, nanofluid and solid respectively.

Neglecting the ratio of the nanolayer thickness to the radius of the original particle, the effective thermal conductivity of the nanofluid can be calculated as follows:

$$\frac{k_{\text{eff}}}{k_f} = \frac{k_s + 2k_f - 2\varphi(k_f - k_s)}{k_s + 2k_f + \varphi(k_f - k_s)} \tag{5.15}$$

Based on effective thermal conductivity k_{eff}, the thermal diffusivity of nanofluid is calculated using equation 5.16.

$$\alpha_{nf} = \frac{k_{\text{eff}}}{(\rho C_p)_{nf,0}} \tag{5.16}$$

In the present study the base fluid and nanofluid considered are water and copper (Cu) respectively and the thermophysical properties are mentioned in Table 5.1.

Table 5.1: Thermophysical properties

Thermophysical properties	**Base fluid**	**Nanoparticle (Cu)**
$\rho\ (kg/m^3)$	997	8933
$C_p\ (J/kgK)$	4180	385
$k\ (W/mK)$	0.607	400
$\mu\ (kg/m-s)$	0.891×10^{-3}	-
$\beta\ (\mathrm{K}^{-1})$	-	0.000051

As mentioned above, the simulations take the inputs of nanoparticles in terms of Pr. Thereby, four cases are considered in the present study taking comparative analysis with volume fraction as 0%, 1%, 3% and 5% and is mentioned in Table 5.2.

Table 5.2: Volume fractions, φ considered in the present study

Volume fraction (φ, %)	**Pr**
0 (Base fluid)	6.14
1	3.35
3	2.75
5	2.3

5.3 Code validation and grid independence test

It is essential to compare the results predicted by the developed computational model with relevant literature to validate the code before proceeding with further simulation. Simulations are performed with water (single phase liquid) throughout the loop. The present computational code is validated with established results by Desrayaud et al. [72].

The simulation is performed taking input parameters as Pr=5.5 and aspect ratio (AR) as AR=1.0. The parameters that appear in the equations are the Rayleigh number, Ra, defined referring to the width

of the loop the Rayleigh number,Ra_{2D}, based on the hydraulic diameter D_h=2D, and the Prandtl number, Pr, which are expressed as:

$$Ra = \frac{g\beta\Delta TW^3}{\vartheta\alpha} = \frac{Ra_{2D}}{(2d)^3}, \quad Pr = \frac{\nu}{\alpha} \tag{5.17}$$

Reynolds number correlation

In particular, Vijayan et al. [73] have demonstrated that the stationary mass flow rate for various uniform diameter loops can be defined as a function of the non dimensional group ($Gr_m\,(D_h/L)$), with Gr_m being the modified Grashof number, and L, the total length of the loop. This non-dimensional group is defined for a plane wall channel by:

$$(\mathrm{Gr}_m\left(\frac{D_h}{L}\right)) = \frac{\mathrm{Ra}_{2D} \times 4 \times (1-d) \times (A-d)}{\mathrm{Pr}^2 \times d \times l} \tag{5.18}$$

where, d is dimensionless channel gap width, $d = D/W$ and l is the dimensionless loop length, $l = L/W$ and D_h is the hydraulic diameter.

Using the above relation, the Reynolds number obtained by present simulation is compared with the Reynolds number (using equation 5.19) obtained by correlation given by established results [71] and is tabulated in Table 5.3.

The correlation proposed by Vijayan [73] can thus be expressed as reported in Desrayaud et al. [72].

$$Re_{2D} = 0.144(Gr_m(D_h/L))^{0.5} = 0.144(\frac{Ra_{2D} \times 4 \times (1-d) \times (A-d)}{Pr^2 \times d \times l})^{0.5} \tag{5.19}$$

Table 5.3: Validation for single phase (water) natural circulation loop

Ra	Re **(present data)**	Re **[72]**
1×10^4	0.9876	1.1848
5×10^4	1.4817	2.6494

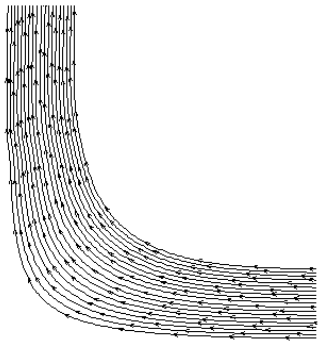

Figure 5.2: Velocity profile at the left corner of the natural circulation loop

Figure 5.2 also shows a close view of velocity profile which also goes according to the physics of the natural circulation loop affirming the correctness of the code. The present work is further validated with the established results [72] in terms of streamlines and isotherms as shown in Figure 5.3 and Figure 5.4.

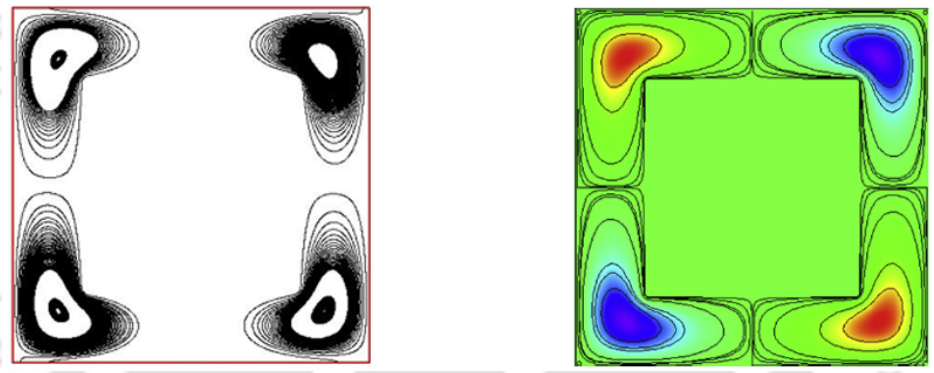

(a)

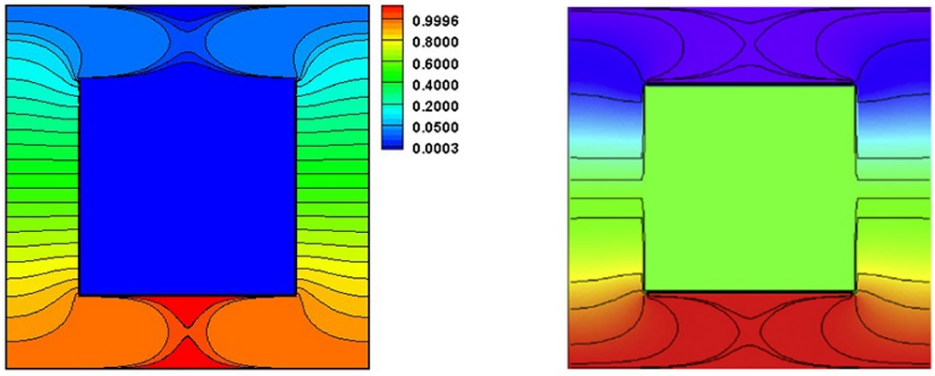

(b)

Figure 5.3: Pseudo-conductive regime, Ra = 10^4, (a) Streamlines, (b) isotherms for AR=1 and d = 0.2.

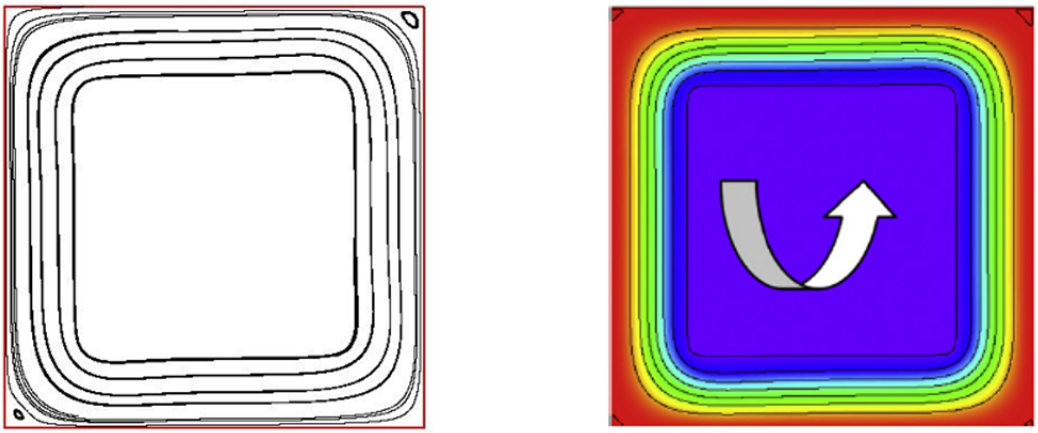

(a)

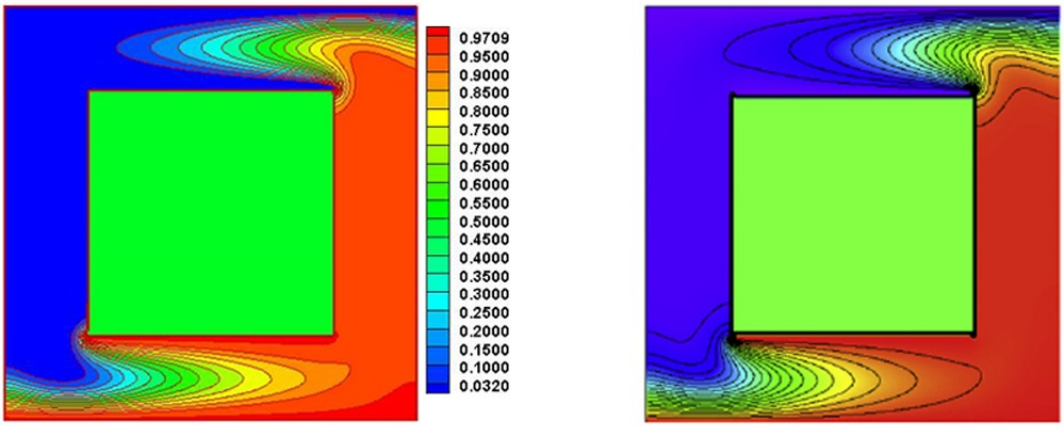

(b)

Figure 5.4: Convective regime for Ra =5$\times$10^4, (a) Streamlines, (b) isotherms AR= 1 and d =0.2

Figure 5.3 and 5.4 shows the comparative depiction of streamlines and isotherms. It is to be noted that, the left figures are from the present study. At low values of the Rayleigh number, Ra= 10^4, no global motion takes place and four recirculation regions of weak motion occur. The streamlines, reported in Figure. 5.3 (a), show four vortices circulating in the clockwise and counter-clockwise directions. The cooler fluid is confined in the upper part of the loop while the hotter fluid is confined in the lower part, each flowing inside the vortices located in the elbows. The temperature field is shown in Figure. 5.3 (b), the isotherms are stratified from the bottom to the top inside the vertical adiabatic legs. The heat is thus transferred by conduction from the lower hot part to the upper cold part of the loop and for this reason the regime has been called “pseudoconductive”.

Streamlines and isotherms for Ra = 5×10^4 are shown in Figure 5.4. The symmetry of the flow and temperature fields corresponding to the pseudo-conductive regime is broken and a central point symmetry sets in. The flow can actually have any of the two directions, i.e. clockwise or counterclockwise. The isotherms, reported in Figure. 5.4 (b), follow the motion of the fluid. The fluid inside the vertical thermally insulated leg is almost isothermal whereas strong temperature gradients characterize the horizontal sections.

Grid independence test

The grid independency is checked using 3 numbers of grid sizes and the value $\overline{Nu}Ra^{1/4}$ is calculated at Pr=5.5 and Ra=10^6. The result is tabulated in table 5.4.

Table 5.4: Grid independence test for natural circulation loop

S.no.	Grid Size	$\overline{Nu}R_a^{1/4}$
1	200 × 200	0.2152
2	250 × 250	0.2283
3	300 × 300	0.2290

Taking the outcomes of Table 5.4 into consideration, grid size 250×250 is used for further simulations. The value of the non-dimensional parameter tabulated above is matched with the established literature [72] and found to be in good agreement with the existing results.

5.3.1 Post processing

i. Nusselt number

The average Nusselt number along bottom hot arm ($\overline{Nu}_b$) and top cold ($\overline{Nu}_t$) arm are respectively calculated using the below mentioned equations 5.20 and 5.21 [58].

$$\overline{Nu}_b = \frac{1}{L_h}\int_0^L Nu_x\, dy \tag{5.20}$$

$$\overline{Nu}_t = \frac{1}{L_c}\int_0^L Nu_x\, dy \tag{5.21}$$

where, Nu_x = - $\frac{\partial\theta}{\partial y}$ are local Nusselt number at all fluid nodes and at the horizontal surfaces respectively.

ii. Entropy generation

The existence of a thermal gradient between the horizontal arms of the loop sets the fluid in a non-equilibrium state which causes entropy generation in the system. According to local thermodynamic equilibrium with linear transport theory, the local entropy generation for two-dimensional Cartesian system is discussed in subsection 3.2.3.

iii. Shear stress

Shear stress refers to the force per unit area exerted by a fluid as it flows past a solid surface. The non-dimensional skin friction coefficient is discussed in section 4.2.

5.4 Results and discussion

A comprehensive assessment of the thermal-hydraulic performance of a natural circulation loop using SRT-LBM is done. The simulations are based on the above validated code and various parameters are considered to investigate their effects on the system. The following parameters are as follows:

(i) **Volume fraction:** The simulations are conducted for different volume fractions (φ) of the nanofluid, specifically 0%, 1%, 3% and 5%.

(ii) **Rayleigh number:** Different Rayleigh numbers (Ra) are considered, namely 10^3, 5×10^4, 10^5, and 10^6.

(iii) ***Inclination angle:*** The simulations account for various inclination angles (ϕ), including 0°, 30°, 60°, and 90°.

(iv) **Aspect ratio:** Three different aspect ratios (AR) are taken into consideration: 0.5, 1, and 2. The aspect ratio represents the ratio of the height to the width of the natural circulation loop.

(v) **Diameter of the loop:** The diameter of the loop is another parameter considered in the simulations. Three different comparative analysis is presented in this section.

(vi) **Non-Boussinesq approximation:** Comparison between both the approximations are presented in this chapter.

By varying these parameters in the simulations, the study aims to assess the thermal-hydraulic performance of the natural circulation loop and understand how these parameters influence the system's behavior. The results obtained from this parametric study can provide insights into optimizing the design and operation of natural circulation loops for enhanced thermal-hydraulic performance.

5.4.1 Effect of nanofluid for various Rayleigh number

The heat transport capability of NCLs highly depends on the mass flow rate generated due to the buoyancy driven flow. It is also to be mentioned that, the gravitational force and friction force are equal. Traditionally, NCL studies have predominantly focused on using pure water as the working fluid. However, the selection of the working fluid significantly affects the system's mass flow rate dynamics. Hence, choosing the appropriate fluid is pivotal in optimizing NCL performance and enhancing heat transfer efficiency.

Recent advancements, as highlighted in section 5.1, have introduced nanofluids as a promising working fluid in Natural Circulation Loops (NCLs). Nanofluids are formulated by dispersing solid nanoparticles, typically at the nanometer scale, into a base fluid with inherently low thermal conductivity, such as water, oil, or ethylene glycol. The primary advantage of employing nanofluids lies in their ability to significantly enhance thermal conductivity compared to the base fluid alone. This enhancement is particularly notable with metallic nanoparticles like aluminum, copper, and silver, which exhibit exceptional thermal conductive properties. As a result, the utilization of nanofluids holds immense potential for improving heat transfer performance and overall efficiency within NCLs.

In this investigation, water serves as the base fluid with a Prandtl number (Pr) of 6.14, while copper (Cu) nanoparticles are introduced into the base fluid gradually with volume fractions (φ) of 0.01 (Pr=3.35), 0.03 (Pr=2.75), and 0.05 (Pr=2.3). Consequently, simulations are conducted at various Rayleigh numbers (Ra), encompassing the range from Pr 6.14 to 2.3. The impact of Pr is analyzed by comparing the four cases through streamlines, isotherms, Nusselt number, and entropy generation, as illustrated in Figures 5.5 through 5.10.

A. **Streamlines contours**

i. **Pr=6.14 (Basefluid,** $\varphi = 0.0$**)**

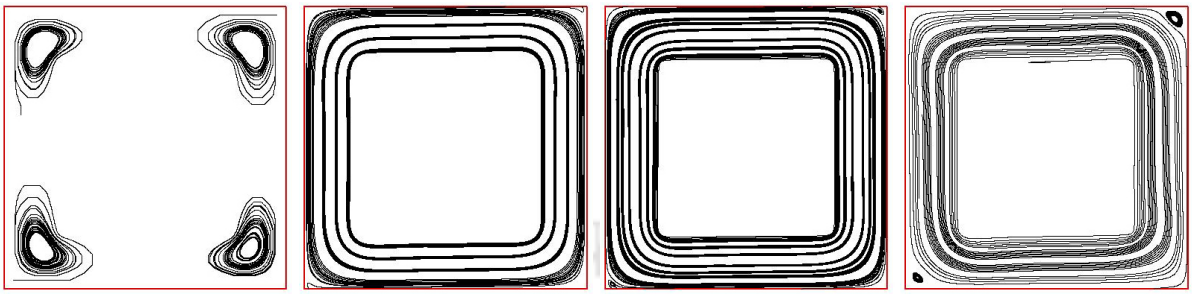

(a) Ra**=10**^{3} **(b)** Ra**=5**$\times$**10**^{4} **(c)** Ra**=10**^{5} **(d)** Ra**=10**^{6}

ii. **Pr=3.35 (**$\varphi = 0.01$**)**

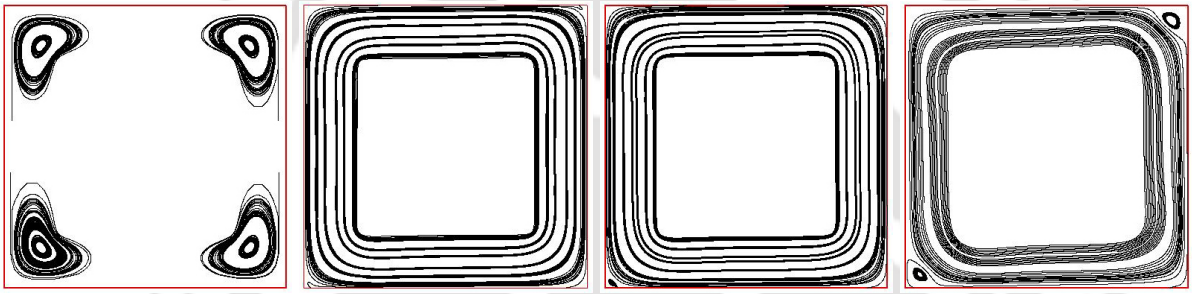

(a) Ra**=10**^{3} **(b)** Ra**=5**$\times$**10**^{4} **(c)** Ra**=10**^{5} **(d)** Ra**=10**^{6}

iii. **Pr=2.75 (**$\varphi = 0.03$**)**

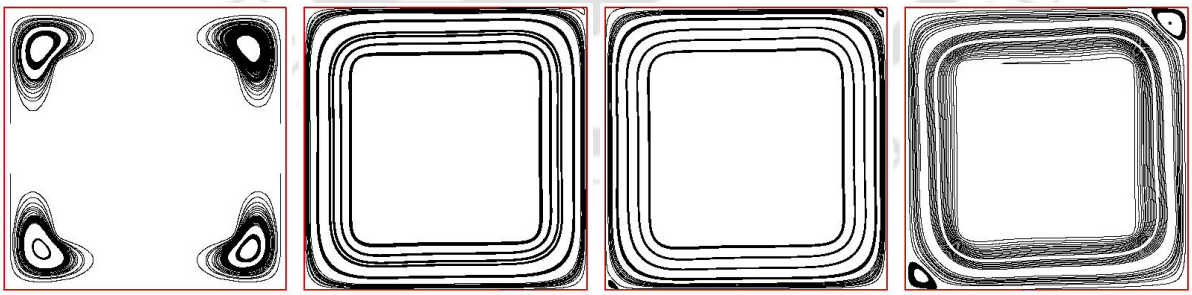

(a) Ra**=10**^{3} **(b)** Ra**=5**$\times$**10**^{4} **(c)** Ra**=10**^{5} **(d)** Ra**=10**^{6}

iv. **Pr=2.3** ($\varphi = 0.01$)

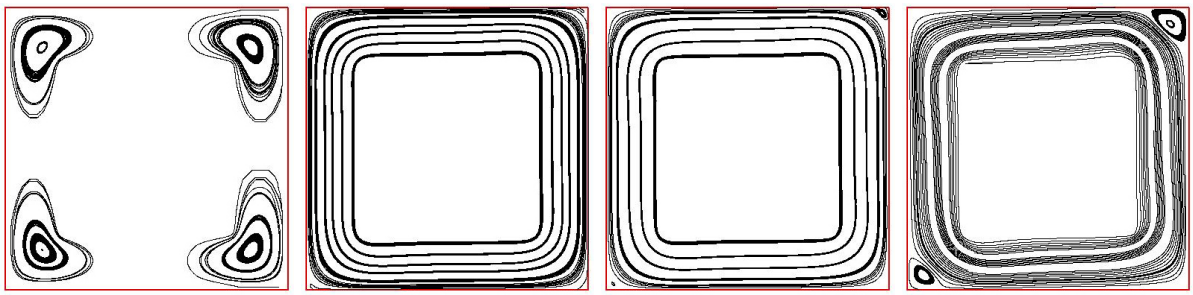

(a) Ra=**10**^{3} **(b)** Ra=**5**$\times$**10**^{4} **(c)** Ra=**10**^{5} **(d)** Ra=**10**^{6}

Figure 5.5: Streamline contours for the study of the effect of volume fraction (φ = 0.0, 0.01, 0.03, and 0.05) of the nanofluid at 4 different Ra.

Pr is the ratio between momentum diffusivity and thermal diffusivity; thus, it only comprises thermophysical properties of a fluid. Grashof's number (Gr) is the ratio between buoyancy force and viscous force; thus, it comprises thermophysical properties and geometric scale. The Ra, which is a function of Pr and Gr is also relevant one and it represents the heat transfer capability in natural circulation.

The streamline contours illustrate that the impact of nanoparticles becomes prominent, particularly at higher buoyancy forces or Rayleigh numbers, where the heat transfer is predominantly convective in nature. This observation holds true across all four cases, indicating the substantial influence of nanoparticles on heat transfer behavior, especially under conditions of elevated buoyancy forces or Rayleigh numbers.This leads to more intense fluid motion and convective heat transfer. At the same time, the presence of nanoparticles in the fluid enhances its thermal conductivity, potentially altering the convective heat transfer characteristics.The conductive mode at Ra= 10^3 is vigilant from the streamline contours for all the case.

It is observed that, the size of secondary vortices increases at higher value of Ra with increase in volume fraction of nanoparticles. This phenomenon stems from the combined effects of heightened thermal conductivity due to nanoparticle introduction, leading to intensified temperature gradients and stronger buoyancy forces reflected by higher Ra values. Moreover, the increment in volume fraction results in the decrement of Pr and hence the momentum diffusivity which hinders the free flow of the working fluid. As a result, the larger secondary vortices improve fluid mixing and heat transfer, showing how nanoparticles affect fluid flow and heat in these systems.

B. **Isotherm contours**

i. **Pr=6.14 (Basefluid,** $\varphi = 0.0$**)**

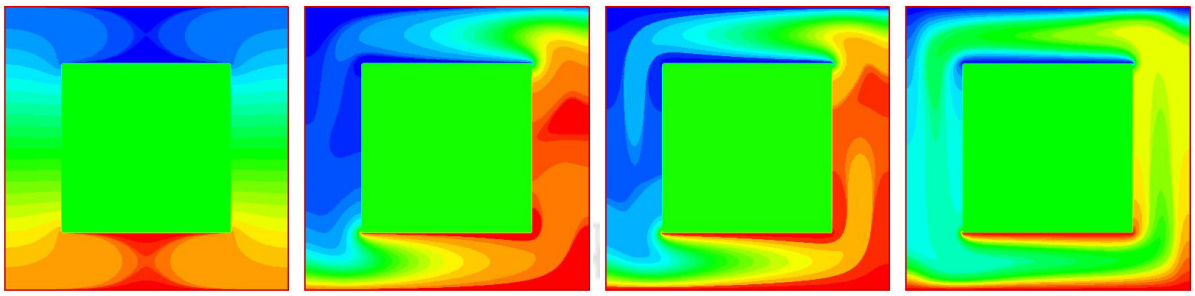

(a) Ra**=10**^{3} **(b)** Ra**=5**$\times$**10**^{4} **(c)** Ra**=10**^{5} **(d)** Ra**=10**^{6}

ii. **Pr=3.35 (**$\varphi = 0.01$**)**

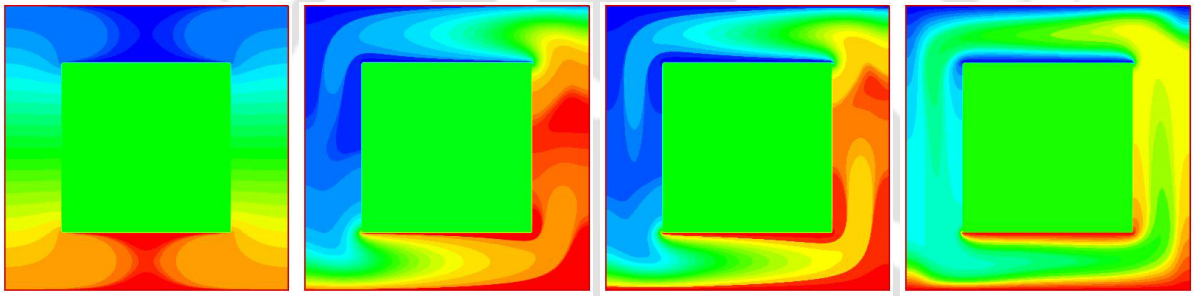

(a) Ra**=10**^{3} **(b)** Ra**=5**$\times$**10**^{4} **(c)** Ra**=10**^{5} **(d)** Ra**=10**^{6}

iii. **Pr=2.75 (**$\varphi = 0.03$**)**

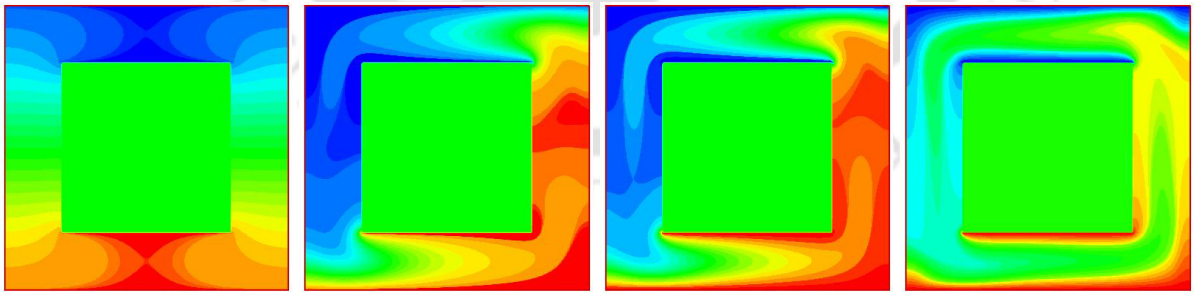

(a) Ra**=10**^{3} **(b)** Ra**=5**$\times$**10**^{4} **(c)** Ra**=10**^{5} **(d)** Ra**=10**^{6}

iv. **Pr=2.3** ($\varphi = 0.01$)

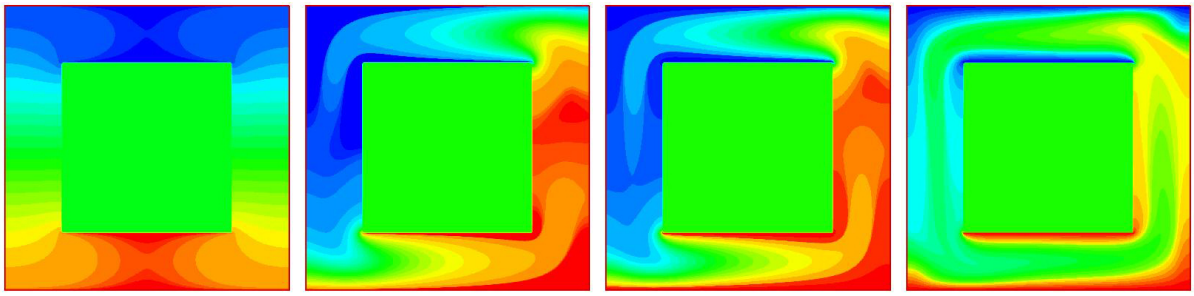

(a) Ra**=10**^{3} **(b)** Ra**=5**$\times$**10**^{4} **(c)** Ra**=10**^{5} **(d)** Ra**=10**^{6}

Figure 5.6: Isotherm contours for the study of effect of volume fraction (φ =0.0,0.01,0.03 and 0.05) of the nanofluid at 4 different Ra (a) Ra=10^3, (b) 5×10^4, (c) Ra=10^5, (d) Ra=10^6

From the isotherm contours it can be derived that, at lower Ra, the heat transfer is mostly due to the conduction mode for all the four cases as confirmed by the horizontal isotherms as shown in the Figure 5.6. These contours indicate minimal fluid movement and temperature gradients across, highlighting the prevalence of conductive heat transfer. However, it is highly convective in nature when the flow occurs at high Ra. This is because, at high Rayleigh numbers the buoyancy forces dominate over the viscous forces, resulting in a highly convective nature of the flow. Convective heat transfer is characterized by the bulk movement of the fluid, where heat is transferred through the motion of fluid particles. In natural circulation loops, higher Ra values indicate stronger buoyancy forces, leading to enhanced convective heat transfer. This means that heat is transferred more efficiently through the movement of the fluid rather than through conduction alone.

Moreover, the improvement in volume fraction of nanoparticles results in overall advancement in heat transfer with the formation of circulating temperature loops. These circulating loops play a vital role in redistributing thermal energy throughout the system. By facilitating the transfer of hot fluid from heat sources to cooler regions and vice versa, circulating temperature loops contribute to improved fluid mixing and heat distribution. This improved fluid circulation ensures a more uniform temperature distribution across the system, consequently enhancing overall heat transfer efficiency. Nanoparticles alter the thermophysical properties of the fluid, such as thermal conductivity, viscosity, and density, thereby influencing fluid dynamics and promoting the formation of circulating temperature loops. The combined effects of buoyancy-driven fluid motion and nanoparticle-induced enhancements in fluid properties result in a more effective and efficient heat transfer process within the fluid system.

The effect of introduction of nanofluids in the base fluid is further discussed below in terms of mass flow rate, Nusselt number, entropy generation and shear stress and is shown in the Figure 5.7 through 5.10.

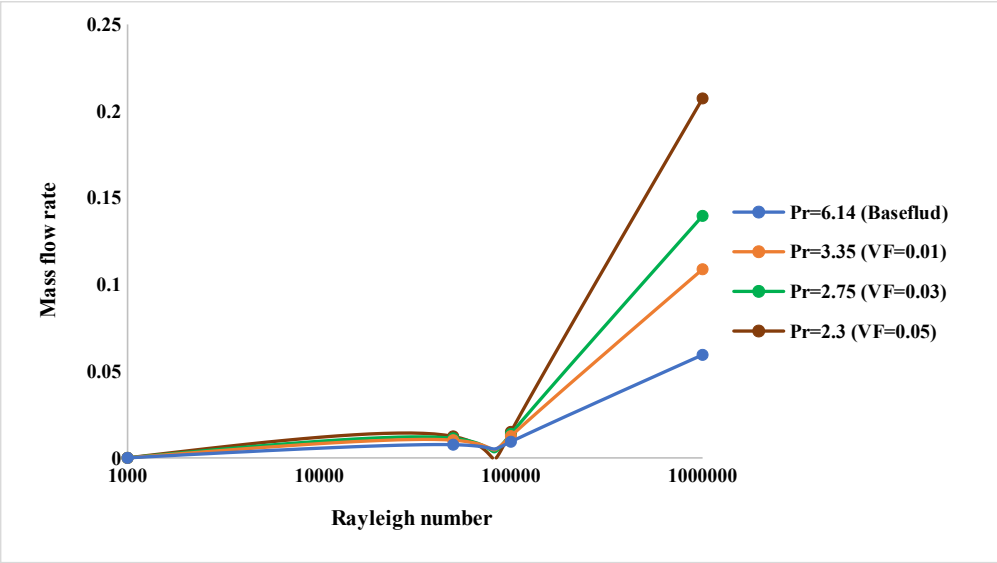

Figure 5.7: Effect of volume fraction on entropy generation.

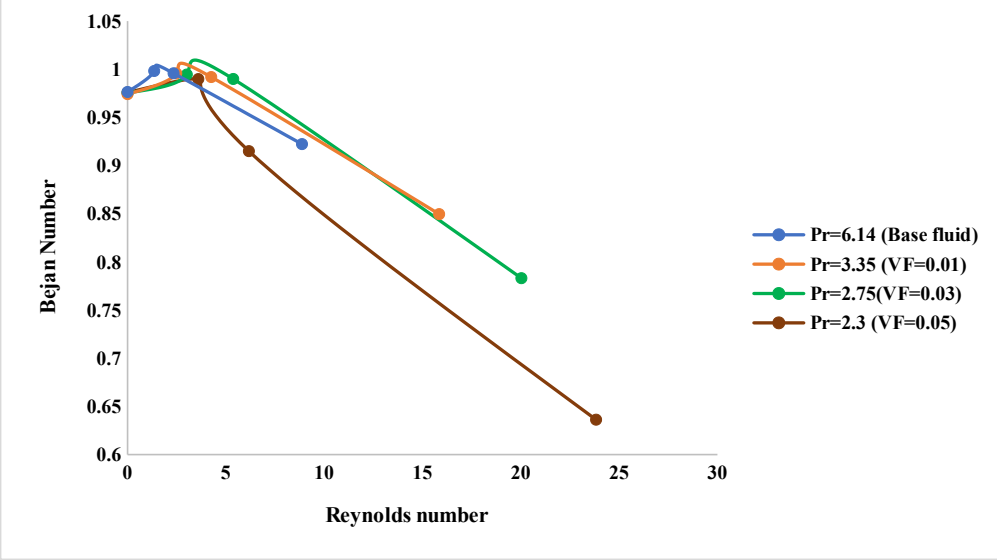

Figure 5.8: Effect of Prandtl number (volume fraction) on Bejan number.

The selection of working fluid aids to the effect on the performance of NCLs. Recently some of works are presented where nanofluids have been used as working fluid in the loop. The prime privilege of nanofluid is its high thermal conductivity than the base fluid. The metallic nanoparticles like aluminum, copper and

silver renders great thermal conductivities [74].

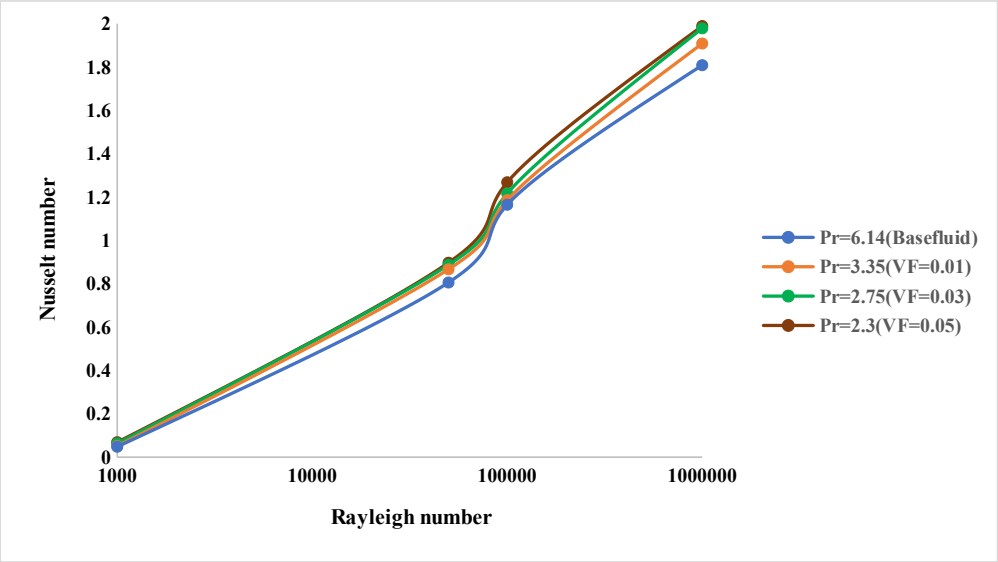

Figure 5.9: Effect of Prandtl number (volume fraction) on heat transfer.

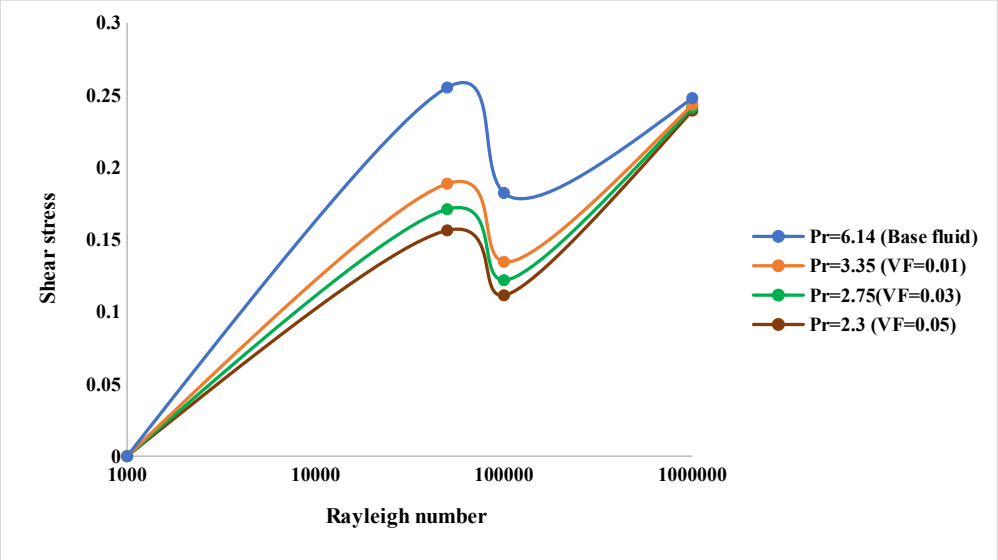

Figure 5.10: Effect of Prandtl number (volume fraction) on shear stress.

Figure 5.7 to 5.10 shows the graphical variations for effect of volume fraction of nanofluid (Pr) on mass flow rate, heat transfer, entropy generation and shear stress. It is well known that, the effective viscosity (μ_{nf}) and effective thermal conductivity (k_{nf}) of the fluid increases with addition of nanoparticles. However, increase in viscosity reduces the convective effect while increment of thermal conductivity enhances the heat transfer which creates a contradictory ambience. Still, fluid momentum which is

produced due to buoyancy force (at high Rayleigh number) aids to overcome the decrement of convection induced by viscosity and we can witness increment of heat transfer and mass flow rate with the added nanoparticles. And the effect is more prominent at high Rayleigh number.

As shown in Figure 5.7, at fixed Ra, the steady-state mass flow rate with lowest Pr (volume fraction=0.05) is highest. If the Ra is increased, the fluid mass flow rate increases due to enhancement of density gradient between hot and cold sections. This is true for both base fluid, water and nanofluids with different concentrations. The trend followed by mass flow rate flows almost a linear curve with Ra; which could be explained with an unwanted increase in shear stress as shown in Figure 5.10.

Entropy generation decreases with addition of nanoparticles. When the volume fraction of nanoparticles is high (lower value of Pr), heat diffuses faster compared to the fluid velocity. As a result, the thermal boundary layer becomes much thicker compared to the velocity boundary layer. This implies that the temperature gradient is more significant and extends over a larger spatial region compared to the velocity gradient. The increment in thermal boundary layer thickness due to the presence of nanoparticles leads to a decrease in entropy generation. Entropy generation is associated with irreversibilities in the system and is influenced by temperature gradients, velocity gradients, and fluid properties. A thicker thermal boundary layer means that the temperature gradient across the boundary layer is more gradual, resulting in reduced temperature differences and subsequently decreased entropy generation. Additionally, the decrease in entropy generation is accompanied by a decrease in shear stress. The shear stress is influenced by the velocity gradients in the fluid, and the presence of nanoparticles can alter the flow characteristics and viscosity, leading to reduced shear stress.

Therefore, we can be conclusive that, the increase in the volume fraction of nanoparticles results in a thicker thermal boundary layer, which reflects in reduced entropy generation and shear stress. This phenomenon can be attributed to the enhanced heat diffusion and altered flow characteristics induced by the nanoparticles in the fluid.

5.4.2 Effect of inclination angle

The simulations are done at various inclination angle (at 0^0, 30^0, 60^0 and 90^0) as stated for Pr=2.3 keeping Ra=10^5. As the current work intends to find the optimize condition for natural circulation loop with minimum entropy generation and high heat transfer capacity. And the fluid with volume fraction of 5% is found to be having minimum entropy generation, hence the rest of the simulations are carried taking

this case into consideration. The angle of inclination (ϕ) is defined by the angle between a left adiabatic wall and the vertical axis in such a way that ϕ = 90° represents the situation of the NCL heated on the left side. The effect is shown below and comparison between all the four cases are depicted in terms of streamlines, isotherms, Nusselt number, entropy generation in Figure 5.11 through 5.17.

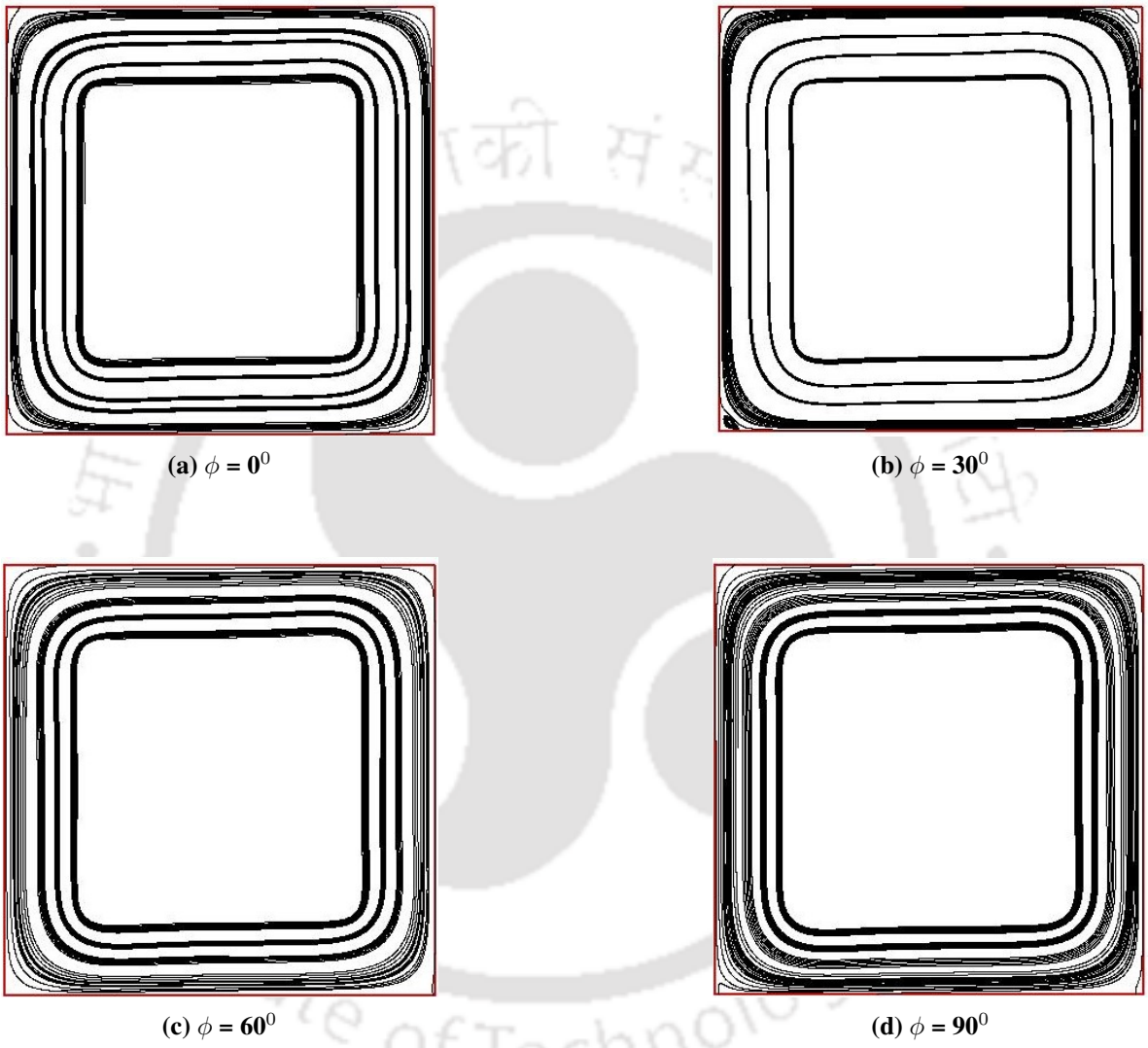

(a) ϕ **= 0**^{0} **(b)** ϕ **= 30**^{0}

(c) ϕ **= 60**^{0} **(d)** ϕ **= 90**^{0}

Figure 5.11: Streamline contours showing the effect of inclination angle (a) $\phi = 0^0$, (b) $\phi = 30^0$, (c) $\phi = 60^0$, and (d) $\phi = 90^0$

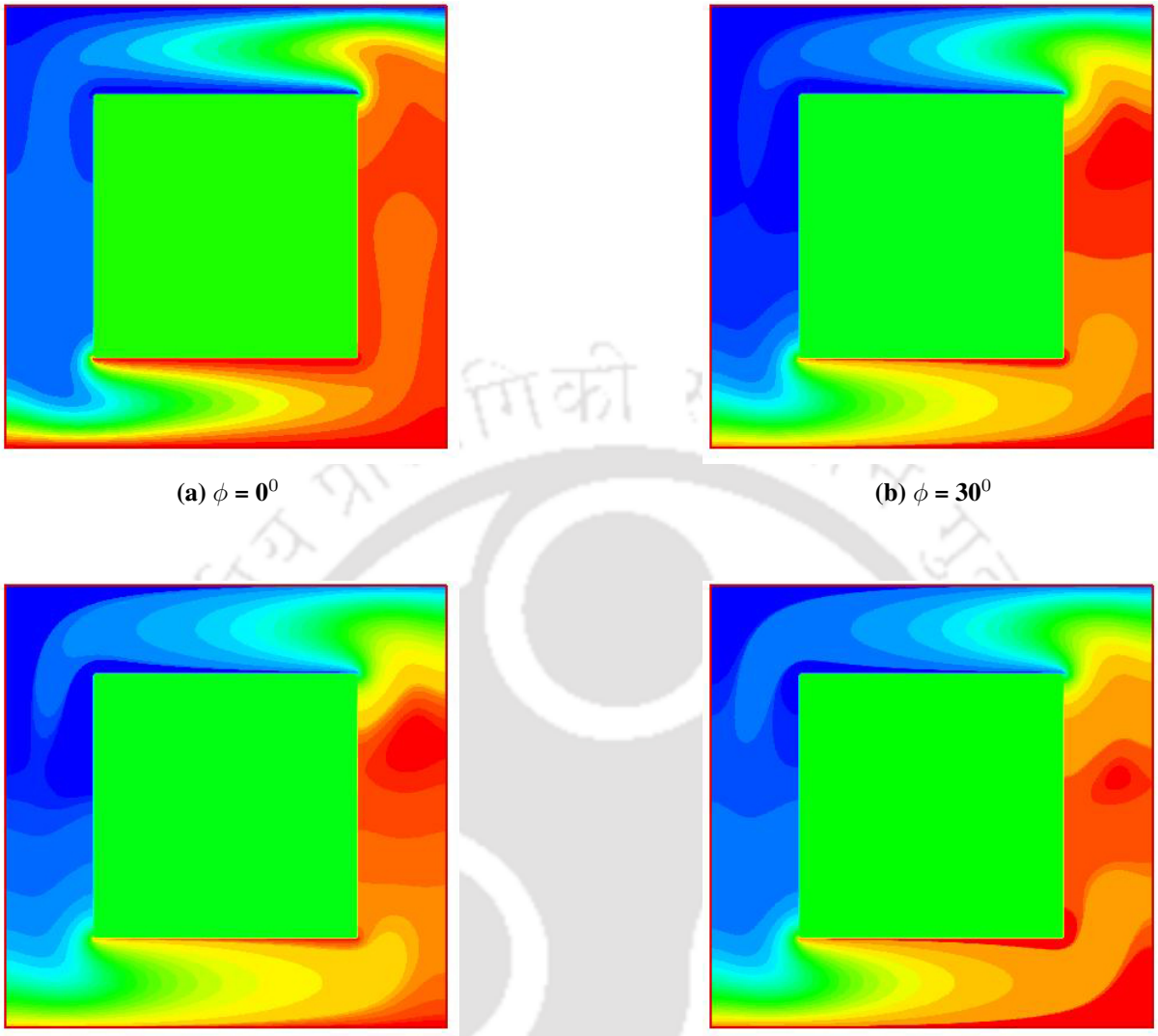

(a) ϕ **= 0**^{0} **(b)** ϕ **= 30**^{0}

(c) ϕ **= 60**^{0} **(d)** ϕ **= 90**^{0}

Figure 5.12: Isotherm contours showing the effect of inclination angle (a) $\phi = 0^0$, (b) $\phi = 30^0$, (c) $\phi = 60^0$ and, (d) $\phi = 90^0$

The study has been carried out for inclination angle ranging from 0° to 90° in the XY plane. It can be observed from the streamline contours that, with increase in tilt angle the gravitational force in the NCL decreases which results in the decrease in driving buoyancy force and the primary fluid flow takes over the secondary vortices which can be seen in lower inclination angle. As the inclination angle of the natural circulation loop increases, the gravitational force acting on the fluid decreases. This reduction in gravitational force is a result of the component of gravity acting against the direction of flow due to the tilt. A decrease in gravitational force impacts the driving buoyancy force in the NCL affecting the overall dynamics of the fluid within the system. With a decrease in the driving buoyancy force, the intensity of

the fluid flow within the system is reduced. The streamline contours show that at lower inclination angles (closer to 0°), secondary vortices are more prominent in the flow pattern. These secondary vortices arise due to the interaction of the fluid flow with the geometry and buoyancy forces. However, as the inclination angle increases, the dominance of the secondary vortices diminishes. The primary fluid flow, driven by the remaining buoyancy forces and the system geometry, becomes more pronounced and takes over the flow pattern.

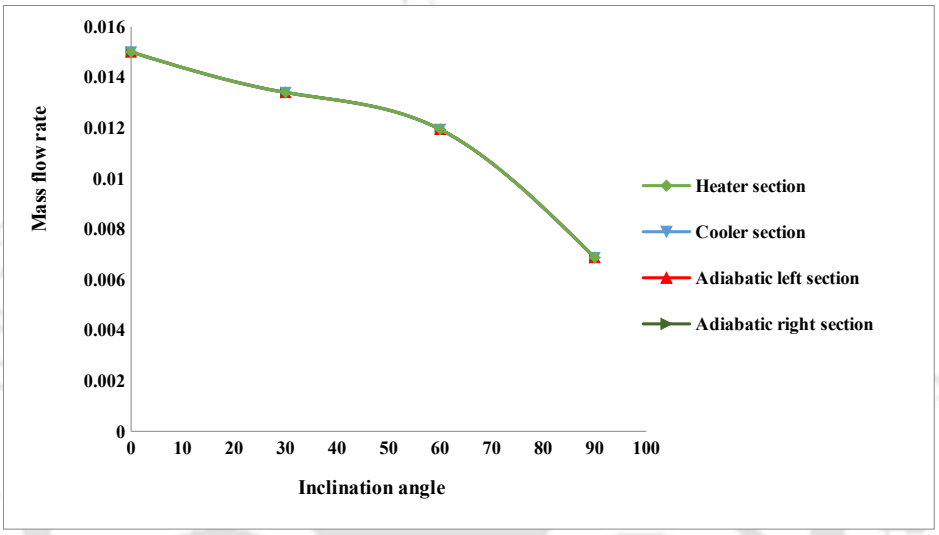

Figure 5.13: Effect of inclination angle on mass flow rate

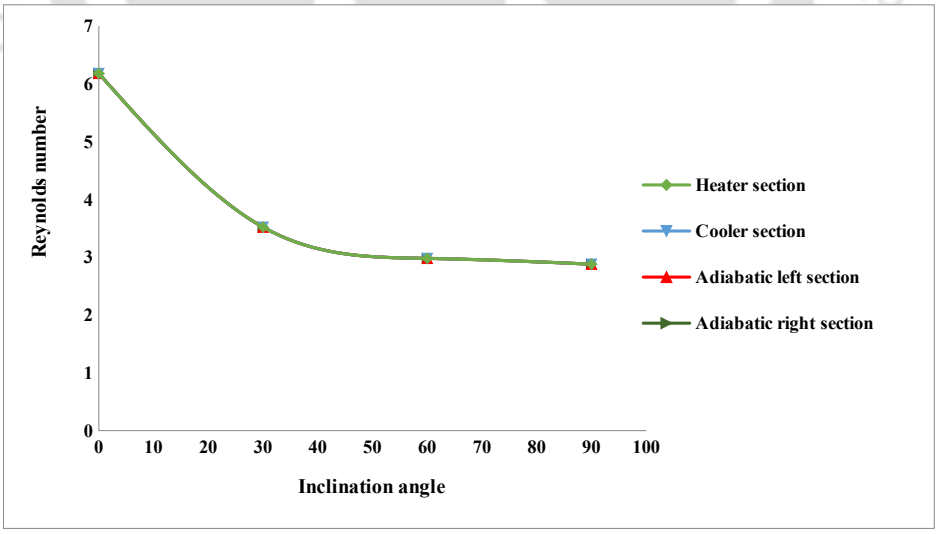

Figure 5.14: Effect of inclination angle on Reynolds number

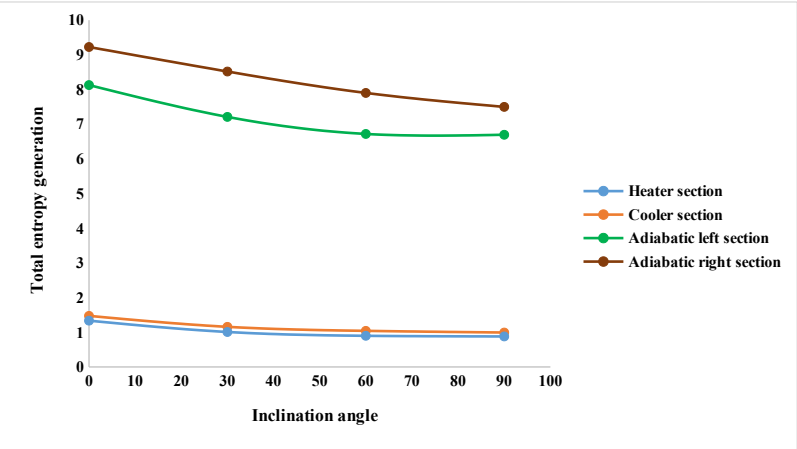

Figure 5.15: Effect of inclination angle on total entropy generation

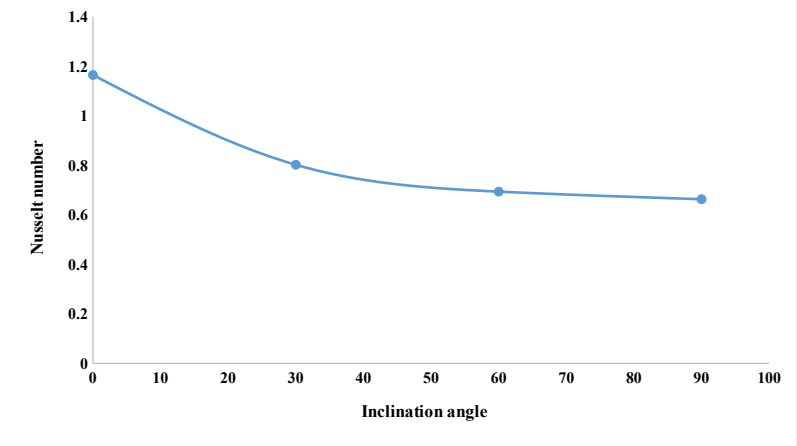

Figure 5.16: Effect of inclination angle on Nusselt number of heater arm

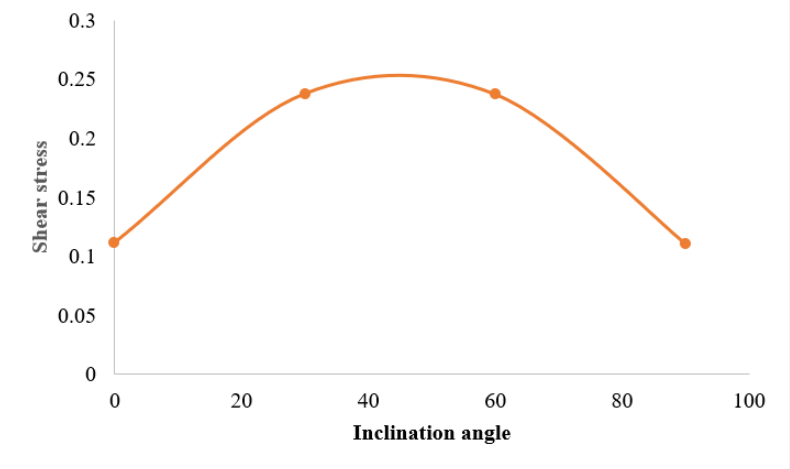

Figure 5.17: Effect of inclination angle on shear stress of heater arm

Based on the observation made by the Figure 5.13 and 5.14, it is noted that the mass flow rate and Reynolds number decrease with an increase in the inclination angle of the natural circulation loop. This decrease can be attributed to two main factors: the decrement of effective loop height and the consequent effects on viscous dissipation rate and the driving buoyancy force. As the inclination angle increases, the effective loop height decreases. The effective loop height refers to the vertical distance between the heat source and heat sink within the natural circulation loop. A reduction in the effective loop height results in a shorter vertical distance for the fluid to circulate, thereby limiting the available space for fluid flow. This leads to a decrease in the mass flow rate. Again, the decrease in the effective loop height affects both the viscous dissipation rate and the driving buoyancy force within the system. Viscous dissipation refers to the conversion of kinetic energy of the fluid into thermal energy due to internal friction. As the effective loop height decreases, the fluid experiences less vertical movement and encounters reduced resistance, resulting in a lower viscous dissipation rate. The combined effect of a lower viscous dissipation rate and reduced driving buoyancy force leads to a decrease in the mass flow rate and, consequently, the Reynolds number.

An important finding of the study is that the total rate of entropy generation decreases as the inclination angle of the natural circulation loop (NCL) increases. This can be attributed to two key factors: the reduction in the effective height differential between the heat source and sink, and the impact of thermal boundary layer thickness on flow restrictions and entropy generation. Further, as mentioned above, when the NCL is tilted, the effective height differential between the source and sink decreases. This reduction in the vertical distance over which the fluid circulates results in a decreased rate of heat transfer (in the heater arm), as depicted in Figure 5.16. Consequently, the overall entropy generation is lowered. Furthermore, Figure 5.15 highlights that the thermal boundary layer thickness in the heater and cooler sections is significantly greater than that of the adiabatic walls. This disparity leads to flow restrictions within the NCL. The thicker thermal boundary layer acts as an insulating layer, impeding heat transfer across the boundary layer and reducing entropy generation. The flow restrictions caused by the thicker thermal boundary layer result in lower flow velocities and decreased shear stress, contributing to a reduction in entropy generation magnitude compared to the adiabatic walls.

According to Figure 5.17, the relationship between shear stress and the inclination angle is depicted. It is evident that as the inclination angle increases, the shear stress initially rises, reaches a maximum, and then declines, eventually attaining a minimum value at an angle of 90°. This behaviour can be attributed to

the varying buoyancy forces within the system. With an increase in the inclination angle, the gravitational force component acting along the direction of flow decreases. Consequently, the driving buoyancy force diminishes. As the driving buoyancy force decreases, the fluid flow experiences less resistance, resulting in an increase in shear stress initially. However, as the inclination angle approaches 90°, the gravitational force acting in the direction of flow becomes negligible. At this point, the driving buoyancy force is minimal, leading to a reduction in shear stress. The minimal buoyancy force at 90° inclination results in lower resistance to flow, causing the shear stress to reach its minimum value.

5.4.3 Effect of aspect ratio

The simulations are done at various aspect ratio (AR=0.5,1,2) as stated for Pr=2.3 (nanofluid with volume fraction of 0.05) keeping Ra=10^5. The aspect ratio of a natural circulation loop typically refers to the ratio of the height to the width (H/W) of the loop. The effect is shown below and comparison between all the three cases are depicted in terms of streamlines, isotherms, Nusselt number, entropy generation in Figure 5.18 through 5.24.

A. Streamlines

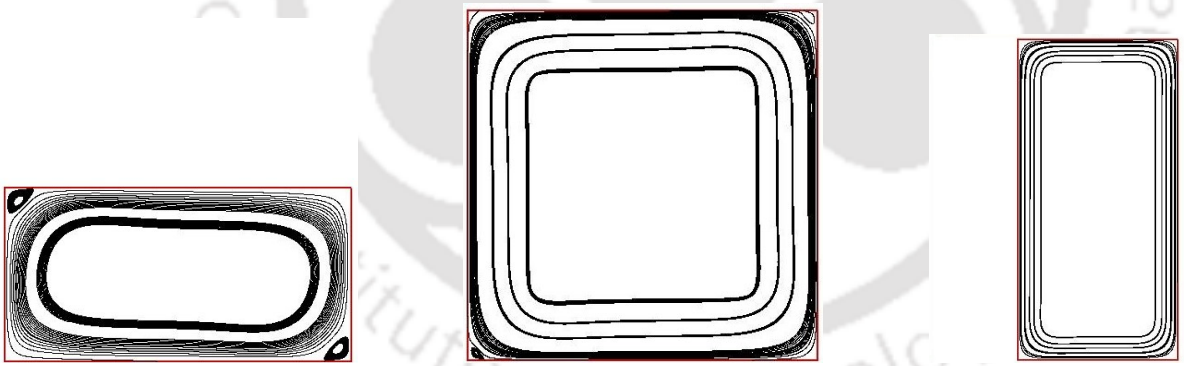

(a) AR=0.5 **(b) AR=1** **(c) AR=2**

Figure 5.18: Streamline contours for the effect of aspect ratio on the natural circulation loop

As the aspect ratio of the natural circulation loop increases, it can be observed from the streamline contours that the secondary vortices merge with the primary flow. This indicates that the secondary flow patterns become less pronounced and are assimilated into the dominant primary flow. The merging of secondary vortices with the primary flow is a consequence of the altered flow dynamics and geometry resulting from the changes in aspect ratio. This can be because of the matter that, a

higher aspect ratio promotes enhanced mixing of the fluid within the loop. The increased space and longer flow path enable better mixing of the fluid, leading to the assimilation of secondary vortices into the primary flow.

B. Isotherms

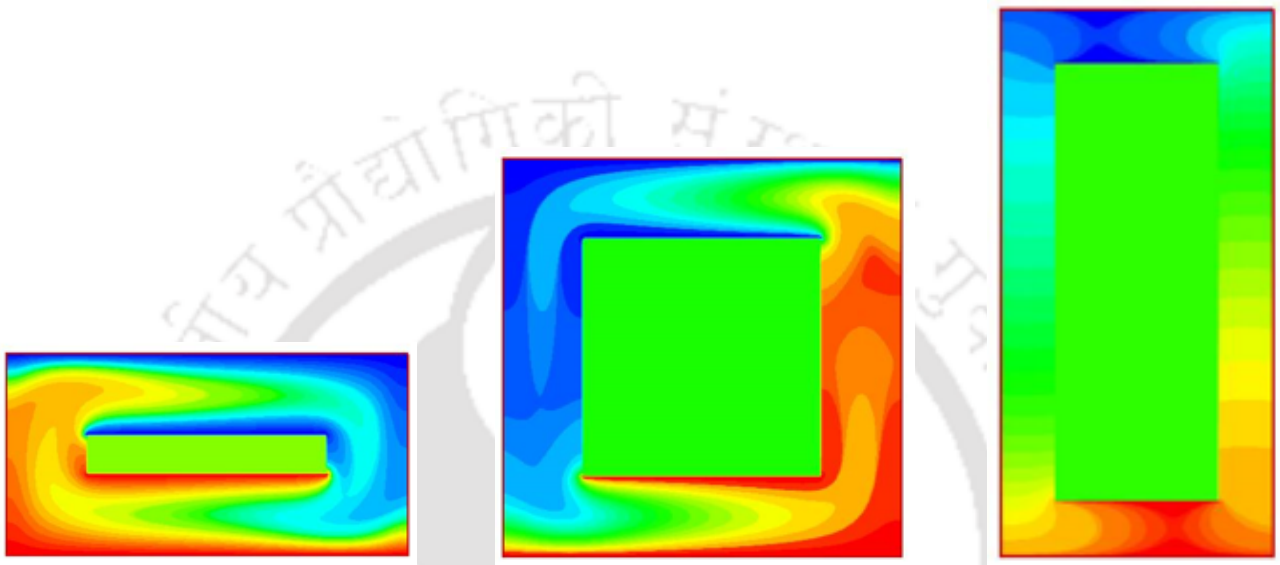

(a) AR=0.5 **(b) AR=1** **(c) AR=2**

Figure 5.19: Isotherm contours for the effect of aspect ratio on the natural circulation loop

At low aspect ratios, the flow and heat transfer in the natural circulation loop predominantly occur in convective mode. However, when the aspect ratio is increased to 2, a significant shift towards conductive heat transfer is observed. This shift is evident from the isotherms, which become nearly parallel to the vertical walls of the loop, indicating the dominance of conduction heat transfer. The reason for this behaviour lies in the variation of aspect ratio. With a lower aspect ratio, the length of the heater and cooler sections is greater in proportion to the overall length of the natural circulation loop. This extended length reduces the influence of buoyancy effects, leading to a diminished convective heat transfer contribution. The findings emphasize the substantial impact of the heater length on the performance of natural circulation loops, even in the context of varying aspect ratios. The length of the heater section plays a crucial role in determining the dominant heat transfer mode, with shorter heaters favouring convective heat transfer and longer heaters promoting conductive heat transfer.

The impact of the aspect ratio of the natural circulation loop (NCL) on various parameters, such

as mass flow rate, Nusselt number, entropy generation, and shear stress, is elaborated below. Detailed graphical representations can be found in Figures 5.20 through 5.24.

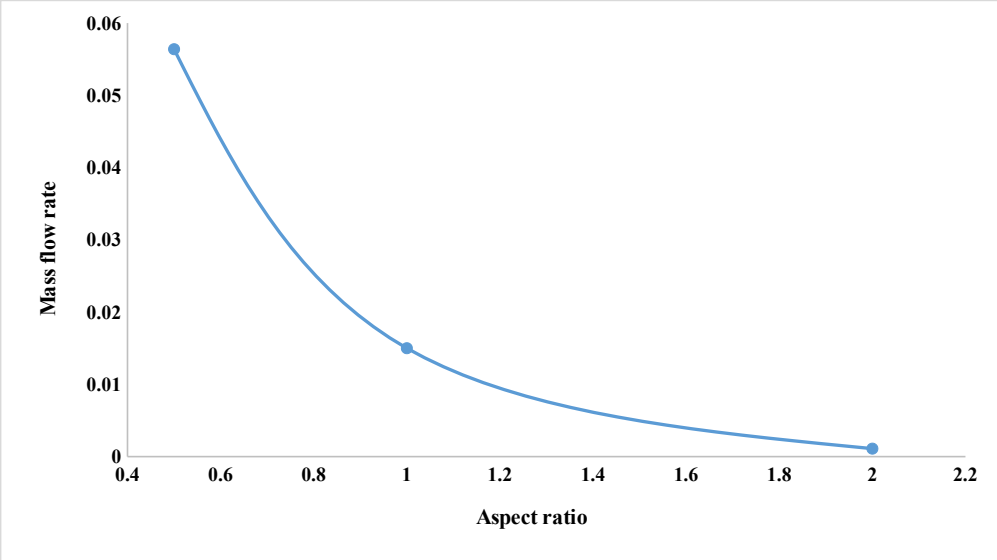

Figure 5.20: Effect of aspect ratio on mass flow rate

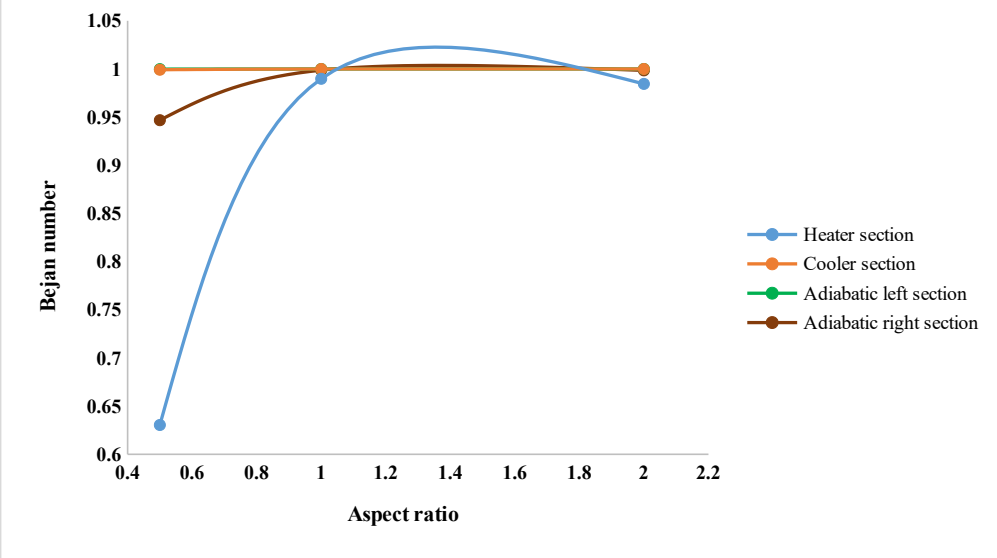

Figure 5.21: Effect of aspect ratio on entropy generation

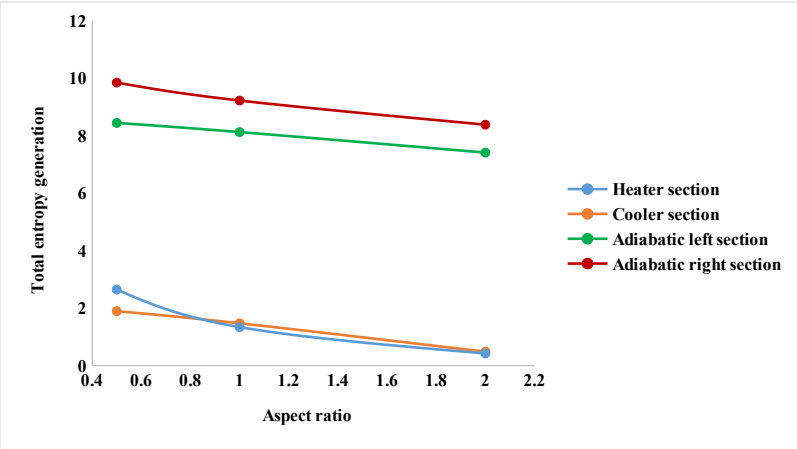

Figure 5.22: Effect of aspect ratio on total entropy generation

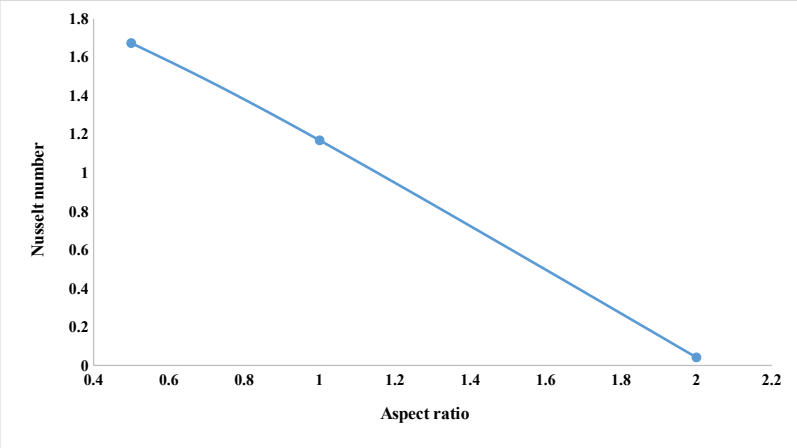

Figure 5.23: Effect of aspect ratio on heat transfer

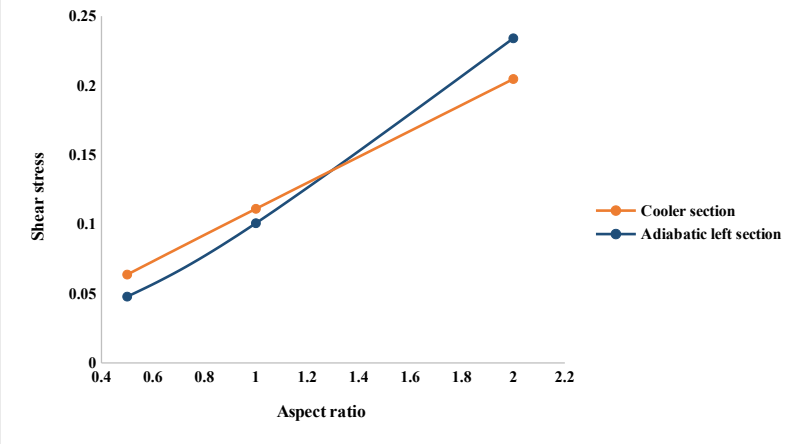

Figure 5.24: Effect of aspect ratio on shear stress

From the plots it can be inferred that, entropy generation for heater and cooler section is lower than the adiabatic walls. This is because in the heater and cooler section, the thermal boundary layer thickness is much higher than the adiabatic walls leading to restriction lower in magnitude as compared to adiabatic walls. Therefore, the observed lower entropy generation in the heater and cooler sections, compared to the adiabatic walls, can be attributed to the significant difference in thermal boundary layer thickness. This finding highlights the influence of thermal boundary layer characteristics on entropy generation and the importance of considering such factors in the analysis of heat transfer and fluid flow within the natural circulation loop.

It is also observed that, AR has a strong influence on entropy generation. When the AR is low, we witness convective heat transfer mode which enhances the boundary effect and so the mass flow rate. However, from the isotherm contours is also evident that increase in AR leads to conduction mode of heat transfer leading to drastic drop of heat transfer and the entropy generation.

Therefore, the observed relationship between aspect ratio, heat transfer mode, and entropy generation highlights the importance of aspect ratio in determining the overall thermal performance and efficiency of the natural circulation loop. The choice of aspect ratio should be carefully considered to optimize heat transfer and minimize entropy generation based on the specific requirements of the system. In the current simulation work, the best suitable aspect ratio is found to be 0.5 amongst the all values (0.5, 1 and 2) with respect to high heat transfer, lower entropy generation and low shear stress.

5.4.4 Effect of diameter of loop

The effect of diameter of natural circulation loop is shown in Table 5.5. The resultant table consists of simulations done for uniform diameter in all the four arms of NCL and non-uniform diameter. Following are the mentioned cases:

Case 1: Uniform diameter of 50 units in all the four arms of NCL.

Case 2: Non uniformity introduced in the cooler section with diameter of 25 units and rest three arms with 50 units.

Case 3: Non uniformity introduced in the heater section with diameter of 25 units and rest three arms with 50 units.

The data are shown in terms of mass flow rate, total entropy (entropy due to heat generation+ entropy generation due to fluid friction), Reynolds number, Nusselt number and shear stress in four

different sections of NCL i.e heater, cooler and two vertical adiabatic arms.

Table 5.5: Data of various parameters simulated for uniform and non-uniform diameter

Heater section	$\dot{m}$	S_T	S_θ	S_ψ	Re	Nu	C_f
Case 1	0.015	1.33954	1.32592	0.013619	6.1719	1.1682	0.11133
Case 2	0.007413	0.9229	0.91521	0.007686	2.99025	0.7346	0.127373
Case 3	0.00483	0.3935	0.38416	0.00933	1.9464	0.2575	0.7822

Cooler section	$\dot{m}$	S_T	S_θ	S_ψ	Re	Nu	C_f
Case 1	0.015	1.47243	1.472373	5.95E-05	6.1719	1.1682	0.111098
Case 2	0.007413	0.73272	0.73266	0.000058	2.99025	0.73278	0.78016
Case 3	0.00483	0.492174	0.49215	0.000024	1.9464	0.2575	0.78488

Adiabatic Left section	$\dot{m}$	S_T	S_θ	S_ψ	Re	Nu
Case 1	0.015	8.128024	8.127969	5.48E-05	6.1719	0.100722
Case 2	0.007413	8.0022	8.00219	0.000022	2.99025	0.10141
Case 3	0.00483	6.9193	6.91936	1.29E-05	1.9464	0.10644

Adiabatic right section	$\dot{m}$	S_T	S_θ	S_ψ	Re	Nu
Case 1	0.015	9.22603	9.21458	0.01145	6.1719	0.10048
Case 2	0.007413	8.08799	8.07749	0.01045	2.99025	0.11093
Case 3	0.00483	7.37852	7.37356	0.00496	1.9464	0.107425

From the data it can be observed that, highest steady mass flow rate is obtained in NCL with uniform diameter and least in NCL with non-uniformity in heater section but is again constant throughout in all the four arms for all three cases.

The observations indicates that the non-uniformity in diameter impacts the buoyancy effect, mass flow rate, heat transfer, and entropy generation within the NCL. The decrease in diameter hampers the buoyancy effect and subsequently affects the mass flow rate and heat transfer. Consequently, the entropy generation,

which is closely related to the heat transfer rate, decreases with the introduction of non-uniformity in diameter. Thus, along with entropy generation, heat transfer rate is also found to minimum in case 3.

Due to decrease in diameter, the steady state Reynolds number also decreases as it is a function of mass flow rate. According to the formal definition of modified Grashof number, it is a function of temperature difference, diameter and height of the loop. This indicates that when the diameter in any section of NCL decreases, it hampers the buoyancy effect resulting in impact on mass flow rate and heat transfer. Also, the entropy generation is directly related to the heat transfer rate and hence with decrease in heat transfer the entropy generation due heat transfer and due to fluid friction and so the total entropy generation decreases with the introduction of non-uniformity in diameter.

Thereby, these findings emphasize the importance of considering the diameter uniformity and its impact on the thermal-hydraulic performance and entropy generation in natural circulation loops. It highlights the interplay between diameter variations, heat transfer, and entropy generation, and the need for careful optimization of system design to achieve desired performance outcomes.

5.4.5 Effect of Non-Boussinesq approximation:

Till now the results are discussed based on the simulations with Boussinesq approximation. However, as research witnessed greater deviations in results when they are obtained with high power loops. Hence, the present motivation of this section is to realize certain deflections at high valued inputs. In the present simulation a comparative result Table (Table 5.6 through 5.8) is shown which depicts a clear distraction of values when the simulations are performed with low and high Rayleigh number of Ra=10^4, Ra=10^5 and 10^6 with the input parameter of Pr=2.3 (volume fraction 5%). The formulation for simulating the natural circulation loop using lattice Boltzmann method with non-Boussinesq approximation is derived with reference to existing work [69] as discussed in subsection 5.2.1.

Table 5.6: Data of various parameters simulated under non-Boussinesq approximation at Ra=10^4

Heater section	$\dot{m}$	S_T	S_θ	S_ψ	Re	Nu	C_f
Non-Boussinesq	0.0124	1.015666	1.00785	0.0078096	3.61	0.8066	0.1563
Boussinesq	0.0124	1.101462	1.00785	0.006792	3.6	0.8971	0.1553

Cooler section	$\dot{m}$	S_T	S_θ	S_ψ	Re	Nu	C_f
Non-Boussinesq	0.0124	1.140086	1.14005	0.0000383	3.61	0.8071	0.15583
Boussinesq	0.0124	1.14008	1.14005	0.0000383	3.6	0.8071	0.1553

Table 5.7: Data of various parameters simulated under non-Boussinesq approximation at Ra=10^5

Heater section	$\dot{m}$	S_T	S_θ	S_ψ	Re	Nu	C_f
Non-Boussinesq	0.015	1.33954	1.32592	0.013619	6.1892	1.1646	-0.11133
Boussinesq	0.015	1.3345	1.3256	0.013618	6.18	1.1646	-0.112

Cooler section	$\dot{m}$	S_T	S_θ	S_ψ	Re	Nu	C_f
Non-Boussinesq	0.015	1.47243	1.4724	0.000057	6.1892	1.1652	0.111098
Boussinesq	0.015	1.47226	1.4722	0.000055	6.18	1.1611	0.111098

Table 5.8: Data of various parameters simulated under non-Boussinesq approximation at Ra=10^6

Heater section	$\dot{m}$	S_T	S_θ	S_ψ	Re	Nu	C_f
Non-Boussinesq	0.2073	2.84054	1.84918	1.033143	23.83	1.989	0.2392
Boussinesq	0.059559	2.107887	1.807398	0.2587	22.93	1.756	0.104491

Cooler section	$\dot{m}$	S_T	S_θ	S_ψ	Re	Nu	C_f
Non-Boussinesq	0.2073	2.149363	2.14473	0.004634	23.83	1.7145	0.224154
Boussinesq	0.059559	2.054679	2.053823	0.000856	22.93	1.7106	0.103066

As it can be observed from the table the non-Boussinesq approximation outperforms with the values obtained for various parameters viz: mass flow rate, entropy generation, heat transfer rate when the simulations are performed for high Ra (such as 10^6). Very insignificant variations in values can be seen for low Ra (such as 10^4, 10^5). The Boussinesq approximation is commonly used to simplify the treatment of temperature-dependent density variations in fluid dynamics simulations. While it works reasonably well for low Rayleigh numbers and small temperature differences making Ra= 10^5) a crtical value in the current study. It becomes less accurate at higher Rayleigh numbers where significant temperature gradients and density variations exist.

The non-Boussinesq approximation produces higher mass flow rates compared to the Boussinesq approximation under the influence of high Ra. The error percentage is found to be 2.48%. This suggests that the non-Boussinesq approximation better captures the fluid behavior and its impact on the mass flow rate within the NCL.

The non-Boussinesq approximation yields higher heat transfer rates compared to the Boussinesq approximation. This indicates that the non-Boussinesq model better accounts for the heat transfer mechanisms and accurately predicts the heat transfer performance of the NCL. As reported in Table 5.8, the error percentage is found to be 13.27%. Also, approximately 3% of difference is reported for entropy generation due to fluid friction (S_Ψ) as compared to entropy generation due to heat transfer (S_θ) which is very mild with 0.23%, indicating that both approaches yield similar results for this specific parameter.

5.5 Summary

The current study is based on numerical simulation of natural circulation loop using LBM determining the influence on introduction of nanofluid as a working medium on it. Parametric study is made for this work and results are depicted in terms of streamlines, isotherms, entropy generation, heat transfer. The focus is kept to get an optimized model of natural circulation loop having minimum entropy generation.

The salient features of the numerical study are as follows:

- The generated entropy strongly depends upon the volume fraction. The total rate of entropy generation is found to be decreased with increase in inclination angle. This is because with tilting the NCL, the effective height differential between the source and sink gets reduced resulting in decreased rate of heat transfer.

- When the AR is low, we witness convective heat transfer mode which enhances the boundary effect and so the mass flow rate.

- The entropy generation (total $\boldsymbol{S_T}$, due to heat transfer $\boldsymbol{S_\theta}$, due to fluid friction $\boldsymbol{S_\Psi}$) is found to be minimum with non-uniform diameter NCL in heater section.

- Significant variation in values of parameters under non-Boussinesq approximation viz. mass flow rate, heat transfer, entropy generation is observed in case of high Ra=10^6 is obtained as compared to the results under Boussinesq approximation. Thus, the non-Boussinesq approximation is favored for simulations involving high Rayleigh numbers due to its improved accuracy in capturing the effects of temperature-dependent density variations on fluid flow and heat transfer. However, for low Rayleigh numbers, the choice between the two approximations may have a minimal impact on the simulation results identifying Ra=10^5 as a critical value beyond which the Boussinesq approximation becomes inadequate for accurate calculations.

- The comparison of Boussinesq and non-Boussinesq approach shows an approximate difference in entropy generation due to fluid friction (S_Ψ) of 3%, and minimal difference of 0.23% is reported for S_θ. This close similarity in results indicates that both the Boussinesq and non-Boussinesq approaches provide nearly the same outcomes for this specific parameter.

भारतीय प्रौद्योगिकी संस्थान गुवाहाटी
Indian Institute of Technology Guwahati

Chapter 6

Effect of thermal boundary conditions on a natural circulation loop

6.1 Introduction

Single-phase Natural Circulation Loops (SPNCLs) are passive devices that efficiently recover and transfer heat in diverse applications, including electronics, solar, geothermal, nuclear reactors, and secondary refrigeration systems. The preference for SPNCLs stems from their simplicity and reliance on natural convection, eliminating the need for mechanical pumps or external power sources. SPNCLs excel in removing excess heat from sources and transferring it to heat sinks or storage mediums in electronics and solar systems. In geothermal and nuclear reactors, SPNCLs play a crucial role in extracting and transferring heat for electricity generation or space heating.

In addition to that, the thermal boundary condition has a significant influence on the performance and behavior of a natural circulation loop (NCL). It is important to carefully design and control the thermal boundary condition to optimize the performance of the NCL. By adjusting parameters such as heat source and heat sink temperatures, insulation, and heat transfer surface area, it is possible to achieve the desired heat transfer rates, fluid velocities, and system stability within the NCL. Also, in practical fields, such as industrial processes or power generation, the heat load can fluctuate due to changing operational conditions. By incorporating a variable temperature boundary condition, the NCL can dynamically adjust to these variations, maintaining stable and efficient heat transfer. This improves the overall thermal performance of the NCL and enables it to handle diverse operating scenarios effectively.

Previous studies on NCLs have witnessed predominant reliability in traditional numerical methods such as the finite volume method. To the best of the authors' knowledge, there is a lack of previous research investigating the impact of different thermal boundary conditions on heat transfer and entropy generation in Natural Circulation Loops (NCLs) using the lattice Boltzmann method (LBM). Therefore, this study aims to fill this research gap by examining these factors and their influence on flow characteristics and thermal efficiency. Thus, in the present work, numerical modeling for the natural circulation loop is done using the lattice Boltzmann method due to its simplicity with a comparative assessment of various thermal boundary conditions.

6.2 Mathematical modeling of the problem

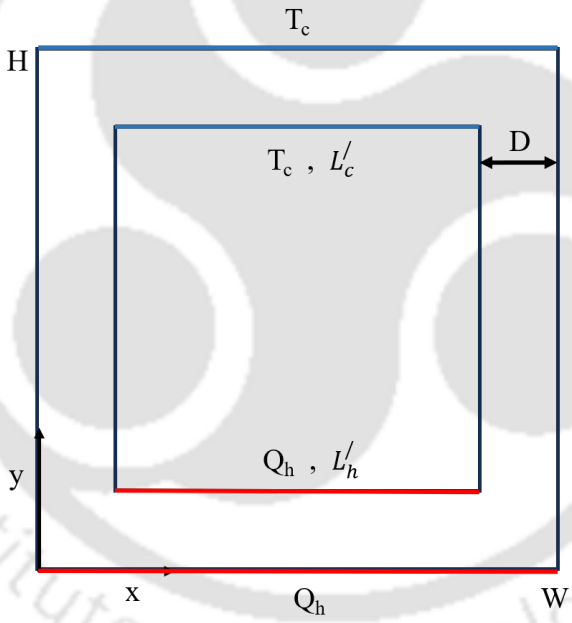

Figure 6.1: Schematic diagram for the computational domain of the natural circulation loop

Figure 6.1 illustrates the flow configuration of the natural circulation loop (NCL) used in the current study, along with its boundary conditions. The NCL consists of two horizontally positioned arms opposite each other, with a heater and a cooler located on these arms. The remaining sections of the loop are well-insulated to minimize heat loss. The dimensions of the NCL are specified as follows: a uniform diameter (D) of 50 mm, a height (H) of 1 m, and a width (W) of 1 m. The heater has an inner length ($L_h^{/}$) of 0.8 m, while the cooler measures an inner length ($L_c^{/}$) of 0.8 m. To analyze the system, dimensionless groups

based on the conservation equations are calculated.

In the present work, the numerical modeling is performed using the lattice Boltzmann method employing the Boussinesq approximation. Thus, as discussed in section 2.3, Guo's model [61] among the 3 force models is considered to calculate the external force F which is defined as the external force per unit volume due to the presence of buoyancy force and is given by:

$$F_i = \rho g \beta (\theta - \theta_m) e_g \tag{6.1}$$

With the above considerations, the density and temperature distribution functions i.e. the f and g are calculated by solving the lattice Boltzmann equation (LBE). After introducing the external force, the general form of lattice Boltzmann equation for the flow field can be written as:

$$f_i(\mathbf{x} + \mathbf{e_i}\Delta t, t + \Delta t) = f_i(\mathbf{x}, t) + \frac{\Delta t}{\tau_v}[f_i^{eq}(\mathbf{x}, t) - f_i(\mathbf{x}, t)] + (\Delta t \times \mathbf{e_i} \times F_i) \tag{6.2}$$

And for the temperature field,

$$g_i(\mathbf{x} + \mathbf{e_i}\Delta t, t + \Delta t) = g_i(\mathbf{x}, t) + \frac{\Delta t}{\tau_g}[g_i^{eq}(\mathbf{x}, t) - g_i(\mathbf{x}, t)] \tag{6.3}$$

Corresponding to the above LBE, respective equilibrium functions for momentum and energy equation are:

$$f^{eq}(\mathbf{x}, t) = w_i \cdot \rho(\mathbf{x}, t) \left[1 + \frac{1}{2}\frac{(\mathbf{e} \cdot \mathbf{u})}{c_s^2} + \frac{3}{2}\frac{(\mathbf{e} \cdot \mathbf{u})^2}{c_s^2} - \frac{1}{2}\frac{(\mathbf{u} \cdot \mathbf{u})}{c_s^2}\right] \tag{6.4}$$

$$g^{eq}(\mathbf{x}, t) = w_i \cdot \theta(\mathbf{x}, t) \left[1 + \frac{(\mathbf{e} \cdot \mathbf{u})}{c_s^2}\right] \tag{6.5}$$

The boundary conditions as illustrated in Figure 6.1 are applied in the following forms:

U=V=0, at x=0, L, $0 \leq y \leq H$, U=V=0, at y=0, H, $0 \leq x \leq L$

$\frac{\partial \theta}{\partial Y} = 0 \;\; at \; X = 1, 0 \leq Y \leq 1$, left adiabatic arm

$\frac{\partial \theta}{\partial Y} = 0 \;\; at \; X = 0, 0 \leq Y \leq 1$, right adiabatic arm

$\theta = T_h / Q_h \quad at \; Y = 0, 0 \leq X \leq 1$, heated bottom arm

$\theta = 0 \quad at \; Y = 1, 0 \leq X \leq 1$, cold top arm

Finally, macroscopic variable for the considered D2Q9 lattice model can be calculated in terms of above variables with the following formulations:

$$\rho = \sum_{i=0}^{8} f_i \tag{6.6}$$

$$\rho u = \sum_{i=0}^{8} f_i \mathbf{e}_i \tag{6.7}$$

$$\theta = \sum_{i=0}^{8} g_i \tag{6.8}$$

6.2.1 Non-dimensional parameters

To identify the appropriate dimensionless parameters for description of natural circulation, following dimensionless variables can be defined:

$$x^* = \frac{x}{L}, \quad y^* = \frac{y}{H}, \quad u^* = \frac{u}{u_0}, \quad v^* = \frac{v}{u_0}, \quad \theta = \frac{T - T_c}{T_h - T_c} \tag{6.9}$$

where, u_0 is a reference velocity that is unknown. The reference velocity can be chosen as:

$$u_0 = \sqrt{g\beta\left(T - T_\infty\right) L}$$

Thereby, $Re = \frac{u_0 L}{\nu} = \frac{\sqrt{g\beta(T-T_\infty)L^3}}{\nu}$. Pr is Prandtl number which reflects the ratio between the momentum and thermal diffusion. Also, another dimensionless number called Grashoff number, Gr holds importance in natural convection which represents the ratio of buoyancy force and the viscosity force acting on the fluid and is given by:

$$Gr = \frac{g\beta(T - T_\infty)L^3}{\nu^2} \tag{6.10}$$

6.2.2 Basic algorithm

The basic algorithm for time-dependent response of the natural circulation loop is depicted in the below Figure 6.2.

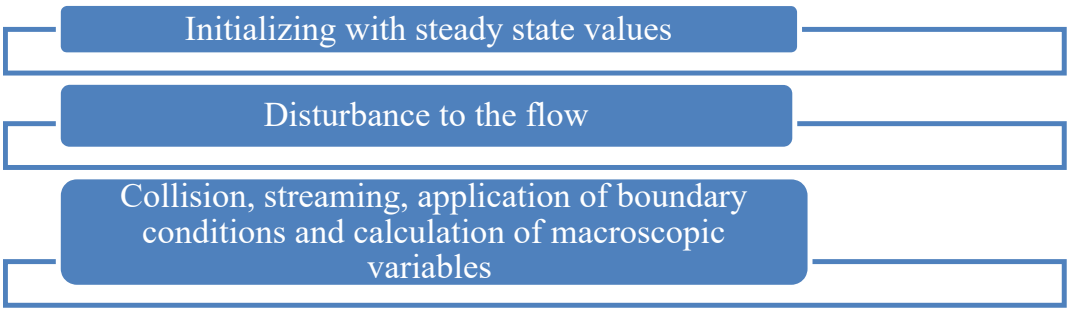

Figure 6.2: Algorithm followed for the code development

In the current study the simulations are performed for the natural circulation loop with two different thermal boundary conditions in order to understand the impact of it on the stability analysis. Following are the cases:

(i) Constant temperature boundary condition;

(ii) Constant and variable heat flux boundary condition.

6.3 Code validation and grid independence test

To ensure the accuracy and reliability of the computational model developed for this study, it is crucial to validate the code by comparing its results with relevant literature. In this case, the simulations are conducted using water as the working fluid (single-phase liquid) throughout the natural circulation loop. To validate the computational code, the results obtained from the simulations are compared with established findings from Desrayaud et al. [72]. This previous study serves as a benchmark for comparison, allowing for an assessment of the accuracy and consistency of the developed computational model.

The simulation is performed taking input parameters as Pr=5.5 and aspect ratio (AR) as AR=1.0. The parameters that appear in the equations are the Rayleigh number, Ra, defined referring to the width of the loop the Rayleigh number,Ra_{2D}, based on the hydraulic diameter D_h=2D, and the Prandtl number, Pr, which are expressed as:

$$Ra = \frac{g\beta\Delta TW^3}{\vartheta\alpha} = \frac{Ra_{2D}}{(2d)^3}, \quad Pr = \frac{\vartheta}{\alpha} \tag{6.11}$$

where, d is dimensionless channel gap width, $d = D/W$ and l is the dimensionless loop length, L/W

Reynolds number correlation

In particular, Vijayan et al.[73] have demonstrated that the stationary mass flow rate for various uniform diameter loops can be defined as a function of the non dimensional group ($Gr_m(D_h/L)$), with Gr_m being the modified Grashof number, and L, the total length of the loop. This non-dimensional group is defined for a plane wall channel by:

$$(Gr_m(D_h/L)) = \frac{Ra_{2D} \times 4 \times (1-d) \times (AR-d)}{Pr^2 \times d \times l} \tag{6.12}$$

Where, d is dimensionless channel gap width, $d = D/W$ and l is the dimensionless loop length, L/W
The correlation proposed by Vijayan [73] can thus be expressed as reported in Desrayaud et al. [71].

$$Re_{2D} = 0.144(Gr_m(D_h/L))^{0.5} = 0.144(\frac{Ra_{2D} \times 4 \times (1-d) \times (AR-d)}{Pr^2 \times d \times l})^{0.5} \tag{6.13}$$

Using the above relation, the Reynolds number obtained by present simulation for two cases and is then compared with the Reynolds number obtained by correlation given by established results [72]. The following are the cases:

(i) Case-1 : Heater with constant temperature

(ii) Case-2 : Heater with heat flux

The validation of the code with constant temperature boundary condition of the heater is reported in Table 5.3.
The validation of the code with constant heat flux boundary condition of the heater is reported in Figure 6.3.

Grid Independence test

(i) The grid independency for the natural circulation loop simulation for constant temperature as discussed in Chapter 5 is checked using 3 numbers of grid sizes and the value $\overline{Nu}Ra^{1/4}$is calculated at Pr=5.5 and Ra=10^6. The result is tabulated in Table 5.4.

Taking the outcomes of grid indenpendency test into consideration, grid size 250×250 shall be used for further simulations.

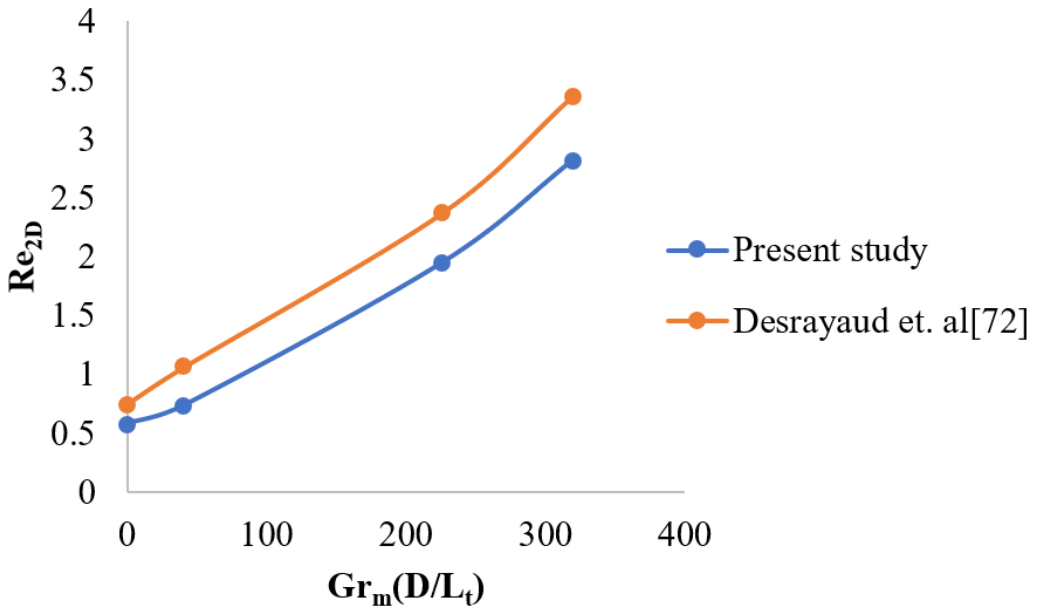

Figure 6.3: Comparison of results (Present study vs Desrayaud et al. [72]) showing Re_{2D} vs $Gr_m(D/L_t)$ for validation of single phase (water) natural circulation loop under constant heat flux boundary condition

(ii) The grid independency for the natural circulation loop simulation for constant heat flux is checked using 4 numbers of grid sizes and the value $\overline{Nu}$ is calculated at Pr=5.5 and Ra=10^5. The result is tabulated in Table 6.1.

Table 6.1: Grid independence test for constant heat flux boundary condition

S.no	Grid size	$\overline{Nu}$
1	150×150	0.8923
2	200×200	1.1154
3	300×300	1.3462
4	350×350	1.3532

Taking the outcomes of Table 6.1 into consideration, grid size 300×300 shall be used for further simulations.

6.4 Results and discussion

With the above discussed algorithm, the simulations are performed with the following variations in input parameters with both constant temperature and constant heat flux boundary conditions.

(i) Rayleigh number: 10^3, 10^4, 10^5, 10^6.

(ii) Prandtl number: 6.14 (base fluid), 3.35 (φ =0.01), 2.75 (φ=0.03), 2.3 (φ=0.05).

(iii) Inclination angle: 0°, 30°,60°,90°.

(iv) Thermal boundary conditions.

The purpose of these simulations is likely to study the behavior of a fluid system under different conditions and analyse the effects of varying Rayleigh numbers, Prandtl numbers, and inclination angles on the system's heat transfer and fluid flow characteristics.

6.4.1 Effect of Rayleigh number

The effect of Rayleigh number at different input values viz Ra=10^3, 10^4, 10^5, 10^6 at constant Pr of 6.14 are numerically studied and are depicted in the forms of streamlines and isotherms in Figure 6.4 and 6.5 with two different temperature boundary conditions.

(i) Constant temperature boundary condition (CT).

(ii) Constant heat flux boundary condition (CHF).

(a) **Streamline and isotherm contours**

The aim of the current study is to show the influence of the temperature boundary conditions on the dynamical behaviour of the loop.At lower Rayleigh numbers (Ra), where the heat transfer is primarily governed by conduction, the fluid near the heated surface gains heat through direct contact (conduction) and transfers it to adjacent fluid layers through molecular interactions. This results in relatively stagnant fluid behavior, with heat transfer occurring mainly through molecular motion. However, as the Rayleigh number increases, indicating a transition to more convective heat transfer, fluid motion becomes more vigorous due to buoyancy forces induced by the temperature gradient.

This convective motion leads to the formation of circulating flow patterns, as evidenced by the streamline contours, facilitating more efficient heat transfer throughout the system. The vector plot is shown in Figure 6.4 (c) illustrating the flow field represented by arrows (vectors).

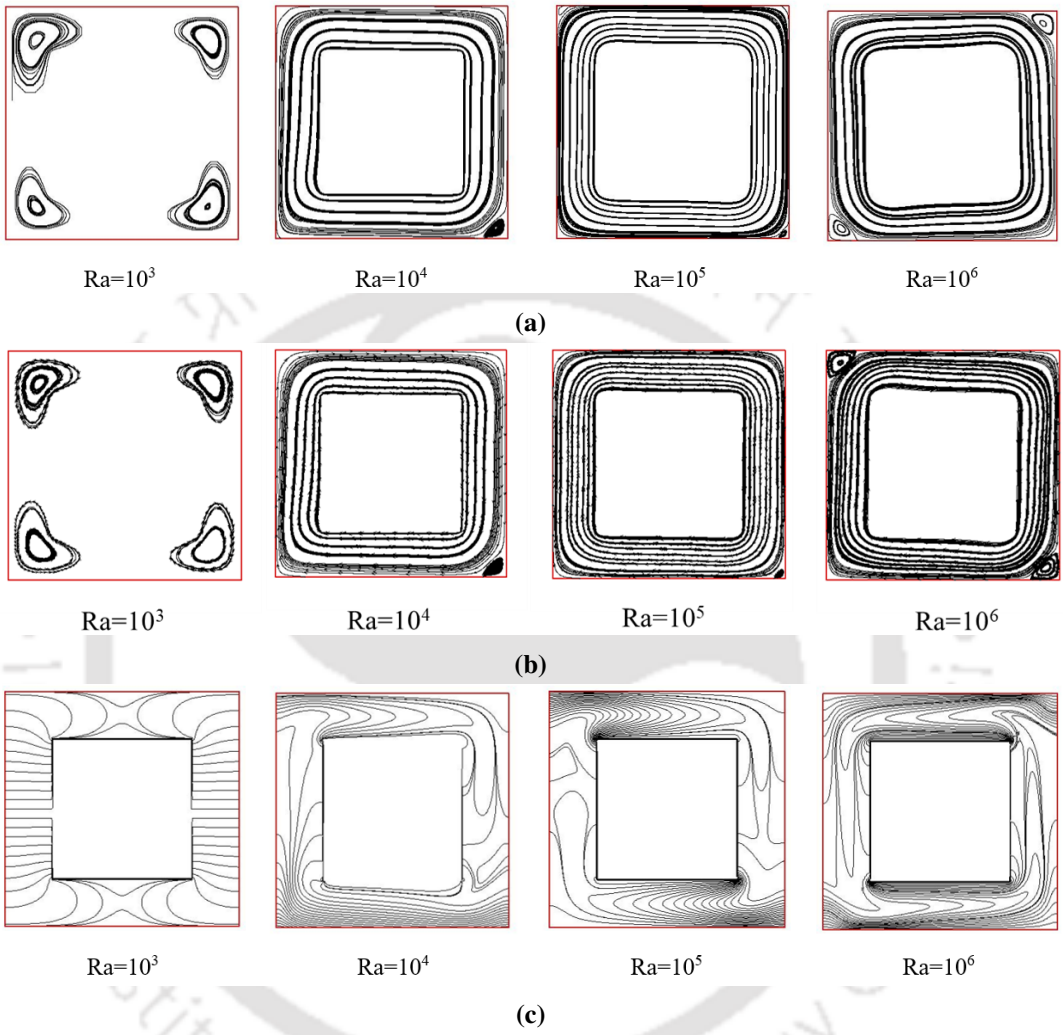

Figure 6.4: Streamlines and isotherms at various Rayleigh numbers for constant temperature boundary condition

Additionally, the alteration of boundary conditions from constant temperature to constant heat flux further enhances convective heat transfer, promoting fluid motion and disrupting the thermal boundary layer near the heated surfaces. This disruption encourages better mixing of fluid layers, resulting in higher heat transfer rates compared to constant temperature boundary conditions. The observation of recirculatory cells at higher Ra values indicates the presence of complex flow structures, with larger vortices near the heater and weaker ones near the cooler, suggesting the influence of buoyancy-driven convection on the flow behavior within the system. Overall, the

observed phenomena underscore the intricate interplay between fluid motion and heat transfer dynamics in buoyancy-driven flow systems, highlighting the importance of boundary conditions in modulating system performance.

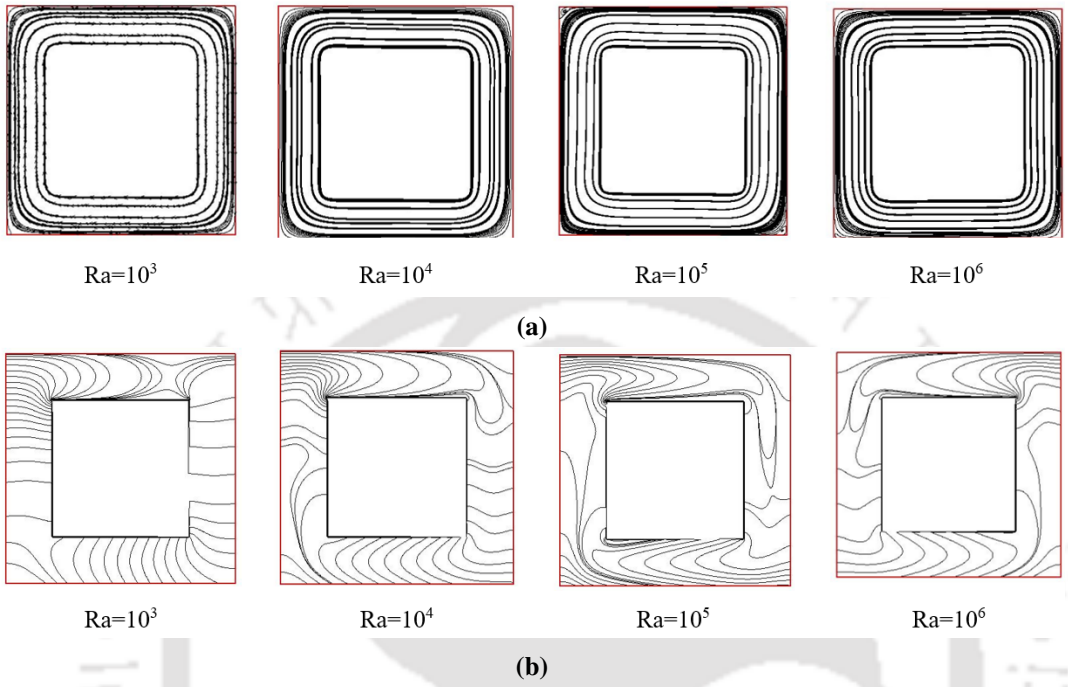

Figure 6.5: (a) Streamlines and (b) Isotherms at various Rayleigh number for constant heat flux boundary condition

(b) Variation in massflow rate

The variation of mass flow rate at different Ra ranging from 10^3-10^6 is shown in Figure 6.6 taking two different temperature boundary condition. The plots are depicted with respect to the dimensionless timestep. It is typically defined as the ratio of the physical timestep to the characteristic timescale of the system.

The observed reduction in oscillation and improved stability with the constant heat flux (CHF) boundary condition compared to the constant temperature (CT) boundary condition can be elucidated through an analysis of the isotherms, which depict the spatial distribution of temperature within the fluid domain. With the initial perturbation applied to both sets of simulations, the fluid undergoes transient behavior characterized by fluctuations in temperature and flow patterns as it approaches a stable, steady state. However, with the CHF boundary condition, the isotherms exhibit a more uniform and organized distribution of temperature throughout the domain. This indicates

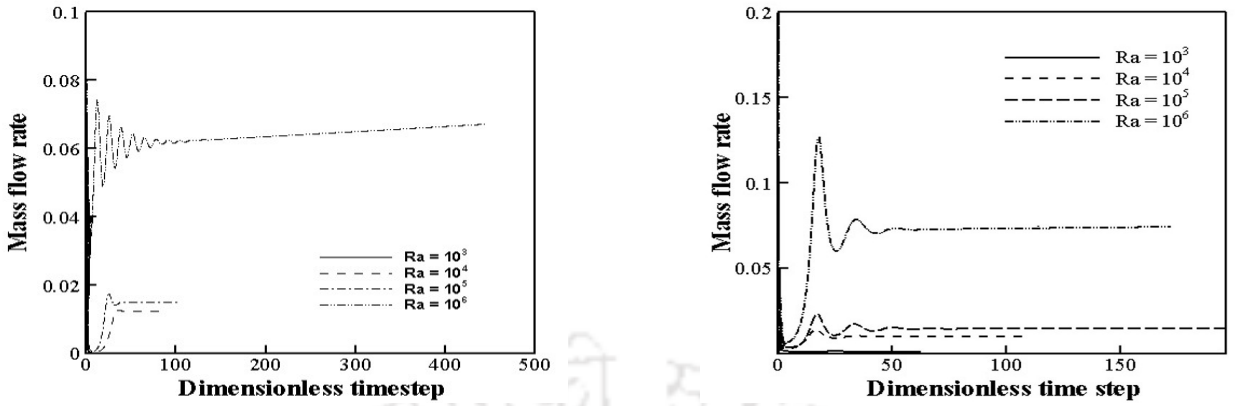

(a) Constant temperature boundary condition **(b) Constant heat flux boundary condition**

Figure 6.6: Variation of mass flow rate at different Ra ranging from 10^3-10^6

that heat is more evenly distributed within the fluid, reducing temperature gradients and minimizing the driving forces for convective motion. Consequently, the fluid experiences less agitation and turbulence, leading to diminished oscillations and faster attainment of stability. In contrast, the CT boundary condition results in less uniform temperature distributions, with localized hot and cold regions driving convective currents and promoting fluid mixing. This leads to more pronounced oscillations and longer transient periods before reaching a stable state. Therefore, the observed differences in temperature distribution between CHF and CT simulations provide insight into the mechanisms underlying the enhanced stability and reduced oscillation associated with the CHF boundary condition.

(c) **Variation in Nusselt number**

The variation of Nusselt number is shown in Figure 6.7 taking two different temperature boundary condition.

The observed higher heat transfer rate with the constant heat flux (CHF) boundary condition compared to the constant temperature (CT) boundary condition can be attributed to the interaction between the Rayleigh number (Ra) and the resulting changes in the Reynolds number (Re). As Ra increases, indicating higher buoyancy forces within the system due to larger temperature differences, Re also increases. Re represents the ratio of inertial forces to viscous forces in the fluid flow and serves as a measure of the flow's energy and turbulence. With higher Re, the fluid flow becomes more vigorous and turbulent, promoting enhanced mixing and heat transfer throughout the system.

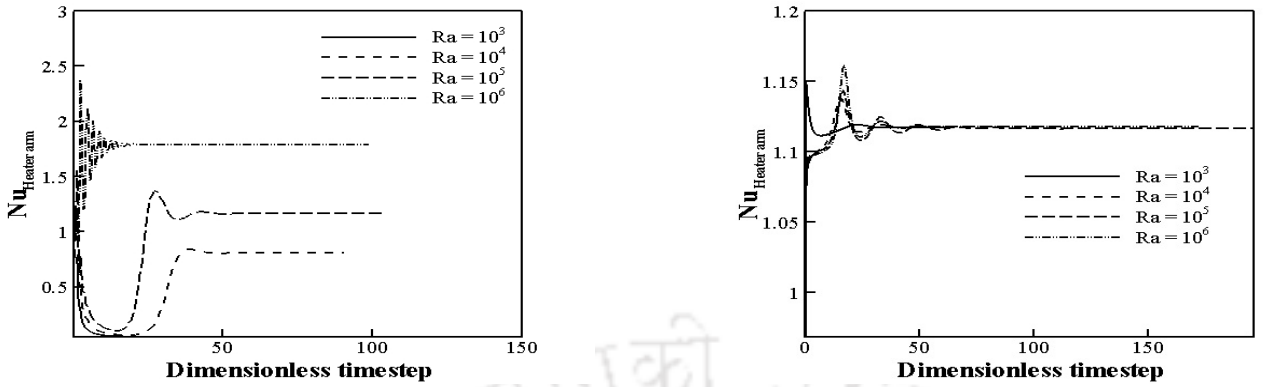

(a) Constant temperature boundary condition **(b) Constant heat flux boundary condition**

Figure 6.7: Variation of Nusselt number at different Ra ranging from 10^3-10^6

Consequently, the convective heat transfer coefficient increases, leading to higher Nusselt numbers (Nu) for both boundary conditions. The increase in Nu signifies greater convective heat transfer per unit area, indicating improved thermal performance. Therefore, the combined effect of increasing Ra, leading to higher Re, results in elevated heat transfer rates and Nusselt numbers, highlighting the influence of fluid dynamics on the heat transfer process in buoyancy-driven flows.

6.4.2 Effect of nanoparticle concentration

The effect of concentration of nanoparticles are studied in term of Prandtl number (Ra=10^5) as an input parameter. The 4 different input values are 6.14 (base fluid), 3.35 (φ=0.01%), 2.75 (φ=0.03%), 2.3 (φ=0.05%) and the results are depicted in the forms of streamlines and isotherms in Figure 6.8 and 6.9 with two different temperature boundary conditions.

(i) Constant temperature boundary condition.

(ii) Constant heat flux boundary condition.

(a) **Streamline and isotherm contours**

It is well known that, the effective viscosity (μ_{nf}) and effective thermal conductivity (k_{nf}) of the fluid increases with addition of nanoparticles. However, increase in viscosity reduces the convective effect while increment of thermal conductivity enhances the heat transfer which creates a contradictory ambience.

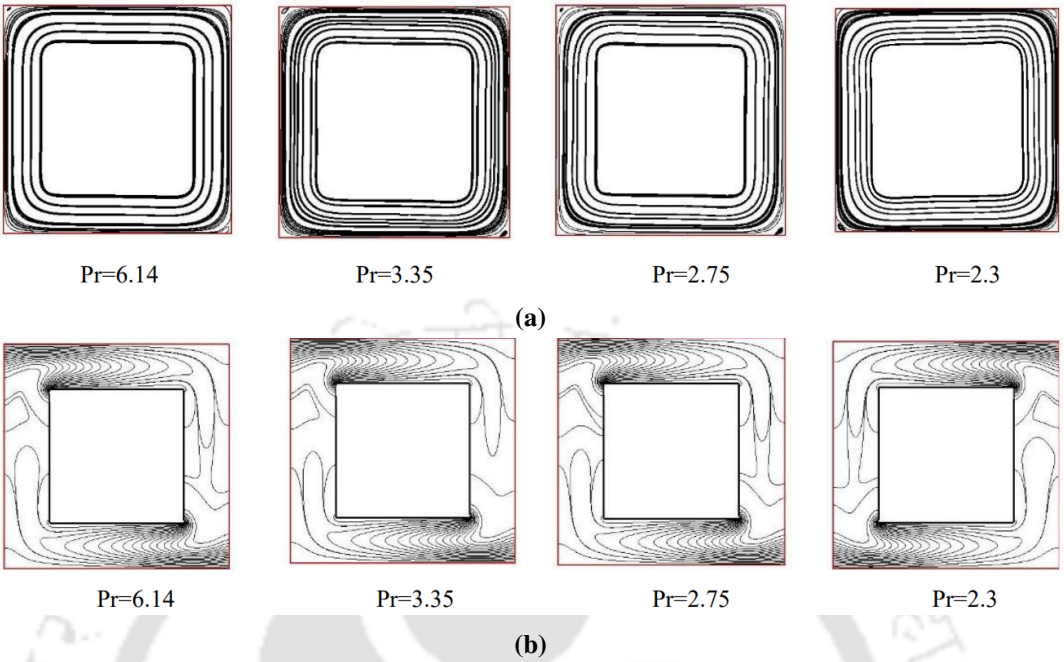

Figure 6.8: (a) Streamlines and (b) Isotherms at various Prandtl number for constant temperature boundary condition

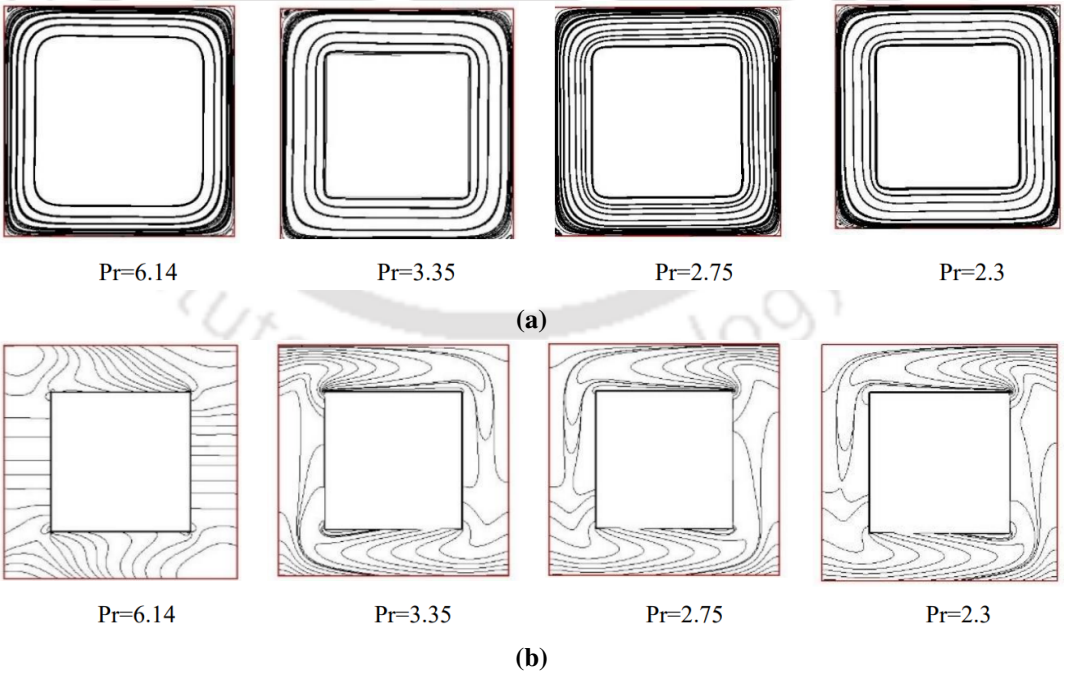

Figure 6.9: (a) Streamlines and (b) Isotherms at various Prandtl number for constant heat flux boundary condition

Still, fluid momentum which is produced due to buoyancy force (at high Rayleigh number) aids to overcome the decrement of convection induced by viscosity and we can witness fully developed flow as shown by means of streamlines in all cases of volume fraction (nanoparticle concentration) in the loop. As we know that, increasing the volume fraction of nanoparticle decreases the Pr and lower Pr implies higher Grashof number or higher buoyancy forces for the same Ra. Hence, strong convective regimes are observed as the Pr lowers down which can also be confirmed the plotted above isotherms.

(b) **Variation in massflow rate**

The variation of mass flow rate at different Prantl number is shown in Figure 6.10 taking two different temperature boundary condition.

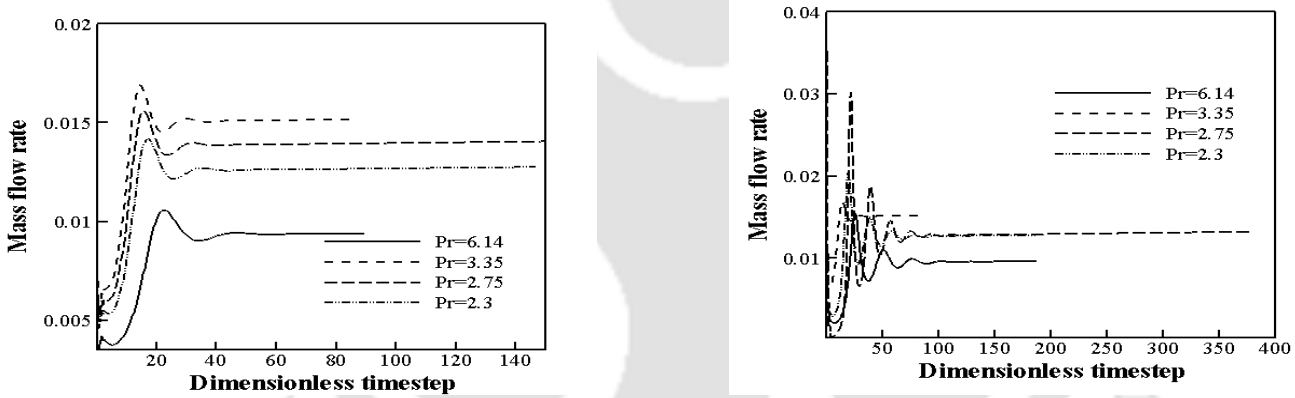

(a) Constant temperature boundary condition **(b) Constant heat flux boundary condition**

Figure 6.10: Variation of mass flow rate at different Pr

As shown in Figure 6.10 higher mass flow rate is achieved with enhancement in Pr. A lower Pr signifies a higher buoyancy force within the fluid, which results in increased fluid motion and turbulence, consequently leading to higher Reynolds numbers (Re). Higher Re values indicate a more energetic flow with greater momentum, facilitating enhanced mass transport and resulting in higher mass flow rates. Additionally, Figure 6.10(a) and 6.10(b) illustrate that the steady mass flow rate is higher with the constant heat flux (CHF) boundary condition compared to the constant temperature (CT) boundary condition. When a CHF boundary is employed, the heat transfer rate remains constant along the boundary. This maintains a higher temperature gradient near the boundary, promoting increased convective heat transfer from the boundary to the fluid.

The enhanced convective heat transfer drives more fluid motion and accelerates mass transport, ultimately leading to a higher mass flow rate. Therefore, the combination of lower Pr, higher Re, and the utilization of a CHF boundary condition collectively contribute to the observed increase in mass flow rate in the system.

(c) **Variation in Nusselt number**

The variation of Nusselt number is shown in Figure 6.11 taking two different temperature boundary condition. The observed trend of higher heat transfer coefficients associated with lower Prandtl numbers

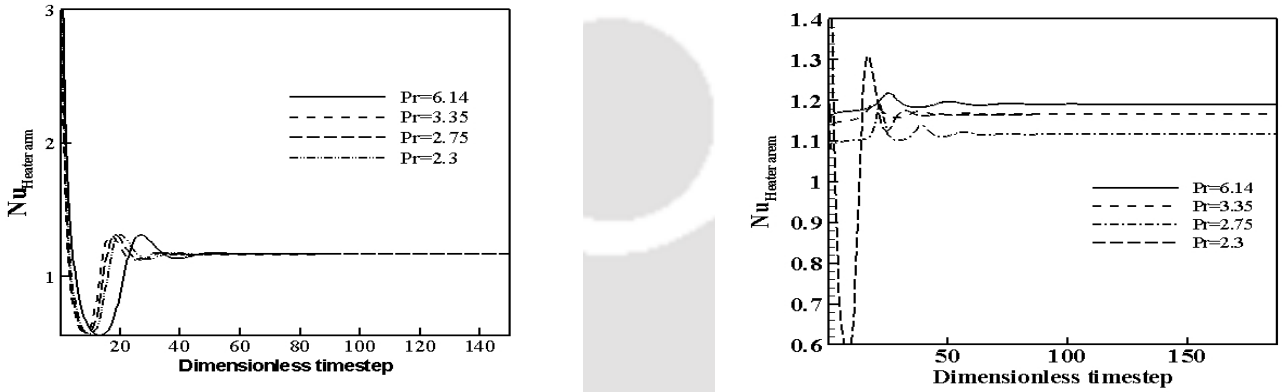

(a) Constant temperature boundary condition **(b) Constant heat flux boundary condition**

Figure 6.11: Variation of Nusselt number at different Pr

(Pr) is consistent with fundamental principles of fluid dynamics and heat transfer. Lower Pr fluids typically exhibit higher velocities due to their lower viscosity, which enhances convective heat transfer. Additionally, lower Pr fluids often have higher thermal conductivities, facilitating more efficient heat transfer through the fluid. As a result, the heat transfer coefficient, which quantifies the rate of heat transfer per unit area per unit temperature difference, tends to be higher for lower Pr fluids. However, when considering the Nusselt number (Nu), which represents the ratio of the convective heat transfer coefficient to the thermal conductivity of the fluid, the picture is nuanced. While higher velocities and thermal conductivities contribute to higher heat transfer coefficients, the denominator in the Nu expression, the thermal conductivity, also increases for lower Pr fluids. Consequently, the overall effect on Nu may not be as pronounced, leading to relatively consistent Nu values across different Pr categories, as depicted in Figure 6.11 (a) and 6.11 (b). Moreover, since the Rayleigh number (Ra) is held constant for the presented results, the dependence of Nu on Ra is consistent, further contributing to the stability of

Nu across different Pr categories. Therefore, the interplay between fluid velocity, thermal conductivity, and Ra value influences the heat transfer characteristics, leading to the observed trends in heat transfer coefficients and Nu.

6.4.3 Effect of inclination angle

The effect of inclination angle at different input values viz 0°, 30°,60° and 90°are numerically studied and are depicted in the form of streamlines and Isotherms in Figure 6.12 and 6.13 with two different temperature boundary conditions.

(i) Constant temperature boundary condition.

(ii) Constant heat flux boundary condition.

The angle of inclination (ϕ) is defined by the angle between a left adiabatic wall and the vertical axis in such a way that ϕ = 90° represents the situation of the NCL heated on the left side.

(a) **Streamline and isotherm contours**

The study has been carried out for inclination angle ranging from 0° to 90° in the XY plane. It can be observed from the streamline contours that, with increase in tilt angle the gravitational force in the NCL decreases which results in the decrease in driving buoyancy force and the primary fluid flow takes over the secondary vortices which can be seen in lower inclination angle and is true for both the temperature boundary condition. Although there is reduction in driving buoyancy force with increase in inclination angle, but stronger convective force is seen with the constant heat flux boundary condition as can be observed in respective isotherms.

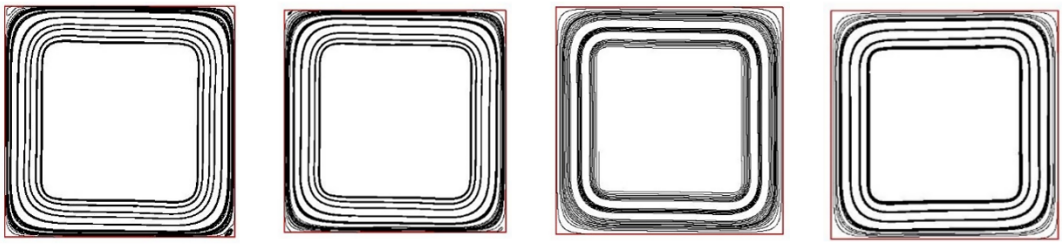

Angle 0° Angle 30° Angle 60° Angle 90°

(a)

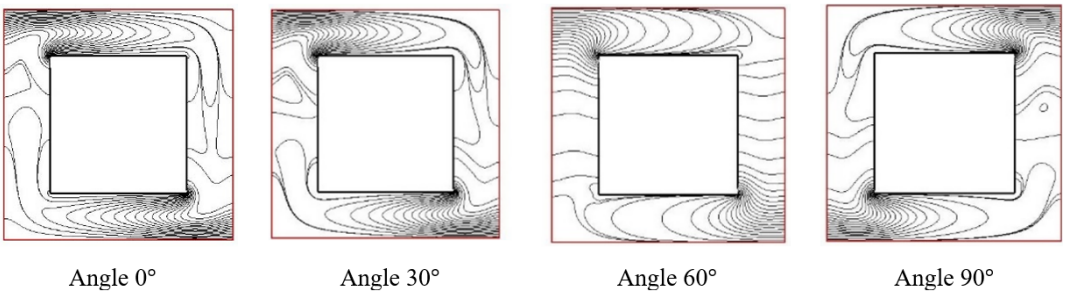

(b)

Figure 6.12: (a) Streamlines and (b) Isotherms at various inclination angle for constant temperature boundary condition

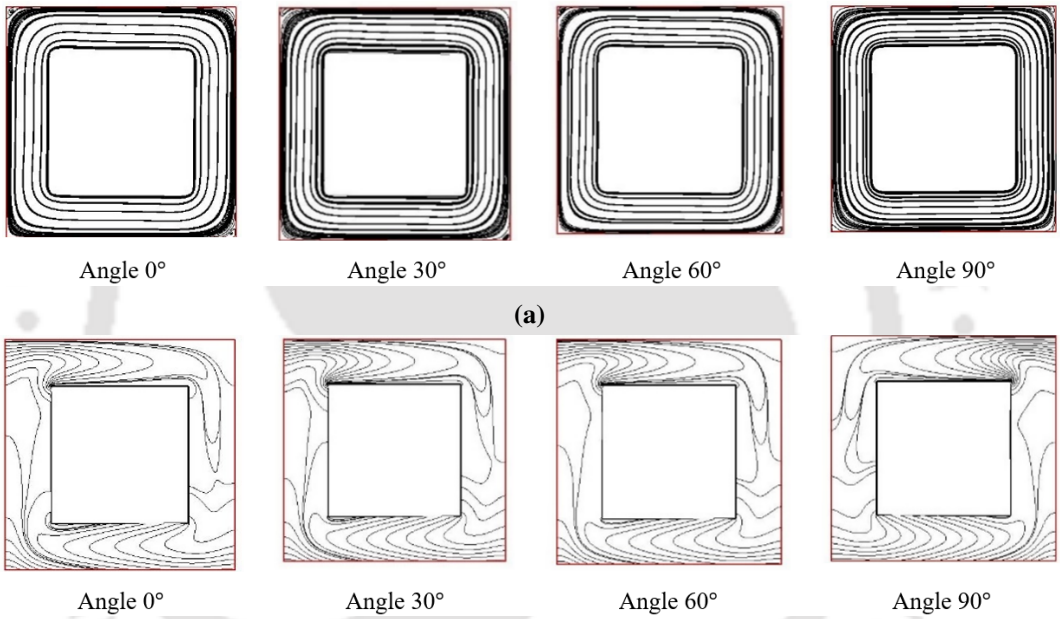

Figure 6.13: (a) Streamlines and (b) Isotherms at various inclination angle for constant heat flux boundary condition

(b) **Variation in massflow rate**

The variation of mass flow rate at different inclination angle is shown in Figure 6.14 taking two different temperature boundary condition.

The observed decrease in steady-state mass flow rate with an increase in the tilt of the natural circulation loop can be attributed to the reduction in the driving buoyancy force caused by the inclination. In a natural circulation loop, buoyancy forces generated by temperature differences drive the flow of fluid through the loop. When the loop is tilted, the gravitational component of

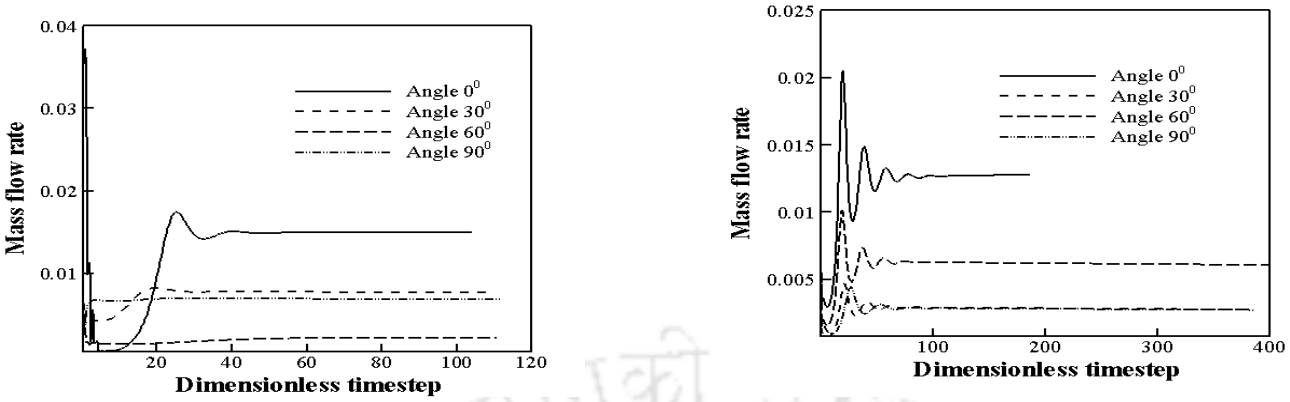

(a) Constant temperature boundary condition **(b) Constant heat flux boundary condition**

Figure 6.14: Variation of mass flow rate at different inclination angle

the buoyancy force is partially opposed by the gravitational force acting perpendicular to the tilt, thereby reducing the effective driving force for fluid circulation. Consequently, the fluid flow rate decreases as the tilt angle increases due to the diminished buoyancy force. However, it's notable that the influence of tilt on convective flow is insignificant when compared to other factors such as temperature differentials and fluid properties. Additionally, the magnitude of the mass flow rate remains equivalent for both constant temperature and constant heat flux boundary conditions, indicating that the choice of boundary condition does not significantly affect the overall flow rate within the loop. Thus, the observed trends in mass flow rate with tilt angle underscore the importance of buoyancy forces in driving natural circulation flow and highlight the relatively minor impact of loop inclination on convective flow dynamics.

(c) **Variation in Nusselt number**

The variation of Nusselt number at different inclination angle is shown in Figure 6.15 taking two different temperature boundary condition.

The increase in inclination angle results in reduction in both Nu and Re as depicted in Figure 6.15. When the inclination angle increases, the magnitude of the body force acting on the fluid decreases. This decrease in the body force subsequently leads to a reduction in the buoyancy force. The buoyancy force is responsible for driving the convective heat transfer in buoyancy-driven flows. Because of the decrease in the buoyancy force, both the Nusselt number and the Reynolds number decrease. The Nusselt number represents the convective heat transfer rate, while the Reynolds number characterizes the flow behavior

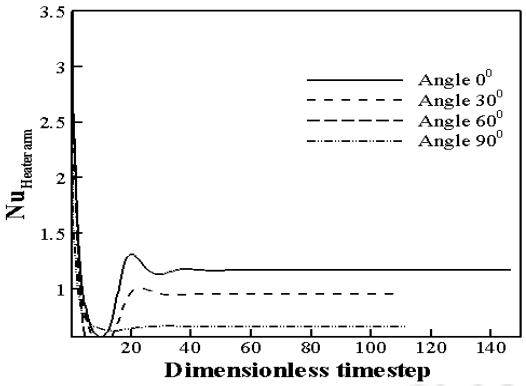

(a) Constant temperature boundary condition

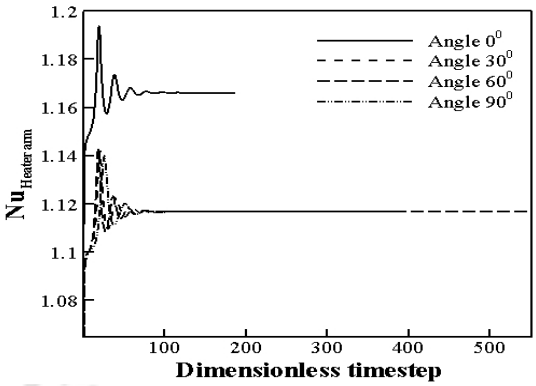

(b) Constant heat flux boundary condition

Figure 6.15: Variation of Nusselt number at different inclination angle

and indicates the relative importance of inertial forces to viscous forces in the fluid flow.

6.4.4 Effect of variation in heat flux boundary condition

This section reports the performed simulations for the working fluid with 0.05% volume fraction (Pr=2.3) taking no inclination in the loop. Here, the effect of different nature of heat flux distribution has been presented.

The considered heat flux distribution are as follows:

(i) Uniform heat flux (CHF): q_{mean}

(ii) Linearly decreasing heat flux (maximum to zero) (LD): $q = q_2 - \frac{(q_2 - q_1)}{L_H} x$

(iii) Linearly increasing heat flux (zero to maximum) (LI): $q = q_1 + \frac{(q_2 - q_1)}{L_H} x$

Where, $q_1 = 0$, q_2= $2q_{mean}$

(iv) Sinusoidal heat flux: q= q_{mean}+ $q_{amp} sinx$

Where, q_{amp}=q_{mean}

(a) **Streamlines and isotherms**

With the above discussions made, the effect of variation in heat flux boundary condition is numerically studied with the simulations taking the input parameters of Pr=2.3, ϕ= 0° and Ra=10^5.

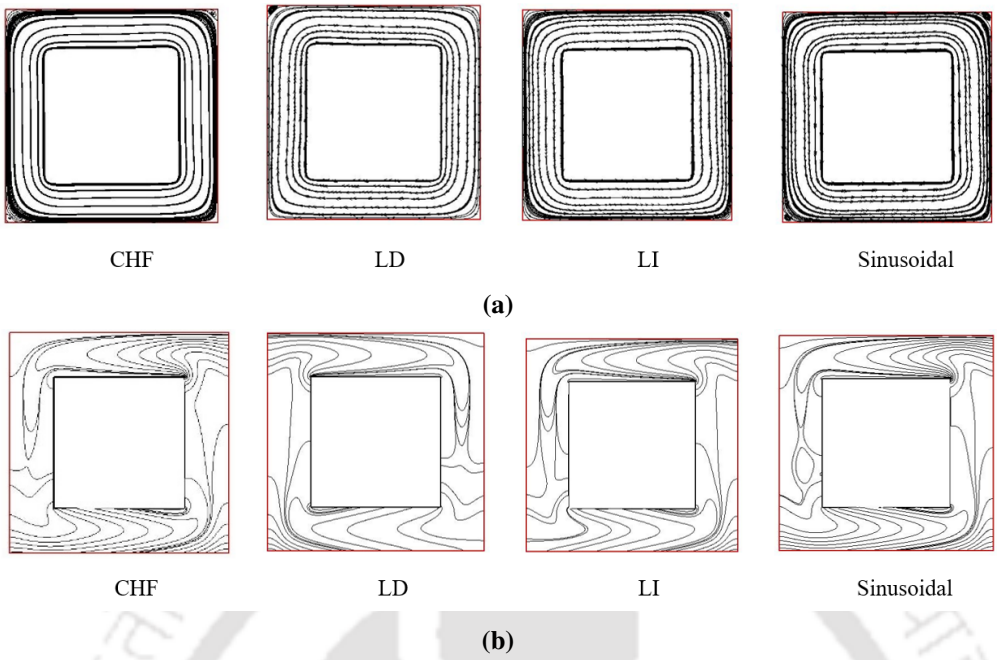

Figure 6.16: (a) Streamlines and (b) Isotherms at various heat flux boundary condition.

A comparative depiction is made in terms of streamlines, isotherms, mass flow rate, Average Nusselt number at heater arm of the loop, total entropy generation (entropy generation due to heat transfer and due to fluid friction) and pressure drop and is shown in Figure 6.16-6.20.

As depicted by the streamlines and isotherms in the Figure 6.16, all the boundary conditions reach a fully developed flow in the loop. However, strongest convective regime is observed in case of linearly decreasing heat flux boundary condition. The gradually decreasing heat input allows the flow to adjust smoothly, minimizing flow instabilities and turbulence. This improved flow stability contributes to enhanced convective heat transfer.

(b) **Variation in mass flow rate**

As seen in the Figure 6.17, with the applied perturbation the natural circulation loop with constant heat flux reaches stability at the earliest followed by linearly increasing and then linearly decreasing. The sinusoidal heat fluxed boundary condition reaches the stability at the last. The applied perturbations could lead to different transient responses in the natural circulation loop with constant heat flux and sinusoidal heat flux boundary conditions. The constant heat flux condition may quickly reach stability due to a more straightforward response to perturbations, while the sinusoidal heat flux condition might take longer to stabilize due to the oscillatory nature of the perturbation.

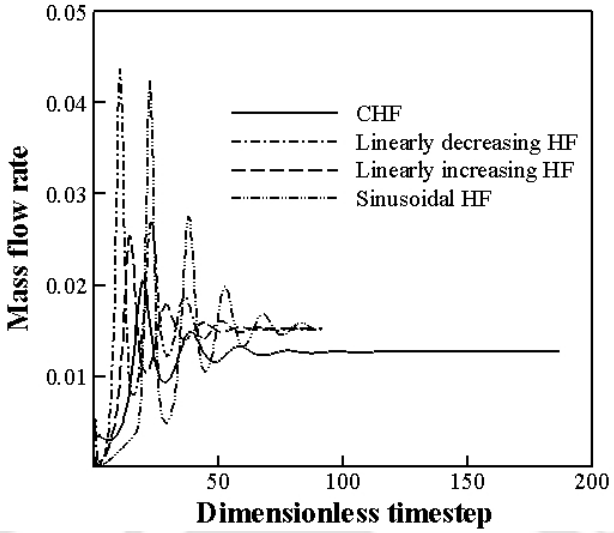

Figure 6.17: Variation of mass flow rate at different heat flux boundary conditions

(c) **Variation in Nusselt number**

As shown in the Figure 6.18, the higher Nu is observed in sinusoidal heat flux and lowest for the constant heat flux. As cited by Kumar et al. [75] the buoyancy-induced flow resonates to a certain frequency of the pulsing heat input, and the resonance phenomena is distinguished by the maximum variations seen in the development of heat transfer with the period of the time-dependent temperature.

Sinusoidal heat flux introduces variations in the temperature gradients and fluid velocities, leading to transient flow patterns and boundary layer dynamics. These fluctuations can create additional mixing and enhanced convective heat transfer, resulting in higher Nusselt numbers compared to a steady and constant heat flux condition.

(d) **Variation in entropy generation**

Figure 6.19 (a) and Figure 6.19 (b) depicts the total entropy generation for the heater arm and cooler arm of the natural circulation loop at various heat flux distributions. The irreversibilities gets stabilised in case of constant heat flux at the earliest. This can be attributed by the fact that, linearly increasing and linearly decreasing heat flux implies increasing buoyancy force resulting in increase in entropy generation.

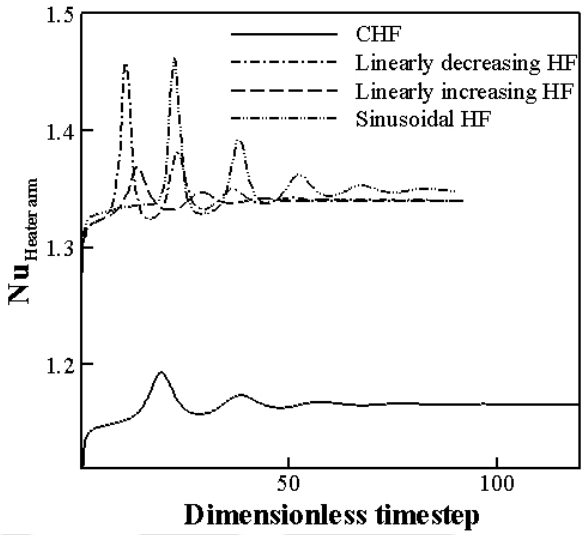

Figure 6.18: Variation of Nusselt number at different heat flux boundary conditions

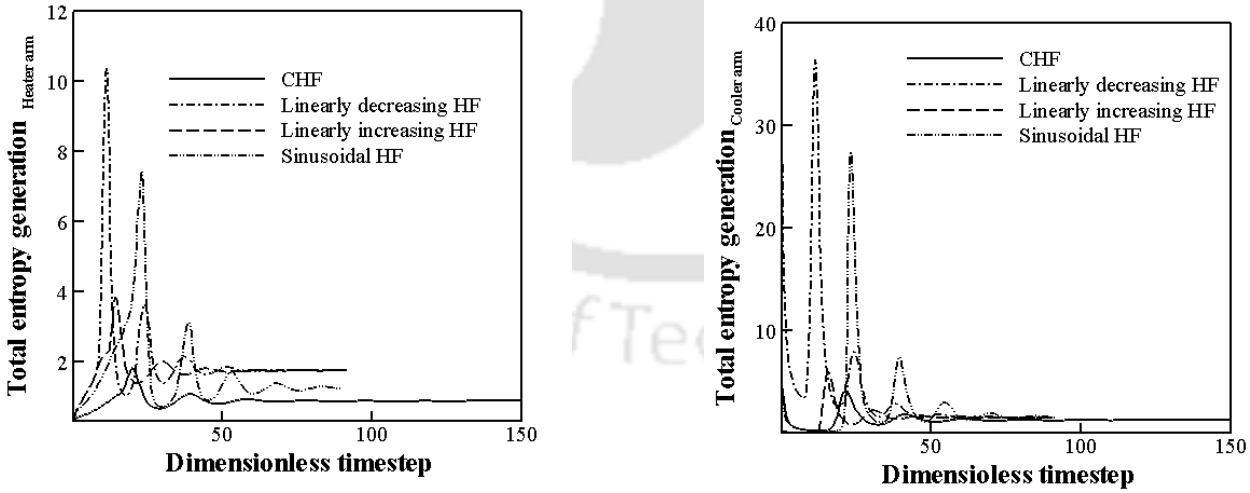

(a) **(b)**

Figure 6.19: Variation of total entropy generation (a) Heater arm and (b) Cooler arm at different heat flux boundary conditions

This may be because, for constant heat flux conditions the system remains relatively balanced and unaffected by external perturbations. On the other hand, the linearly increasing and decreasing heat flux (LD and LI) conditions lead to higher entropy generation as the system needs to adjust to changing heat inputs and associated fluid flow patterns, resulting in more irreversibilities. Amongst the four cases, LI flux conditions comes to steady conditions at the earliest.

(e) **Variation in pressure drop**

Figure 6.20 depicts the pressure drop in the heater and cooler arm of the natural circulation loop at various flux distribution. Higher fluctuation is observed with the sinusoidal heat flux boundary condition which also shows lower heat transfer in this case. Sinusoidal heat flux leads to unsteady flow conditions at times, which can disrupt the flow patterns and induce flow separation, creating low-pressure regions that contribute to higher pressure drop. This can also be supported by the discussion made on mass flow rate. As mentioned above, sinusoidal heat flux condition might take longer to fully develop the flow (Figure 6.17), which can lead to higher pressure drop due to high flow resistance.

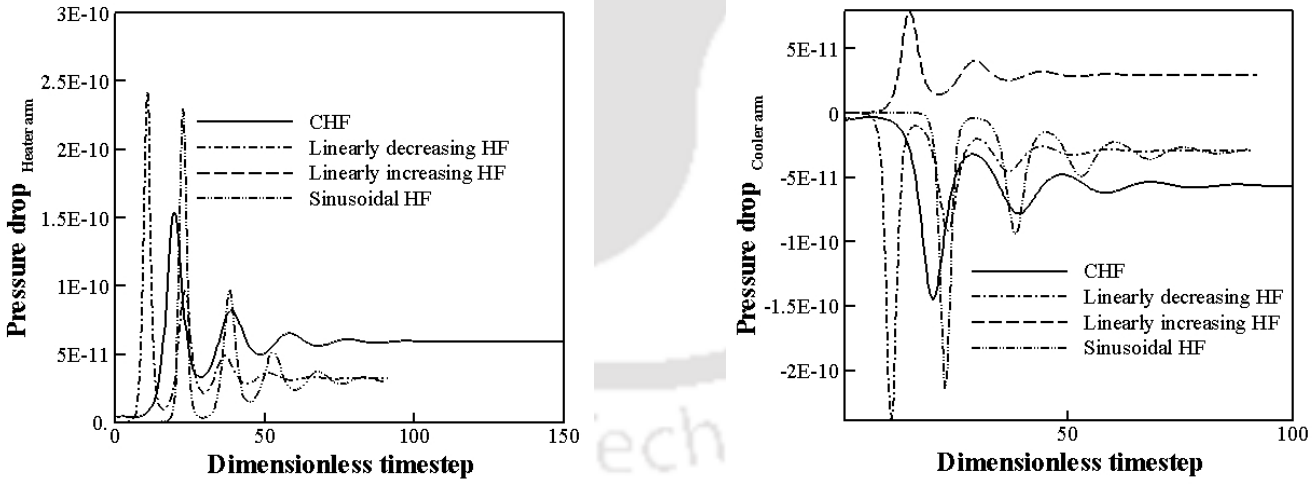

Figure 6.20: Variation of pressure drop (a) for heater arm (b) for cooler arm at different heat flux boundary conditions

6.5 Summary

The study in the horizon of gravity driven flows is much explored by the researchers and scientists due its wide applications in industrial field. In the present work, parametric analysis for the natural circulation loop (NCL) is done. For NCL, simulations are carried out with Rayleigh number ranging between 10^3<Ra<10^6 and Prandtl number 6.14,3.35,2.75 and 2.3. Further, the study is explored to determine the influence of thermal boundary conditions at various heat flux environment.

The salient features of the numerical study on natural circulation loop are as follows:

(i) Increasing both Prandtl number (Pr) and Rayleigh number (Ra) affects flow and temperature fields, leading to an increase in heat transfer rate due to enhanced thermal diffusivity and stronger buoyancy-driven flow.

(ii) In a closed loop system like the NCL, mass flow rate remains constant when the flow reaches a steady state. This is due to the conservation of mass, where the mass entering a section of the loop must equal the mass exiting that section. As long as there are no external factors influencing the flow, the mass flow rate should remain constant within each arm of the loop.

(iii) As the Rayleigh number increases, it indicates stronger buoyancy forces driving the flow. This can cause the boundary layers near the heated surface to become thinner. Thinner boundary layers result in a more efficient heat transfer, leading to an increase in the Nusselt number. The Nusselt number represents the convective heat transfer coefficient normalized by the conductive heat transfer coefficient.

(iv) Higher heat transfer rate is found to be in case of sinusoidal heat flux condition which introduces fluctuations in temperature gradients and fluid velocities, causing transient flow patterns and changes in boundary layer dynamics. These variations promote additional fluid mixing, leading to enhanced convective heat transfer and resulting in higher Nusselt numbers compared to a steady and constant heat flux condition.

(v) Highest fluctuation in entropy generation is seen in case of linearly decreasing flux condition as compared to other heat flux boundary conditions.

(vi) Irreversibilities refer to energy losses or inefficiencies in a thermodynamic system. In the case of constant heat flux boundary conditions, the heat transfer remains constant across the boundary. This can lead to a more stable and predictable thermal distribution, reducing the occurrence of energy losses associated with fluctuations or variations in the heat transfer process. As a result, irreversibilities tend to stabilize earlier in systems with constant heat flux.

भारतीय प्रौद्योगिकी संस्थान गुवाहाटी
Indian Institute of Technology Guwahati

Chapter 7

Conclusions and future scope of work

7.1 Conclusions

This thesis introduces a practical and significant lattice Boltzmann Method (LBM) for buoyancy-driven flow involving a single fluid phase. The fluid simulation is carried out in two dimensions using the D2Q9 lattice and the LBGK method. The developed LBM codes are versatile and demonstrate excellent performance across a wide range of problems and is employed to conduct parametric studies using properties like Ra, Pr, ϕ, Re as input parameters in distinct cases as mentioned below. While the fundamental LBM is retained, special attention is given to ensure accurate and realistic parameterizations. Throughout the thesis, the presented results are thoroughly validated, both qualitatively and quantitatively, through rigorous exercises. The findings are supported by a wealth of figures and tables, enhancing the credibility of the results, particularly in cases where flow configurations had not been previously studied. The major accomplishments of the thesis will be outlined and discussed in the following sections.

The thesis begins by conducting simulations of various benchmark isothermal and thermal flow problems. The primary aim was to validate the developed LBM code by comparing its results with those obtained from established numerical techniques. This validation process served to ensure the accuracy of the LBM code while providing the author with a deeper insight into its fundamental structure.

Further, the thermal lattice Boltzmann method (TLBM) is employed to study a natural convection problem. In this study, the flow configuration features four walls with a no-slip impermeable velocity boundary condition. The left wall maintains a uniformly high temperature, while the right vertical wall is uniformly cooled. The top and bottom walls are thermally insulated. Although the Boussinesq approx-

imation is widely used, its accuracy is constrained when dealing with significant temperature differences. As a result, alternative methods are necessary to accurately model cases with larger temperature variations. This motivated the author to explore the performance of a natural convection cavity by comparing the results obtained through both Boussinesq and non-Boussinesq approaches. Notably, there has been no prior reporting on the application of such a LBM algorithm in this context to the best of the author's knowledge, making this investigation novel and valuable. The results show that, as the Rayleigh number (Ra) increases, the heat transfer mechanism transitions from conduction to convection takes place. At low Ra, conduction dominates, while at higher Ra, convection becomes more significant, impacting the Nusselt number (Nu) and entropy generation. Non-Boussinesq simulations show higher entropy and Nu values compared to Boussinesq approximations for all Ra values, as temperature-dependent fluid properties lead to increased entropy generation. As Ra increases, entropy generation due to fluid friction (S_Ψ) becomes more prominent, surpassing entropy generation from heat transfer (S_θ) at Ra=10^6. This highlights the increasing role of fluid friction in overall entropy production beyond this critical value. Thus, understanding and controlling Ra are crucial for optimizing heat transfer efficiency and reducing entropy generation.

Furthermore, the research is extended to address mixed convection problems within cavities, with a particular emphasis on investigating various influential parameters and optimizing their effects on mixed convection heat transfer and entropy generation—an aspect not previously explored. The study employs numerical simulations using the thermal Lattice Boltzmann Method (LBM) on three different cavity configurations. The three distinct cases are: (i) Top lid moving in forward direction and bottom lid is kept stationary (Case 1); (ii) Both top and bottom lids moving in forward direction (Case 2); (iii) Both top and bottom lids moving in opposite direction (Case 3). The main motivation behind this work is to comprehensively investigate the fluid dynamics inside the cavity, considering the combined impact of both lid driving and buoyancy effects during mixed convection. This investigation aims to shed light on new insights and outcomes in this field. The results reveal that increasing the Richardson number (Ri) and Reynolds number (Re) enhances heat transfer and net entropy generation. The Prandtl number's impact becomes significant at higher values, promoting better heat transfer rates and circulation loops that increase entropy generation. Among the three cavity configurations, case 1 exhibits the lowest irreversibility and heat transfer rate. The inclination angle (ϕ) influences Nusselt number and entropy generation, with optimal values observed at $\phi = 40^\circ$ for cases 1 and 2 and $\phi = 50^\circ$ for case 3. Fluid

friction contributes significantly to entropy generation, particularly at high Ri and Re, while the friction coefficient responds differently to Ri and Re. The aspect ratio variation and velocity ratio between the top and bottom lids also impact heat transfer and irreversibility. Also, decreasing the velocity ratio improves performance by reducing irreversibility while maintaining satisfactory heat transfer rates.

Next, the thermal-hydraulic performance of a single-phase natural circulation loop (SPNCL) is investigated, with a particular emphasis on the impact of nanofluids. The lattice Boltzmann method (LBM) is chosen for numerical modelling due to its simplicity and versatility in handling various parameters. Additionally, the modelling incorporates the essence of the non-Boussinesq approximation, adding novelty to the research. The flow configuration of the SPNCL consists of isothermal boundary conditions with a horizontal heater and cooler positioned on its arms, while the remaining sections of the loop are insulated. The primary goal is to optimize the model of the natural circulation loop to minimize entropy generation and enhance its overall performance. The investigation reveals several important findings. Firstly, entropy generation is influenced significantly by the volume fraction, with a reduction observed as the inclination angle increases due to decreased heat transfer rates caused by tilting the NCL. Secondly, lower aspect ratios result in a convective heat transfer mode, enhancing boundary effects and mass flow rate. Thirdly, adopting a non-uniform diameter NCL in the heater section minimizes entropy generation. Moreover, for simulations involving high Rayleigh numbers ($Ra = 10^6$), the non-Boussinesq approximation outperforms the Boussinesq approximation in capturing temperature-dependent density effects. However, for low Rayleigh numbers, both approximations yield similar outcomes. The comparison between the two approaches reveals minor differences in entropy generation due to fluid friction (S_Ψ) and heat transfer (S_θ). Overall, this comprehensive study provides valuable insights into the thermal-hydraulic behavior of natural circulation loops, guiding the optimization of such systems with reduced entropy generation and improved performance.

The study of natural circulation loops (NCLs) is extended to include transient simulations using the Boussinesq approximation to simplify the algorithm and focus on recording the time-dependent response under various thermal boundary conditions. Notably, there is a lack of prior research investigating the impact of different thermal boundary conditions on heat transfer and entropy generation in NCLs using the lattice Boltzmann method (LBM). The simulations cover a range of Rayleigh numbers ($10^3 < Ra < 10^6$) and Prandtl numbers (6.14, 3.35, 2.75, and 2.3) for the NCL. The considered thermal boundaries include isothermal (CT), constant heat flux (CHT), linearly increasing (LI), linearly decreasing (LD), and

sinusoidal heat flux conditions.

The effects of Prandtl number (Pr) and Rayleigh number (Ra) on flow and temperature fields are analyzed, revealing that higher values of Pr and Ra lead to increased heat transfer rates due to improved thermal diffusivity and stronger buoyancy-driven flow. The mass flow rate remains constant in the closed-loop NCL once a steady state is reached, governed by mass conservation principles. The impact of different heat flux boundary conditions on heat transfer and entropy generation is explored, with the sinusoidal heat flux condition demonstrating higher heat transfer rates due to induced temperature and velocity fluctuations, enhancing convective heat transfer through fluid mixing. Conversely, the linearly decreasing flux condition exhibits the highest fluctuation in entropy generation among the different heat flux boundary conditions. The concept of irreversibilities in thermodynamic systems is also discussed, highlighting the stabilization of systems with constant heat flux boundary conditions due to a more predictable thermal distribution, reducing energy losses associated with heat transfer fluctuations. Overall, this comprehensive investigation provides valuable insights into the transient behavior of NCLs under various thermal boundary conditions, offering potential applications in optimizing heat transfer efficiency and minimizing entropy generation in energy systems and engineering fields. The LBM coupled with the Boussinesq approximation proves to be a robust approach for studying the thermal-hydraulic performance of NCLs and paves the way for future advancements in related research areas.

In conclusion, the thesis successfully achieves its objectives by providing a comprehensive understanding of buoyancy-driven flow phenomena through the application of the lattice Boltzmann Method. By addressing various thermal scenarios and exploring optimization strategies, valuable insights are gained into enhancing heat transfer efficiency and minimizing entropy generation in natural circulation loops and related systems. The culmination of this research not only contributes to the advancement of knowledge in the field but also lays the groundwork for future investigations in thermal-fluid dynamics and engineering applications.

Additionally, it is noteworthy that the studied buoyancy-driven flow phenomenon exhibits robust performance under certain physical or boundary conditions. This observation underscores the practical relevance and applicability of the findings, suggesting potential avenues for the design and optimization of thermal systems and processes.

Thus, the introduction of a robust lattice Boltzmann Method (LBM) tailored for buoyancy-driven flow in a single fluid phase, employing the D2Q9 lattice and LBGK method for efficient two-dimensional fluid

simulations is highlighted with the following key findings:

(i) Application of the thermal Lattice Boltzmann Method (TLBM) to examine natural convection phenomena, including a comparative analysis between Boussinesq and non-Boussinesq approaches, revealed nuanced temperature variation effects at critical $Ra = 10^5$.

(ii) Novel exploration of mixed convection scenarios within cavities, emphasized the interplay between lid driving and buoyancy effects on heat transfer and entropy generation.

(iii) The key parameters such as Richardson number (Ri), Reynolds number (Re), and Prandtl number are identified, elucidating their significant influences on heat transfer dynamics and circulation patterns.

(iv) Optimization of cavity configurations to determine optimal inclination angles ϕ, aspect ratio and velocity ratio between top and bottom lids offers strategies for enhancing heat transfer efficiency while mitigating irreversibility effects.

(v) Key findings investigating the thermal-hydraulic performance of a single-phase natural circulation loop (SPNCL)include significant influence of volume fraction on entropy generation, reduction with increased inclination angle, and enhancement of convective heat transfer with lower aspect ratios. Adoption of non-uniform diameter NCL in the heater section minimizes entropy generation. Non-Boussinesq approximation outperforms Boussinesq for high Rayleigh numbers, while both yield similar outcomes for low Rayleigh numbers.

(vi) Extension of the study is made to include transient simulations using the Boussinesq approximation, exploring the impact of different thermal boundary conditions on heat transfer and entropy generation in NCLs using LBM. Investigation covers a range of Rayleigh and Prandtl numbers, as well as various thermal boundary conditions such as isothermal, constant heat flux, linearly increasing, linearly decreasing, and sinusoidal heat flux conditions.

(vii) Analysis reveals that higher Pr and Ra values lead to increased heat transfer rates, with mass flow rate remaining constant once steady state is reached. Different heat flux boundary conditions exhibit varied effects on heat transfer and entropy generation, with sinusoidal heat flux condition

demonstrating higher heat transfer rates and linearly decreasing flux condition exhibiting highest fluctuation in entropy generation.

(viii) The irreversibilities in thermodynamic systems highlights stabilization of systems with constant heat flux boundary conditions, reducing energy losses associated with heat transfer fluctuations. Overall, the research offers insights into transient behavior of NCLs under diverse thermal conditions, with potential applications in optimizing heat transfer efficiency and minimizing entropy generation.

7.2 Future scope of work

Throughout this thesis, a significant effort was made to develop and advance the application of the SRT-LBM in the domain of single-phase buoyancy-driven flows. However, there is still potential for further exploration and improvement, particularly in the area of two-phase modeling. As a result, several recommendations can be made for future research in this field:

(i) In the context of two-phase flow, buoyancy-driven flow remains an important area of study. Future research can focus on enhancing the accuracy and capabilities of numerical methods, such as the Lattice Boltzmann Method (LBM), in simulating two-phase buoyancy-driven flows. Investigations should explore phase interactions, heat transfer, and fluid dynamics in various geometries and conditions for practical applications.

(ii) To improve the accuracy of non-Boussinesq approximation in simulations, a non-uniform grid can be employed. By adjusting the grid spacing based on temperature gradients, regions with higher thermal variations can be better resolved, leading to more precise predictions of fluid behavior and heat transfer in natural circulation loops and other buoyancy-driven flow systems. This approach enhances the fidelity of non-Boussinesq simulations and contributes to a more comprehensive understanding of the thermal-hydraulic performance in such scenarios.

(iii) Lattice Boltzmann Method (LBM) studies focusing on compressible flow are limited, and most of them only consider Mach numbers less than or equal to one. However, there is potential for expanding LBM's capabilities to handle higher Mach numbers, despite the challenges involved. Extending LBM to higher Mach numbers could open new possibilities for simulating and understanding compressible flow phenomena in various engineering and scientific applications.

(iv) During the thesis work, the author realized the demand for high computational time to obtain converged solutions of the numerical investigations. Hence, it is advisable to implement parallelization techniques to achieve computational acceleration as a future scope.

(v) While experimental studies have established the functional relationship between different dimensionless parameters in the case of natural circulation loops, it is recommended to conduct extensive experiments and develop correlations to further investigate and understand the system's behavior. These experiments can provide valuable insights and complement the existing data, enabling more accurate predictions and correlations for the thermal-hydraulic performance of natural circulation loops.

भारतीय प्रौद्योगिकी संस्थान गुवाहाटी
Indian Institute of Technology Guwahati

Bibliography

[1] U. Ghia, K. Ghia, and C. T. Shin, "High-re solutions for incompressible flow using the Navier-Stokes equations and a multigrid method," *Journal of Computational Physics*, vol. 48, no. 3, pp. 387–411, 1982.

[2] R. Iwatsu, J. Hyun, and K. Kuwahara, "Mixed convection in a driven cavity with a stable vertical temperature gradient," *International Journal of Heat and Mass Transfer*, vol. 36, no. 6, pp. 1601–1608, 1993.

[3] E. dos Santos, G. Piccoli, F. França, and A. Petry, "Analysis of mixed convection in transient laminar and turbulent flows in driven cavities," *International Journal of Heat and Mass Transfer*, vol. 54, no. 21, pp. 4585–4595, 2011.

[4] E. Erturk and C. Gokçol, "Fourth-order compact formulation of Navier–Stokes equations and driven cavity flow at high Reynolds numbers," *International Journal of Numerical Methods for Fluids*, vol. 50, no. 4, pp. 421–436, 2006.

[5] J. Indukuri and R. Maniyeri, "Numerical simulation of oscillating lid-driven square cavity," *Alexandria Engineering Journal*, vol. 57, no. 4, pp. 2609–2625, 2018.

[6] M. Sheikholeslami, S. Shehzad, F. Abbasi, and Z. Li, "Nanofluid flow and forced convection heat transfer due to Lorentz forces in a porous lid-driven cubic enclosure with hot obstacle," *Computational Methods and Applied Mechanics*, vol. 338, pp. 491–505, 2018.

[7] A. Prasad and J. Koseff, "Combined forced and natural convection heat transfer in a deep lid-driven cavity flow," *International Journal of Heat and Fluid Flow*, vol. 17, pp. 460–467, 1996.

[8] T. Cheng and W. Liu, "Effect of temperature gradient orientation on the characteristics of mixed convection flow in a lid-driven square cavity," *Computers and Fluids*, vol. 39, no. 6, pp. 965–978, 2010.

[9] K. Gangawane and B. Manikandan, "Mixed convection characteristics in lid-driven cavity containing heated triangular block," *Chinese Journal of Chemical Engineering*, vol. 25, no. 10, pp. 1381–1394, 2017.

[10] M. Wessels, D. Schmeling, J. Bosbach, and C. Wagner, "On the impact of the aspect ratio on the formation of large-scale structures in turbulent mixed convection in a cuboidal sample," *International Journal of Heat and Fluid Flow*, vol. 76, pp. 231–241, 2019.

[11] M. Chakkingal, J. de Geus, S. Kenjereš, I. Ataei-Dadavi, M. Tummers, and C. Kleijn, "Assisting and opposing mixed convection with conjugate heat transfer in a differentially heated cavity filled with coarse-grained porous media," *International Communications in Heat and Mass Transfer*, vol. 111, p. 104457, 2020.

[12] R. Taher and C. Abid, "Experimental determination of heat transfer in a Poiseuille-Rayleigh-Benard flow," *Heat and Mass Transfer*, vol. 54, no. 5, pp. 1453–1466, 2018.

[13] R. Zhu, P. Zhou, J. Li, and C. Zhou, "CFD model evaluation in mixed convection with high Richardson number," *International Journal of Heat and Mass Transfer*, vol. 149, p. 119133, 2020.

[14] C. Gau, C. Liu, T. Huang, and W. Aung, "Secondary flow and enhancement of heat transfer in horizontal parallel-plate and convergent channels heating from below," *International Journal of Heat and Mass Transfer*, vol. 42, no. 14, pp. 2629–2647, 1999.

[15] O. Rahli, R. Bennacer, K. Bouhadef, and D. Ameziani, "Three-dimensional mixed convection heat and mass transfer in a rectangular duct: case of longitudinal rolls," *Numerical Heat Transfer Part A: Applications*, vol. 59, no. 5, pp. 349–371, 2011.

[16] P. Rodriguesa, C. Bisernib, C. de Escobara, L. Rochac, L. Isoldia, and E. dos Santosa, "Geometric optimization of a lid-driven cavity with two rectangular intrusions under mixed convection heat transfer: A numerical investigation motivated by constructal design," *International Communications in Heat and Mass Transfer*, vol. 117, p. 104759, 2020.

[17] A. Ozsunar, S. Baskaya, and M. Sivrioglu, "Numerical analysis of Grashof number, Reynolds number and inclination effects on mixed convection heat transfer in rectangular channels," *International Communications in Heat and Mass Transfer*, vol. 28, no. 7, pp. 985–994, 2001.

[18] L. Bammou, K. Omari, S. Blancher, Y. L. Guer, B. Benhamou, and T. Mediouni, "A numerical study of the longitudinal thermoconvective rolls in a mixed convection flow in a horizontal channel with a free surface," *International Journal of Heat and Fluid Flow*, vol. 42, pp. 265–277, 2013.

[19] J. Meyer and M. Everts, "Single-phase mixed convection of developing and fully developed flow in smooth horizontal circular tubes in the laminar and transitional flow regimes," *International Journal of Heat and Mass Transfer*, vol. 117, pp. 1251–1273, 2018.

[20] J. Meyer, M. Everts, N. Coetzee, K. Grote, and M. Steyn, "Heat transfer coefficients of laminar, transitional, quasi-turbulent and turbulent flow in circular tubes," *International Communications in Heat and Mass Transfer*, vol. 105, pp. 84–106, 2019.

[21] A. Bashir, M. Everts, R. Bennacer, and J. Meyer, "Single-phase forced convection heat transfer and pressure drop in circular tubes in the laminar and transitional flow regimes," *Experimental Thermal and Fluid Science*, vol. 109, p. 109891, 2019.

[22] M. Everts and J. Meyer, "Flow regime maps for smooth horizontal tubes at a constant heat flux," *International Journal of Heat and Mass Transfer*, vol. 117, pp. 1274–1290, 2018.

[23] P. Vijayan, M. Sharma, and D. Saha, "Steady state and stability characteristics of single-phase natural circulation in a rectangular loop with different heater and cooler orientations," *Annals of Nuclear Energy*, vol. 31, no. 8, pp. 925–945, 2007.

[24] P.K.Vijayan, V.K.Bhojwani, M.H.Bade, M.Sharma, A.K.Nayak, D.Saha, and R.K.Sinha, "Investigations on the effect of heater and cooler orientation on the steady state, transient and stability behaviour of single-phase natural circulation in a rectangular loop," *Technical report, India*, 2002.

[25] N. Kumar, J. Doshi, and P. Vijayan, "Investigations on the role of mixed convection and wall friction factor in single-phase natural circulation loop dynamics," *Annals of Nuclear Energy*, vol. 38, pp. 2247–2270, 2011.

[26] X. Guo, Z. Sun, J. Wang, S. Yu, and L. Gao, "Numerical simulation of the transient behaviors in an open natural circulation system with a large scale," *Annals of Nuclear Energy*, vol. 77, pp. 83–93, 2014.

[27] D. Basu, S. Bhattacharyya, and P. Das, "Development of a unified model for the steady-state operation of single-phase natural circulation loops," *Applied Thermal Engineering*, vol. 62, pp. 452–462, 2013.

[28] A. Rahmani, A. Boutriaa, and A. Hadef, "An experimental approach to improve the basin type solar still using an integrated natural circulation loop," *Energy Conversion and Management*, vol. 93, pp. 298–308, 2015.

[29] M. Krishnani and D. N. Basu, "Computational stability appraisal of rectangular natural circulation loop: Effect of loop inclination," *Annals of Nuclear Energy*, vol. 107, pp. 17–30, 2017.

[30] P. K. Vijayan, A. K. Nayak, D. Saha, and M. R. Gartia, "Effect of loop diameter on the steady state and stability behaviour of single-phase and two-phase natural circulation loops," *Science and Technology of Nuclear Installations*, vol. 2008, p. 672704, 2008.

[31] D. Basu, S. Bhattacharyya, and P. Das, "Development of a unified model for the steady-state operation of single-phase natural circulation loops," *International Journal of Heat and Mass Transfer*, vol. 62, pp. 452–462, 2013.

[32] A. K. Nayak, P. K. Vijayan, D. Saha, and V. V. Raj, "Mathematical modelling of the stability characteristics of a natural circulation loop," *Mathematical and Computer Modelling*, vol. 22, no. 9, pp. 77–87, 1995.

[33] S. Choi and J. Eastman, "Enhancing thermal conductivity of fluids with nanoparticles," *ASME International Mechanical Engineering Congress and Exposition*, vol. 231, pp. 99–105, 1995.

[34] K. Khanfer, K. Vafai, and M. Lightstone, "Buoyancy-driven heat transfer enhancement in a two-dimensional enclosure utilizing nanofluids," *International Journal of Heat and Mass Transfer*, vol. 46, pp. 3639–3653, 2003.

[35] H. Oztop and E. Abu-Nada, "Numerical study of natural convection in partially heated rectangular enclosures filled with nanofluids," *International Journal of Heat and Fluid Flow*, vol. 29, pp. 1326–1336, 2008.

[36] M. Mamourian, K. M. Shirvan, R. Ellahi, and A. Rahimi, "Optimization of mixed convection heat transfer with entropy generation in a wavy surface square lid-driven cavity by means of taguchi approach," *International Journal of Heat and Mass Transfer*, vol. 102, pp. 544–554, 2016.

[37] M. Roy, S. Roy, and T. Basak, "Role of moving horizontal walls on entropy generation during mixed convection within entrapped triangular cavities," *International Communications in Heat and Mass Transfer*, vol. 85, pp. 92–99, 2017.

[38] R. Nayak, S. Bhattacharyya, and I. Pop, "Heat transfer and entropy generation in mixed convection of a nanofluid within an inclined skewed cavity," *International Journal of Heat and Mass Transfer*, vol. 102, pp. 596–609, November 2016.

[39] H. Abbassi, M. Magherbi, and A. Brahim, "Entropy generation in Poiseuille-Benard channel flow," *International Journal Thermal Science*, vol. 42, pp. 1081–1088, 2003.

[40] H. Khorasanizadeh, M. Nikfar, and J. Amani, "Entropy generation of Cu-water nanofluid mixed convection in a cavity," *Eur. J. Mech. B. Fluids*, vol. 37, pp. 143–152, 2013.

[41] M. Bahiraei, A. R. Gorjaei, and A. Shahidian, "Investigating heat transfer and entropy generation for mixed convection of CuO-water nanofluid in an inclined annulus," *Journal of Molecular Liquids*, vol. 248, pp. 36–47, 2017.

[42] J. Boussinesq, *Theorie Analytique de la Chaleur*. Gauthier-Villars, Paris, 1897.

[43] D. Josef, *Stability of Fluid Motions II*. Springer, Berlin, 1976.

[44] A. Oberbeck, "Ueber die warmeleitung ¨ der flüssigkeiten bei berücksichtigung der stromungen ¨ infolge von temperaturdifferenzen," *Annual Rev Chem*, vol. 7, p. 271, 1879.

[45] D. Gray and A. Giorgini, "The validity of the Boussinesq approximation for liquids and gases," *Int. J. Heat Mass Transf.*, vol. 19, no. 5, pp. 545–551, 1976.

[46] J. Frohlich, P. Laure, and R. Peyret, "Large departures from Boussinesq approximation in Rayleigh-Benard problem," *Physics of Fluids A: Fluid Dynamics*, vol. 4, no. 7, 1992.

[47] Y. Zhang and Y. Cao, "A numerical study on the non-Boussinesq effect in the natural convection in the horizontal annulus," *Physics of Fluids*, vol. 040902, 2018.

[48] M. Krishnani and D. Basu, "On the validity of Boussinesq approximation in transient simulation of single-phase natural circulation loops," *International Journal of Thermal Sciences*, vol. 105, pp. 224–232, 2016.

[49] F. Massaioli, R. Benzi, and S. Succi, "Exponential tails in 2-dimensional Rayleigh-Benard convection," *Europhys. Lett.*, vol. 21, no. 3, p. 305, 1993.

[50] A. Bartoloni, C. Battista, S. Cabasino, and P. Paolucci, "LBE simulations of Rayleigh-Benard convection on the ape100 parallel processor," *Int. J. Mod. Phys. C*, vol. 4, pp. 993–1006, 1993.

[51] R. Benzi, R. Tripiccione, F. Massaioli, S. Succi, and S. Ciliberto, "On the scaling of the velocity and temperature structure functions in Rayleigh-Benard convection," *Europhys. Lett.*, vol. 25, p. 341, 1994.

[52] J. Burgos, I. Cuesta, and C. Salvena, "Numerical study of laminar mixed convection in a square open cavity," *Int. J. Heat Mass Transfer*, vol. 195, pp. 165–174, 2016.

[53] B. Chopard and M. Droz, *Cellular Automata Modelling of Physical Systems*. Cambridge University Press, 1998.

[54] G. McNamara and G. Zanetti, "Use of the Boltzmann equation to simulate lattice gas automata," *Physical Review Letters*, vol. 61, no. 20, pp. 2332–2335, 1988.

[55] S. Hou, Q. Zou, S. Chen, G. Doolen, and A. Cogley, "Simulation of cavity flow by the lattice Boltzmann method," *Journal of Computational Physics*, vol. 118, pp. 329–347, 1995.

[56] T. Kruger, H. Kusumaatmaja, A. Kuzmin, O. Shardt, G. Silva, and E. Viggen, *The Lattice Boltzmann Method: Principles and Practice*. Springer, 2016.

[57] S. Succi, E. Foti, and F. Higuera, "Three-dimensional flows in complex geometries with the lattice Boltzmann method," *Europhysics Letter*, vol. 10, pp. 433–438, 1989.

[58] P. L. Bhatnagar, E. P. Gross, and M. Krook, "A model for collision processes in gases," *Physical Review*, vol. 94, no. 3, pp. 511–525, 1954.

[59] Y. Peng, C. Shu, and Y. T. Chew, "Simplified thermal lattice Boltzmann model for incompressible thermal flows," *Physical Review E*, vol. 68, p. 026701, 2003.

[60] L. S. Luo, "Lattice-gas automata and lattice Boltzmann equations for two-dimensional hydrodynamics," Ph.D. dissertation, Georgia Institute of Technology, 1993.

[61] X. Shan and H. Chen, "Simulation of nonideal gases and gas-liquid phase transitions by the lattice Boltzmann equation," *Physical Review E*, vol. 49, pp. 2941–2948, 1994.

[62] Z. Guo and C. Shu, *Lattice Boltzmann method and its applications in engineering*. World Scientific,Singapore, 2013.

[63] H. Dixit and V. Babu, "Simulation of high Rayleigh number natural convection in a square cavity using lattice Boltzmann method," *International Journal of Heat and Mass Transfer*, vol. 49, pp. 727–739, 2006.

[64] S. Suslov and S. Paolucci, "Stability of natural convection flow in a tall vertical enclosure under non-Boussinesq conditions," *International J. heat mass transfer*, vol. 38, no. 12, pp. 2143–2157, 1995.

[65] D. Chenoweth and S. Paolucci, "Natural convection in an enclosed vertical air layer with large horizontal temperature differences," *J. Fluid Mech.*, vol. 169, pp. 173–210, 1986.

[66] H. Huang and X.-Y. Lu, "Simulation of gas flow in microtubes by lattice Boltzmann method," *International Journal of Modern Physics C*, vol. 20, no. 8, pp. 1145–1153, 2009.

[67] M. Bouafia, S. Hamimid, and M. Guellal, "Non-Boussinesq convection in a square cavity with surface thermal radiation," *International Journal of Thermal Sciences*, vol. 96, pp. 236–247, 2015.

[68] M. Moallemi and K. Jang, "Prandtl number effects on laminar mixed convection heat transfer in a lid-driven cavity," *Int. J. Heat Mass transfer*, vol. 35, no. 8, pp. 1881–1892, 1992.

[69] M. Bahiraei, A. R. Gorjaei, and A. Shahidian, "Investigating heat transfer and entropy generation for mixed convection of CuO-water nanofluid in an inclined annulus," *Journal of Molecular Liquids*, vol. 248, pp. 36–47, 2017.

[70] P. Mayeli and G. Sheard, "A comparison between Boussinesq and non-Boussinesq approximations for numerical simulation of natural convection in an annulus cavity," *21st Australasian Fluid Mechanics Conference Adelaide, Australia 10-13 December 2018*, 2018.

[71] M. Sahu, J. Sarkar, and L. Chandra, "Transient thermo-hydraulics and performance characteristics of single-phase natural circulation loop using hybrid nanofluids," *International Communications in Heat and Mass Transfer*, vol. 110, 2020.

[72] G. Desrayaud, A. Fichera, and G. Lauriat, "Two-dimensional numerical analysis of a rectangular closed-loop thermosiphon," *Applied Thermal Engineering*, vol. 50, pp. 187–196, 2013.

[73] P. Vijayan, "Experimental observations on the general trends of the steady state and stability behaviour of single-phase natural circulation loops," *Vol 215(1-2)*, pp. 139–152, 2002.

[74] Z. Ghorbanali and S. Talebi, "Investigation of a nanofluid-based natural circulation loop," *Progress in Nuclear Energy*, vol. 129, 2020.

[75] M. Kumar and P. K. Mondal, "Bejan's flow visualization of buoyancy-driven flow of a hydromagnetic casson fluid from an isothermal wavy surface," *Physics of Fluid*, vol. 33, 2021.

भारतीय प्रौद्योगिकी संस्थान गुवाहाटी
Indian Institute of Technology Guwahati